UNIVERSITÀ DEGLI STUDI DI PADOVA

Sede Amministrativa: Università degli Studi di Padova

Dipartimento di Scienze Chimiche

Scuola di Dottorato di Ricerca in Scienza e Ingegneria dei Materiali

XXV ciclo

STUDY OF THE STRUCTURE AND THE ELECTRONIC PROPERTIES OF THE OXIDE/OXIDE INTERFACES IN MIXED METAL OXIDES

Direttore della Scuola : Ch.mo Prof. Gaetano Granozzi

Supervisore : Ch.mo Prof. Gaetano Granozzi

Dottorando : Askia Enrico Reeder

To my dearest love Samantha

my dearest daughter Maria Ester

and our dearest parents

ABSTRACT

A very important role is played by metal oxides in many areas of chemistry, physics, and materials science. Transition metal and rare-earth metal elements are able to form a large diversity of oxide compounds which can adopt an ample array of atomic structures and electronic properties that can exhibit metallic, semiconductor, or insulator characteristics. In technological applications, metal oxides are used in the fabrication of microelectronic components, sensors, fuel cells, coatings to protect surfaces against corrosion, and as catalysts. In this thesis we have decided to study two known catalytic materials Zirconia-Titania and Ceria-Titania mixed oxides. For both materials bibliography principally concerns powders thus in order to better study their interfaces, of which a deeper study is still lacking, we decided to deposit zirconia and ceria as thin films onto rutile TiO_2(110).

We first studied the zirconia-titania system by depositing an ultra-thin film of zirconium oxide via a metal-organic precursor: Zirconium Tetra *tert*-Butoxide. The deposition was carried at three different substrate temperatures 677 K, 738 K, 773 K in five stages of a minute each and the results were traced by using XPS. The chemical characterization via XPS showed an interesting chemistry undergoing on the substrate's surface and we have observed the formation of carbonaceous species at the interface. Zirconium appeared to be at its highest oxidation state while titanium was seen to undergo reduction with each successive deposited layer. The ratio of the Zr/Ti signals showed that zirconia didn't completely wet the surface. Furthermore, no long range order was observed via LEED. XPD measurements showed that zirconia does not form a substitutional oxide with titania. However with the aid of computer simulation we deduced that very likely zirconia forms nanochains on the surface of TiO_2(110). This surface was exposed to 100 L of pyridine to test its acidity.

In the case of ceria, we have deposited the oxide on a heated TiO_2(110) substrate via metal evaporation from a Mo crucible since the process is rather easy and garners clean deposits. During deposition the substrate was kept at 677 K and in an O_2 environment of $5.2 \cdot 10^{-6}$mbar, and, in order to obtain an ordered homogeneous surface the sample was further annealed in the same environment at 900 K. Through LEED imaging different phases were observed and were dependent on sample history and film thickness. Via computer simulation these phases were then referred to the parent oxide in order to better comprehend the difference in respect to the bulk phase. All films showed cerium present at Ce(III). Ultra-violet Photoelectron Spectroscopy showed the electronic properties of the film showing a binding energy shift and the population of Ce4f states due to stabilization of Ce(III) by TiO_2(110). The reactivity of the ceria-titania system was the probed by using methanol and ethanol. Results showed that the addition of ceria opened the dehydrogenation path from alcohol to aldehyde. We have

observed that oxygen pre-oxidation of the CeO_x-TiO_2(110) system had an impact on its selectivity by opening also a dehydration path from methanol and ethanol to respectively, methane and ethylene. This alternative path was viable only for low cerium oxide coverages as interaction with the substrate was needed for dehydration to occur. Aldehyde formation was seen to occur at mild temperatures (330 K) and was independent of film thickness. Subsequently, ceria-titania mixed oxide powders were characterized via XPS and we have observed that for increasing amount of cerium the element gradually became present at its highest oxidation state Ce(IV). By XPS we have also determined the formation of a very intimate composite between the two oxides by observing the increasing the full width at half maximum of the Ti2p peak for increasing amounts of cerium. Furthermore, compositional calculation showed that cerium had the tendency to disperse within the titania particles. These data helped to uncover a possibly good recipe for the formation of cerium titanate a composite with good oxygen storage capacity.

ABSTRACT

Un ruolo molto importante è svolto dagli ossidi metallici in molti settori della chimica, fisica e scienza dei materiali. I metalli di transizione e le terre rare sono in grado di formare una grande diversità di composti ossidici che possono adottare un'ampia gamma di strutture atomiche ed proprieta' elettroniche che possono esibire caratteristiche metalliche, semiconduttrici o isolanti. In applicazioni tecnologiche, gli ossidi metallici sono impiegati nella fabbricazione di componenti microelettronici, sensori, celle a combustibile, rivestimenti per proteggere le superfici dalla corrosione, e come catalizzatori. In questa tesi abbiamo deciso di studiare due noti materiali catalitici: gli ossidi misti di Zirconia-Titania Ceria-Titania. Per entrambi i materiali la bibliografia riguarda principalmente le polveri quindi, al fine di studiare meglio le loro interfacce, di cui uno studio più approfondito e' tuttora neccessario, abbiamo deciso di depositare film sottili di ossido di zirconio e ossido di cerio su rutilo TiO_2(110).

Abbiamo prima studiato il sistema zirconia-titania depositando un film ultra-sottile di ossido di zirconio mediante un precursore metallo-organico: Zirconio Tetra *tert-butossido.* La deposizione è stata effettuata a tre diverse temperature del substrato 677. K, 738 K, 773 K in cinque fasi di un minuto ciascuno. La caratterizzazione mediante XPS ha mostrato una chimica interessante sulla superficie del substrato e abbiamo osservato la formazione di specie carboniose all'interfaccia. Lo zirconio sembrava essere nel suo piu' alto stato di ossidazione mentre il titanio è stato visto gradualmente ridursi con ogni successive strato di deposito. Il rapporto dei segnali Zr/Ti ha mostrato che la zirconia non ha completamente coperto la superficie. Inoltre,tramite LEED non si e' osservato nessun ordine a lungo raggio. Misure XPD ha mostrato che la zirconia non forma un ossido di sostituzione con la titania. Tuttavia, con l'ausilio

di simulazione al computer abbiamo dedotto che la zirconia forma, molto probabilmente nanocatene sulla superficie di TiO_2(110). Questa superficie è stato esposta a 100 L di pyridinina per testarne la acidita'.

Nel caso di ceria, abbiamo depositato l'ossido su un substrato riscaldato di TiO_2 (110) tramite evaporazione del metallo da un crogiolo Mo poiché il processo è piuttosto facile e fornisce depositi puliti. Durante la deposizione il substrato è stata mantenuto a 677 K in un ambiente di $5{,}2 \cdot 10^{-6}$ mbar di O_2, e, al fine di ottenere una superficie omogenea e ordinata il campione è stato ulteriormente sottoposto a trattamento termico nello stesso ambiente a 900 K. Tramite la tecnica LEED sono state osservate differenti fasi dipendenti dalla storia del campione e dallo spessore del film. Tramite simulazione al computer queste fasi sono stati poi riferite rispetto al biossido di cerio per meglio comprendere le differenze rispetto alla fase massiva. Tutti i film hanno mostrato cerio presenti come Ce(III). La Spettroscopia Fotoelettronica a Ultravioletti ha mostrato le proprietà elettroniche del film che mostra uno spostamento in energia di legame e un popolamento degli stati Ce4f. Questo e' dovuto alla stabilizzazione di Ce (III) da parte di TiO_2 (110). Si e' volute osservare la reattività del sistema ceria-titania nei confronti di metanolo ed etanolo. I risultati hanno mostrato che l'aggiunta di ceria ha aperto il percorso della deidrogenazione degli alcoli ad aldeidi. Abbiamo osservato che la pre-ossidazione con ossigeno del sistema CeO_x-TiO_2(110) ha avuto un impatto sulla sua selettività aprendo anche un percorso di disidratazione di metanolo ed etanolo rispettivamente a metano ed etilene. Questa via alternativa era valida solo per basse coperture di ossido di cerio avendo osservato che l'interazione con il substrato è stato necessario perche' avvenga la disidratazione. La formazione di aldeidi fu osservata avvenire a temperature piuttosto (330 K) ed essere indipendente dallo spessore del film. Successivamente sono state caratterizzate tramite XPS delle polveri di ossidi misti di ceria e titania. Abbiamo osservato che per quantità crescenti di cerio l'elemento diventa gradualmente sempre piu' presente al suo stato di ossidazione più alto Ce (IV). Con XPS abbiamo anche determinato la formazione di un composito molto intimo tra i due ossidi osservando l'aumento della larghezza a metà altezza del picco Ti2p per quantità crescenti di cerio. Inoltre, la determinazione della composizione ha mostrato che il cerio ha la tendenza di disperdersi all'interno delle particelle di titania. Questi dati hanno contribuito a scoprire una possibile buona ricetta per la formazione di cerio titanato; un composito con buona capacità di stoccaggio di ossigeno.

CONTENTS

Chapter 2-Experimental Apparatus

Chapter 3-Titanium Dioxide

Chapter 4-The Zirconia-Titania system

Chapter 5-The Ceria-Titania system

Chapter 6-Conclusions

Surface science has dedicated large efforts in the field of the growth of ultrathin film oxides on oxides. A factor explaining the large interest on these composite materials is represented by the relatively ease of assembling together different oxides with different functionalities, obtaining multifunctional platforms capable of integrating complex tasks and to perform advanced operations[1]. The peculiar properties of the oxide/oxide interfaces can arise either from the structural (epitaxial) relationship between the two oxides or from specific chemical interactions at the interface. In the former case it is interesting to observe if the ultrathin film forms a new phase with no bulk counterpart; in the latter, of interest is the possibility to tailor the chemical properties, which finally influence the chemisorption/catalytic properties of the composite material[2]. In fact, catalysts are typical nanomaterials, perhaps the first nanomaterials in wide applications. Catalysis at such a small scale has been the subject of research and development for many years, and indeed the new and remarkable properties of nanomaterials will further influence modern society[3] in many ways. Nanosized materials would not be so interesting and, both, nanoscience and nanotechnology would not be so attractive and exciting fields if nanosystems would behave like their bulk counterparts. Industrial progress and the scientific ability to make, model and manipulate such small systems have introduced a new era which is gaining momentum with every discovery of novel size-induced phenomena. The origin of these properties in nanomaterials depends basically on two contributions: extrinsic (surface phenomena) and intrinsic (quantum confinement effects). The surface to volume ratio increases rapidly when decreasing particle size. Superficial atoms display different properties due to the presence of asymmetric interactions, i.e., in one side they have atoms to interact with but towards the external surface, as evidenced by the number of dangling bonds, this is less so. The same happens with bulk materials but it is not relevant because in bulk the number of atoms at the surface is considerably smaller than that at the volume. This asymmetry is responsible for surface phenomena such as lattice distortion which is needed for accommodating the interacting forces and keeping the total energy as lowest as possible due to the fact that surface atoms have higher energy than those of the bulk. This accommodation of the system has a consequence on its properties, i.e., they exhibit a gradient near the surface which is relevant up to a critical length l_c[4]. The size of this critical length depends on the

potential interaction between the constituents of the nanoparticles and determines two regimes for bulk and surface-based properties of the nanoparticles, i.e., for $D >> lc$ ($D << lc$) the properties of the nanoparticles are mainly determined by the bulk (surface) properties[4, 5]. When a given material has, at least, one dimension being reduced to nanoscale the electronic wavevectors becomes quantized and the system exhibits discrete energy levels. The length scale limit is the de Broglie wavelength, λdB, of an electron in one specific direction. Thus nanoscale systems can be classified by the number of dimensions below λdB. We call a two-dimensional (2D) system one that has only one dimension lower than λdB; good examples are nanosheets. When two dimensions are lower than λdB we have a One-dimensional (1D) system; nanowires and nanotubes belong to this category. Special cases are the so-called quantum dots whose all three dimensions are lower than λdB and we name these as 0D systems. Their energy spectra are discrete and the system can be viewed as an artificial atom.

There are several techniques for growing nanoscale materials and one of these is chemical vapor deposition. The growth of a film by deposition from the vapor phase allows the production of drastically different phases depending on growth conditions, through an independent and careful control of particle size size and composition and kinetic energy of the atoms of the deposit, in ways precluded to massive phase crystal growth. The control of the thermodynamic parameters allows a direct epitaxial deposition in preferential directions. Unfortunately, working away from thermodynamic equilibrium conditions, the film often shows a high defectuality. Furthermore, the kinetic factors play a fundamental role in processes involving surface diffusion of the species involved in the epitaxial growth, both horizontally and vertically. When the diffusion is too slow to reach equilibrium conditions, one can obtain metastable phases. The substrate of choice in this thesis was rutile TiO_2(110) because its surface and chemical properties are the most studied as demonstrated by the extensive literature[6, 7]. Thus, this substrate is a good system to discover and test properties of new deposited films. For this study we have chosen to study the oxides of zirconium and cerium. Zirconia has been widely used in many technical applications such as gas sensors, protective coatings and heterogeneous catalysis. In particular, in heterogeneous catalysis, zirconia has been used in many catalytic reactions not only as the metal catalysts' support but also as the catalyst itself; it can be also used as an additive to improve the catalytic performances of the catalysts[8]. Cerium oxide is currently under extensive investigation because of its intriguing physical-chemical properties deriving from the presence of different oxidation states. These are associated with the unfilled 4f electron shell, which make cerium oxide a promising material for various applications and devices. Because of its prominent ability to store and release oxygen, the use of ceria is attractive for catalysis and fuell cells[9]. Both of these oxides have been studied in powder form , when mixed with titania having recently gained

importance as photocatalytic materials[10, 11] however, a detailed study of the interface is still lacking and hence we undertook the task of doing so. We believe that the deposition of an ultra-thin film is the best way to study the composition and structure of the interface of these oxides on rutile. In the case of ceria we further investigated its reactivity by using two probe molecules: methanol and ethanol. The recent finding of the $Au/CeO_x/TiO_2(110)$ system as an effective water-gas-shift catalyst[12] and more importantly the use of the CeO_2-ZrO_2 system as an effective alcohol dehydrogenation[13-15] for fuel production spurned us in finding if the CeO_2-TiO_2 would work just as well.

The structure of the thesis is as follows:

In **Chapter 1** I will outline the surface science investigation techniques used to characterize our samples.

In **Chapter 2** I will briefly describe the experimental apparatus.

In **Chapter 3** I will briefly describe the substrate used for film deposition.

In **Chapter 4** I will present and discuss the results obtained from ZrO_2 deposition.

In **Chapter 5** I will outline and discuss the results observed from CeO_2 deposition.

In **Chapter 6** I will present the conclusion and perspectives.

References:

1. H. Y. Hwang, Y. Iwasa, M. Kawasaki, B. Keimer, N. Nagaosa and Y. Tokura, *Nat Mater*, 2012, **11**, 103-113.
2. J. N. Armor, *Catal Today*, 2011, **163**, 3-9.
3. G. Centi and S. Perathoner, *Catal Today*, 2008, **138**, 69-76.
4. A. Alves, F. Berutti and F. Sánchez, in *Nanostructured Materials for Engineering Applications*, eds. C. Bergmann and M. Andrade, Springer Berlin Heidelberg, Editon edn., 2011, pp. 93-117.
5. A. Filho and S. Fagan, in *Nanostructured Materials for Engineering Applications*, eds. C. Bergmann and M. Andrade, Springer Berlin Heidelberg, Editon edn., 2011, pp. 5-22.
6. U. Diebold, *Surface Science Reports*, 2003, **48**, 53-229.
7. C. L. Pang, R. Lindsay and G. Thornton, *Chem Soc Rev*, 2008, **37**, 2328-2353.
8. Y. Han and J. Zhu, *Top Catal*, 2013, **56**, 1525-1541.
9. B. Kaemena, S. D. Senanayake, A. Meyer, J. T. Sadowski, J. Falta and J. I. Flege, *The Journal of Physical Chemistry C*, 2012, **117**, 221-232.
10. M. J. Muñoz-Batista, M. N. Gómez-Cerezo, A. Kubacka, D. Tudela and M. Fernández-García, *Acs Catal*, 2013, **4**, 63-72.
11. A. Kitiyanan, S. Sakulkhaemaruethai, Y. Suzuki and S. Yoshikawa, *Compos Sci Technol*, 2006, **66**, 1259-1265.
12. J. B. Park, J. Graciani, J. Evans, D. Stacchiola, S. Ma, P. Liu, A. Nambu, J. Fernandez Sanz, J. Hrbek and J. A. Rodriguez, *Proceedings of the National Academy of Sciences of the United States of America*, 2009, **106**, 4975-4980.
13. G. A. Olah, *Angewandte Chemie International Edition*, 2005, **44**, 2636-2639.
14. M. Ni, D. Y. C. Leung and M. K. H. Leung, *Int J Hydrogen Energ*, 2007, **32**, 3238-3247.
15. V. Subramani and C. Song, in *Catalysis: Volume 20*, The Royal Society of Chemistry, Editon edn., 2007, vol. 20, pp. 65-106.

CHAPTER 1

INVESTIGATION TECHNIQUES

1.1 X-RAY PHOTOELECTRON SPECTROSCOPY

It is beyond the scope of this work a description and a detailed discussion of the characteristics of X-ray photoelectron spectroscopy **(X**-ray **P**hotoelectron **S**ectroscopy, also known as ESCA: Electron Spectroscopy for Chemical Analysis); Comprehensive information can be found in many texts generally dealing with the nature surface analysis,[1-3] as highlighted be the acronym this spectroscopy exploits the well-known photoelectric effect.

Thanks to this phenomenon, discovered by Einstein, an electron ejected due to the process of photoemission has a kinetic energy equal to:

$$E_k = h\nu - E_{b.} \qquad (1.1)$$

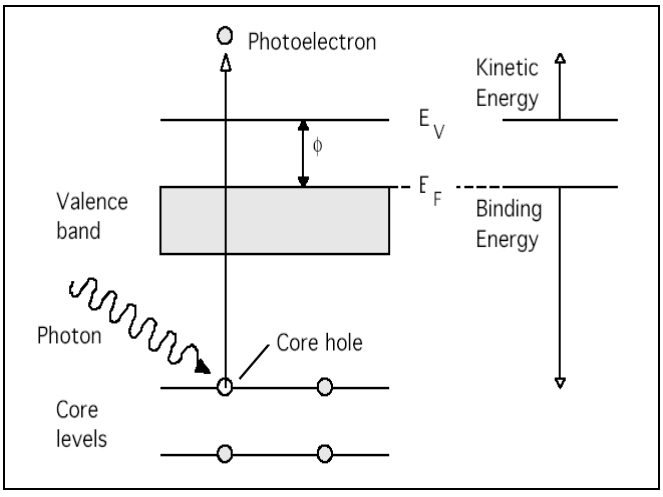

Fig 1.1: Diagram of the energy levels of a metal sample in electrical contact with a spectrometer during an XPS process.

In which, by the law of energy conservation, an incident photon transfers all its energy $h\nu$ to an electron bound to an atom with energy E_b. The binding energies are well known and characteristic of each element so that the measurement of E_b for atoms constituting a solid represents analysis technique of the material.

In the case of a solid metallic sample an electrical contact is made with the spectrometer, so that their electrochemical potentials (or Fermi levels) are equal. In passing from the surface of the sample to the spectrometer, the photoelectron will feel a potential equal to the difference between the work function of the spectrometer ϕ_{spec} and that of the sample ϕ_c. The kinetic energy on the surface of the latter, E_k^1, is measured as E_k within the analyzer such that:

$$E_k = E_k^1 + (\phi_c - \phi_{spec}). \quad (1.2)$$

Taking the Fermi level as reference we can rewrite the equation:

$$h\nu = E_b^F (k) + E_k + \phi_{spec}, \quad (1.3)$$

where $E_b^F (k)$ is the *binding energy* relative to the Fermi level. It can be seen that the work function of the sample ϕ_c is not involved. Additional care is used towards insulating samples due to charging phenomena and therefore uncertainty in locating the Fermi level within the band gap, in these cases the *binding energies* should be reported to the limits of the valence bands which are available in an XPS spectrum. Assuming that the wave function of the system is expressed as a single Slater determinant of single-electron orbitals, for each discrete value of E_b (which corresponds to a specific peak in the spectrum) we can associate the binding energy for the specific single-electron level from which the photoemission originates.

The X-ray beam is obtained from sources constituted by anodes of aluminum, magnesium, silicon or zirconium (in my work, I have used the first two) which are subjected to high energy electron bombardment, resulting in ionization of *core* levels and subsequent irradiative relaxation. The exploited emission energies are the $K_{\alpha 1}$ and $K_{\alpha 2}$ which are relative to the $2p_{3/2} \rightarrow 1s$ and $2p_{1/2} \rightarrow 1s$ decays. The energies and bandwidths characteristic of the two XPS sources used are shown in the table below, the bandwidth affects the resolution of photoelectron energy.

Line	**Energy (eV)**	**Linewidth (eV)**
Mg K_α	1253.6	0.7
Al K_α	1486.6	0.85
Si K_α	1739.5	1.0
Zr M_ξ	151.4	0.77

A photoelectronic spectrum is generally characterized by a primary structure, given by the *core* levels, valence levels and Auger series, and a secondary fine structure, which highlights the limitations of the single-electron approximation. High energy X-rays are used for *core* levels, whereas for the emission of

valence electrons low energy X-rays or UV radiation (3-100 eV) are used. In this case we speak of photoelectronic spectroscopies in the ultraviolet regions or **UPS** (**U**ltraviolet **P**hotoelectron **S**pectroscopy).

This technique uses as light source a He discharge lamp with energies in the range from 21.2 - 40.8 eV, which are sufficient to allow the analysis of valence band of many solids. The intensity of the sources are high with very narrow exciting linewidths so that the energy resolution of these experiments is generally limited by the analyzer. With UPS we study the electronic configurations in the valence shells and bonding orbitals present in a solid rather than determine its chemical composition.

1.1.1 Primary structure of an XPS spectrum

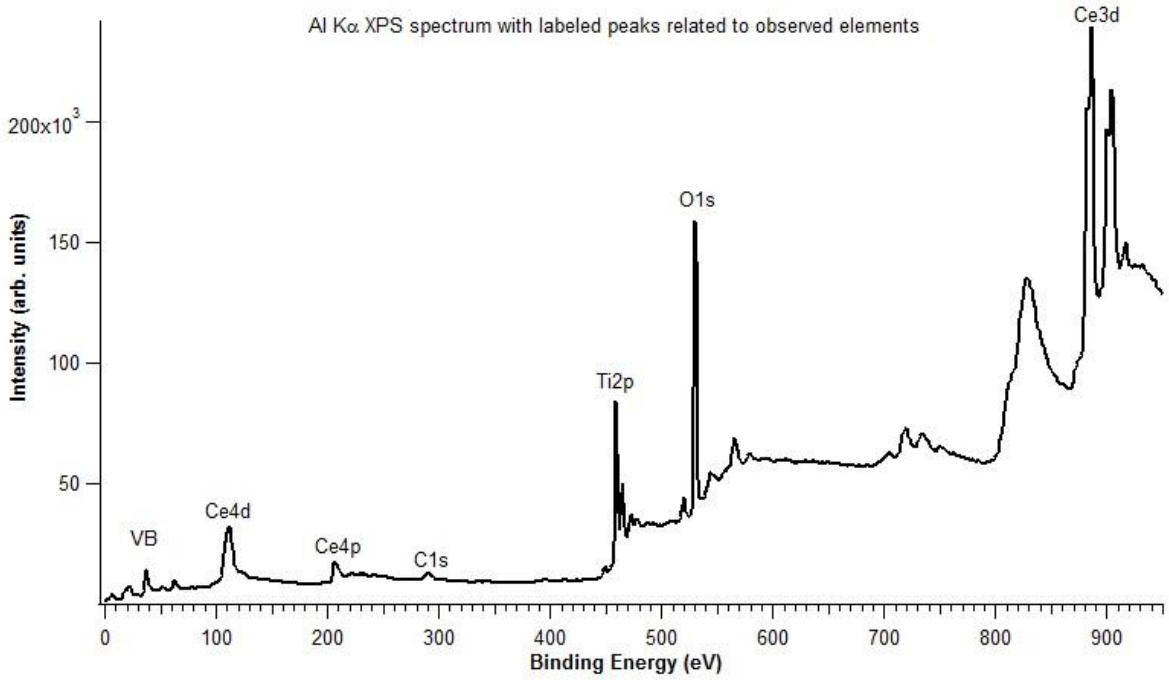

Figure 1.2: XPS AlKα spectrum, you can see the peaks relating to Ce4d, Ce4p, C1s, Ti2p, O1s and Ce3d.

The absorption of the photon occurs within a time estimated at 10^{-16} sec after which follows ionization by expulsion of an electron from one of the *core* levels (appearing in a photoelectron spectrum with peaks at *binding energies* above 20 eV) , or valence, and the kinetic energy is analyzed.

The spectrum exhibits a typical structure consisting of sharp peaks and long tails in the entire range of investigation. The peaks correspond to characteristic energies of electrons that escape from the solid without energy loss due to inelastic collisions. The tails with the highest energy are related to electrons that have been subjected to inelastic *scattering* with loss of energy along their path exiting the solid.

Photoemission from electronic states p, d and f with non-zero orbital moment produce a doublet of spin-orbit, for example $3d_{3/2} \rightarrow 3d_{5/2,}$ where the subscripts correspond to the value of the total angular momentum $J_+ l + m = s = 5/2$ and $J_- = l - m_s = 3/2$. The ratio of the peak intensities is given by the ratio $(2J_- 1) / (2J_+ 1)$, in this case 2:3.

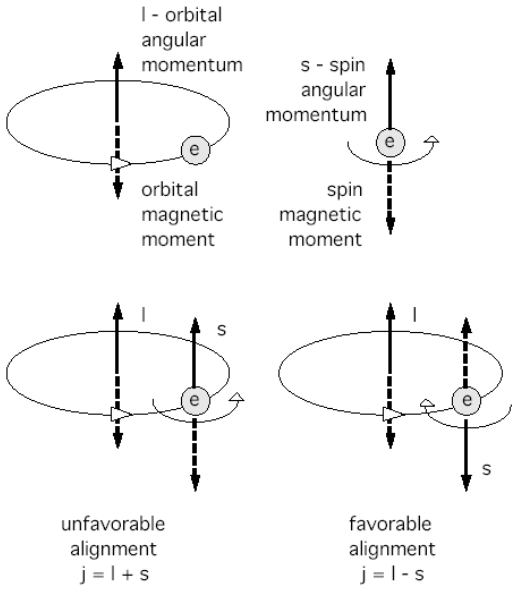

Fig 1.3: pictorial representation of the possible spin-orbit coupling.

The amplitude of a single peak, however, intended as the width at half maximum or FWHM *(Full Width* at *Half Maximum)* corresponds to the convolution of three contributions. ΔE_n is the natural width of the *core* level, correlated to the lifetime of the excited ionic state resulting from the photoionization process via the Heisenberg uncertainty principle; ΔE_p is the line width of the exciting X-ray source; ΔE_a is the resolution of the analyzer:

$$\Delta E = \sqrt{\Delta E_a^2 + \Delta E_p^2 + \Delta E_n^2} \qquad (1.4)$$

This equation assumes that individual components have a Gaussian behavior. The peaks that are very close together and un-resolved giving rise to a band structure below 20 eV, in binding energy, are due to electrons coming from the levels involved in the formation of delocalized orbitals or bonding: for this they are known as **valence levels**. The upper limit of the valence band for conductive materials is the Fermi level, taken as zero by convention on the binding energy scale. The relative intensity of a photoelectron peak depends firstly on photoemission cross section of the energy levels of the

investigated elements (see section 1.1.2) which, in the case of the valence levels, are less intense than *core* levels.

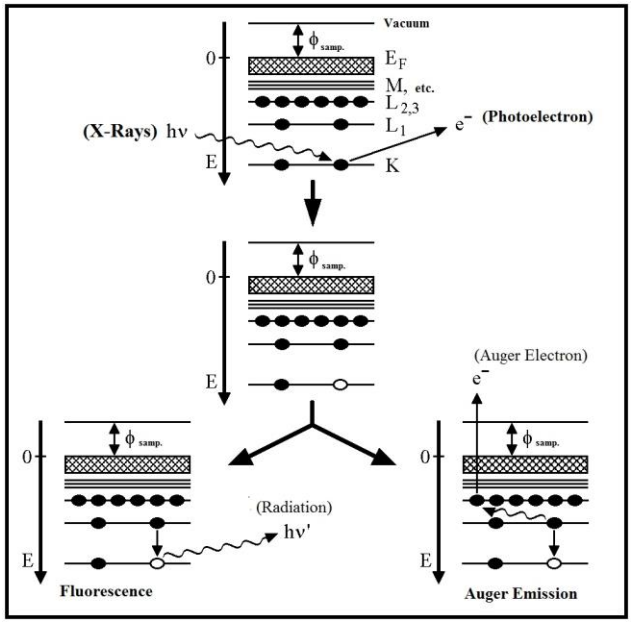

Figure 1.4: Relaxation modes for a *core* electron hole caused by a photoionization event; we have distinguished the fluorescence and Auger emission processes.

In Figure 1.4, we can observe that in XPS after photoemission, the outer shells of the atom undergo relaxation, thanks to the Coulomb attraction generated by the core, after the removal of an electron inside the *core,* (2s or 2p electron from the L shell) with the formation of a hole. This hole can be filled by an electron in the M shell (3s, 3p and 3d) or from the valence band (V). The energy released can give rise to luminescence or ionize a second electron from the shells M or V. In the latter case, the process is called **Auger-type** and is dominant in elements with atomic number $Z \leq 35$. The energy of an Auger peak is independent of incident photon energy while the energy of a photoelectron varies linearly with the incident photon energy.

1.1.2 Secondary structure of the XPS spectrum

As a result of the formation of a vacancy in the inner shell through the ejection of a photoelectron, the rearrangement of the outer shell orbital may not necessarily proceed to the atomic ground state of the hole[4]. The outer electrons can also enter an excited state *(electron shake-up)* or into the continuum *(electron shake-off),* and thus less energy is transferred to the outgoing electron. These transitions that produce final excited states result in a satellite structures at the high *binding energy* (lower kinetic energy) part of the photoemission peaks.

The exact *binding energy* of an electron in an element also depends on its chemical environment. If we consider a *core* level, the energy of an electron in this state is determined by the Coulomb interaction with other electrons and the attractive potential of the nucleus. Any change in the near chemical environment of the element will evolve into a spatial redistribution of valence electrons and thus the formation of a different potential felt by the *core* electron. This redistribution influences the potential of the *core* electrons and results in a variation of their *binding energy* and is called *chemical shift*. This concept is based on the idea that internal electrons perceive an energy alteration due to the variation of the contribution in the valence shell to the potential, based on the chemical bond of the external electron. In practice, the valence electrons are attracted away or towards the nucleus depending on the type of bond. The greater the electronegativity of the atoms in the vicinity and the more displaced the electronic charge from the atom will be and greater will be the *binding energy* observed for the *core* electrons.

1.1.3 Quantitative analysis: attenuation length and inelastic cross section

That being said we will introduce two quantities that will help us to analyze the Photoelectronic spectroscopy: the inelastic attenuation length **(I**nelastic **M**ean **F**ree **P**ath) and the photoemission cross section of emitting elements.

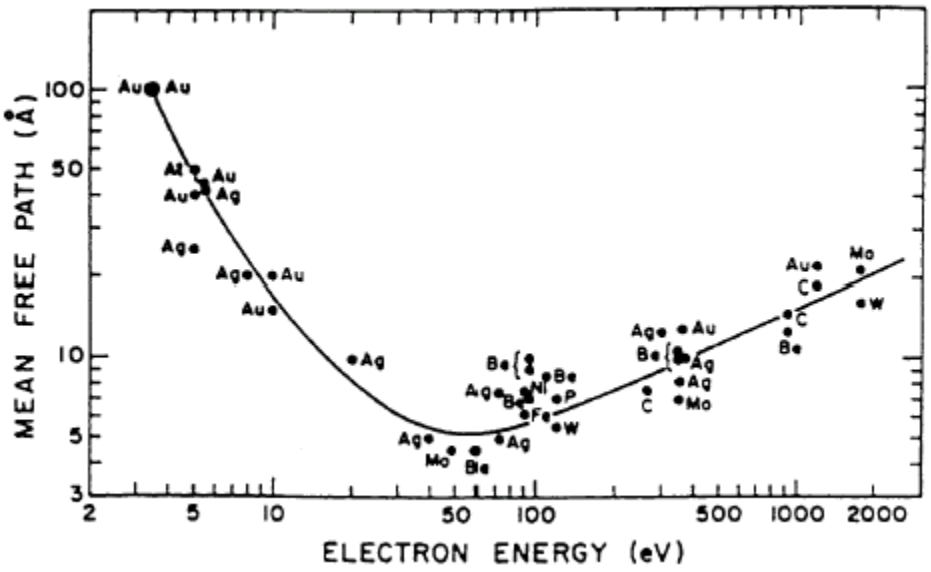

Figure 1.5: Experimental dependence of the inelastic attenuation length of the photoelectron kinetic energy for different solids.

The **inelastic attenuation length**, indicated with Λ_e, in a first approximation coincides with the mean free path of the electron between two inelastic collisions. In the typical range of energies for XPS, Λ_e (E_k) follows the empirical law:

$$\Lambda_e(E_k) = \frac{A}{E_k^2} + BE_k^{1/2} \tag{1.5}$$

With *A* and *B* constants tabulated for a number of elemental solids, inorganic and organic compounds and adsorbed gases and E_k is the electron energy in eV. A perfect, rigorous method to include inelastic attenuation is not yet available, its value can be obtained from theory and aimed experiments, Tanuma, Powell and Penn[5-10] have found an empirical formula, called TPP-2 that can calculate the IMFP for electrons of 50-2000 eV. The formula is expressed as:

$$\Lambda_e = \frac{E_k}{\left\{E_p^2\left[\beta\ln(\gamma E_k) - \left(\frac{C}{E_k}\right) + \left(\frac{D}{E_k^2}\right)\right]\right\}} \tag{1.6}$$

$$E_p(eV) = 28.281\left(\frac{N_v\rho}{M}\right)^{1/2} \tag{1.7}$$

E_p is the plasmonic energy for a gas of free electrons, ρ is the density of the bulk material in g / cm^3, N_v is the number of valence electrons per atom or molecule, *M* is the molecular or atomic weight and E_g is the band gap energy, the other terms, dependent on material, correspond to:

$$\beta = \frac{-0.0216 + 0.944}{\left(E_p^2 + E_g^2\right)^{1/2} + 7.39\cdot10^{-4}\rho} \tag{1.8}$$

$$\gamma\frac{0.191}{\sqrt{\rho}} \tag{1.9}$$

$$C = 1.97 - \frac{0.91N_v\rho}{M} \tag{1.10}$$

$$D = 53.4 - \frac{20.8N_v\rho}{M} \tag{1.11}$$

Knowing that photoelectron intensity follows a Lambert-Beer law type (1.12) it is easy to show that 95% of the detected intensity refers to a thickness equal to $3\Lambda_e$.

$$I = I_0\exp\left[\frac{-z}{\Lambda_e(E_k)sen\theta}\right] \tag{1.12}$$

The electrons that lose energy inelastically interacting with the solid contribute to the background. The upward trend of the latter toward low kinetic energies reflects the trend of photoelectron density and therefore the inelastic scattering events for each new emission channel. Based on this knowledge, we

can say that the low values of Λ_e for typical XPS energies give this technique a high surface sensitivity which can be increased by performing measurements at grazing angles.

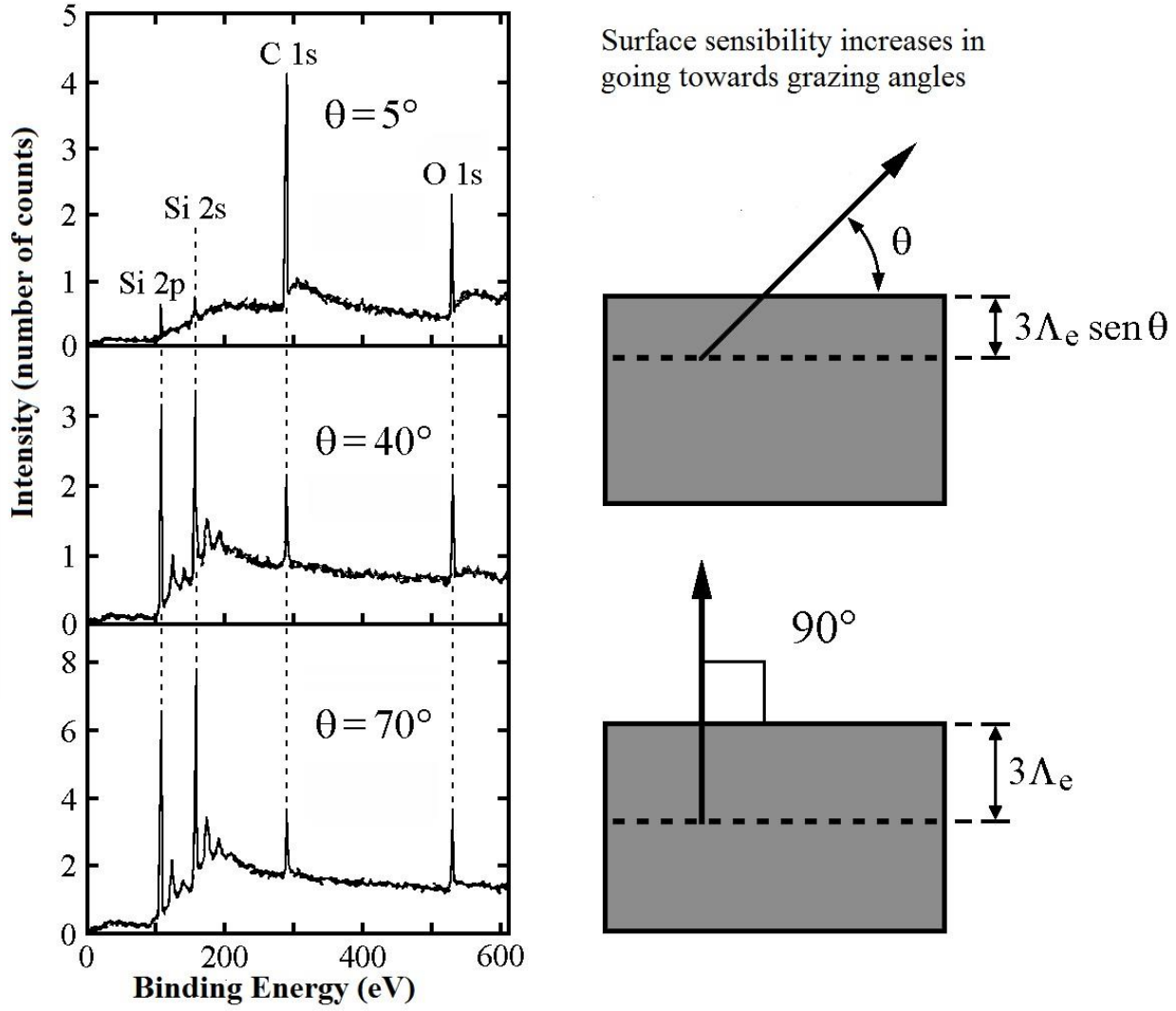

Figure 1.6: Dependence of sampled vertical depth by the angle between direction of analysis and sample surface. To the left are reported the XPS spectra of the *core* levels: Si 2p, Si 2s, C 1s and O 1s, of a sample of Si with a thin surface film (~ 4 Å) of oxide and an outer carbon contamination of thickness of approximately 1 monolayer. Note the strong intensification, for small θ, of the O 1s and C 1s signals associated with the species on the **surface**.

An analysis of this type is called **ARXPS (A**ngle **R**esolved **XPS),** and allows the sampling of a thickness of the order of a few atomic layers; one can then perform nondestructive depth profiles, going back even to the growth mode of a deposited thin layer (see next paragraph). The ratio between the number of electrons emitted per unit time and the number of incident X photons per unit area in unit time (the

flow of X-rays) is said total **photoemission cross section**. In the case of an amorphous solid affected by a non-polarized radiation, σ is expressed mathematically by the following equation:

$$\sigma_{nl}(E_k) = \int \frac{d\sigma_k}{d\Omega} \cdot d\Omega \tag{1.13}$$

where σ_{nl} refers to the photoelectron's originating orbital (n,l), Ω is the analyzer's solid acceptance angle and the photoemission differential cross section $\frac{d\sigma_k}{d\Omega}$ is given by the expression:

$$\frac{d\sigma_k}{d\Omega} = \frac{\sigma_{nl}(E_k)}{4\pi} \cdot \left[1 - \frac{1}{2}\beta_{nl}(E_k) \cdot \left(\frac{3}{2}\cos^2\alpha - \frac{1}{2}\right)\right] \tag{1.14}$$

where $\beta_{nl}(E_k)$ is the parameter of asymmetry that characterizes the angular distribution of emitted photoelectrons and α is the angle between the direction of propagation of the incident radiation and the direction of analysis. Once these factors are known, one can trace, if one wants to make a quantitative analysis, the atomic percentage concentration of the i-th species in the sample directly from the measure of the entire intensity (after inelastic background subtraction) of the produced photoelectron peak by means of the following relationship:

$$C_i = \left(\frac{A_i}{S_i}\right) \cdot \left[\frac{1}{\sum_j \frac{A_j}{S_j}}\right] \cdot 100 \tag{1.15}$$

A_i is the area of the peak and S_i is the sensitivity factor specific to a particular atomic species. S is related to the aforementioned magnitudes by the relation:

$$S_i = K \cdot \left(\frac{d\sigma}{d\Omega}\right) \cdot \Lambda_e(E_k) \tag{1.16}$$

where K is an instrumental factor considered independent from the kinetic energy as it cancels out in the ratio for the calculation of the percentage concentration.

1.2 ARXPS

The **A**ngle **R**esolved **XPS** is a particular mode of acquisition of photoemission data that allows the obtainment of depth profiles in a non-destructive way. When applied to the growth of thin films of homogeneous composition this technique allows the obtaining of information on the growth mode and thickness of the film: appropriate photoelectronic peaks relating to *overlayer* and the substrate are

acquired starting from grazing up to normal angles. Peak areas are then calculated as their ratio between the signal coming from the film and the one coming from the substrate, after the elimination of the inelastic background[11]. To make accurate calculations it is necessary to know the inelastic mean free path (IMFP).

1.2.1 Intensity of the peaks

In general, the intensity $N_{k,}$ of a peak originated from a photoelectronic lower shell of an atom *k,* can be calculated by integrating the intensity differentials d N_k originated in different volume elements of the sample under examination; each of these intensity differences can be written as the following product, where *x, y,* and *z* indicate the position within the sample:

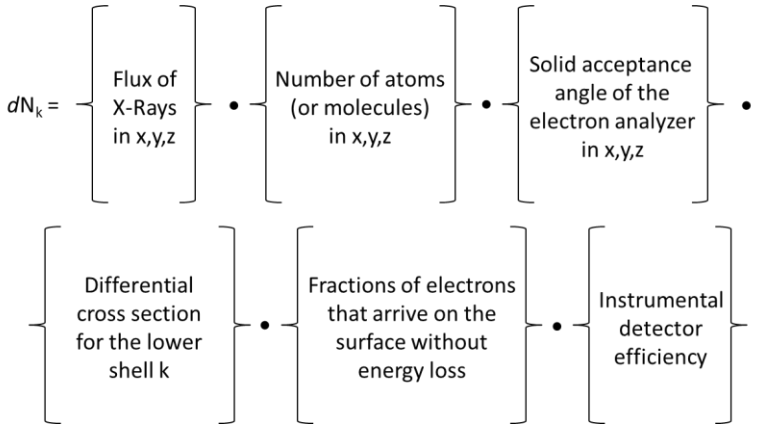

The expression is quite general and with some simple assumptions from it one can get a quick equation to calculate the total intensity N_k of a photoelectronic peak generated from a solid sample.

It is assumed that the sample is ideally flat and polycrystalline and that the reflection and refraction at the surface are negligible (usually[12, 13] this happens for $\phi_x \leq 1°$ both for incident and outgoing X-rays) thus $\phi_x = \phi_x^*$ and $\theta = \theta^*$.

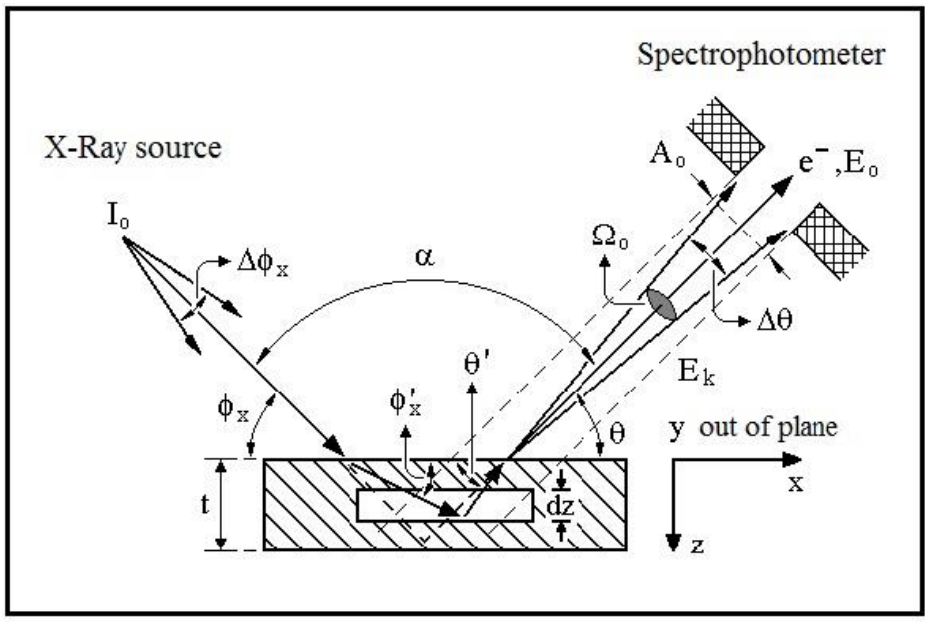

Figure 1.7: Geometry of an XPS experiment to be used as model for the intensities of photoelectron peaks from solid samples.

In the first term of the expression, a uniform beam I_0 of X-rays, with an angular divergence of $\Delta\phi_x$, invests a solid sample of thickness t (for simplicity $t >> \Lambda_e$) forming an angle ϕ_x with its surface. The X-rays penetrate to a depth *z,* where they are absorbed producing a photoelectron, which, released from the sample, moves according to the direction of the incident X-rays; the direction of analysis is given by the construction geometry of the instrument (here 55°). The absorption of X-rays along the path that goes from the surface of the sample to the element volume d *x,* d *y,* d *z,* where the photoemission takes place, causes a diminishing of the incident beam's intensity, following an exponential law similar to that previously illustrated for photoelectrons but with an inelastic attenuation length Λ_x in the order of μm. Because the X-ray penetration capacity is about 1000 times greater than that for photoelectrons, we can consider that along the thickness analyzed, the X-ray flux, the first term of the expression (top), is constant and will be indicated simply as I_0.

The fifth term in the expression above regards the number of photoelectrons that manages to reach the surface, and formula 1.12 can be used.

The second term of the equation at the top corresponds to the **atomic density** of the element analyzed at a given depth within the sample multiplied by the volume element sampled:

$$\rho(z) \cdot dx \cdot dy \cdot dz \qquad (1.17)$$

The third and fourth term in the expression of dN_k correspond to the *probability that a photoelectron of kinetic energy E_k is emitted within the solid acceptance angle of the analyzer,* it is directly proportional to the differential photoemission cross section averaged over the entire solid angle, multiplied by the

acceptance angle, the value of which will depend by the *x, y* coordinates, the angle θ and by the electron energy:

$$\sigma_{nl}(E_k) = \int \frac{d\sigma_k}{d\Omega} \cdot d\Omega \qquad (1.18)$$

The **differential photoemission cross section** can be calculated, in the case that the sample is amorphous and the incident radiation is non-polarized, using the formula 1.14 where:

$$\sigma_{nl}(E_k) = \int \frac{d\sigma_k}{d\Omega} \cdot d\Omega \qquad (1.19)$$

is the **total photoemission cross section**, defined as the *ratio between the number of electrons emitted per unit of time and the number of incident X photons per unit area in unit time;* β_{nl} (E_k) is the parameter of asymmetry that characterizes the angular distribution of photoelectrons emitted, α is the angle between the direction of propagation of the incident radiation and the direction of signal detection; subscripts *n* and *l* are the quantum numbers that indicate the originating level of the photoelectron.

The values α_{nl} (E_k) and β_{nl} (E_k) can be calculated and, usually, are tabulated for the main excitation sources (Mg K_α and Al K_α). The sixth term of the expression defines the efficiency of the detector, which can be less than 1 if all the electrons collected in the solid angle Ω are counted, and more than 1 in the case the instrument possesses a signal amplification system. Detector efficiency generally is a function of photoelectron kinetic energy, and is denoted by D_0 (E_k). Under these assumptions we obtain the final expression for an infinitesimal intensity:

$$dN_k = I_0 \cdot [\rho_k(z) \cdot dx \cdot dy \cdot dz] \cdot \left[\frac{d\sigma_k}{d\Omega} \cdot \Omega_0(E_k, \theta, x, y)\right] \cdot \left[\exp\left(\frac{-z}{\Lambda_e(E_k) \cdot sen\theta}\right)\right] \cdot [D_0(E_k)] \qquad (1.20)$$

This is the formula of the intensity of the photoelectron peak generated in an infinitesimal unit volume, and that, in order to obtain the total intensity, must be integrated over the whole volume analyzed. We now use this formula in some model systems.

1.2.2 Semi-infinite substrate

In the case of a sample of infinite thickness *(t* >>Λ_e) and assuming, for simplicity, that the sample has a constant composition, i.e. $\rho_z = \rho$ and that electron density is uniform, it is possible to integrate dN_k on thickness *t* to obtain:

$$N_k^t = I_0 \cdot \rho_k \cdot D_0(E_k) \cdot \frac{d\sigma_k}{d\Omega} \cdot \frac{\left[1 - \exp\left(\frac{-t}{\Lambda_e(E_k) \cdot sen\theta}\right)\right]}{\frac{1}{\Lambda_e(E_k) \cdot sen\theta}} \cdot \int \Omega_0 \cdot I_0 \cdot dx \cdot dy \tag{1.21}$$

where the integral of *dx·dy* is extended over the entire surface of the sample. All terms of the previous expression that depend on the characteristics of the spectrometer are enclosed in what is called *the response function* of the instrument that, relative to peak *k* is:

$$R_k(E_k, \theta) = D_0(E_k) \cdot \int \Omega_0 \cdot I_0 \cdot dx \cdot dy \tag{1.22}$$

so that the expression of N_k^t becomes:

$$N_k^t = R_k(E_k, \theta) \cdot \rho_k \cdot \frac{d\sigma_k}{d\Omega} \cdot \frac{\left[1 - \exp\left(\frac{-t}{\Lambda_e(E_k) \cdot sen\theta}\right)\right]}{\frac{1}{\Lambda_e(E_k) \cdot sen\theta}} \tag{1.23}$$

Considering the sample of infinite thickness ($t \to \infty$, $e^{-2} \to 0$) we obtain:

$$N_k^\infty = R_k(E_k, \theta) \cdot \rho_k \cdot \frac{d\sigma_k}{d\Omega} \cdot \Lambda_e(E_k) \cdot sen\theta \tag{1.24}$$

Referring to Figure **1.7** one can notice how the analysis system is appropriately described in terms of a solid acceptance angle, Ω_0, projected on an effective area, A_0, measured perpendicularly to the trajectory of the electrons, so the electrons analyzed by the instrument are those emitted from the surface $A = A_0 / sin\,\theta$ inside the angle Ω_0. So the *response function* of the instrument can be expressed as follows:

$$R_k(E_k, \theta) = D_0(E_k) \cdot \Omega_0(E_k) \cdot I_0 \cdot \frac{A_0(E_k)}{sen\theta} \tag{1.25}$$

where it is shown that the terms $D_0(E_k)$, $\Omega_0(E_k)$, and $A_0(E_k)$ depend on photoelectron kinetic energy. Thus, substituting 1.25 in 1.24 gives:

$$N_k^\infty = I_0 \cdot \rho(z) \cdot \frac{d\sigma_k}{d\Omega} \cdot \Omega_0(E_k) \cdot D_0(E_k) \cdot A_0 \cdot \Lambda_e(E_k) \tag{1.26}$$

The **signal is then independent of the angle** θ. Actually, each instrument has its own non-linear response: this may be due to the fact that at grazing angles the area actually analyzed (i.e. the projection of the analyzer's opening on the surface) can become greater than the area of the sample, or due to specific instrumental factors, such as a non-uniform X-ray flux.

The result expressed by 1.26 is very important and allows the obtaining of quantitative data on sample composition by XPS measurements. In fact, although the absolute value of the peak is not easily predictable, as the precise factors I_0, Ω_0, A_0 and D_0 should be known, no problem arises during calculation of the ratio between the areas of the two peaks coming from the same sample, as such terms are deleted when assuming their dependence on kinetic energy to be negligible. It then becomes possible starting from equation 1.26 to derive the ratio between the atomic density of the two considered species *k* and k^*, thanks to the formula:

$$\frac{\rho_k(z_1)}{\rho_{k^*}(z_1)} = \frac{N_k}{N_{k^*}} \cdot \frac{\frac{d\sigma_k}{d\Omega}}{\frac{d\sigma_{k^*}}{d\Omega}} \cdot \frac{\Lambda_e(E_k)}{\Lambda_e(E_{k^*})} \qquad (1.27)$$

where N_k is the integrated area of the photoelectron peak after subtraction of the increasing inelastic background (see Figure 1.2) caused by the Bremsstrahlung effect. This phenomenon, that means *deceleration radiation*, occurs whenever charged particles, in our case electrons, lose energy traversing a material. Classical physics tells us that an accelerated particle emits radiation and this acceleration is caused, for example, by the deflection of an electron in the electrostatic field of an atom while the charged particle passes through matter. This effect generates a continuous spectrum of photons with energy up to the incident radiation, thus providing a background noise. In our case, the analyzer counts electrons thus we will observe their progressive loss in kinetic energy as they progress towards lower kinetic energies (i.e. towards higher *binding energy).* In respect to the incident radiation the lost component lost will gradually increase and this provides the characteristic "step" appearance of a XPS spectrum, where each step represents an increase of the background noise.

1.2.3 Substrate thickness *t*

In the case where the sample has a thickness *t* comparable with $\Lambda_e(E_k)$ we will have that with increasing angle θ the sampled depth becomes greater than *t,* with a decrease of the signal according to the formula

$$N_k(\theta) = I_0 \cdot \rho(z) \cdot \frac{d\sigma_k}{d\Omega} \cdot \Omega_0(E_k) \cdot D_0(E_k) \cdot A_0 \cdot \Lambda_e(E_k) \cdot \left[1 - \exp\left(\frac{-t}{\Lambda_e(E_k) \cdot sen\theta}\right)\right] \qquad (1.28)$$

and thus

$$N_k(\theta) = N_k^{\infty}\left[1 - \exp\left(\frac{-t}{\Lambda_e(E_k) \cdot sen\theta}\right)\right] \qquad (1.29)$$

1.2.4 Substrate with a uniform film of thickness *t*

In this case it is expected that going from a grazing angle θ to one close to the normal, the intensity of the peak from the substrate will tend to increase while that of the film to decrease, according to the following formulas:

Peak *k* from **the substrate** with kinetic energy E_k:

$$N_k(\theta) = I_0 \cdot \rho(z) \cdot \frac{d\sigma_k}{d\Omega} \cdot \Omega_0(E_k) \cdot D_0(E_k) \cdot A_0 \cdot \Lambda_e(E_k) \cdot \left[1 - \exp\left(\frac{-t}{\Lambda_e^*(E_k) \cdot sen\theta}\right)\right] \quad (1.30)$$

and thus

$$N_k(\theta) = N_k^{\infty}\left[1 - \exp\left(\frac{-t}{\Lambda_e^*(E_k) \cdot sen\theta}\right)\right] \quad (1.31)$$

Peak *f* from **the film** with kinetic energy E_f:

$$N_f(\theta) = I_0 \cdot \rho(z) \cdot \frac{d\sigma_f}{d\Omega} \cdot \Omega_0(E_f) \cdot D_0(E_f) \cdot A_0 \cdot \Lambda_e^*(E_f) \cdot \left[1 - \exp\left(\frac{-t}{\Lambda_e^*(E_f) \cdot sen\theta}\right)\right] \quad (1.32)$$

and hence

$$N_f(\theta) = N_f^{\infty}\left[1 - \exp\left(\frac{-t}{\Lambda_e^*(E_f) \cdot sen\theta}\right)\right] \quad (1.33)$$

It must be noted that for the attenuation length, in the exponential equation 1.31, was taken into account that the film is the material which causes the attenuation (hence the use of the apex), while the energy at which Λ_e is calculated, it is of course that of the peak from the substrate.

By calculating the ration $\frac{N_f(\theta)}{N_k(\theta)}$ the following equation is obtained:

$$R(\theta) = \frac{N_f(\theta)}{N_k(\theta)} = \frac{N_f^{\infty}}{N_k^{\infty}} \cdot \left[1 - \exp\left(\frac{-t}{\Lambda_e^*(E_f) \cdot sen\theta}\right)\right] \cdot \left[\exp\left(\frac{-t}{\Lambda_e^*(E_k) \cdot sen\theta}\right)\right] \quad (1.34)$$

Even in this case, neglecting the dependence of the factors Ω_0, A_0 and D_0 to the photoelectron energy, which cancel out, the final expression is reached:

$$\frac{N_f^{\infty}}{N_k^{\infty}} = \frac{\rho_f^* \cdot \left(\frac{d\sigma_f}{d\Omega}\right) \cdot \Lambda_e^*(E_f)}{\rho_k \cdot \left(\frac{d\sigma_k}{d\Omega}\right) \cdot \Lambda_e(E_k)} \tag{1.35}$$

Thus, by knowing the values of the attenuation lengths $\Lambda_e^*(E_f)$, $\Lambda_e^*(E_k)$ and $\Lambda_e(E_k)$ of the atomic densities in the two materials, and the *cross section,* it is possible to obtain on the curve of $R(\theta)$ as a function of $sin(\theta)$ and thickness *t.*

1.2.5 Substrate for a fraction γ covered by islands of a film of uniform thickness *t*

In this case the signal from the substrate will be expressed for the fraction γ by the equation 1.31 and for the fraction (1 - γ) by the function 1.26

$$N_k(\theta) = N_k^{\infty} \cdot \left[(1-\gamma) + \gamma \cdot \exp\left(\frac{-t}{\Lambda_e^*(E_k) \cdot sen\theta}\right)\right] \tag{1.36}$$

while the signal from the film will have an intensity of the type expressed by the function 2.33it will weigh only for a fraction γ

$$N_f(\theta) = \gamma \cdot N_f^{\infty} \cdot \left[1 - \exp\left(\frac{-t}{\Lambda_e^*(E_f) \cdot sen\theta}\right)\right] \tag{1.37}$$

For which the ratio $R(\theta)$ between the two signals will be:

$$R(\theta) = \frac{N_f(\theta)}{N_k(\theta)} = \frac{N_f^{\infty}}{N_k^{\infty}} \cdot \gamma \cdot \left[1 - \exp\left(\frac{-t}{\Lambda_e^*(E_f) \cdot sen\theta}\right)\right] \cdot \left[(1-\gamma) + \gamma \cdot \exp\left(\frac{-t}{\Lambda_e^*(E_k) \cdot sen\theta}\right)\right]^{-1} \tag{1.38}$$

This formula has the advantage of being general and to include the equation 2.34 as a particular case in which γ = 1. By calculating, through fitting, with the equation 1.38 the experimental curve $R(\theta)$ as a function of $sin(\theta)$ it is then possible to obtain the values of γ and *t,* in addition to determining whether the growth type is layer upon layer or islands.

It must, however, be highlighted that the discussion considers an ideal system, and how in reality there may be complicating effects, i.e. variations in peak intensity not related to variations in density ρ.These include: the non-constant angular response of the instrumentation, the refraction of the electrons from surface for very grazing angles, surface roughness, and especially effects of elastic scattering,

particularly for ordered and monocrystalline and materials. In the latter case, in fact, there can be variations in peak intensity of up to 50% - 70%, so that a possible approach is to make the scan along a polar azimuthal direction for which the scattering effects are minimal, or perform various polar scans along multiple non-equivalent azimuthal directions, and then average the results.

1.3 XPD – X-RAY PHOTOELECTRON DIFFRACTION

In the photoelectron diffraction (PD) technique we observe the variation of peak intensity relative to a present chemical species in a monocrystalline material or in function of the analysis direction or energy of the exciting radiation.

Generally the sources used have an excitation line at a fixed energy (Al Kα, Mg Kα and low energy X-rays), in this case the modulation of a photoelectronic signal is recorded in reference to the direction of detection, and one speaks of angle-resolved photoelectron diffraction (**ARXPD**) or simply **XPD** (**X**-ray **P**hotoelectron **D**iffraction), when instead we use the continuous variation of incident photon beam energy while maintaining a fixed X-ray direction of incidence and photoelectron detection, this takes the name of energy resolved electron diffraction *(Energy Scanned Photoelectron Diffraction)* or **ARPEFS** (**A**ngle **R**esolved **P**hoto **E**mission **F**ine **S**tructure) and requires the use of synchrotron light sources. The geometry used in an experiment of *Photoelectron Diffraction* is the following

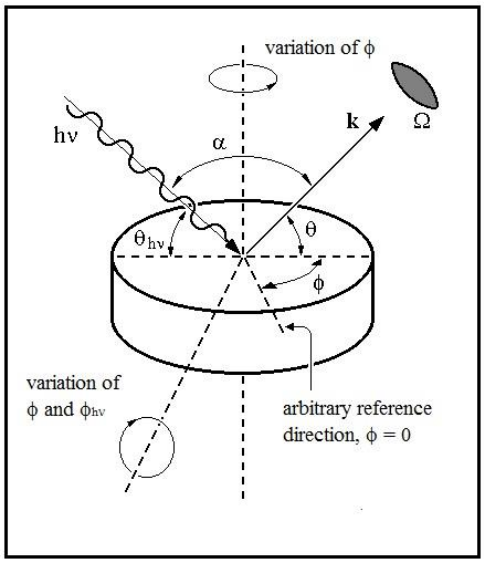

Figure 1.8: Typical geometry to execute experiments of angle resolved photoelectron analysis: we define the azimuth angle ϕ, the polar angle θ, the direction of incident photon $h\nu$, the direction of photoemission **k**, the angle α between the two directions and finite amplitude given by the solid angle Ω of the electrostatic analyzer.

The X-ray beam affects the sample with an angle $\theta_{h\nu}$ respect to the surface of the crystalline sample causing the emission of photoelectrons that are collected by the analyzer along the direction defined by the vector **k** within the solid angle Ω. The vector **k** is defined by the **polar angle** θ respect to the surface, and by the ϕ **azimuthal angle** measured with respect to an arbitrary reference axis on the surface, normally one of the high symmetry directions of the examined single crystal cell. Finally, a high precision manipulator permits the varying of θ and ϕ with great accuracy.

In a typical experiment XPD it is possible to vary the angle θ, maintaining ϕ constant, in which case it is called polar scans **PPD** (**P**olar **P**hotoelectron **D**iffraction), or change ϕ and maintain θ constant, in which case we speak of azimuthal scans **APD** (**A**zimuthal **P**hotoelectron **D**iffraction). A complete set of data can be obtained by acquiring the signal throughout the entire 2π hemisphere (**2π diagram**). In this case, the data can be designed in a compact manner by means of a stereographic projection.

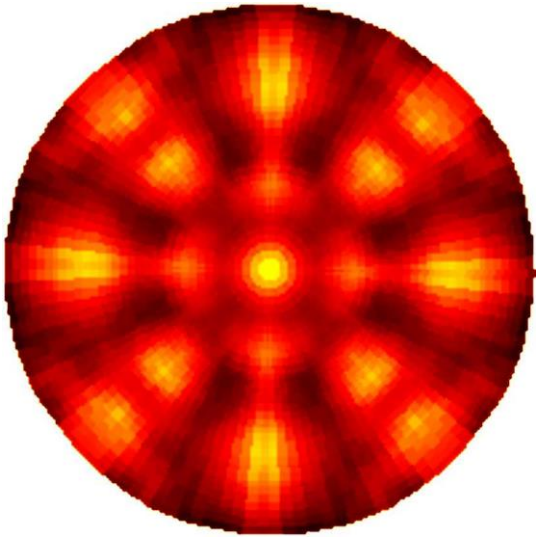

Figure 1.9: stereographic 2π projection made on the Ni2p signal on a NiO(100) surface

The registered intensity oscillations are due to the photo-emitted core electrons, where thanks to their wave nature are subjected to diffusion events due to atoms near to the emitting species.

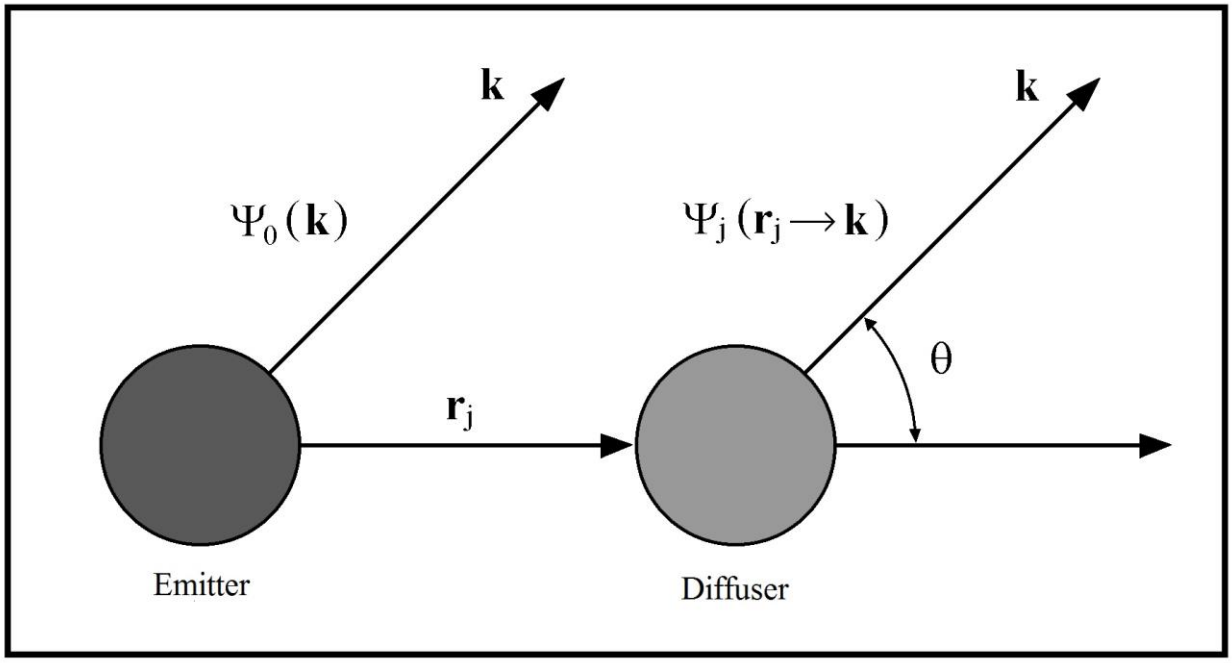

Figure 1.10: Illustration of a diffusion event; Ψ_0 is the primary wave while Ψ_j is the secondary wave originated from the *scattering* of the primary wave by the diffuser, θ is the *scattering* angle, r_j is the distance emitter-diffuser and k is the wave vector.

The interference between the components of the photo-emitted coherent wavefront, said **primary wave** $\Psi_{0,}$ which reaches the analyzer without undergoing scattering events and **secondary waves** Ψ_j spread by the atoms that surround the emitter, generates modulations of intensity as a function of the direction of analysis (XPD) or kinetic energy of the outgoing photoelectron (ARPEFS).

In XPD analysis, the collected photoelectron wave can be considered divided into two components:

$$\Psi(\mathbf{k}) = \Psi_0(\mathbf{k}) + \sum_j \Psi_j(\mathbf{k}) \qquad (1.39)$$

where the subscript "0" refers to the primary wave and the subscript "j" to the scattered waves. The elastic scattering is a phenomenon that varies the direction of the emitted photoelectron wave vector without changing the magnitude, or energy; all those processes that otherwise result in a loss of energy are defined inelastic scattering events.

Upon variation of **k**, the detected intensity modulation is expressed as:

$$I(\mathbf{k}) = \left| \Psi_0(\mathbf{k}) + \sum_j \Psi_j(\mathbf{k}) \right|^2 \qquad (1.40)$$

which depends mainly on the various contributions of various $\Psi_j(\mathbf{k})$.

The photoelectron intensity oscillations can be 50% - 70% and are quantified by the degree of **anisotropy** percentage:

$$\chi = \frac{I_{\max} - I_{\min}}{I_{\max}} \cdot 100 \tag{1.41}$$

With I_{max} and I_{min}, respectively the maximum and minimum intensity of the modulation.

In a specific direction the overall photoelectron intensity wave can be very different from the value it would have in the absence of atoms and diffusers and would correspond to the intensity of sole primary wave. Furthermore, it is essential that the **structural environment** near each emitter is the **same** so that the interference conditions are the same for all the photoelectron waves emitted by atoms of the same species; In fact, since between the photoemission phenomena from two different atoms of the same species there is no temporal relationship, the total lack of a structural order around the emitter atom makes the differences in geometric path between the primary wave and the scattered waves, when it passes from one transmitter to another, completely random.

From what has just been said it is clear that for the XPD technique **structurally ordered samples** (single crystals) are essential; an amorphous sample would produce a modulation averaged over all the random processes of constructive and destructive interference, canceling the effects of diffraction. However it is not required a long range translational order (> 100Å), as in the LEED (which will be described later), and the explanation for this difference lies in the different origin of the spread of the electron beam: while in LEED it originates externally to the sample, keeping its coherence, in XPD it originates internally and the photoemission processes from distinct atoms are not correlated in time. Furthermore, the emitted photoelectron wave undergoes elastic scattering only by atoms **very close to the emitter**, due to the strong inelastic attenuation it undergoes propagating within the solid at the energies of a typical XPD experiment. In practice: **the photoelectron diffraction is a structural probe sensitive to short-range surface order, with atomic and chemical status specificity**.

1.3.1 Features

It is easily understandable how photoelectron diffraction derives directly from electron spectroscopy offers the opportunity to perform at the same time a **compositional analysis** and a **structural** investigation of the sample, the intensity modulations can be registered for **different elements** present in the surface region of the sample (*selvedge*) and for **different core levels** of the **same element**, distinguished by different binding energies. In addition, via measurements with high energy resolution, one can observe diffraction curves of an element present in the sample in **different chemical states**, by exploiting the chemical shift phenomenon.

Photoelectron diffraction, coupled with photoelectron spectroscopy, from which it inherits **surface sensitivity**, is able to reveal the growth of ultrathin pseudomorphs layers, their reticular geometry, the nature of their interface with the substrate or interdiffusion between the atoms of the *overlayer* and those of the substrate, the surface reconstruction and, thanks to the strong intensity maximums due to

forward scattering effects (see below), allows the identifying of bond the directions. Furthermore, by exploiting the scattering of an intramolecular adsorbate, the XPD may explain the geometry with which it binds to the surface of a substrate or whether there are equivalent chemisorption sites; instead exploiting the interference between the photo-emitted wave by an adsorbate atom and diffused by the substrate can reveal the relative position of the former to the latter.

Between the primary wave and the diffused waves there are well defined **phase ratios**, as they result from the same photoemission event, and it is this correlation that allows the phenomena of **interference**. In a first analysis interference can be either constructive or destructive, depending on the geometrical path difference between the components constituting the overall photoelectron wave; varying the polar angle or azimuth meets the conditions of constructive interference, identified by the intensity maximums in the XPD curves.

1.3.2 Electron-atom diffusion phenomena: semi-classical and qualitative description

We now discuss the physical phenomena that occur in the XPD technique. In case the De Broglie wavelength of a diffused particle is much smaller than the distance which separates it from the potential diffuser, scattering can be described in a convenient and adequate way by a semi-classical model, where the trajectories of particles, considered as point-like bodies, are easily calculated knowing the diffuser potential. The photoelectron diffraction is at the limits of validity for this model, but it can provide a useful qualitative view of the phenomenon.

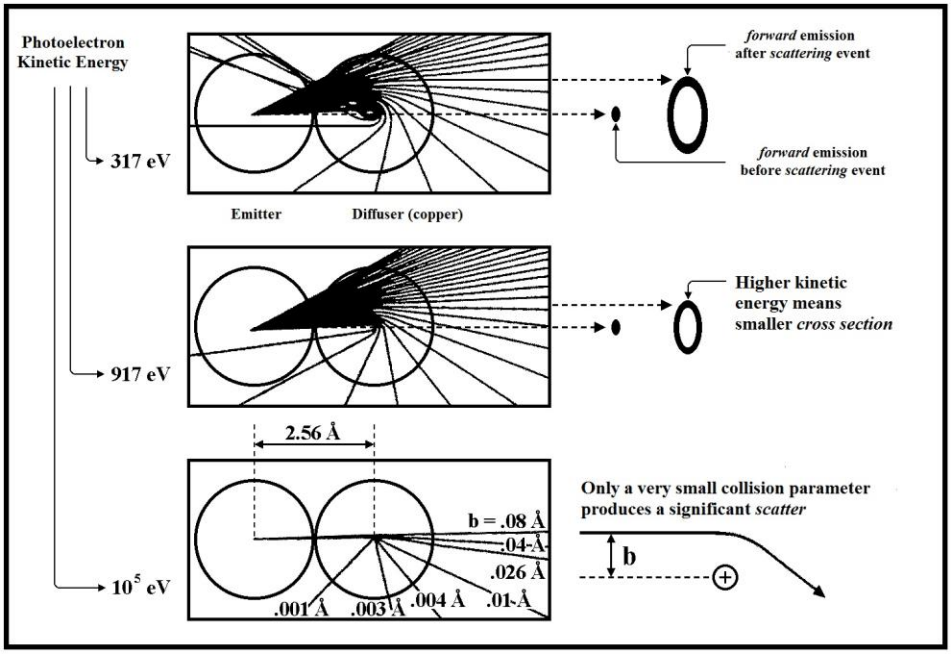

Figure 1.11: Classical trajectories for an electron crossing the potential of a Cu atom. The example illustrates the dependence of the impact parameter *b* from the kinetic energy of the electron.

In figure 1.11 are represented the phenomena of elastic scattering for electrons, at different kinetic energies, emitted from a copper atom and interacting with the potential associated with a second copper atom placed at the distance of 2.56 Å from the emitter. The trajectories were calculated classically, i.e. assuming that the electron is a point particle, while the potential of the diffuser atom was obtained with accurate quantum mechanical calculations of SCF (*Self Consistent Field*) type. From the figure, it is of immediate deduction that:

a) the diffusion angle is greater the nearer the electron passes to the nucleus of the diffuser atom.

b) at equal diffusion angles, the higher is the electron energy, the greater must be the approach near the nucleus, thus increasing kinetic energy; the impact parameter *b* for significant scattering decreases.

In other words, for high-energy electrons (over 1keV) the crystalline lattice appears essentially as an empty space, however for lower energies the electron can undergo significant deflections even in the outer zones of the diffuser atom. In figure 2.12 we observe that at low kinetic energies, i.e at 50 eV, the electron can undergo a large deflection already in the outer region of the potential diffuser, since the force required is small. Here the potential varies with Z_{eff} / r, or rather much more rapidly than 1 / r (with r as the distance from the scattering center), as the effective nuclear charge Z_{eff} increases very rapidly with decreasing r, as the photoelectron gradually penetrates the shielding orbitals. For small changes of the collision parameter strong variations in the diffused of electron trajectory are produced.

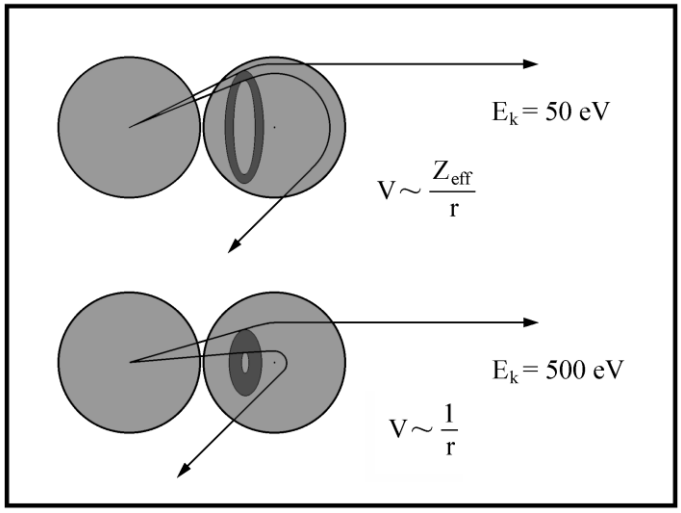

Figure 1.12: Illustration of the semi-classical collision parameter's dependence for the *forward scattering* and large angle *scattering* from the kinetic energy of the diffused electron.

At higher energies, in order for the deflection to be remarkable the impact parameter must decrease down to the areas close to the diffuser nucleus where the potential exerts a relatively large attractive force. In this region shielding orbitals have already largely been penetrated and effective potential varies as 1 / r, i.e. more slowly than in outlying areas. Only a substantial variation of the collision parameter is capable of giving a large angle scattering.

1.3.3 Scattering factor

The agreement between the quantum-mechanical approach and the semi-classical style is very good, as is shown by the figure below: in it is reported the result of the calculation of the diffusion amplitude or scattering factor $|f(\theta)|$ according to the semiclassical model for a photoelectron of 500 eV, in the approximation of a plane wave, incident on a copper atom. We inserted in the same graph the trend on data obtained with the rigorous quantum mechanical method. The two curves are fully comparable, confirming the validity of the semi-classical model for these energies.

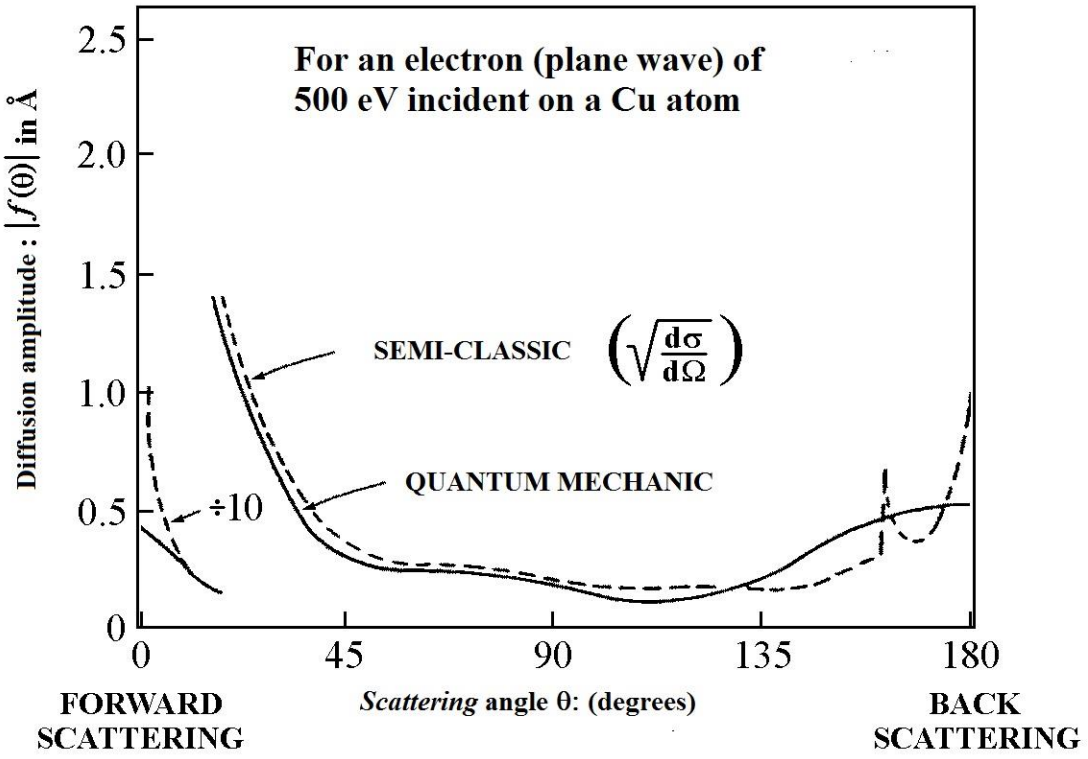

Fig 1.13: Comparison of semiclassical and quantum mechanical calculation of the *scattering* factors as a function of θ (from *forward scattering* to *backscattering*) for photoelectrons at 500 eV incident on a Cu atom.

The physical meaning of the scattering factor, which quantifies all possible diffusion phenomena, can be deduced from its square:

$$|f(\theta)|^2 = \frac{d\sigma}{d\Omega} \tag{1.41}$$

In which:

$$\frac{d\sigma}{d\Omega} = \frac{b}{sen\theta} \cdot \left(\frac{d\theta}{db}\right)^{-1} \tag{1.42}$$

where $d\sigma = 2\pi b \cdot db$ is the collision area, $d\Omega = 2\pi \cdot sen\theta \cdot d\theta$ is the solid angle within which fall the scattered electrons and b is the impact parameter. The ratio defines the **scattering differential cross section** which, in analogy with the differential photoemission cross section, is defined as the ratio between the number of scattered electrons within the solid angle $d\Omega$, in a unit of time, and the number of electrons incident on the center of the scattering per unit area per unit time. In other words, the square of the scattering factor expresses the probability that a single stream of particles of defined time $\hbar\mathbf{k}$, incident on the scattering center, undergoes a deflection of an angle θ with respect to the direction of incidence.

1.3.4 Forward scattering

The relevant factor in the appearance of the XPD technique is certainly the increase of intensity of the photoelectric signal in the direction defined by the internuclear emitter-diffuser, which is called zero-order interference effect (*zeroeth order scattering*) or *forward scattering* (FS) effect or even *forward focusing*, and which is much more evident the greater the kinetic energy of the photoelectron.

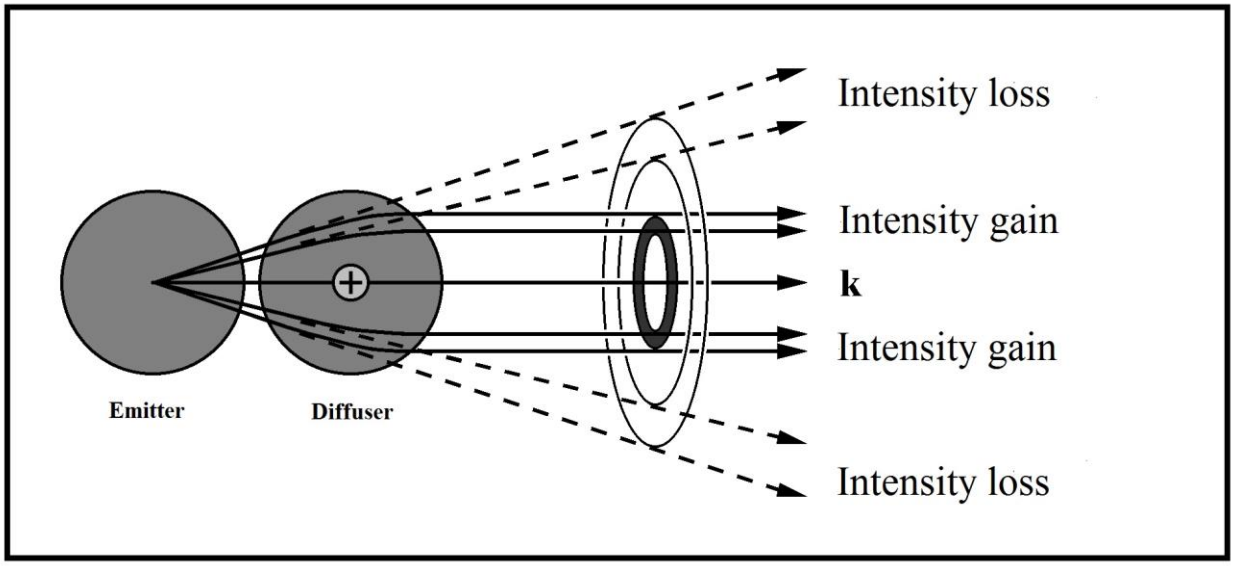

Figure 1.14: Visual description of the *forward scattering* effect undergone by a photoelectron wave when it passes through an attractive potential.

It can be seen from Figure 1.14 that a major portion of the emitted photoelectron wave is deflected by the attractive potential of the atom in a direction coincident with the diffuser internuclear axis. Given that there is a cylindrical symmetry around this axis, the amplitudes of the waves scattered in this direction are all in phase, giving rise, through constructive interference, to a considerable gain in photoelectron intensity corresponding to a scattering angle of 0˚.

The force of deflection that acts on the photoelectron is directly proportional to the atomic number of the diffuser and this explains the increase in *forward scattering* when passing from light elements to the heavier ones. For electrons with kinetic energy of a few hundred eV, the effect of FS is irrelevant if they are produced from a hydrogen atom, weak but clearly detectable if due to carbon, nitrogen, oxygen and very strong for elements heavier than chlorine, though at some point the shielding effect by the electrons of the inner shells of the diffuser atom compensates the growth of the nuclear charge, thereby reaching a saturation; for example, it is experimentally demonstrated that nickel and gold do not show very different FS.

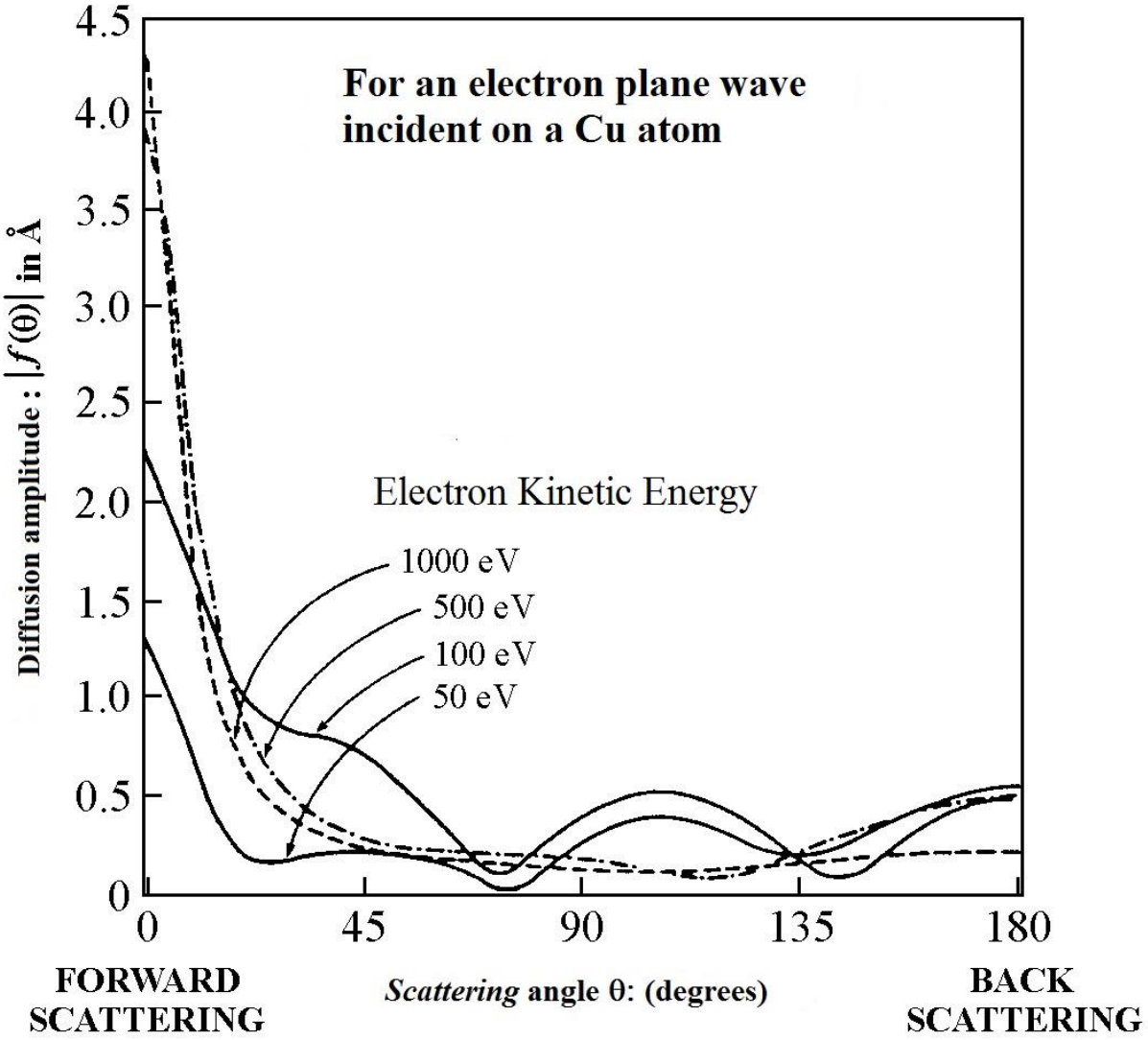

Figure 1.15: Quantum-mechanical calculations of *scattering* factors, as a function of the angle of diffusion, for photoelectron plane waves of different energies incident on a Cu atom.

The physical origin of the phenomenon of FS is illustrated by the figure above, where we have shown the trends of diffusion amplitude $|f(\theta)|$ of a plane wave as a function of scattering angle for different values of incident photoelectron kinetic energy. Observing the curves, one immediately understands that for low kinetic energies the *scattering* factor has values not negligible in the whole range of scattering angles: from $\theta = 0^\circ$ (FS) to $\theta = 180^\circ$ (backscatter or *Back Scattering* (BS)).

As already explained referring to Figure 1.11 at low energies a small variation of the direction of incidence is sufficient, i.e. the impact parameter *b*, to cause striking changes in the trajectories of photoelectrons. It may well happen that for two different values of the impact parameter, and hence to different geometric paths, one obtains the same scattering angle; resulting trajectories correspond to

coherent portions of the photoelectron wave, but these portions are not in phase and may therefore interfere destructively explaining the presence of local minima in the curves of the scattering amplitudes at low energies. These facts, together with the high probability of multiple scattering events of electrons for little energy, make it quite complicated the interpretation of photoelectron diffraction data below 100 eV, and forces one to proceed with caution in assigning events to FS maximum intensity of the XPD modulations at energies below 200-300 eV.

Already at 500 eV (Figure 1.16), the result of the calculation $|f(\theta)|$ shows a very accentuated *forward scattering* maximum, of an order of magnitude more intense than the maximum relative to the direction of *back scattering*. The effect of FS becomes even more prevalent if you increase the kinetic energy of the photoelectron, once exceeded 500 eV the only relevant diffusion event occurs for $\theta = 0$ ˚. It was also demonstrated that with gradually increasing energy the *forward scattering* peaks, in the XPD curves, become narrower.

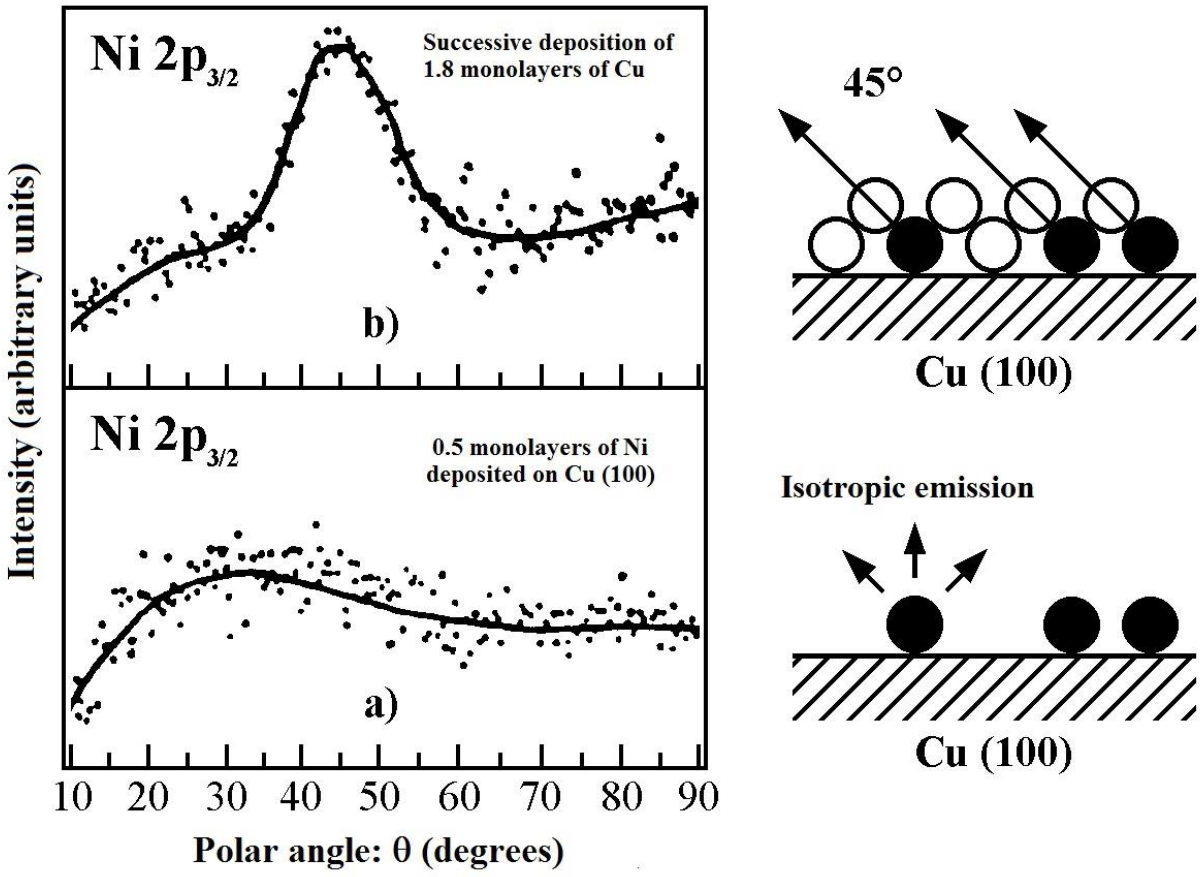

Figure 1.16: Example of *forward scattering*. In a) the emission level from the $2p_{3/2}$ of Ni is isotropic because Ni atoms are on the surface. In b) due to the presence of an epitaxial layer of Cu an intense peak of FS is observed at a polar angle of 45°, because the atoms of Cu are on top of those of Ni.

1.3.4 Interference to higher orders and *back scattering*

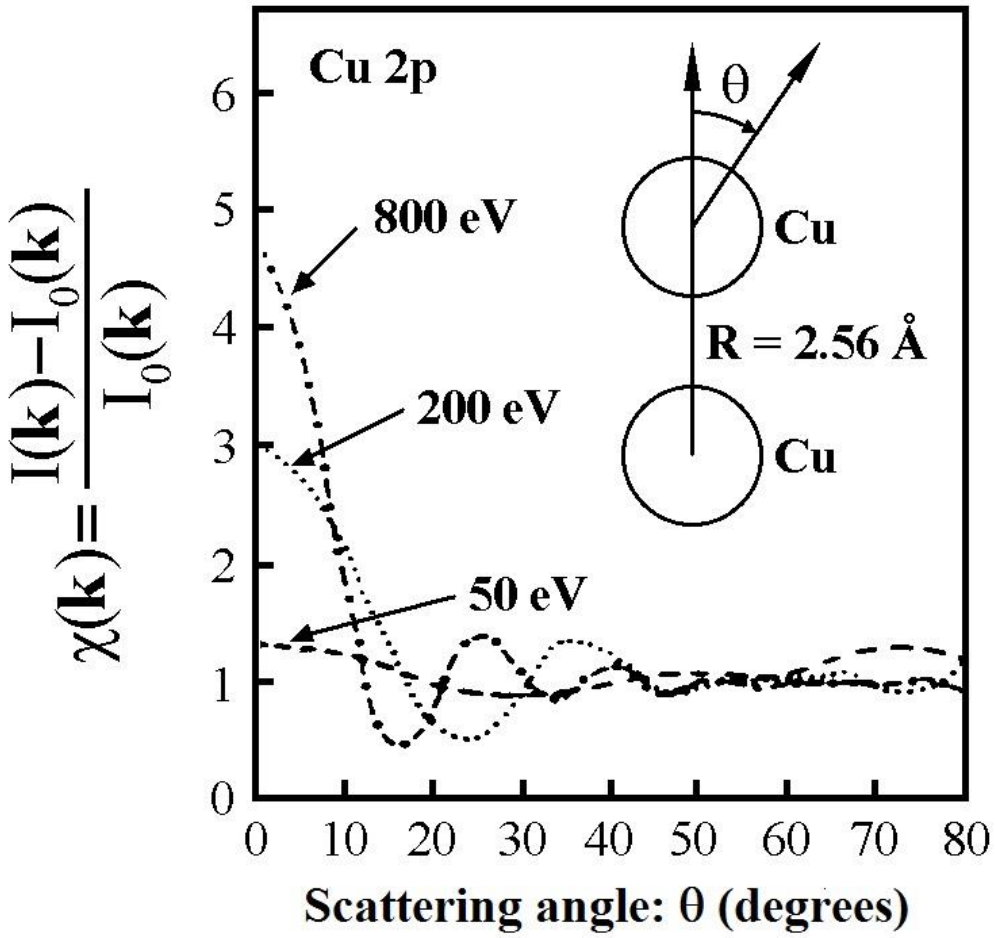

Fig 1.17: normalized photoelectron intensity $\chi(\mathbf{k})$ for electrons at different energies. The maximums at increasing angles represent interference peaks of higher order.

The phenomenon of *forward scattering* gives no information on the interatomic distances, because the geometric phase difference between primary wave and diffused wave fronts is zero (Figure 1.18a). As with any interference phenomenon, the maximum is obtained each time that differences in optical paths correspond to phase differences between portions of the wave: $2n\,\pi / \lambda$ where n is an integer; FS peak is related to the value of n = 0 (zero order).

The information on the distances between atoms are contained in first order constructive interferences (Figure 1.18b) and higher order (Figure 1.17), associated with *scattering* angles higher than 0˚.Unfortunately, the kinetic energies typical of an XPD analysis, when the FS dominates, first order peaks are already rather weak and the probability of high angle *scattering* events is significantly

reduced, which is why signals relating to higher order constructive interference are visible only as a fine structure effects, sometimes less intense and overlapping the FS structures.

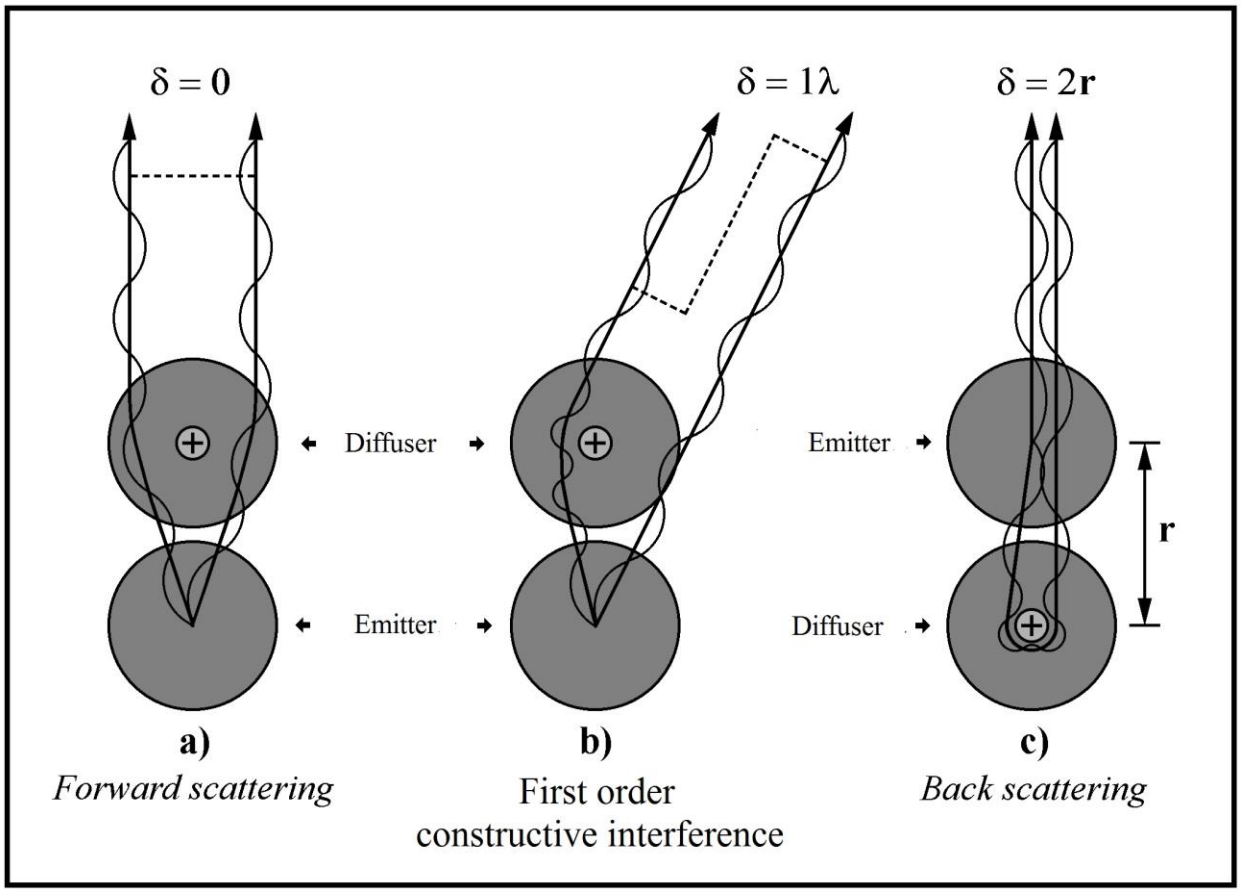

Figure 1.18: Distinction between *forward scattering*, first order constructive interference and *back scattering*, δ is the difference between geometric paths.

Correct information (with a precision of ± 0.02Å) on bond distances are obtained using the ARPEFS technique that allows you to vary at will the kinetic energy of the photoelectron emitted by the synchrotron light. The technique usually works in the energy range that goes from a few dozen to a few hundred eV, where the probability of high angle *scattering* events is high. In particular, the ARPEFS permits to work in *back scattering* conditions (Figure 1.18c), i.e. at an diffusion angle of 180˚; in BS geometry the maximum appear when the wavelength of the photoelectron is equal to an integer multiple of **r**, where **r** is the distance between the transmitter and the diffuser, then the conditions of constructive interference depend heavily on **r** and occur when the optical path difference between the primary wave and the diffused waves equals 2**r**.

Unfortunately, not always the event of FS is sufficient to reveal the structure of the studied surface, a more correct approach to the interpretation of the experimental data (especially when investigating surfaces at low coatings) is based on the comparison between them and the simulation XPD curves

calculated from different theoretical models of surfaces analysis. A method based exclusively on the identification of the intensity maxima with interatomic directions can lead to erroneous conclusions: some maximums, species at intermediate energies, may in fact be due to higher order interference phenomena. The exact correlation between experimental and simulation data may be made quantitative by the use of **R factors** (***R**eliability factors*); initially developed for LEED and suitable to photoelectron diffraction. Regarding the quantitative discussion of the photoelectron diffraction phenomenon, one can choose a relatively simple model that considers only single scattering (*SS*) events between the emission and detection of photoelectrons, or a more rigorous model which takes into account multiple scattering events (not treated here).

1.3.5 Single *Scattering*

Previously, we considered only systems composed of an emitter and a diffuser atom, we have implicitly assumed a single possible *scattering* event for each emitted photoelectron wave. The treatment of such model is largely successful in variable angle photoelectron diffraction experiments; this simplification originates from the strongly anisotropic nature of the scattering amplitudes for photoelectron kinetic energies exceeding a few hundred eV (Figure 1.14). Considering only *single scattering* events drastically reduces the complexity of the problem and, therefore, calculation time.

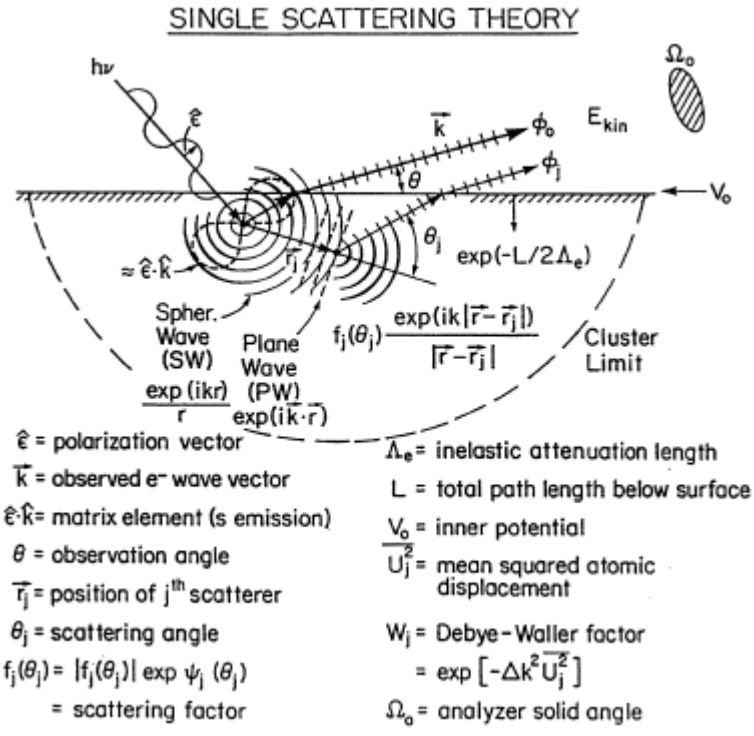

Figure 1.19: Schematic illustration of the processes involved in the photoelectron diffraction. A core level photoelectron propagates and the primary wave is diffused in the area around the near-neighbors

of the emitting atom. The directly emitted and diffused parts are coherent and their interference pattern is detected.

The intensity detected by the detector is given by the square of the wave function of the final state after excitation with X-rays:

$$I(\mathbf{k}) = |\Psi(\mathbf{k})|^2 \tag{1.43}$$

where $\Psi(\mathbf{k})$ denotes the wave function of the final state, and **k** is the wave vector of the electron detected. The wave function $\Psi(\mathbf{k})$ combines all the primary wave and the secondary waves spread from neighboring atoms. Considering the *single scattering* wave function approximation of the primary and all the diffused waves according to the relation:

$$I(\mathbf{k}) = \left| \Psi_0(\mathbf{k}) + \sum_l \Psi_l(\mathbf{k}) \right|^2 \tag{1.44}$$

where $\Psi_0(\mathbf{k})$ is the primary wave of the emitter along the direction of analysis and $\Psi_l(\mathbf{k})$ is the single scattered wave by atom *l* . The intensity is then equal to:

$$I(\mathbf{k}) \propto |\Psi_0(\mathbf{k})|^2 + \sum_l \left(\Psi_0^*(\mathbf{k}) \cdot \Psi_l(\mathbf{k}) + \Psi_0(\mathbf{k}) \cdot \Psi_l^*(\mathbf{k}) \right) + \sum_l \sum_k \Psi_l(\mathbf{k}) \cdot \Psi_k^*(\mathbf{k}) \tag{1.45}$$

1.4 LEED

The acronym LEED stands for (**L**ow **E**nergy **E**Lectron **D**iffraction)[14-17] this surface survey technique was born in 1927 when Davisson and Germer observed that when a beam of mono-energetic electrons incident on a surface of monocrystalline nickel, electrons elastically diffused emerged in preferential directions, which could be explained by the diffraction of these by the periodic distribution of the atoms in the crystalline sample. Since this is a diffraction technique the theory had already been developed by Laue in 1912 who first developed the mathematical treatise by studying the X-ray diffraction by a crystalline sample. Subsequently this treatise was simplified by Bragg and Ewald who introduced the use of a geometric construction for interpreting patterns arising from crystal lattices. Unfortunately, this technique of investigation began to be widely used only after the development of ultra-high vacuum (UHV) technique as the required conditions of sample cleanliness are quite stringent, and this is guaranteed precisely from operating at very low pressures.

From the principle of the wave-particle duality developed by de Broglie we know that a flow of particles with velocity v and mass *m* can be associated to a wavelength $\lambda = h / m v$, where *h* is Planck's constant ($h = 6.626 \cdot 10^{-34}$ J · s), while the energy $\Delta E = h \nu$. From here we see that electrons with energy of 100 eV have a wavelength of 1.23 Å, comparable to the interatomic distances in a crystal lattice. In

LEED technique electrons have energy between 20 and 300 eV, which correspond to wavelengths between 2 and 0.5 Å. The limit of inelastic scattering processes is within 5 - 10 Å, the penetration depth of the electron beam, allowing a surface sensitivity relative to the last atomic layers.

An electron beam can be seen as a succession of waves of incident electrons perpendicular to sample surface. These waves will be diffracted by regions of high local electron density such as, for example, the surface atoms which will thus be considered as points of diffraction. When this happens the outgoing scattered waves from an atom interfere with those diffused from adjacent atoms, and where there is constructive interference, they add up to each other, generating new wave fronts. The conditions for constructive interference are given by the Laue equations:

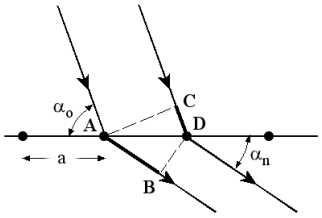

Figure 1.20: Illustration showing geometric construction for path differences of incident waves.

$$\mathbf{a} \bullet \mathbf{S} = a \cdot \cos \alpha_n \qquad (1.46)$$

$$\mathbf{a} \bullet \mathbf{S_0} = a \cdot \cos \alpha_0 \qquad (1.47)$$

The difference in the path of the incident waves is:

$$a \cdot (\cos \alpha_n - \cos \alpha_0) = \mathbf{a} \bullet (\mathbf{S} - \mathbf{S}_0) = n_x \lambda \qquad (1.48)$$

Where **a** is the vector of the unit cell while **S** and $\mathbf{S_0}$, respectively, the vectors of the incident and diffracted electron beam; $n_x \lambda$ indicates the integer number of wavelengths, the path difference of the waves must be an integer multiple of the wavelength in order to have constructive interference. Since a crystal is composed of identical and repeated units, also the atoms present on the surface will be interspersed and spaced in a periodic fashion. If for these the constructive interference condition is satisfied, given the nature of the crystal it will be the same for the other diffused by all the atoms of the same row. Since this row of atoms has a one-dimensional symmetry cones will form around its axis representing a region where there is a finite probability of finding the electron during a constructive interference.

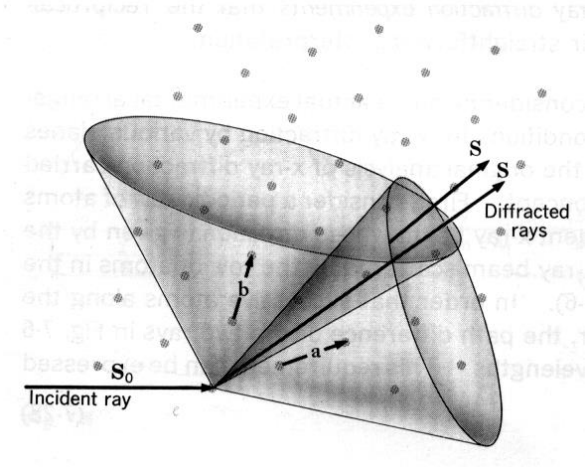

Figure 1.20 illustrates the diffraction cones where we note that the diffracted rays exist only in the overlapping area of the two cones.

A two-dimensional periodic arrangement with interatomic distances *a* and *b* generate two sets of diffraction conditions which must be valid at the same time, namely,

$$a \cdot \left(\cos\alpha_n - \cos\alpha_0\right) = \mathbf{a} \bullet \left(\mathbf{S} - \mathbf{S}_0\right) = n_x \lambda \tag{1.49}$$

$$b \cdot \left(\cos\beta_n - \cos\beta_0\right) = \mathbf{b} \bullet \left(\mathbf{S} - \mathbf{S}_0\right) = n_y \lambda \tag{1.50}$$

The new set of cones also gives the only permitted areas of constructive interference. Given the constraints that must be simultaneously satisfied, the only regions in which we can find the electron will be at the intersection of these cones, or their vertexes; the only point they have in common with each other. Thus when an electron is diffracted by a two-dimensional arrangement of atoms it can only diffuse away from the surface along a set of lines passing through the points of intersection.

Bragg examined by Laue photographs and noticed that some points had an elongated shape and deduced that this was because the x-rays underwent specular reflection on a "plane" of regularly arranged atoms and even if it is not physically correct it allows us to greatly simplify Laue theory by using a geometric treatise.

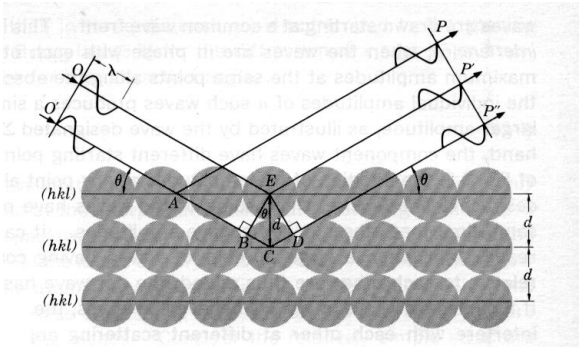

Figure 1.21: Bragg's geometric treatise; notice the crystal planes.

By simple trigonometric building you arrive to Bragg's law:

$n\lambda = 2d\sin\theta$. (1.51)

Where θ represents the "Bragg angle" for which there is the most intense diffraction and d is the distance between the planes (*hkl*) and $\mathbf{d}_{hkl}$ is a vector placed perpendicularly to each plane. From Bragg's law we can then construct a reciprocal lattice starting from a real one, i.e. assigning the interatomic distances *a* and *b* of the latter cell vectors **a** and **b**. The vectors of the reciprocal lattice cell $\mathbf{a}^*$ and $\mathbf{b}^*$ will be perpendicular, respectively, to **b** and **a** with a magnitude equal to the inverse of the distances between the rows of atoms with distance *b* and those with distance *a*. For this reason, the points of the reciprocal lattice actually represent a set of diffracted, real, planes.

In 1913 Ewald was the first to interpret, in the form of reciprocal space, the Laue lattice patterns using, as did Bragg, a geometric treatise based on the conservation of energy and momentum of scattered electrons. He built in reciprocal space the crystal lattice and by placing as the origin of a sphere of radius $1 / \lambda$ the diffuser lattice point formulated that the lattice points (the set of real planes) intersecting this sphere were those for which diffraction was obtained since they were placed at the Bragg angle in respect to the incident beam $\mathbf{S_0}$ (often known as **k**). The vector difference between the diffracted ray **S** (or rather **k'**) and that incident I provides the lattice vector that is perpendicular to the real plane (*hkl*). This is obtained as the only solution of the Laue equations:

$(\mathbf{S} - \mathbf{S}_0) / \lambda = h\,\mathbf{a}^* + k\,\mathbf{b}^* + l\cdot\,\mathbf{c}^* = \mathbf{d}^*_{hkl}$ (also known as vector diffraction **K**) (1.52)

Where *h*, *k*, and *l* are the Miller indices and $\mathbf{d}^*_{hkl}$ will have magnitude equal to $1/d_{hkl}$, i.e. equal to the inverse of the distance between the real planes calculated by Bragg's law.

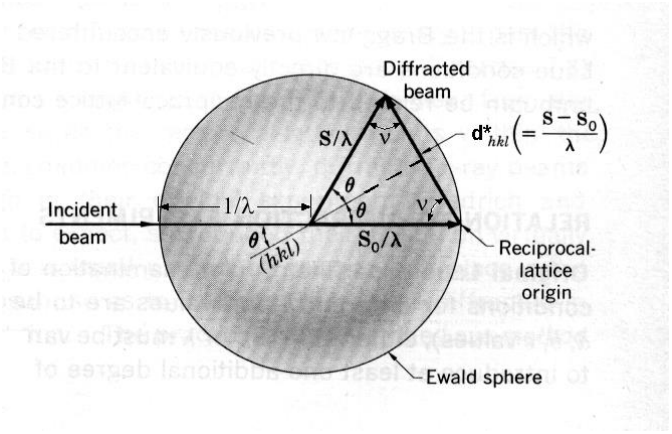

Figure 1.22: Ewald sphere with the calculation of the diffraction vector **K**

The theories of Laue and Bragg calculated however, diffractions only for precise angles a condition verified for infinite crystals, experimentally, however, measurements were made on thin layers and it was noted that diffraction was also observed in a range of angles around those of Bragg. The contraction of a dimension meant that the points of the crystal lattice actually form bars or relrods, (**RE**ciprocal **L**attice **ROD**s). Diffraction is then observed every time the Ewald sphere intersects a *relrod* and no longer only in a reciprocal lattice point so that a wider range of angles are available. An interesting case occurs when the Ewald sphere does not intersect the *relrod*; in this case the diffraction vector **K** will be equal to: $\mathbf{K} = \mathbf{d}^*_{hkl} + \mathbf{s}$ where **s** is the vector of the distance between *relrod* and Ewald sphere. We Will observe then, diffraction points with intensity decreased the magnitude of **s** .This implies that for thin layers more diffraction points are observed; furthermore, given the use of low energy (20-300 eV) the radius of the Ewald sphere is large and therefore with increased points of intersection.

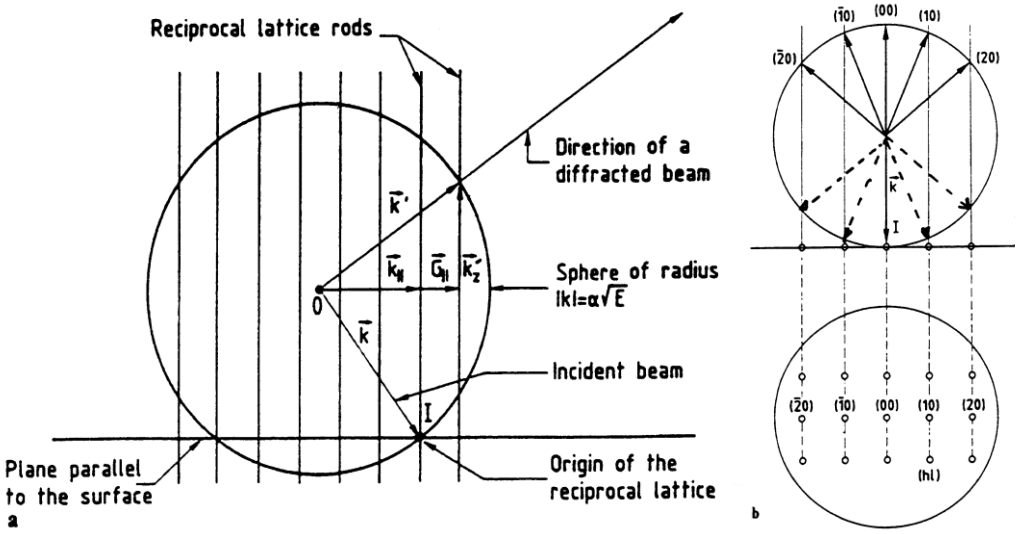

Figure 1.23 (a) Construction of the Ewald sphere for surface diffraction, (b) Identification of the reflections at normal incidence.

It is important to remember that the image analysis LEED gives information on the frequency of the atoms on the surface and on the symmetry of the total, but gives no immediate indications about the location of individual atoms. Thus **the low energy electron diffraction is a technique for the investigation of superficial long range order** (<100Å).

1.4.1 Analysis of the diffraction pattern

The diffraction patterns represent the image of the reciprocal lattice of the sample. So, through the analysis of the positions of the *spots* one can be back-track to the symmetry of the lattice and the actual size of the unit cell of the surface, given the close dependence of the two geometric patterns.

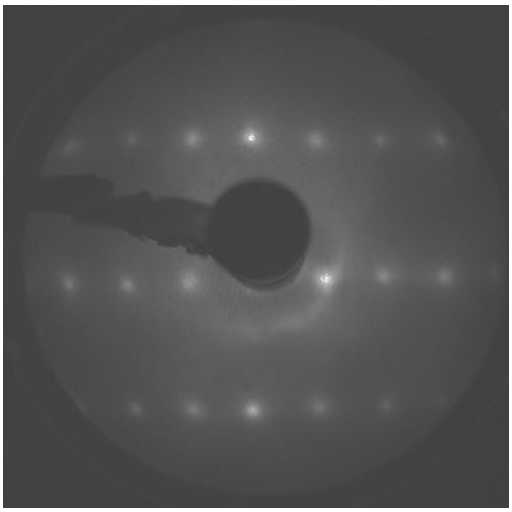

Figure 1.24: LEED image of a surface of the TiO_2 (110) - (1x1)

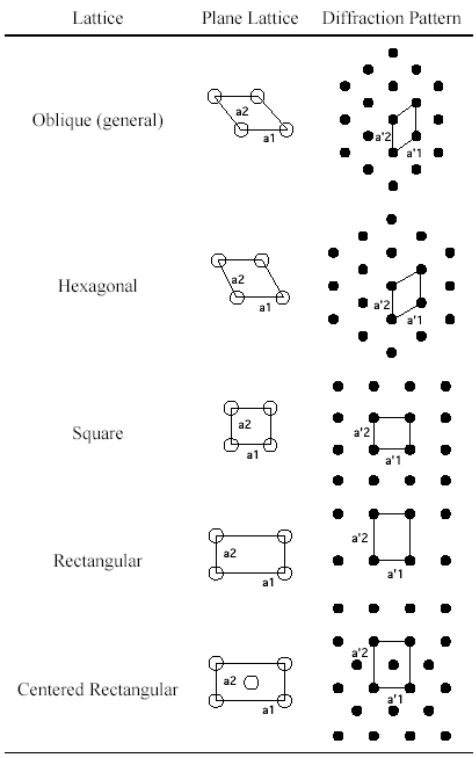

Figure 1.25: Representation of real and reciprocal lattice of the corresponding two-dimensional lattices.

Generally, variations in the periodicity of the surface cause changes in the *pattern* of diffraction that are observable and easily interpreted in terms of the new two-dimensional symmetry. This is the case, for example, of gas adsorbed on the surfaces of crystals; usually the atoms are arranged according to arrangements with periodicity that are integer multiples of the spacing of the substrate.

The adsorbed species on surfaces of single crystals frequently show a long-range order, forming a well defined *overlayer* structure. The new surface periodicity is described in relation to the structure of the substrate according to two notations:

- *Matrix notation*
- *Wood notation*

Any ordered structure surface can be described by only two parameters that define the cell; $\mathbf{a_1}$ and $\mathbf{b_1}$ for the substrate and $\mathbf{a_2}$ and $\mathbf{b_2}$ for the overlayer. The first type of notation is the more general system of describing structures and can be applied to all ordered deposits: simply correlates the cell parameters of the two structures according to the following expression:

$$\mathbf{a_2} = G_{11}\,\mathbf{a_1} + G_{12}\,\mathbf{b_1} \qquad (1.53)$$

$$\mathbf{b_2} = G_{21}\,\mathbf{a_2} + G_{22}\,\mathbf{b_2} \qquad (1.54)$$

or by using a matrix:

$$\begin{pmatrix} \mathbf{a}_2 \\ \mathbf{b}_2 \end{pmatrix} = \mathbf{G} \begin{pmatrix} \mathbf{a}_1 \\ \mathbf{b}_1 \end{pmatrix} \qquad (2.55)$$

Where *G* is a 2x2 matrix that contains the information on the relative spatial relationships between the two patterns:

$$G = \begin{bmatrix} G_{11} & G_{12} \\ G_{21} & G_{22} \end{bmatrix} \qquad (1.56)$$

Therefore in the same way as you can define the matrix *G* in real space (or direct), you can define a matrix G^* in reciprocal space. It can be shown that the relations used to obtain the elements of the matrix *G* from the matrix G^* are the following:

$$g_{11} = \frac{g^*_{22}}{\det G^*} \quad g_{12} = \frac{g^*_{21}}{\det G^*}$$
$$g_{21} = \frac{g^*_{12}}{\det G^*} \quad g_{22} = \frac{g^*_{11}}{\det G^*} \qquad (1.57)$$

Therefore the values of the cell constant in real space image are immediately obtainable from the analysis of the spots of a LEED. The area of the unit cell for the two lattices is defined as:

$$S_{substrate} = |a_1 \wedge b_1| \quad (1.58)$$

and

$$S_{film} = |a_2 \wedge b_2| \quad (1.59)$$

The relationship between the two unit areas coincides with the determinant of matrix *G*, and its value can be used in the classification of the possible mutual relations of the two lattices. If the determinant is an integer, there is a simple relationship between the two lattices, which are said to be "simply related", in this case the surface lattice is called **super-lattice**. If the value is a rational number, patterns coincide at regular intervals and the two structures are said to be *commensurate* , the superstructure is called **lattice of coincidence** . If the determinant is an irrational number, there are no systematic connections between the two lattices, the superstructure will then be called *incommensurate* or **inconsistent** .

The *Wood's notation* is easier and is most commonly used, albeit only valid for simply related structures.

1.5 TEMPERATURE PROGRAMMED DESORPTION [18-20]

1.5.1. Fundamental Principles

1.5.1.1 Physisorption and Chemisorption

Adsorption takes place when an attractive interaction between a particle and a surface is strong enough to overcome the disordering effect of thermal motion. When the attractive interaction is essentially the result of van-der-Waals forces then physisorption takes place. Physisorptive bonds are characterised by dissociation energies below approximately 50 kJ/mol. Chemisorption occurs when the overlap between the molecular orbitals of the adsorbed particle and the surface atoms permit the formation of chemical bonds, which are characterized by dissociation energies typically exceeding 50 kJ/mol. Note that chemisorption is often an activated process, *i.e.*, the formation of a chemisorptive bond requires that an activation barrier is overcome. Moreover, the chemisorption interaction can weaken the intra-molecular bonds and in some cases leads to a dissociation of the molecule (dissociative chemisorption). The elementary reaction steps occurring during this reaction are summarized in **Figure 1.26**. The kinetic aspects regarding the adsorption/desorption processes are well described by the Langmuir isotherm, that relates the surface coverage to the gas pressure on the surface.

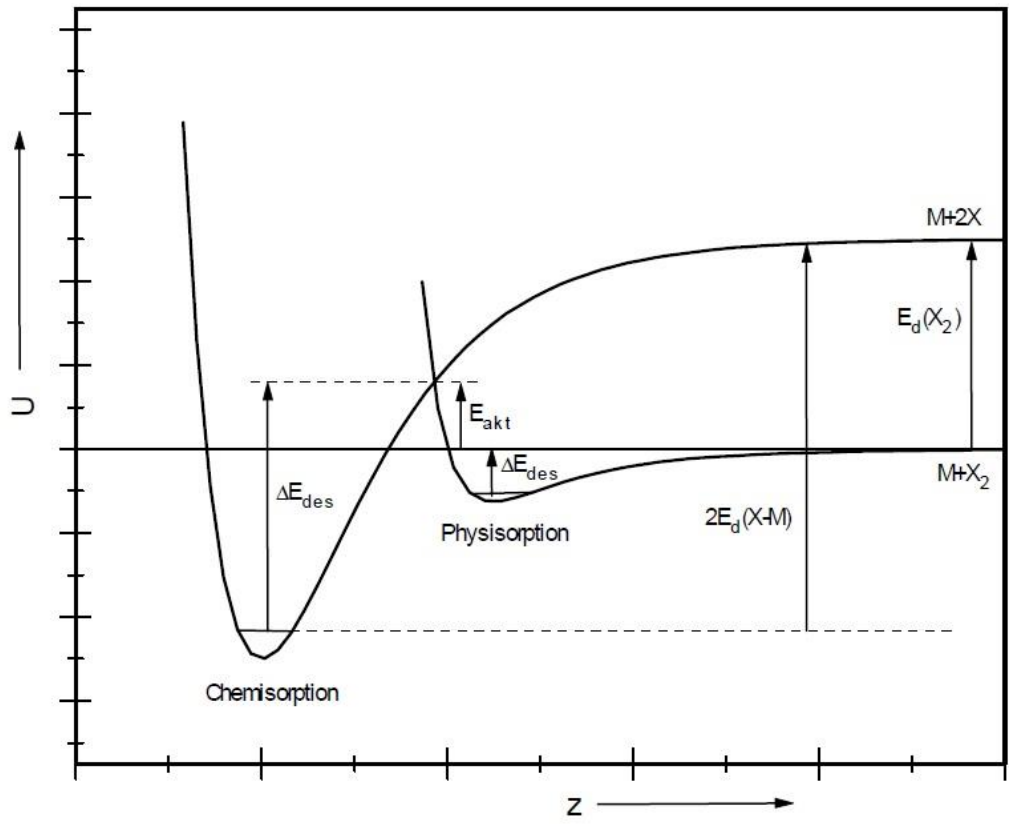

Figure 1.26: Schematic potential diagram for the activated, dissociative adsorption of a diatomic molecule X_2 that approaches a substrate surface along the trajectory z. The physisorption potential has been assumed to be a *Lennard-Jones* potential, whereas chemisorption is described in this diagram by a *Morse* potential.

1.5.2 Thermodynamic View of Adsorption: The Heat of Adsorption

The temperature dependence of the gas pressure *p* required for equilibrium between the adsorption and desorption can be calculated with the Clausius-Clapeyron equation. If we assume that equilibrium is defined by a constant ratio Θ between the number N_{ads} of adsorbed particles and the number N_{surf} of adsorption sites available at a surface (in the following, this ratio shall be referred to as the *surface coverage* $\Theta = N_{ads}/N_{surf}$) then the condition for chemical equilibrium between adsorbate and gas phase particles is equality of the chemical potentials of the particles in both phases, *i.e.* $d\mu_{ads} = d\mu_{gas}$. Neglecting the volume of the condensed surface phase one obtains:

$$\left(\frac{\partial \ln p}{\partial T}\right)_{\Theta} = \frac{q_{isost}}{RT^2} \tag{1.60}$$

q_{isost} is called the *isosteric heat of adsorption* and is a differential heat, *i.e.*,

$$q_{isost} = (\partial H/\partial \Theta)_T\,. \tag{1.61}$$

However, note that alternative definitions for equilibrium can be chosen, which depend on the parameter set used for the characterization of the adsorption/desorption equilibrium. For example, instead of defining equilibrium by a constant surface coverage one can require a constant pressure ϕ at the surface. In this case we obtain a Clausius-Clapeyron equation that contains a different heat q_{eq},

$$\left(\frac{\partial \ln p}{\partial T}\right)_{\phi} = \frac{q_{eq}}{RT^2} \tag{1.62}$$

which is now called the *equilibrium heat of adsorption.* It is an integral heat, *i.e*.

$$q_{eq}(\phi) = \int_0^{\phi} dH_T(\phi')d\phi' \tag{1.63}$$

1.5.3 Kinetics of Adsorption and Desorption

1.5.3.1 Langmuir Adsorption Isotherms

Adsorption isotherms describe the surface coverage as a function of the gas pressure over the sample. The most important adsorption isotherm for the discussion of adsorption/desorption phenomena is the *Langmuir* adsorption isotherm, which is based on the following assumptions:

• Adsorption is localised, i.e., the adsorbed particles are immobile.

• The substrate surface is saturated at Θ = 1 ML (monolayer), *i.e*., when all adsorption sites are occupied.

• There are no interactions between the adsorbed particles.

In this case, we obtain for the rates of adsorption and desorption

$r_{ad}(\Theta) = A_n\, p(1-\Theta)^n$ (1.64)

$r_{des}(\Theta) = B_n\Theta^n$ (A_n, B_n = const., n = 1, 2). (1.65)

From the condition for a dynamic equilibrium $|r_{ad}| = |r_{des}|$ it follows that

$$\Theta_n = \frac{(b_n p)^{1/n}}{1+(b_n p)^{1/n}} \quad (b_n = b_n(T) = A_n/B_n = \text{const.}, n = 1, 2) \tag{1.66}$$

For n = 1 we have a first order rate law for adsorption and desorption. For n = 2 we have a second order process, which corresponds, e.g., to dissociative adsorption and recombinative desorption of diatomic molecules. Note that the dissociation of molecules can often be suppressed by lowering the temperature of the surface. An example is the adsorption of O_2 on Ag(110), which is dissociative at room temperature, but non-dissociative (n = 1) at 150 K

Normally any kinetic study involves the monitoring the concentration of any one of the species in the reaction as a function of both mostly time and also sometimes temperature. However, in the Temperature Programmed techniques (TPX) since time and temperature are interrelated by the expression $T(t) = T_0 + \alpha t$ (where T is the temperature at any time t, T_0 is the start temperature and α is the heating rate that is (dT/dt) in the units of K/sec), it provides a means to study two variables of a reaction at the same time, this method has attracted considerable attention. There are a range of techniques for studying surface reactions based on temperature sweep. Molecular adsorption on surfaces can be studied using temperature-programming to discriminate between processes with different activation parameters. Temperature programmed techniques can be reduction, oxidation, reaction, and hence there can be a number of TPX techniques where X stands for the process that is being studied. Experimentally too, this method of analysis is simple requiring a simple pressure gauge or a chemical analytical tool like gas chromatograph or a mass spectrometer. Even a pressure measurement as a function of time and temperature may be sufficient in some instances. The basic experiment is very simple, involving the following two steps in the case of desorption

1. Adsorption of one or more molecular species onto the sample surface at low temperature (frequently 300 K, but sometimes sub-ambient).

2. Heating of the sample in a controlled manner (preferably so as to give a linear temperature ramp) while monitoring the evolution of species from the surface back into the gas phase.

The data obtained from such an experiment consists of the intensity variation (the concentration of the desorbed species) of each recorded mass fragment as a function of time / temperature. In the case of a simple reversible adsorption process it may only be necessary to record one signal - that is attributable to the molecular ion of the adsorbate concerned.

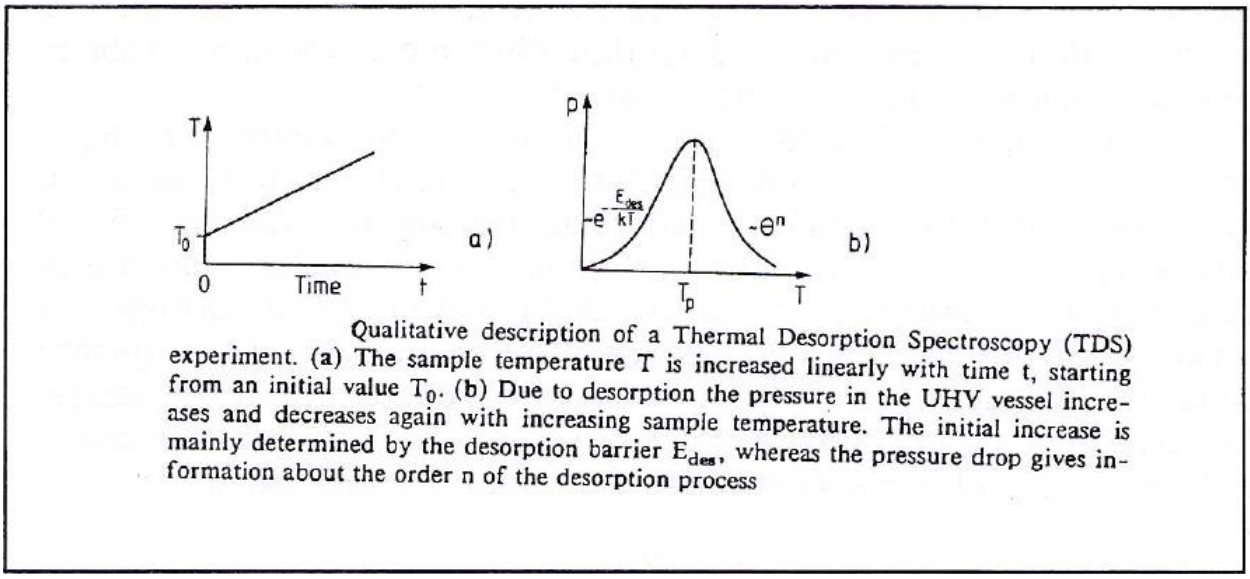

Qualitative description of a Thermal Desorption Spectroscopy (TDS) experiment. (a) The sample temperature T is increased linearly with time t, starting from an initial value T_0. (b) Due to desorption the pressure in the UHV vessel increases and decreases again with increasing sample temperature. The initial increase is mainly determined by the desorption barrier E_{des}, whereas the pressure drop gives information about the order n of the desorption process

Figure 1.27: Qualitative description of a Thermal Desorption Spectroscopy.

Since mass spectrometric detection is used normally the sensitivity of the technique is good with attainable detection limits below 0.1% of a monolayer of adsorbate.

The following points are worth noting:

1. The area under a peak is proportional to the amount originally adsorbed, i.e. proportional to the surface coverage.

2. The kinetics of desorption (obtained from the peak profile and the coverage dependence of the desorption characteristics) give information on the state of aggregation of the adsorbed species e.g. molecular or dissociative adsorption.

3. The position of the peak (the peak temperature) is related to the enthalpy of adsorption, i.e. to the strength of binding to the surface.

If there is more than one binding state for a molecule on a given surface (and if these have significantly different adsorption enthalpies) then one will be able to discriminate them from the multiple peaks in the TPD spectrum.

1.5.3.2 Polanyi-Wigner Equation[21]

The principle of microscopic reversibility demands that a reaction passes through exactly the same states irrespective of whether it proceeds forward or backward. Adsorption and desorption can therefore be described by the same set of rate equations. Desorption rate is usually expressed by a rate law of n^{th} order:

$$r_{des} = \frac{d\Theta}{dt} = k_n \cdot \Theta^n \qquad (1.66)$$

If the rate constant k_n is described by the *Arrhenius* equation

$$k_n = \nu_n \cdot \exp\left(-\frac{\Delta E_{des}^{PW}}{RT}\right) \qquad (1.67)$$

then the rate law is usually referred to as the *Polanyi-Wigner* equation:

$$r_{des} = \frac{d\Theta}{dt} = \nu_n \cdot \exp\left(-\frac{\Delta E_{des}^{PW}}{RT}\right) \cdot \Theta^n \qquad (1.68)$$

which defines the activation energy of desorption ΔE_{des}^{PW} and which we will simply call E_a^{des}.

In a temperature programmed desorption experiment temperature and time are related by the expression

$\boldsymbol{T = T_o + \beta t}$ and $\mathbf{d}\boldsymbol{T = \beta}\mathbf{d}\boldsymbol{t}$,

where T_0 is the starting temperature and β is the heating rate.

The intensity of the desorption signal, $I(T)$, is proportional to the rate at which the surface concentration of adsorbed species N is decreasing. This can be expressed as

$$I(T) \equiv dN/dT = (\nu N^n/\beta) \exp(-E_a^{des}/RT) \quad (1.69)$$

Where N and Θ are tied in this equation:

$$\Theta = \frac{N}{AM_0} \quad (1.70)$$

Where A is the area of the absorbed phase and M_0 is the number of surface substrate atoms per unit area.

This problem can also be understood in terms of some graphical representation. The equation for signal intensity consists of two terms corresponding to the surface coverage and the exponential term. At low temperatures, the exponential term is small and it increases with increase of temperature and the increase is significant when the value of RT is equal to E_a. On the other hand, the coverage dependent term remains constant initially and decreases rapidly as the desorption temperature is approaching and attains the value of zero at some temperature.

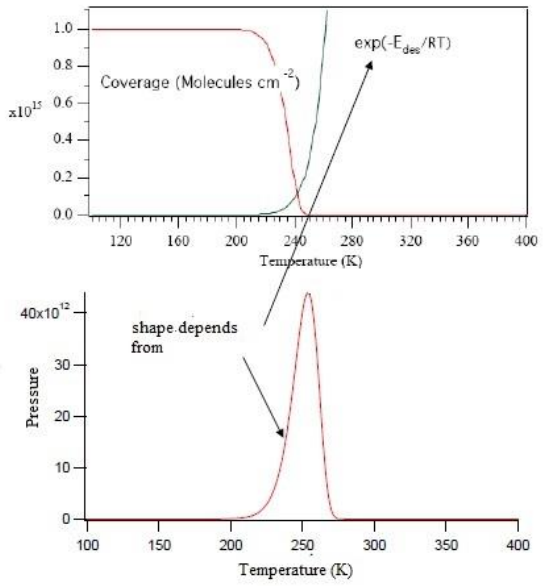

Figure 1.28: Graphic displaying dependency of signal intensity from coverage and exponential term.

Let us consider a simple case for understanding the nature of desorption traces one will obtain. The case that is considered is (1) adsorption is as a molecular species and (2) the order of desorption is unity.

The maximum in the desorption trace (that is the signal $I(T)$ will attain a maximum value) will occur when (dI/dT) = 0, i.e. when

$$(d/dT)\{(\nu N/\beta) \exp(-E_a^{des}/RT)\} = 0 \quad (1.71)$$

This can be re-written taking into account that surface coverage N itself is a function of temperature

$$(vN/\beta)\cdot(E_a^{des}/RT)\exp(-E_a^{des}/RT) + (v/\beta)\exp(-E_a^{des}/RT)\cdot dN/dT = 0 \quad (1.72)$$

Substituting for d*N*/d*T* , one gets

$$(vN/\beta)\cdot\mathbf{[}(E_a^{des}/RT) - (v/\beta)\exp(-E_a^{des}/RT)\mathbf{]}\cdot(\exp(-E_a^{des}/RT)) = 0 \quad (1.73)$$

The solution is given by setting the expression in square brackets to be equal to zero,

i.e. $E_a^{des}/RT_p^2 = (v/\beta)\exp(-E_a^{des}/RT_p)$,

where T_p represents the peak maximum temperature. One can notice that:

1. Depending on the value of E_a^{des} the peak maximum temperature also varies, higher the value of E_a^{des} higher will be the peak temperature Tp.

2. The peak maximum temperature is independent of the initial coverage.

3. The shape of the trace will depend on the rate of desorption process and it will decrease rapidly after the desorption maximum.

More detailed quantitative information on TPD is beyond the scope of this book and they can be found elsewhere.

In general this technique can provide a variety of information on various aspects of adsorption and catalysis. They are:

1. Mechanistic aspects of reaction under study.

2. Identification of the nature of active sites, binding states of adsorbed species binding energy of the adsorbed species.

3. The influence of preparation procedures on the catalysts developed.

4. Effects of active phase, chemical composition, promoter dispersion, surface groups.

5. Active phase support interaction, alloy/compound formation.

References:

1. W. M. LC Feldman, *Fundamentals of Surface and Thin Film Analysis*, 1986, **Elsevier**.
2. M. S. D. Briggs, *Practical Surface Analysis, Second Edition, Volume 1, Auger and X-Ray Photoelectron Spectroscopy* 1990, **Wiley**.
3. C. R. B. C S Fadley, A D Baker, *Basic Concepts of X-ray Photoelectron Spectroscopy, in Electron Spectroscopy, Theory, and Thechniques Apllications*, 1978, **Pergamon Press**.
4. M. Eusebio, *University of Padua*, 2003.
5. S. Tanuma, C. J. Powell and D. R. Penn, *Surface and Interface Analysis*, 1988, **11**, 577-589.
6. S. Tanuma, C. J. Powell and D. R. Penn, *Surface and Interface Analysis*, 1991, **17**, 911-926.
7. S. Tanuma, C. J. Powell and D. R. Penn, *Surface and Interface Analysis*, 1991, **17**, 927-939.
8. S. Tanuma, C. J. Powell and D. R. Penn, *Surface and Interface Analysis*, 1993, **20**, 77-89.
9. S. Tanuma, C. J. Powell and D. R. Penn, *Surface and Interface Analysis*, 2003, **35**, 268-275.
10. S. Tanuma, C. J. Powell and D. R. Penn, *Surface and Interface Analysis*, 2005, **37**, 1-14.
11. N. Beatham and A. F. Orchard, *Journal of Electron Spectroscopy and Related Phenomena*, 1979, **16**, 77-86.
12. B. L. Henke, *Physical Review A*, 1972, **6**, 94-104.
13. M. Mehta and C. S. Fadley, *Physics Letters A*, 1975, **55**, 59-61.
14. G. Granozzi, *Lecture notes of the course of Solid State Chemistry and Surfaces*, 1999, **Vol 2**.
15. www.matter.org.uk/diffraction/.
16. P. Hofmann, *Lecture Notes on Surface Science*, 2005.
17. http://capsicum.me.utexas.edu/ChE386K/.
18. G. Granozzi, *Lecture notes of the course of Solid State Chemistry and Surfaces*, 1999, **Vol 6**.
19. M. G. S L M Schroeder, *Lecture Notes - Advanced Physical Chemistry Laboratory*, 2002, **FU Berlin**.
20. J. A. W. Elliott and C. A. Ward, *The Journal of Chemical Physics*, 1997, **106**, 5677-5684.
21. D. K. Chakrabarty and B. Viswanathan, *Heterogeneous Catalysis*, New Age Science, Limited, 2009.

Chapter 2

2.1 Experimental Apparatus

The experiments presented in this thesis were performed on two different UHV chambers:

The High Resolution XPS and AR-XPD experiments were performed in a multi technique UHV chamber (figure A) equipped with a 5 degree of freedom (x, y, z, polar angle θ and azimuthal angle ϕ) manipulator and the possibility to heat the sample up to 1000 K, a four grid rear-LEED, a double anode (Mg/Al) X ray source interfaced with a 5 channeltrons electron hemispherical analyzer, an UV radiation source (used for UPS, HeI and HeII photon excitation energies), two e-beam water cooled evaporators, a QMS for the residual gas analysis and a filament ion gun. This chamber was principally used for ZTB experiments where the vial containing the precursor was connected via a gas line to the preparation chamber; the same line was also connected to an oil pump to vacuum the precursor in order to facilitate evaporation and eliminate residual gases. The vial and precursor one mounted were freeze-pump-thawed for several cycles in order to eliminate contaminating gases. During depositions ZTB was introduced into the chamber via a retractable leak valve connected to a nozzle that could bring the precursor within 3 cm of the substrate's surface. This chamber was also used for the growth of ceria films with an e-beam evaporator (OMICRON EFM 3) with crucible. Initially two conditions were used, both in an oxygen environment of 5.2×10^{-6} mbar for 10 minutes: sample at RT and heated at 600 K during growth. The former condition gave the most oxidized ceria and a subsequent annealing at 900 K helped to make the deposit more homogeneous albeit more reduced. However for the small thicknesses required to study the interface, cerium was always present in its Ce(III) oxidation state independently from preparation method. Thus for the lower growth deposition was conducted in UHV at RT followed by annealing in 300 L oxygen at 900K for 5 min.

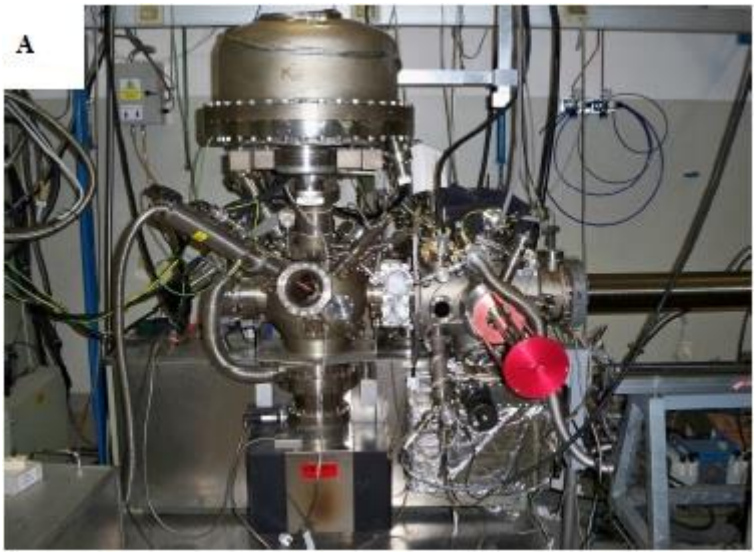

the TPD experiments were performed in a multi technique UHV chamber (figure B), equipped with a 4 degree of freedom (x, y, z and polar angle θ) manipulator and the possibility to heat the sample up to 1000 K and down to 110 K, an high sensibility QMS, a four grid rear-view LEED, a double anode (Mg/Al) X ray source interfaced with a single channeltron electron hemispherical analyzer (CLAM 2), one e-beam water cooled evaporators and a cold cathode ion gun. The sample is mounted on two 0.30 mm thick Ta wires welded onto a Ta sheet and glued with an electrical insulating ceramic glue by CERAMACO. The temperature is measured through a welded K type thermocouple. Moreover, the QMS is covered by a glass cylinder with a small aperture facing the sample at ca. 2 mm. This setup is necessary to focus the analysis on the desorption from the sample surface, avoiding any other contribution. In this chamber we tested the reactivity of ceria. Via a gas line oxygen, methanol and ethanol were dosed to conduct such tests.

CHAPTER 3

3.1 TITANIUM DIOXIDE

Titanium as the other transition metals can access various oxidation states (0 to +4) even if the best known ones are the +3 and + 4. In the latter, the most stable, the metal forms with oxygen various structures of oxides. The three most important are anatase, brookite and rutile of which the structure is shown in Figure 1.2.

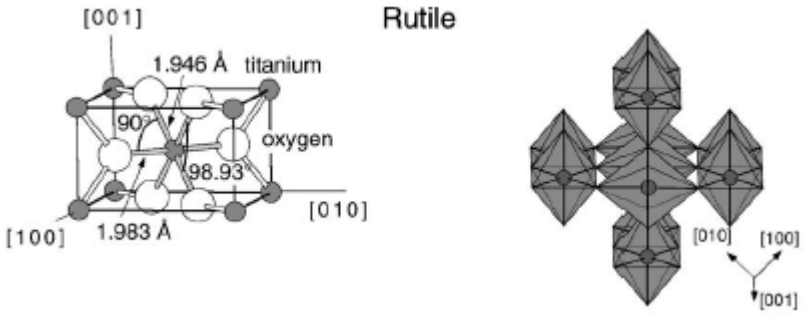

Figure 3.1: Shows the unit cell of rutile to the left while the arrangement and mode of crystal growth is shown on the right.

Among the various oxides of Ti, rutile is the most stable and is the most studied in the field of surface science. In truth, the fact of using a well-known model allows to better study and highlights the properties of any film deposited on this structure. As seen in the figure, rutile has a tetragonal structure with cell constants: **a** = **b** = 4.584 Å and **c** = 2.953 Å with the central titanium atom surrounded by six oxygens. In the figure we see that the crystal is built in a succession of octahedra that ordered either along the short side or the long one in an alternating fashion. In figure 1.3 is represented the surface (110) the most stable of the three low index surfaces.

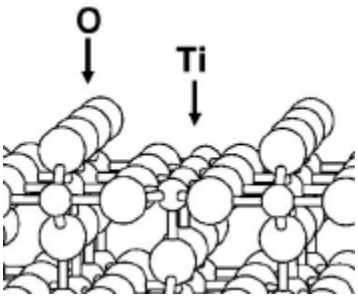

Figure 1.3: Here is shown the surface (110) of TiO_2. We have highlighted the bridging oxygen atoms and the “uncovered” titanium atoms.

As can be seen it consists of alternate rows of “uncovered” (five-fold coordinated) titanium atoms, and with bridging oxygen atoms (six-fold coordinated), where the former are characterized by having a pendant bond that protrudes perpendicularly from the surface. We may also identify two types of oxygen atoms: the three-fold coordinate ones (present in the bulk and that link together the titanium atoms) and the two-fold coordinate ones forming the bridging oxygen atoms. The surface is terminated with bridging oxygen atoms because, in this way, the number of Ti-O bonds that need to be "broken" per unit length is the same, both along the imaginary line that runs along the bridging oxygen atoms, and along the line that runs along the direction of five-fold coordinated Ti. The presence of coordinative unsaturation causes a relaxation of the surface structure (figure 1.4) so that the five-fold coordinated titanium atoms undergo a slight sag, while the oxygen atoms will move in the opposite direction in an attempt to increase the total coordination[1].

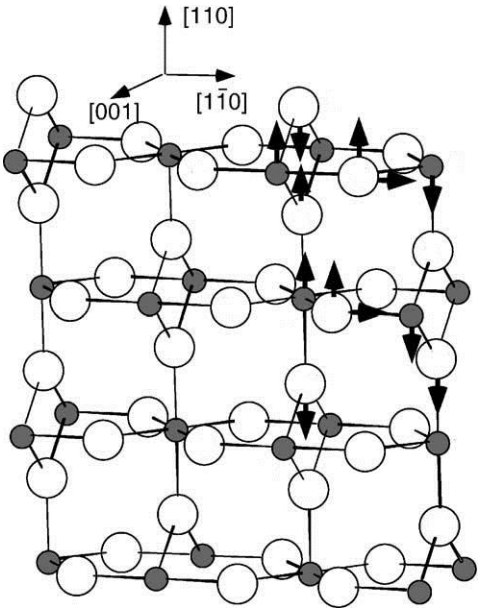

Figure 3.2: highlighted is the displacement of Ti atoms and O following the relaxation of the surface.

3.1.1 Reduced TiO_2 (110)

The annealing in UHV or *sputtering* treatment reduces the TiO_2 (110) surface by creating oxygen vacancies. The figure below shows two measurements of photoemission from the valence band to

demonstrate the presence of such vacancies. It is called *"blue"* TiO_2 due to the formation of color centers that manifest as a blue color (d-d transitions).

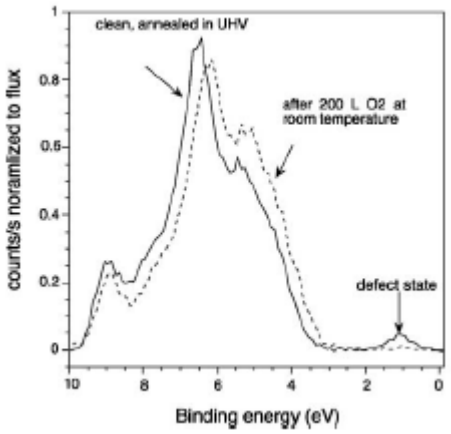

Figure 3.3: Shows the UPS spectrum of titania showing, in the continuous line, when it is defective and splintered when it is stoichiometric.

The solid line represents the crystal reduced after *sputtering* and *annealing* in ultra high vacuum. The other line shows instead the change after exposure to oxygen. We can observe that the defective state on the right disappears after the treatment, as oxygen goes to fill the vacancies, highlighted by a partial occupation of the 3d band (peak centered at about 1 eV). The *blue-*TiO_2 is a semiconductor of n-type as in the presence of oxygen vacancies corresponding electrons act as donor states. In any case, from the structural point of view obtaining the reduced surface by *sputtering* does not necessarily imply that it is also totally disordered, indeed LEED images have shown a long-range disorder, but X-ray Photoelectron Diffraction measurements showed that there continues to be a short-range order. Usually the damage caused by the sputtering can be healed by annealing in UHV, although, at high temperatures, further defects are formed. The heat treatment in UHV makes the surface flatter due to the formation of extensive terraces.

The treatment of reduced titania with gaseous oxygen leads to a restructuring of the crystal due to re-oxidation. The bulk sub-stoichiometric TiO_{2-x} contains in addition to O vacancies interstitial Ti which shows a diffusivity at high temperatures. It was observed to migrate to the surface and react with O_2 in order to form TiO_2. This will result in a color loss from the crystal and a change in the surface structure.

3.1.2 Stoichiometric TiO_2 (110)

This type of structure can be obtained by a light heat treatment of the stoichiometric solid or by re-oxidation, in oxygen atmosphere, of reduced titania. The color centers disappear and with them the intense blue color. Thus a crystal of stoichiometric TiO_2 is characterized by a pale yellow color.

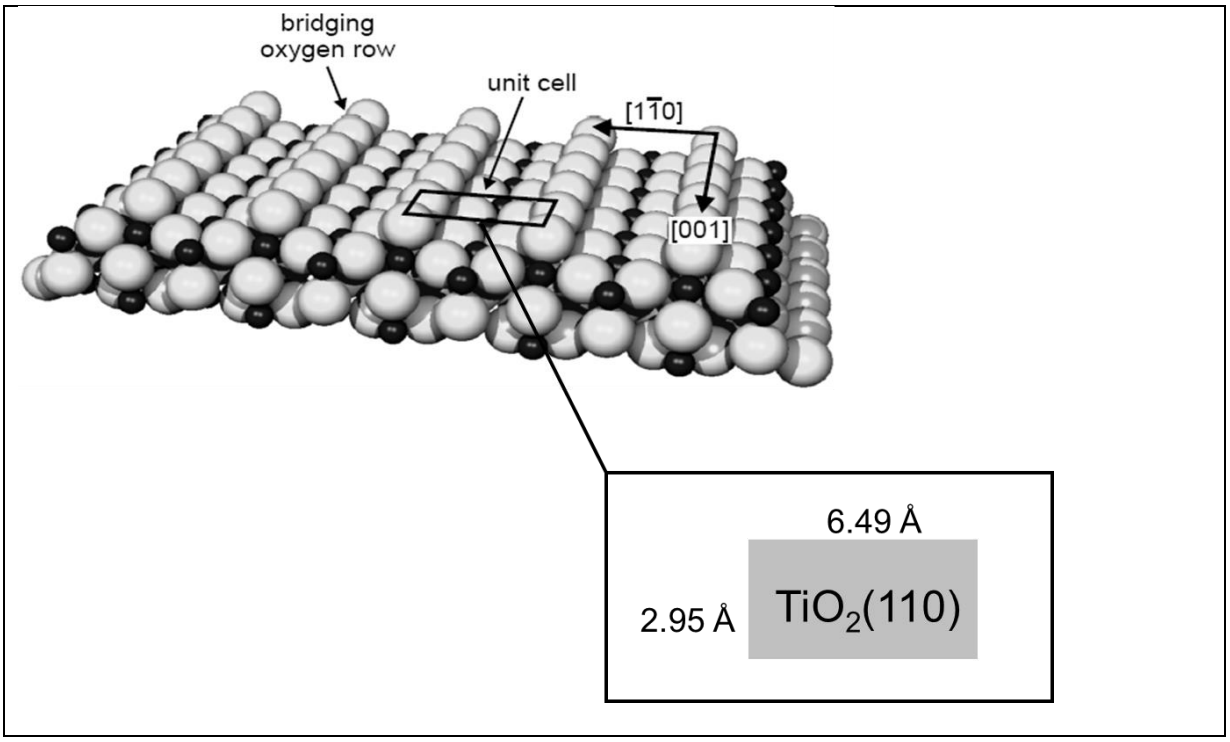

Figure 3.4: TiO_2(110) surface with unit cell and principal directions.

In the above figure we have reported an image of the TiO_2(110) surface where, highlighted, are the principal directions [001] and [1-10]. In the figure (Fig.2) below we have reported the resulting LEED pattern obtained after a cleaning treatment. In the picture we have highlighted the surface unit cell and the aforementioned directions; in reciprocal space the long cell border corresponds to the [001] direction and the short one to [1-10].

Surface structure variations depending on the pressure of gaseous oxygen, the temperature of the crystal and the density of defects in the bulk are so numerous that one can imagine a wide and varied chemistry of the TiO_2 (110) - (1x1) surface of. In any case, as reported by Diebold[1], if you want to use (1x1) surfaces the best crystals are the light-blue ones, which a happy medium between the *blue* (very reduced) and *yellow* (stoichiometric) types. An annealing in oxygen of any treated surface (by *sputtering* or annealing in UHV) will result in stoichiometric surfaces (1x1). However, if one starts with crystals that are too small then significant changes in surface morphology may occur; thus pre-caution should be used even against used oxygen. If this turns out to have impurities such as water, then

this will occupy the vacant sites preventing a correct reconstruction of the surface, also, the same oxygen can dissociate on vacancies to form highly reactive radicals. All these aspects give titania a range of interesting reactivity for a wide variety of surface chemistry experiments.

3.1.3 Cleaning the sample

We have used as substrate an epi-polished rutile TiO_2 crystal provided by MaTecK, and this was mounted on a rotating sample holder with two Mo clips holding the substrate and a K-thermocouple in place. In order to avoid insulating problems via charge accumulation on the top of the sample the K-thermocouple during XPS measurements was earthed on the exterior of the instrument. The samples were cleaned via sputtering treatments of 2.0 keV with an Ar^+ flux of about $5 \cdot 10^{-7}$ mbar at an angle of 45˚ respect to surface normal for 20 minutes. This was followed by an annealing in UHV for 5 minutes at 923 K which helped to form a stoichiometric surface, via diffusion of bulk O^{2-}, and wide (110) terraces as well as, through the introduction of O vacancies, good sample conductivity. Various cleaning cycles were undertaken until the surface was free from contamination, chiefly Carbon and Potassium, and a well-defined LEED pattern was visible. We have described previously that the surface unit cell is 2.95 Å x 6.49 Å respectively along the [001] and [1-10] directions and thus we expect to observe a LEED characterized by a rectangular pattern.

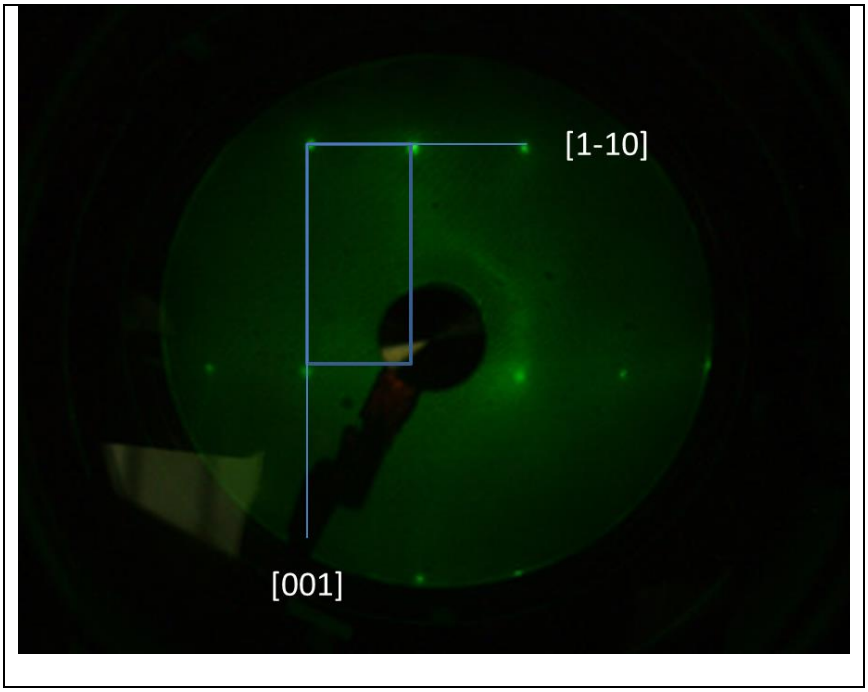

Figure 3.5: LEED of the clean TiO_2(110) surface taken at 53 eV. Highlighted are the unit cell and the corresponding crystallographic directions.

References:

1. U. Diebold, *Surface Science Reports*, 2003, **48**, 53-229.

CHAPTER 4

THE ZIRCONIA – TITANIA SYSTEM

4.1 Zirconium Dioxide

Recently nanostructured materials have gained interest in the scientific and engineering communities due to their differing chemical, electrical, optical and magnetic properties in respect to their bulk phases.

Zirconia has a wide range of existing and potential technological applications, e.g. high temperature fuel cells [1], gas sensing and other relevant appliances such as extra-corporeal dialysis filters, ceramic compounds and optical devices [2,3]. The properties that establish the use of zirconia in material science applications include its high melting point, low thermal conductivity and high mechanical and corrosion resistance. In the field of catalysis, zirconia is employed both as support and active component. For example, it has been investigated as a catalyst for partial oxidation, dehydration, isomerization of hydrocarbons, dehydrogenation of alkanes, synthesis of olefins from alcohols [4,5]. As a component of mixed oxide acid–base bifunctional catalysts [6] and methanol synthesis catalysts [7]. Finally, it has been demonstrated as a thermally-stable support in the catalytic combustion of methane [8]. Its most important catalytic application is in three-way automotive catalytic converters, where it is considered essential to stabilize the ceria active component [9]. Moreover, one of its recently uncovered aspects is its possible use in the photocatalytic reduction of greenhouse gasses [10], especially in conjunction with titania [11]for environmental [12] and energy applications [13]. Nowadays, among the many routes explored to maximize its photocatalytic properties, much work is being devoted to evaluate the performances in mixed oxides.

The spatial arrangement of the atoms in zirconia is characterized by distinct crystallographic structures, characterizing a property known as polymorphism. Its three phases, or crystal structures, are characterized by specific geometry and dimensional parameters: monoclinic, tetragonal and cubic.

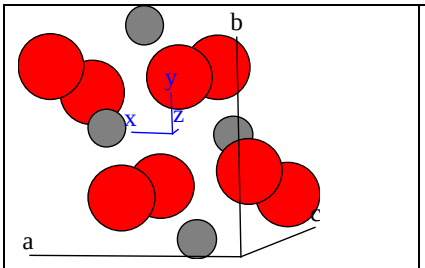

Fig. 4.1a

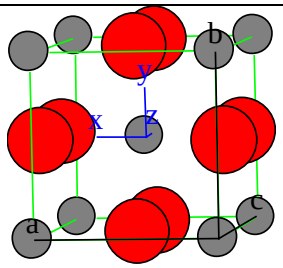

Fig. 4.1b

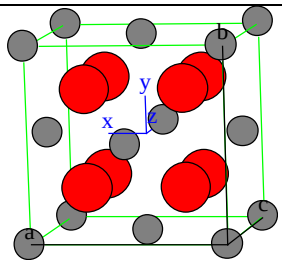

Fig. 4.1c

Figure 4.1: the three crystallographic structures of zirconia: (a) monoclinic, (b) tetragonal, (c) cubic.

Pure zirconia has a monoclinic structure at room temperature, which is stable up to 1170°C. Between this temperature and 2370°C, tetragonal zirconia is formed, while cubic zirconia is formed at temperatures above 2370°C. After processing, and depending on the cooling process, the tetragonal phase becomes monoclinic at about 970°C. Due to polymorphism, pure zirconia cannot be used at elevated temperatures due to a large volume change (3-5%) which occurs during cooling to the monoclinic phase. This change is sufficient to exceed the elastic and fracture limits, resulting in cracks and flaws in ceramics. Above I have depicted the three phases: monoclinic (Figure 4.1a) zirconia belongs to the $P2_{1/c}$ space group, whereas tetragonal (Figure 4.1b) belongs to the $P4_2/nmc$, finally cubic (Figure 4.1c) belongs to Fm3m. Progressing from monoclinic to cubic structure and volume changes are readily apparent. Thus one solution to this problem is doping the oxide with aliovalent cations such as Ca^{2+}, Mg^{2+} or Y^{3+} which stabilize the tetragonal and cubic forms at room temperature. Electrostatic neutrality in these doped materials is maintained by oxygen vacancies thus local atomic environments are very different from the corresponding pure tetragonal and cubic phases. The three phases are insulators with reported experimental band gap values for monoclinic, tetragonal and cubic, obtained via vacuum-ultra violet spectroscopy, are respectively 5.78 eV (*m*-ZrO_2), 5.83 eV (*t*-ZrO_2) and 6.1 eV (*c*-ZrO_2) [14].

4.1.2 ZrO_2 - TiO_2 Mixed Oxides

One of the recently uncovered aspects of the zirconia/titania mixed oxide is its possible use in the photocatalytic reduction of greenhouse gasses [10], [11], for environmental [12] and energy applications [13]. Nowadays, among the many routes explored to maximize its photocatalytic properties, much work is being devoted to evaluate the performances in mixed oxides. Recently [15] it has been demonstrated that, while interfaces between identical oxides substantially decrease the number of trapped charges, TiO_2-ZrO_2 heterojunctions give rise to a clear beneficial effect to the photocatalytic activity. Actually, there is an effective interfacial charge separation across nanometer-sized TiO_2-ZrO_2 interfaces attributed to the diminished charge carrier recombination in ZrO_2. In addition, ZrO_2-TiO_2 mixed oxides have attracted much attention because they show both better thermal stability and modified surface acidity properties with respect to the bare ZrO_2 [16] and literature is quite extensive [17], [18], [19], [20].

Despite the interest for their catalytic and photocatalytic applications a systematic characterization of the interface composition and properties of these mixed oxide system is still lacking. To our best knowledge there are only few examples in the literature where true substitutional $Ti_{(1-x)}Zr_xO_2$ mixed oxides have been characterized. In the first case the authors used a laser ablation procedure, while in the latter the samples were prepared with an inverse microemulsion methods [21], [22].

We have therefore undertaken an accurate work based on the premises of Surface Science aiming at the preparation and characterization of ultra-thin film of $ZrO_2/TiO_2(110)$. The growth has been carried out by ultra-high-vacuum (UHV) chemical vapor deposition (CVD) and the films have been characterized by photoemission spectroscopy (XPS) and diffraction (XPD). The goal is putting on a firm basis the description of chemical and structural characterization of the ZrO_2/TiO_2 interface.

4.1.3 Use of Zirconium Tetra *tert*-Butoxide as precursor

Zirconia Tetra *tert*-Butoxide was the chosen precursor for this study. Because line-of-sight techniques such as sputtering or metal evaporation are limited by defects and pinholes and for an oxide such as zirconia, which crack easily due to thermal expansion, an alternative way of deposition was sought for. Furthermore, zirconium metal has a high melting point (2128 K), and a low vapor pressure (10^{-5} bar at 2639 K) making its use energetically costly and difficult. First studied by D. C. Bradley [23] as a precursor for electronic and ceramic materials ZTB showed a capability of being purified to a high degree by distillation and sublimation in vacuo. Furthermore, the metal is strongly bonded to the alkoxide group which contain more than enough oxygen to form the oxide. In his study Bradley also reported the importance of surface hydroxyl groups in the thermal deposition of ZTB. In fact, the decomposition of ZTB is initiated, at elevated temperatures, by a self-catalyzed reaction due to trace impurity hydroxyl groups present in ZTB, on the internal surface of the vacuum chamber and finally on hydroxyls present on the substrate's surface. Afterwards, the chemically adsorbed *tert*-butoxy intermediate undergoes β-hydride elimination to deposit ZrO_2 and regenerate the hydroxyl groups:

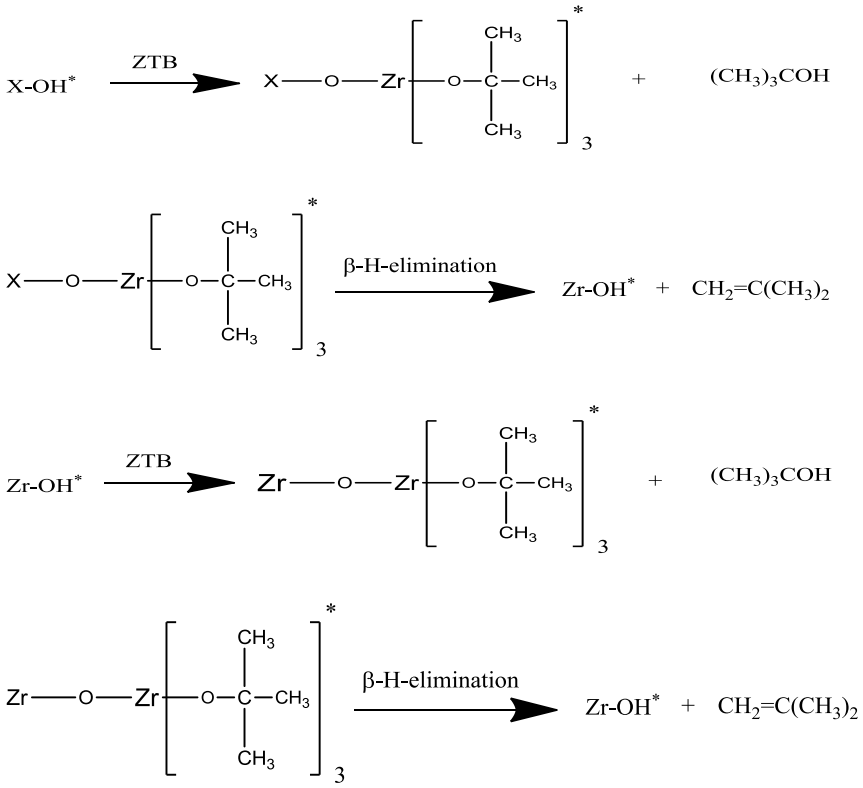

Cameron et al.[24] proposed the above reaction mechanism on Si(100) for temperatures up to 723 K whereas at higher temperatures precursor pyrolysis competed with β-H elimination thus slowing the growth rate. Burleson et al.[25] took the physical adsorption equilibrium of ZTB molecules on ZrO_2 surface

into consideration, and extracted the kinetic parameters of deposition reactions. The stoichiometry of the deposition reaction can be expressed as

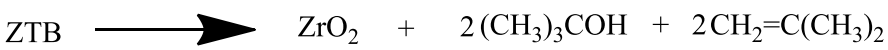

$$ZTB \longrightarrow ZrO_2 + 2(CH_3)_3COH + 2CH_2{=}C(CH_3)_2$$

Therefore, a mass balance on oxygen can be maintained during deposition without using additional oxygen gas or water[26]. Additionally, the dehydration reaction of alcohols at elevated temperatures is well known.

$$(CH_3)_3COH \longrightarrow CH_2{=}C(CH_3)_2 + H_2O$$

ZTB was then studied for potential in electronic applications due to the need of researching for high-k dielectric materials [27] and demonstrated an overall higher thermal stability and higher dielectric constant compared to SiO_2. The zirconia/silicon system was further studied observing by products and growth rates [24],[28] and an interesting study was conducted by Karlsson et al.[29], [30] where the initial stages of ZTB deposition on silicon substrates were studied and various carbon interface species were observed. Recently the successfulness of ZTB was further demonstrated in the production of flexible electronic at RT [31] and its use in memory device applications [32]. Because of the high plethora of ZTB literature in CVD techniques and its continuing usefulness in the industry our choice fell on this precursor for our study of the ZrO_2/TiO_2 system.

4.1.4 The ZrO_2/TiO_2(110) model catalyst preparation

In this chapter I will report on the work done on the ZrO_2/TiO_2 model catalyst during my doctoral studies. In this work zirconia was deposited onto the substrate via metal-organic chemical vapor deposition (MOCVD) method through the use of Zirconium Tetra *tert*-Butoxide (ZTB). We have used as substrate an epi-polished rutile TiO_2 crystal provided by MaTecK, and this was mounted on a rotating sample holder with two Mo clips holding the substrate and a K-thermocouple in place. The samples were cleaned via sputtering treatments with 2.0 kV Ar^+ flux (P= $5 \cdot 10^{-7}$ mbar) at an angle of 45˚ respect to surface normal for 20 minutes. This was followed by an annealing in UHV for 5 minutes at 923 K that helped to form a stoichiometric surface and wide (110) terraces, while the introduction of O vacancies, assured a good sample conductivity. Various cleaning cycles were undertaken until the surface was free from contamination, mainly Carbon and Potassium, and a well-defined LEED pattern was visible [33],[34]. Since ZTB is extremely hygroscopic, the precursor was inserted in a UHV vial in a dry box, in order to avoid ambient moisture. After this, the UHV vial was connected via a gas line to the preparation chamber. The vial and precursor were freeze-pump-thawed for several cycles in order to eliminate contaminating gases. ZTB was introduced into the chamber via a leak valve connected to a bellow and a nozzle, 3 cm away from the substrate's surface. During the deposition a quadrupole mass spectrometer (QMS, PFEIFFER Prisma 80) was used to monitor isobutylene, the main product resulting from the

decomposition on the surface of ZTB, as already verified by Cameron et al. [24]. QMS was used together with a pressure gauge to correctly read the pressure during depositions.

The experimental procedure to effectively deposit ZrO_2 on TiO_2(110) required a long optimization of the experimental parameters. It was shown by other authors [29, 30] that the ZTB decomposition process might form, at different temperatures, various carbonaceous residues, especially at low temperatures, when the decomposition rate is particularly slow. An initial deposition was carried out at three different temperatures 677K, 738K, 773K and in five stages of a minute each at a pressure of $1.3 \cdot 10^{-7}$mbar, subsequent depositions to ensure monolayer thicknesses were undertaken at a lower pressure of $1.3 \cdot 10^{-8}$mbar. The results were traced by using XPS. We defined the MonoLayer (ML) as the thickness of tetragonal ZrO_2 half cell length along [001] (2.63 Å).

XPS and XPD experiments were performed in a multi-technique UHV chamber equipped with a 5 degree of freedom (x, y, z, polar angle θ and azimuthal angle ϕ) manipulator [35] and the possibility to heat the sample up to 1000 K, a four grid rear-LEED, a double anode OMICRON (Mg/Al) X ray source interfaced with a 5 channeltrons VG ESCALAB electron hemispherical analyzer, a He-plasma UV radiation source (used for UPS, HeI and HeII photon excitation energies). All the XPS measurements were performed at RT using non-monochromatized Al-Kα radiation ($h\nu$ = 1486.6 eV) and a pass energy of 50 eV, for the survey, and 20 eV for the high-resolution spectra. Simulation of the XPD patterns were obtained by the EDAC software [36].

4.1.5 Chemical characterization of ZrO_2 films

In this section we will analyze the XPS spectra obtained from the ZrO_2 deposits of increasing thickness (6.3 ML, 15.1 ML and 21 ML) grown with a substrate temperature of 680, 740 and 780 K, respectively. For space saving, in Figure 1 we report only the XPS data acquired from the thinnest (1.3 ML) ZrO_2 deposit. The Zr 3d peaks reported in Figure 4.2(a) reveal that zirconium ions are always in the Zr^{+4} oxidation state. The Zr $3d_{5/2}$ peak is centered at a binding energy (BE) of 182.9 eV, while for thicker deposits shifts up to 183.3 eV. According to literature data [37] this corresponds to a non-stoichiometric oxide. A similar behavior was observed on a previous paper [27] where the Zr $3d_{5/2}$ was centered at 184 eV for the thicker films and showed ca. 0.6 eV shift to lower BE for thinner films. The Ti 2p peak (Figure 4.2(b)) did not show any significant shift, thus excluding band bending. In all cases the Ti 2p signal is characterized by the presence of a weak shoulder at 457.8 eV that highlights the presence of Ti^{3+}. Although not purveyed in this paper, depositions undertaken at higher temperatures show progressively more reduction of the Ti^{4+} centers, hence furthering the hypothesis of bulk oxygen diffusion. We instead observe (Figure 4.2(c)) a shift of 0.3 eV in the O 1s peak, from 530.4 to 530.7 eV with increasing thickness. The BE values relative to the O 1s peaks in the case of the pure oxides are quite close: 530 eV for TiO_2 and 530.5 for ZrO_2. Thus, we assume the shift is due to the increased amount of deposited ZrO_2, although this observation offers no help in discerning whether the interface is a mixed oxide. The O 1s peak shows also a weak shoulder at ca. 532 eV. At higher thickness this shoulder becomes progressively

smaller, but never disappears. This indicates either the presence of oxygen atoms not in proper bulk configuration [38] or, as pointed out by Karlsson et al. , this shoulder is most probably due to hydroxyl groups formed upon precursor decomposition. The C 1s (Figure 4.3(a),(b),(c)) spectra lineshape is rich of information about the ZTB decomposition on TiO_2 surface. By looking at the XPS spectra taken at different temperatures (680, 740 and 780 K) and coverages we observe different carbonaceous components. Iso-butylene (or iso-butene) was evidenced by Cameron et al. [24],[39] as the major by product of the interaction of ZTB on Si(100) via β-elimination from tert-butanol. In particular, Karlsson et al. noted that bonds form with the Si surface, and observed mainly Si-C compounds and bound methyls while C-O bonds were found only on Si(111). In our work due to the oxidic nature of the surface we observe, according to the XPS measurements, different reaction products. Robbins et al. [40] studied the reactivity of isobutene with TiO_2(110) and verified that methacrolein formed on the surface. Assuming the β-elimination mechanism to occur, isobutene can be formed after decomposition of ZTB on the surface. Thus, a hypothetical although speculative interpretation of the C1s spectra can be the assignments of the components C1 through C3 to methacrolein, where C1 are the methyl and methylene carbon atoms $C^*H_2=C(C^*H_3)CHO$. C2 is related to the carbon atom next to the carbonyl one $CH_2=C^*(CH_3)CHO$ and finally the C3 corresponds to the carbonyl carbon atom $CH_2=C(CH_3)C^*HO$. The last component C4, as suggested by the very high binding energy value can be assigned only to oxalate or carbonate species. This finding was confirmed by Korhonen et al. [41] where in the methanol synthesis the hydroxyl species of zirconia are responsible for the formation of formate or carbonate species that are important intermediates of the reaction. This would suggest an interaction with both substrate and over-layer as the by-products envisaged by Cameron et al., which are isobutylene and *tert*-butanol, either react with titania or with the surface hydroxyls present on surface Zr atoms. This is further reinforced by the fact that this feature is strongly dependent on the deposition temperature, tending to disappear above 750 K. Finally, the fact that we observe no components at binding energies lower than 284 eV, corresponding to carbides, suggests that iso-butene does not form either Ti-C or Zr-C bonds, but rather its by-products remain trapped at the interface. The amount of carbonaceous species as deduced from XPS decreases with increasing deposition temperature passing from 15-20% at 680 and 640 K down to less than 10% for the highest deposition temperature (we assume the carbon contamination concentrated mainly at the interface layer). Interestingly, the carbon amount decreases by increasing the film thickness at 780 K, while in the case of the lower deposition temperatures thicker films have higher amount of carbonaceous species.

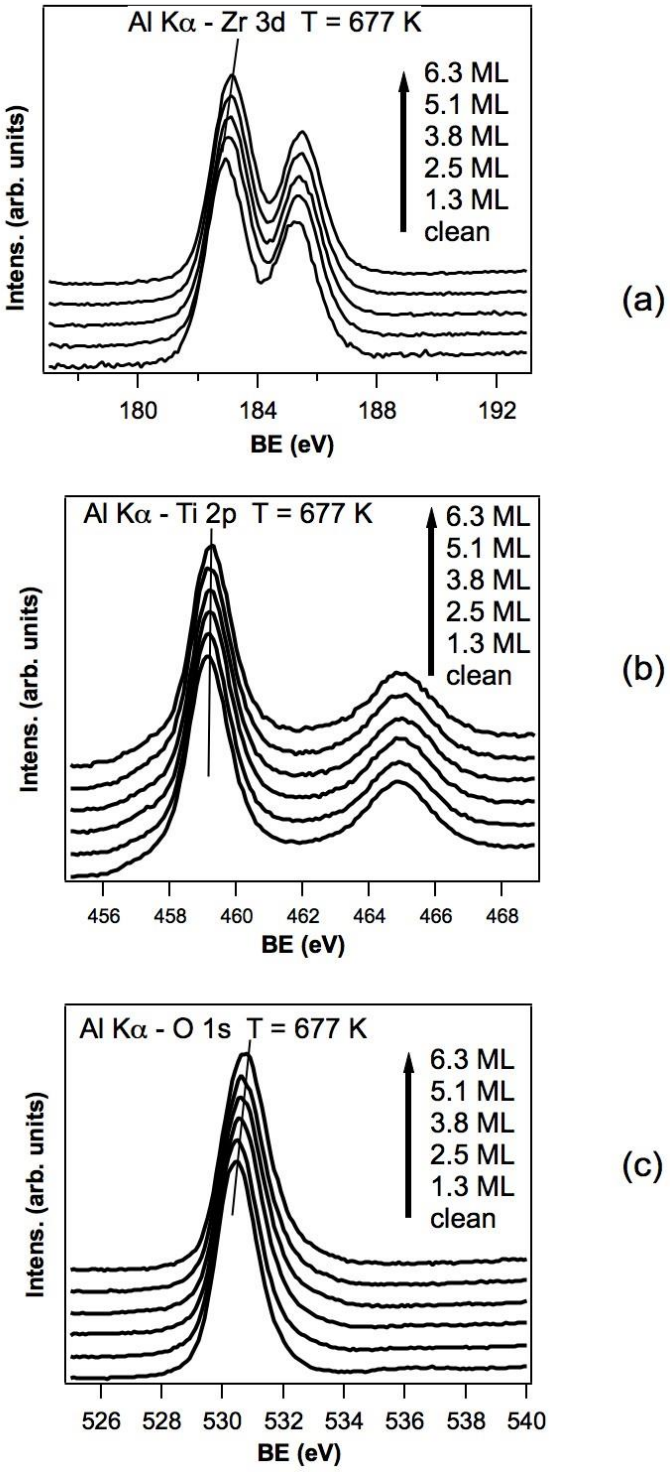

Figure 4.2: AlKα XPS spectra from $ZrO_x/TiO_2(110)$ grown at 677 K. Zr 3d, Ti 2p and O 1s signals refer to a ZrO_x increasing coverage, as indicated by the arrow.

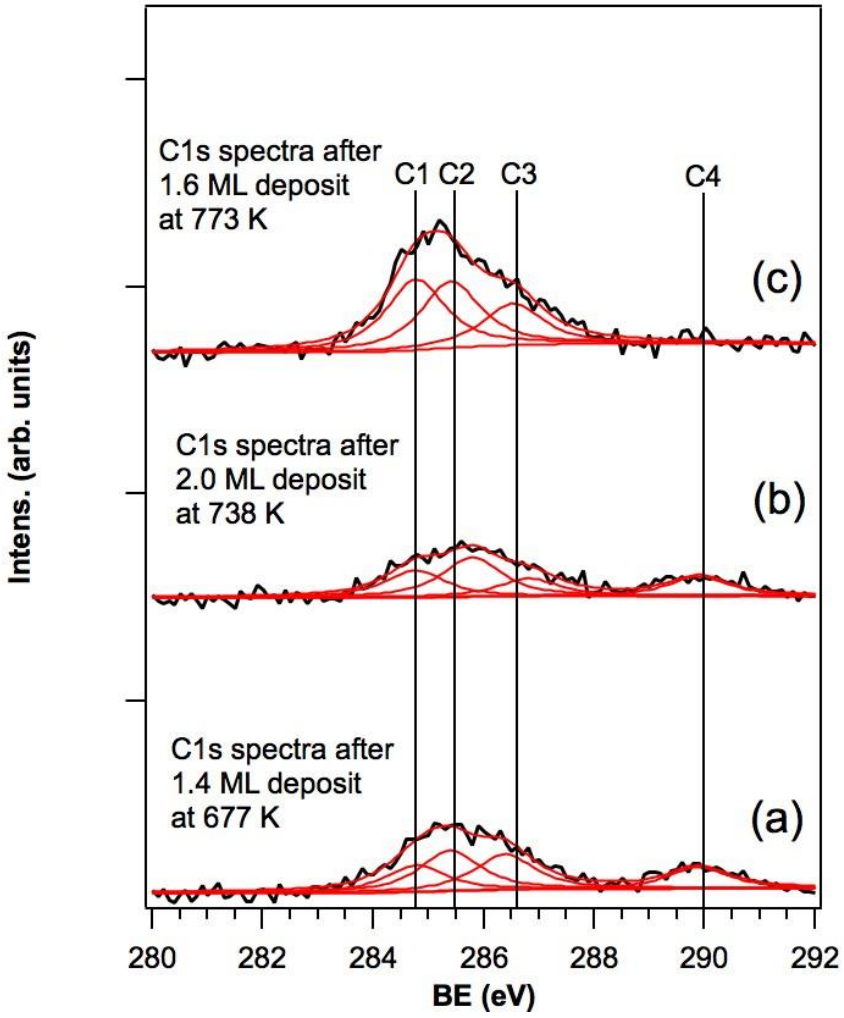

Figure 4.3: AlKα XPS C 1s spectra referring to ZrO_x deposits obtained at different temperatures. Components corresponding to aliphatic and oxygen bound carbon atoms are indicated by the C1, C2 and C3 labels. The peak corresponding to carbonate or oxalate component is indicated by the C4 label.

In order to have some evidence of the presence of a mixed oxide at the interface we report in figure 3 the behavior of Ti 2p and Zr 3d signals at increasing deposition times (red curve and dots refer to Zr 3d signal, black curve and dots refer to Ti 2p signal). In order to be independent from X-ray source photon flux and sample position the Ti2p and Zr 3d signals were normalized with respect to the O 1s peak intensity that we expect to be virtually constant considering the identical stoichiometry of the two oxides. In the case a sharp interface is formed one would expect the Ti signal to decrease by following a perfect exponential attenuation, while it is immediately evident from the data reported in figure 3, that this is not the case. The Ti 2p signal appears rather constant at deposition times higher than 2 and 3 minutes, in the case of films grown at 677 K (figure 4.4(a)) and 738 K (figure 4.4(b)) respectively, while in the case of the highest growth temperature the signal is constant only after deposition times higher

than 4 minutes. The highest deposition temperature corresponds to the highest deposition rate, as deduced by the Zr 3d/Ti 2p ratio. The rather constant intensity of the Ti 2p signal, obtained in the case of the lowest growth temperature and lowest deposition rate, is due to the diffusion of Ti^{4+} ions through a thinner ZrO_2 film (assuming the diffusion rate of Ti^{4+} almost constant in the studied temperature range). These data, nevertheless, do not tell us whether a truly mixed oxide forms at the interface (with substitution of Zr^{4+} by Ti^{4+}) or if a simple mixture of the two oxides is obtained. In this last case the Zr 3d/Ti 2p signal can be fitted, in the case of the thicker deposits (where the eventual contribution of a mixed oxide at the interface is limited), according to a "patched overlayer" growth mode [42] allowing to estimate the thickness and the growth rate of the grown ZrO_2 films. Our data can be very nicely fitted by assuming this model. Finally, by reporting the ln(r) as function of 1/T where r is the growth rate (figure 4.5) it is possible to estimate the activation energy for the decomposition of ZTB on TiO_2(110). The obtained value is 56 ± 12 kJ/mol , whereas the same reaction on Si (100) was found to be about 49kcal/mol [24].

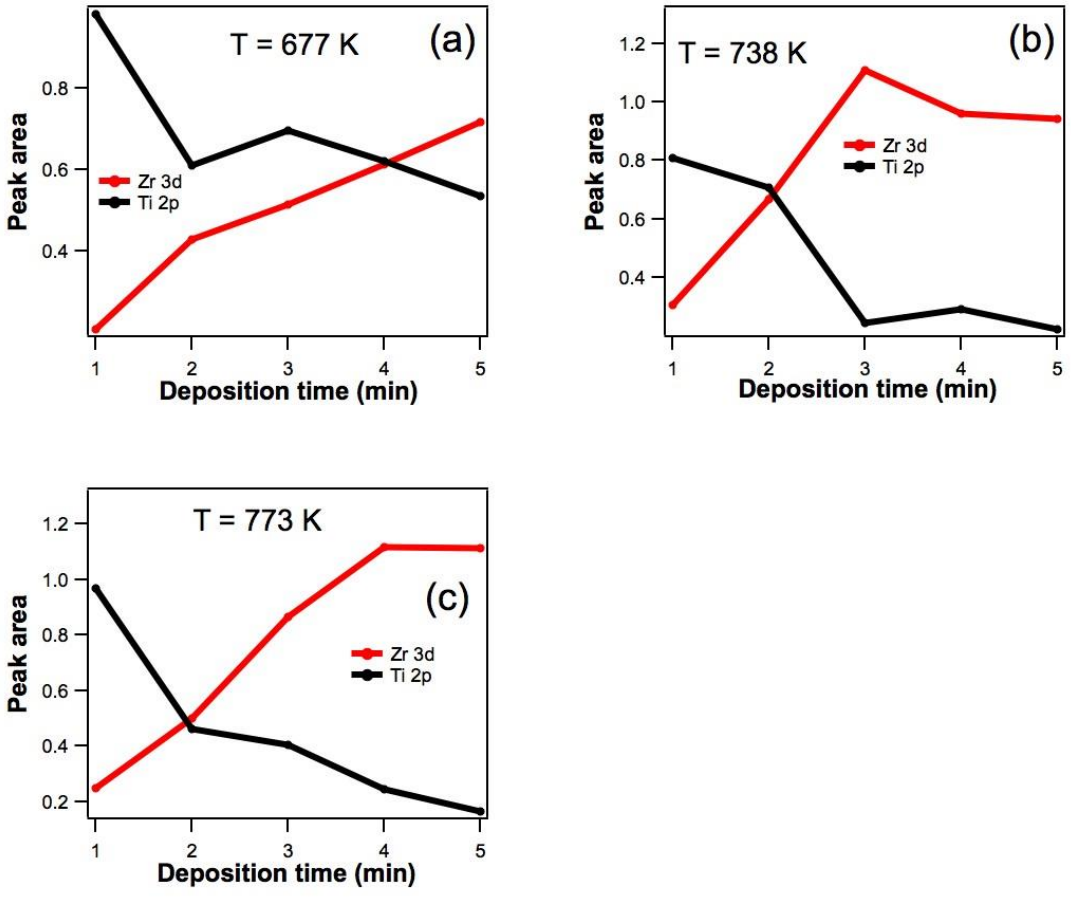

Figure 4.4: Ti 2p and Zr 3d intensities as function of the deposition times. Graph (a), (b) and (c) correspond to increasing deposition temperatures. All intensities values are normalized to the O 1s intensity.

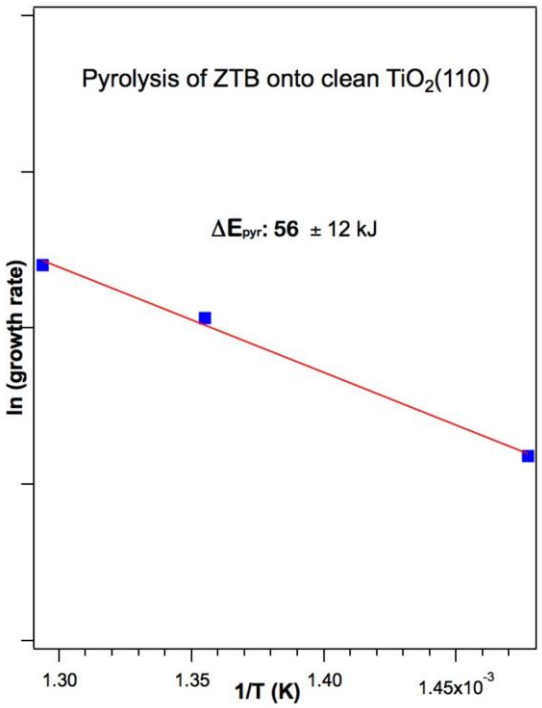

Figure 4.5: Graph of the logarithm of the growth rate, obtained from ARXPS measurements, as function of 1/T. The calculated slope corresponds to the activation energy for pyrolysis of ZTB on TiO_2(110).

As a final comment we would like to point out that our data show a different trend from those found by Cameron et al. in their paper. These authors in fact claim that carbon poisoning slowed the film growth as more carbon was deposited at higher temperatures. Karlsson et al.[29] , as well, claimed that the decrease in the growth rate was due to the formation of an extended interface layer, followed by the formation of ZrO_2 that prevented the diffusion of Si on the surface. In their case, Si was assumed to favour the decomposition of ZTB. In our findings (Figure 4.5) the film growth is faster and with less carbon at higher temperatures. We thus assume that, since titania is a reducible oxide, the depositions at higher temperatures implies the diffusion of bulk oxygen atoms towards the surface, forming oxidized carbon species (CO and CO_2) that could easily desorb from the surface.

4.1.6 Structure of the interface

Preliminary considerations suggest that of the three zirconia polymorphs (i.e. monoclinic, tetragonal and cubic) the tetragonal one has the lowest mismatch value with respect to the TiO_2(110) surface.

A possible epitaxial relation as depicted in figure 4.6 can be ZrO_2(001)[100]//TiO_2(110)[1-11] with a mismatch of about 3% along direction [1-11] and about 9% along direction [1-1-5] of TiO_2.

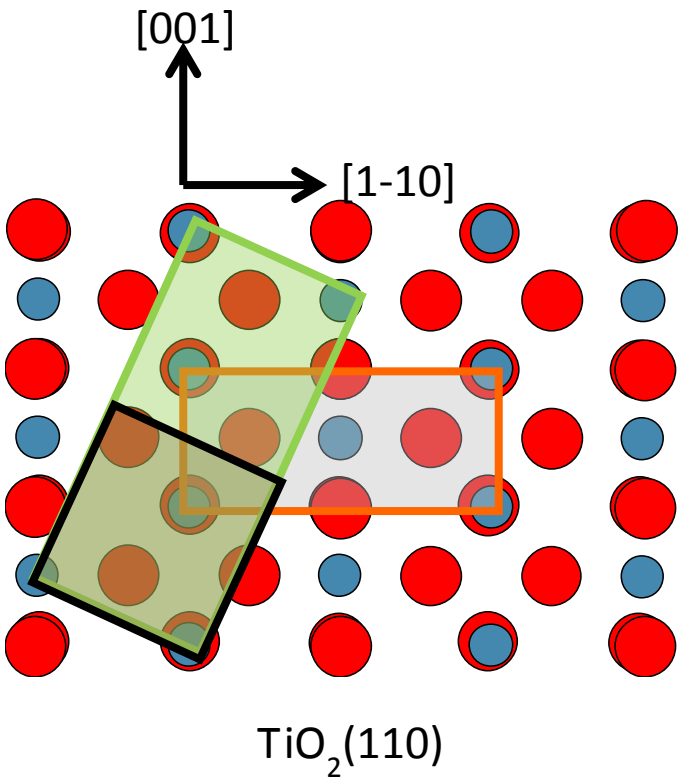

Figure 4.6: Epitaxial relation between tetragonal $ZrO_2(001)$ and $TiO_2(110)$. Blue circles correspond to Ti atoms, red circles to O atoms. The ZrO_2 unit cell is highlighted in black, while two adjacent cells are indicated by the green transparent rectangle.

If this hypothesis is true one expects to see a LEED pattern with a rotated superstructure with respect to the $TiO_2(110)$ pattern. On the contrary, we observe that LEED images are showing diffused patterns, for coverages up to 1.3 ML, identical to those of $TiO_2(110)$ (1x1). Thus, we have acquired Azimuthal Photoelectron Diffraction scans in order to achieve some information about the Zr ions crystallographic sites. We remind that XPD is known for being a very useful and straightforward tool to identify the eventual formation of surface alloys and in any case to get information about the short range order around each emitting atom [34,43]. In Figure 4.7 we report the forward scattering directions for a clean $TiO_2(110)$ surface where (a) and (b) represent side views of the surface aligned with the [001] and [1-10] directions, respectively. The arrows indicate the main forward scattering events with take off angles measured with respect to the surface. In figure 4.8(a) we report the azimuthal Ti 2p scans acquired from a clean $TiO_2(110)$ surface, in figure 4.8(b) the Ti 2p azimuthal scans are acquired from a $TiO_2(110)$ surface after growth of 1.3 ML of ZrO_x, and in figure 4.8(c) the curves refer to the Zr 3d signal from the same sample. If we look at the Ti 2p azimuthal scan it is very easy to identify the [100] and [1-10] directions containing the 2 symmetry planes of this surface and corresponding respectively to Ti-O bonds and Ti-Ti metal-metal forward scattering directions. When the analysis direction corresponds to the Ti-O bond we see a forward scattering peak at a polar angle of about 38-39° from the surface, while if the analysis

direction is aligned with the Ti-Ti direction we find a forward scattering peak at a polar angle of 45°. The azimuthal scans referring to the Zr 3d signal, although somewhat similar to the Ti 2p ones show a different pattern and in particular we notice that the forward scattering peak aligned with direction [1-10] that is so evident in the case of the Ti 2p at a polar angle of 45°, is hardly visible in the case of Zr 3d. This means that Zr^{4+} and Ti^{4+} are not occupying the same crystal sites and there is no formation of a substitutional oxide. This observation is not unexpected since Ti and Zr have very different sizes and Zr, in ZrO_2, is characterized by and eightfold coordination of oxygen ions. In figure 8(a) we report the 2π XPD plot acquired from the Zr 3d signal after growth of 1.3 ML of ZrO_x from θ=24° to 60° from the surface. In this way one can have a more complete information about the diffraction behavior of photoelectrons emitted from Zr 3d. The diffraction pattern shown in figure 4.9(a) is somewhat similar to the one measured in the case of VO_x nanoclusters grown on TiO_2(110) at coverages as low as 0.3 ML [44]. In that case the combination of photoemission and photoelectron diffraction techniques based on synchrotron radiation with DFT calculations, allowed the identification of those nanostructures with exotic V_4O_6 nanoclusters, holding vanadyl groups although the vanadium oxidation state is formally +3. In our case we have a higher surface coverage, compatible with the one found in the case of RuO_x nanochains grown on TiO_2(110). In particular, we can notice that the only strong diffraction feature appears, aligned with direction [001] of the substrate, at a polar angle of 40° from the surface. Other, less pronounced features, can be seen at a polar angles of 46°, aligned with direction [1-10], about 30° and shifted by 32-33° from direction [1-10] and at θ=56° and shifted by 45° from direction [1-10] (see arrows in figure 4.9(a)). This pattern is quite well reproduced by assuming the formation of Zr_2O_3 nanochains, similar to the model suggested by Rodriguez et al. et al. for RuO_x nanostructures on TiO_2(110), but including the substitution of some Ti ions by Zr in the topmost layer of TiO_2(110)[45]. This model is reported in figure 4.10. A satisfactory agreement is obtained assuming the substitution of both 5-fold Ti ions and Ti bound to the bridging oxygen of TiO_2(110) surface. As can be easily seen in figure 4.9(b) the Zr_2O_3 nanostripes model reproduces the strong forward scattering feature corresponding to the formation of Zr-O bonds with oxygen in a bridging configuration and also the weaker features indicated by the arrows. The corresponding R-factor value is 0.7, better than those obtained assuming the formation of Zr_3O_6 nanostripes, also with substitutional Zr ions at the interface (1.06), only Zr_2O_3 nanostripes (no substitutional Zr in the topmost layer – figure 7(c)) (R-factor=0.77) or Zr_3O_6 nanostripes (R-factor= 0.78 – figure 4.9(d)) that, on the contrary, do not reproduce the weak features at grazing angles, although implying a common +4 oxidation state for Zr. The not fully satisfactory agreement between theory and experiment is probably due to the much higher anisotropy value characterizing the calculated patterns. The agreement with the Zr_2O_4 nanostripes model (figure 4.9(f)), also implying a +4 oxidation state for Zr, is very poor as can be easily seen in the figure. As a final comment we would like to point out that the formation of an interface layer with a formally Zr^{+3} [46] species is also in tune with the XPS data that show a progressive shift of the Zr 3d peak from 182.9 to 183.3 eV in the case of thicker deposits.

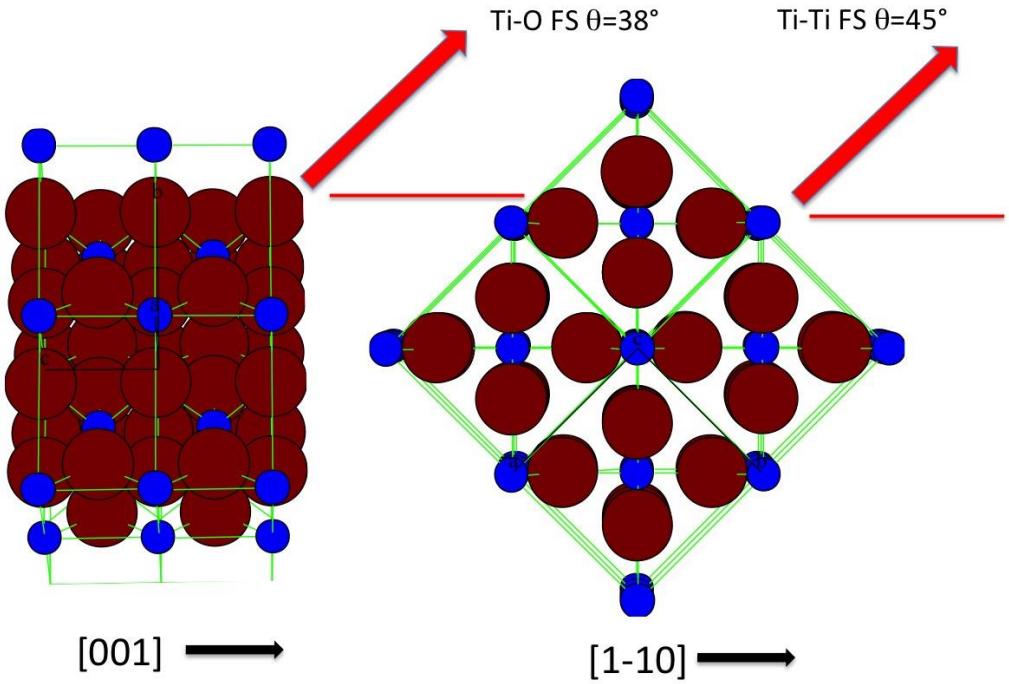

Figure 4.7: Views of rutile-TiO_2 with principal forward scattering directions, indicated by the arrows. The polar angles are measured with respect to the surface.

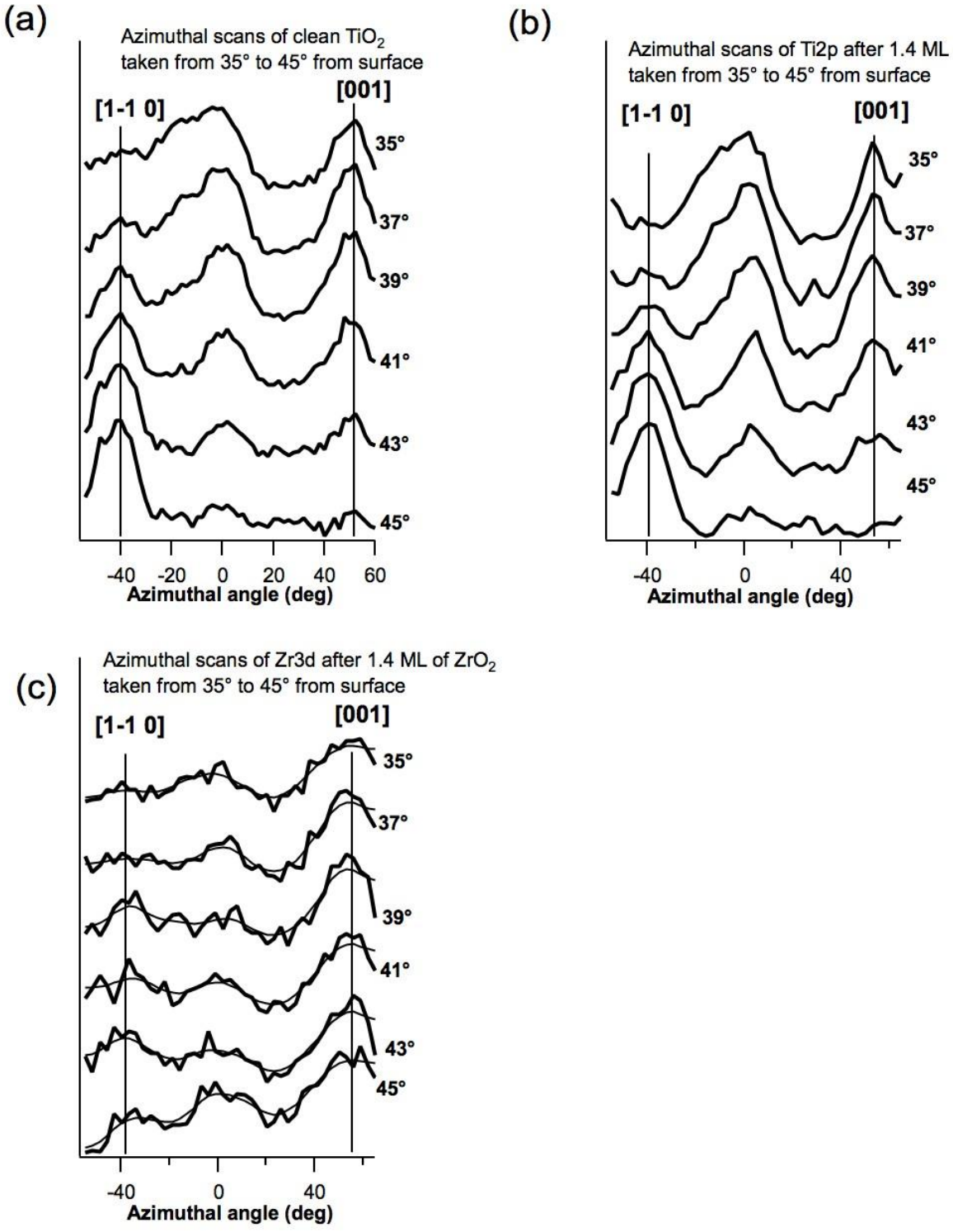

Figure 4.8: Azimuthal photoelectron diffraction scans obtained from a clean TiO_2(110) surface (Ti 2p signal) and after deposition of 1.4 ZrO_x ML (Ti 2p and Zr 3d signals).

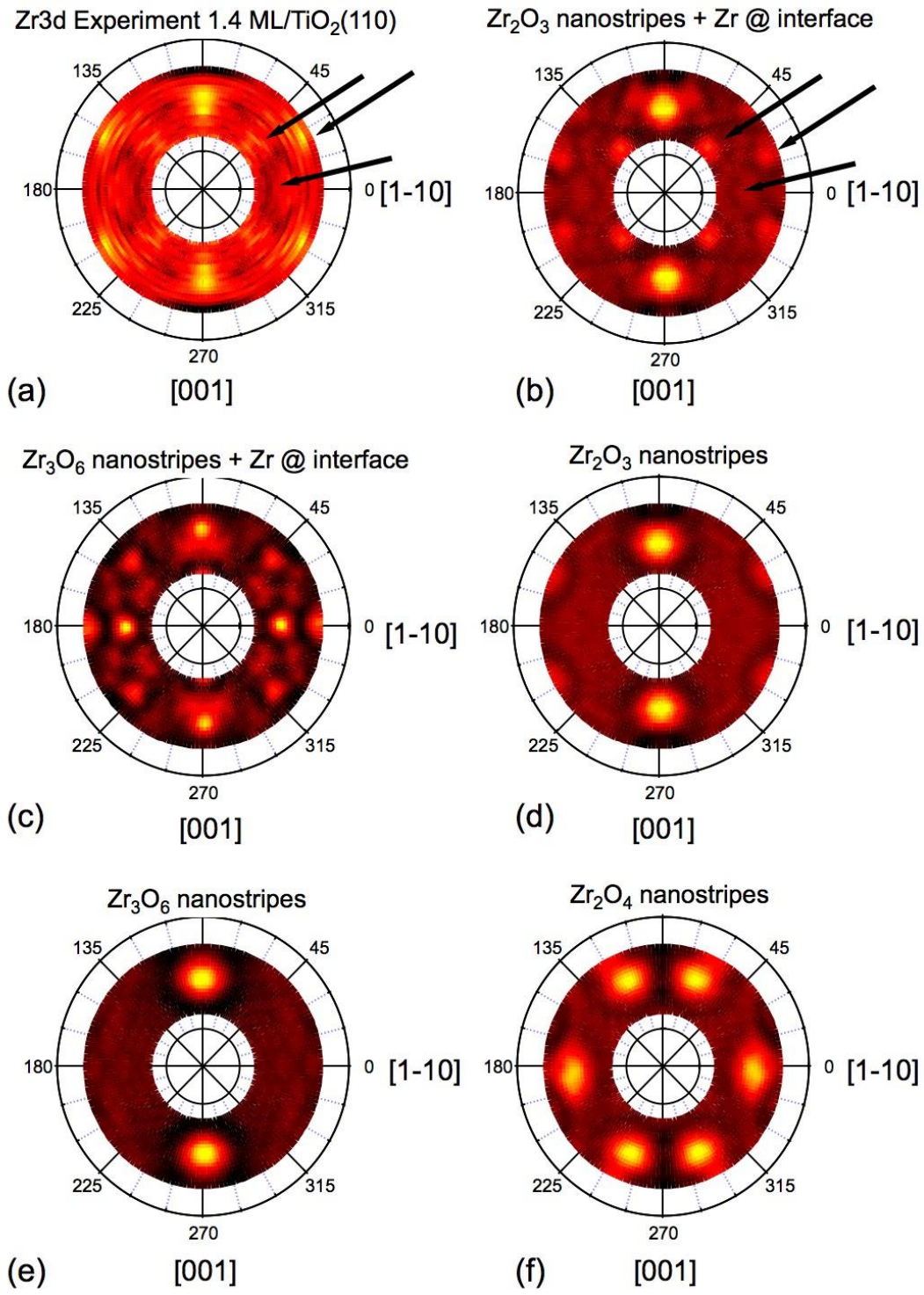

Figure 4.9: (a) Stereographic projections of XPD curves obtained from 1.3 ML of ZrO_x on TiO_2(110). The data are acquired from Θ =24° to 60° from the surface. (b) – (f) SW-MS simulations of XPD patterns obtained assuming different models.

Figure 4.10: Zr_2O_3 nanochain model corresponding to XPD simulated pattern reported in figure 8(b). The Zr-O bond length is assumed = 2.10 Å; Zr atoms are blue-green, Ti atoms are gray and oxygen atoms are red.

In order to have a further validation of this model we have exposed the surface after deposition of 1.3 ML of $ZrO_x/TiO_2(110)$ to 100 L of pyridine and compared the adsorbed amount with that chemisorbed on a clean $TiO_2(110)$ surface. The chemisorption site of pyridine on $TiO_2(110)$ is the 5-fold coordinated Ti atom, the acid site, and 4-fold coordinated Ti atoms at step edges [47]. In the case of the ZrO_x nanochain model the 5-fold Ti acid sites are occupied by the ZrO_x nanostructures, while the only possible adsorption sites could be on the sides of the nanochains. In figure 4.11 we report the XPS N 1s signal recorded after exposure to 100 L of pyridine of a $TiO_2(110)$ surface and a 1.3 ML $ZrO_x/TiO_2(110)$. By taking into account the Ti atom density of $TiO_2(110)$ (1.05×10^{15} at/cm^2) and Zr atom density of tetragonal $ZrO_2(001)$ (7.33×10^{14} at/cm^2) it is easy to verify that 1.3 ML of ZrO_2 correspond to 0.9 ML of rutile-TiO_2 and therefore one expects the amount of chemisorbed pyridine to be 1/10 of the amount on $TiO_2(110)$. The amount desorbed from 1.3 ML $ZrO_x/TiO_2(110)$, according to the N 1s XPS area, is about 1/5 of that adsorbed on $TiO_2(110)$. This behavior indicates that some of the pyridine is adsorbed on uncovered 5-fold coordinated Ti sites, as expected, but eventually also on disordered ZrO_2 or on lateral sites.

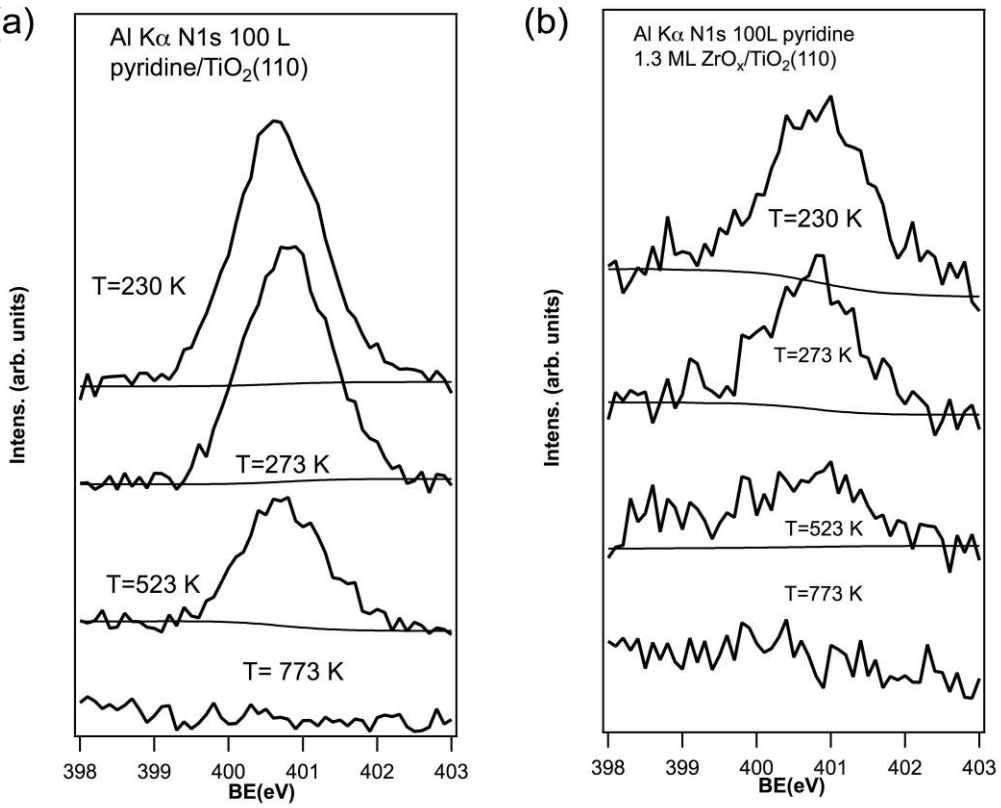

Figure 4.11: N1s signal after exposure to 100 L of pyridine of a TiO_2(110) surface (a) and (b) 1.3 ML ZrO_x/TiO2(110) surface.

4.1.7 Conclusions

ZTB was a quite convenient precursor for the formation of zirconia films. The obtained Zirconia films for coverages higher than 3-4 ML were free from carbonaceous species. The optimization of the deposition procedure allowed us to obtain a satisfactorily, reproducible, linear film growth, even by varying the pressure. The interface showed some carbon contamination that although un-bound to metal atoms of either substrate or film (no metal carbides), nevertheless warped the deposit's crystal structure. Contamination at the interface was found to be unavoidable and spectacularly tough [48] as depositions in an oxygen environment or long oxidized annealing only partially removed it. Furthermore, the carbonaceous species observed demonstrate a complex interplay with the substrate that only appears at the interface with the appearance of methacrolein. This suggests a different reactivity compared to the one proposed by Karlsson et al.[29] where silicon-carbides were formed. The contamination may not have necessarily been a bad thing as previous experiments [49,50] have demonstrated that the presence of carbon is useful in zirconia and mixed ZrO_2-TiO_2 based catalysts in the dehydrogenation of alkanes by preventing particle sintering and augmenting selectivity.

There is a great difference in the sol-gel preparation techniques, highly used in the industry, in respect to the deposition of a thin film in UHV. In the former methods a mixed oxide with highly acidic properties is reasonably obtainable whereas in the case of zirconia deposition via ZTB on silicon[30,25], copper[48] and rutile no mixed oxides were clearly observed. However and definitely more important the interface study for these three substrates was the richest in information of interfacial properties. In fact studies on silicon observed from the formation of micro-dimensional grains of which the shape was strongly temperature dependent to carbon diffusion within the bulk and thus resulted in the formation of surface dimer vacancy structures. In regards to copper studies by Paulidou and Nix demonstrated the growth of an epitaxial zirconia films showing a hexagonal pattern at the LEED. Finally in this study we then observed the formation of an interface layer most probably consisting in Zr_2O_3 nanochains aligned along direction [001] and partial substitution of Ti ions by Zr in the outermost layer of the substrate as evidenced by XPD scans and MS-SW simulations.

Computational studies by Martinez et al. [51] demonstrated how methanol and water dissociate at bridging oxygen vacancies and at reduced step edges thus a plausibile hypothesis would be that initial ZTB molecules would adsorb onto these sites. Further studying of this work's system via STM would clarify structure of Zr_2O_3 nanochains and especially verify the hypothesis. Furthermore, a study of the zirconia-titania system obtained via metal evaporation would be interesting as carbon contamination, which didn't affect the obtaining of a LEED pattern in Paulidou and Nix's study, would be avoided and thus probably a long range order would be observed on TiO_2(110) or even the obtaining of a superficial alloy.

References:

1. S. P. Jiang and S. H. Chan, *J Mater Sci*, 2004, **39**, 4405-4439.
2. P. W. Peacock and J. Robertson, *Appl Phys Lett*, 2003, **83**, 2025-2027.
3. M. Copel, M. Gribelyuk and E. Gusev, *Appl Phys Lett*, 2000, **76**, 436-438.
4. K. Tanabe and T. Yamaguchi, *Catal Today*, 1994, **20**, 185-197.
5. T. Yamaguchi, *Catal Today*, 1994, **20**, 199-217.
6. J. Fung and I. Wang, *J Catal*, 1996, **164**, 166-172.
7. T. C. Schilke, I. A. Fisher and A. T. Bell, *J Catal*, 1999, **184**, 144-156.
8. S. Yang, A. Maroto-Valiente, M. Benito-Gonzalez, I. Rodriguez-Ramos and A. Guerrero-Ruiz, *Applied Catalysis B: Environmental*, 2000, **28**, 223-233.
9. R. J. Farrauto and R. M. Heck, *Catal Today*, 1999, **51**, 351-360.
10. Y. Kohno, T. Tanaka, T. Funabiki and S. Yoshida, *Phys Chem Chem Phys*, 2000, **2**, 5302-5307.
11. A. Kitiyanan, S. Sakulkhaemaruethai, Y. Suzuki and S. Yoshikawa, *Compos Sci Technol*, 2006, **66**, 1259-1265.
12. Y. Paz, *Applied Catalysis B: Environmental*, 2010, **99**, 448-460.
13. B. O'Regan and M. Gratzel, *Nature*, 1991, **353**, 737-740.
14. R. H. French, S. J. Glass, F. S. Ohuchi, Y. N. Xu and W. Y. Ching, *Phys Rev B*, 1994, **49**, 5133-5142.
15. N. Siedl, M. J. Elser, J. Bernardi and O. Diwald, *The Journal of Physical Chemistry C*, 2009, **113**, 15792-15795.
16. H. Zou and Y. S. Lin, *Applied Catalysis A: General*, 2004, **265**, 35-42.
17. B. M. Reddy and A. Khan, *Catalysis Reviews*, 2005, **47**, 257-296.
18. L. Liang, Y. Sheng, Y. Xu, D. Wu and Y. Sun, *Thin Solid Films*, 2007, **515**, 7765-7771.
19. K. V. R. Chary, G. V. Sagar, D. Naresh, K. K. Seela and B. Sridhar, *The Journal of Physical Chemistry B*, 2005, **109**, 9437-9444.
20. S. Livraghi, F. Olivero, M. C. Paganini and E. Giamello, *The Journal of Physical Chemistry C*, 2010, **114**, 18553-18558.
21. B. Mitu, S. Vizireanu, R. Birjega, M. Dinescu, S. Somacescu, P. Osiceanu, V. Pârvulescu and G. Dinescu, *Thin Solid Films*, 2007, **515**, 6484-6488.
22. M. D. Hernández-Alonso, J. M. Coronado, B. Bachiller-Baeza, M. Fernández-García and J. Soria, *Chem Mater*, 2007, **19**, 4283-4291.
23. D. C. Bradley, *Chem Rev*, 1989, **89**, 1317-1322.
24. M. A. Cameron and S. M. George, *Thin Solid Films*, 1999, **348**, 90-98.
25. D. J. Burleson, J. T. Roberts, W. L. Gladfelter, S. A. Campbell and R. C. Smith, *Chem Mater*, 2002, **14**, 1269-1276.
26. K. Kukli, M. Ritala and M. Leskelä, *Chem Vapor Depos*, 2000, **6**, 297-302.
27. Y.-S. Lin, R. Puthenkovilakam, J. P. Chang, C. Bouldin, I. Levin, N. V. Nguyen, J. Ehrstein, Y. Sun, P. Pianetta, T. Conard, W. Vandervorst, V. Venturo and S. Selbrede, *J Appl Phys*, 2003, **93**, 5945-5952.
28. J. P. Chang, Y.-S. Lin and K. Chu, *Journal of Vacuum Science Technology B*, 2001, **19**, 1782-1787.
29. P. G. Karlsson, J. H. Richter, J. Blomquist, P. Uvdal, T. M. Grehk and A. Sandell, *Surf Sci*, 2007, **601**, 1008-1018.
30. P. G. Karlsson, E. Göthelid, J. H. Richter and A. Sandell, *Surf Sci*, 2008, **602**, 1803-1809.
31. B. H. Lee, S. Cho, J. K. Hwang, S. H. Kim and M. M. Sung, *Thin Solid Films*, 2010, **518**, 6432-6436.
32. D. Panda and T.-Y. Tseng, *Thin Solid Films*, 2013, **531**, 1-20.
33. K. F. McCarty, *Surf Sci*, 2003, **543**, 185-206.

34. M. Li, W. Hebenstreit, L. Gross, U. Diebold, M. A. Henderson, D. R. Jennison, P. A. Schultz and M. P. Sears, *Surf Sci*, 1999, **437**, 173-190.
35. G. Granozzi and M. Sambi, *Adv Mater*, 1996, **8**, 315-326.
36. F. J. G. de Abajo, M. A. Van Hove and C. S. Fadley, *Physical Review B*, 2001, **63**.
37. S. Harel, J. M. Mariot and C. F. Hague, *Surf Sci*, 1992, **269**, 1167-1172.
38. K. Sakamoto, H. M. Zhang and R. I. G. Uhrberg, *Phys Rev B*, 2003, **68**, 075302.
39. B. J. Gould, I. M. Povey, M. E. Pemble and W. R. Flavell, *J Mater Chem*, 1994, **4**, 1815-1819.
40. M. D. Robbins and M. A. Henderson, *J Catal*, 2006, **238**, 111-121.
41. S. T. Korhonen, M. Calatayud and A. O. I. Krause, *The Journal of Physical Chemistry C*, 2008, **112**, 6469-6476.
42. C. S. Fadley, *Prog Surf Sci*, 1984, **16**, 275-388.
43. G. A. Rizzi, A. E. Reeder, S. Agnoli and G. Granozzi, *Surf Sci*, 2006, **600**, 3345-3351.
44. L. Artiglia, S. Agnoli, A. Vittadini, A. Verdini, A. Cossaro, L. Floreano and G. Granozzi, *J Am Chem Soc*, 2013, **135**, 17331-17338.
45. F. Yang, S. Kundu, A. B. Vidal, J. Graciani, P. J. Ramírez, S. D. Senanayake, D. Stacchiola, J. Evans, P. Liu, J. F. Sanz and J. A. Rodriguez, *Angewandte Chemie International Edition*, 2011, **50**, 10198-10202.
46. S. X. Luo, F. M. Wang, Z. S. Shi and F. Xin, *Mater Res Innov*, 2009, **13**, 64-69.
47. A. Paulidou and R. M. Nix, *Phys Chem Chem Phys*, 2005, **7**, 1482-1489.
48. A. Trunschke, D. L. Hoang, J. Radnik, K. W. Brzezinka, A. Brückner and H. Lieske, *Applied Catalysis A: General*, 2001, **208**, 381-392.
49. D. L. Hoang, H. Preiss, B. Parlitz, F. Krumeich and H. Lieske, *Applied Catalysis A: General*, 1999, **182**, 385-397.
50. U. Martinez, L. B. Vilhelmsen, H. H. Kristoffersen, J. Stausholm-Møller and B. Hammer, *Phys Rev B*, 2011, **84**, 205434.

CHAPTER 5

THE CERIA-TITANIA SYSTEM

5.1 CERIUM DIOXIDE

The most significant of the rare earth metal oxides in industrial catalysis is certainly ceria[52]. It has an important role in two of the most important commercial catalytic processes such as three way catalysis and fluid catalytic cracking and is a basic component of a number of technologically relevant materials with practical applications. Thus, ceria finds application in several catalytic processes such as the treatment of SO_x gasses derived from fluid catalytic cracking and auto-exhausts[53, 54], treatment of liquid wastes via catalytic wet oxidation[55], as catalysts for low temperature water gas shift (WGS) reactions[56, 57] when used in conjunction with Au or Pt. Further uses of ceria can be found in oxygen sensors[58], oxygen permeation membrane systems[59], fuel cells[60], chemical-mechanical polishing for glass ceramics and microelectronics[61], and finally this oxide also finds use in the medicinal field[62].

CeO_2 crystallizes in the fluorite crystal structure with space group Fm3m which consists of a face-centered cubic (f.c.c.) unit cell of cations with anions occupying the octahedral interstitial sites. This can also be seen as a superposition of a f.c.c. lattice of cations (Ce^{4+}) with lattice constant a = 5.411 Å, and a simple cubic lattice of anions (O^{2-}) with lattice constant a/2. In this structure (Fig. 1), each cerium cation is coordinated by eight nearest-neighbor oxygen anions, while each oxygen anion is coordinated by four nearest neighbor cerium cations. Pure CeO_2 is pale yellow in color probably due to Ce(IV)–O(-II) charge transfer[63]. When treated in a reducing atmosphere at elevated temperatures, CeO_2 is known to form a continuum of oxygen-deficient, nonstoichiometric CeO_{2-x} oxides (with $0 < x \leq 0.5$) and changes to blue in color and becomes almost black when grossly non-stoichiometric. Under extreme reduction, CeO_2 becomes the hexagonal sesquioxide Ce_2O_3 (P3m1) [64].

$$CeO_2 \rightleftharpoons Ce_2O_3 + 1/2\ O_2$$

However, as highlighted by the reaction above, even after loss of considerable amounts of oxygen from its lattice and formation of a large number of oxygen vacancies, cerium oxide is readily re-oxidized to CeO_2 by exposure to an oxidizing environment. This last property makes ceria one of the most important materials for oxygen storage.

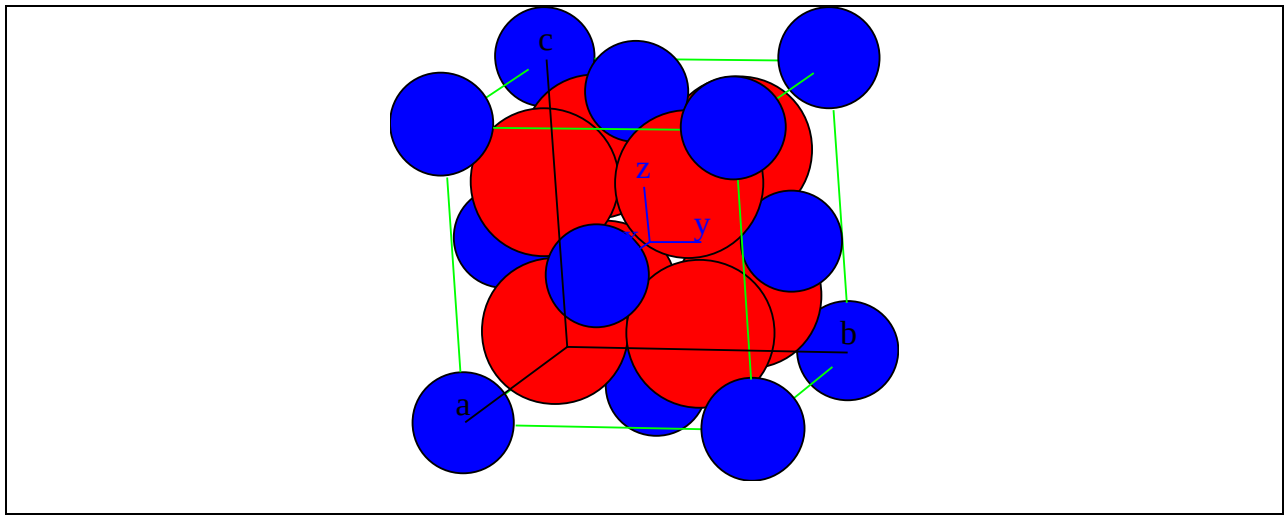

Figure 5.1: unit cell of CeO_2.

Oxygen vacancies dominate the electronic and chemical properties of ceria and are mobile at elevated temperatures[65] forming linear vacancy clusters that expose exclusively Ce^{3+} ions to the gas phase. The immediately adjacent sites instead remain as pure Ce^{4+} ions[66]. Furthermore, the groups of exposed Ce^{3+} ions on CeO_2 are potentially potent surface sites in regards to catalysis and photocatalysis, due to the fact that adsorbed gases or catalytic reaction intermediates could interact simultaneously with several Ce^{3+} ions.

By decreasing its size down to the nanoscale level ceria acquires unique characteristics absent in bulk ceria materials[67]. Here, oxygen vacancies form more readily and because the surface area of ceria nanoparticles with respect to their volume is dramatically increased[68, 69] the oxygen exchange and redox reactions are highly enhanced enabling the particles to regenerate their activity. Recently one dimensional (1D) nanocrystalline materials such as nanorods and nanowires have been reported by Yu et al.[70] while Wang et al.[71] studied 2D ceria nanoplates and their increased oxygen storage capacity in respect to their 3D counterparts prepared by combustion and hydrothermal methods.[71] In summary the oxygen exchange and redox properties of ceria suggest novel properties ranging from the biomedical, such as protection against cellular damage from oxidative stress and inflammation, to the technological such as the fast oxidation of organic dyes without the need of hydrogen peroxide.[72]

5.1.1 Ceria – Titania Mixed Oxides

The interaction of metals with various oxides has been studied for years due to their high use in heterogeneous catalysis. The mixing of oxides adds further to the variety of catalytic behavior and this was observed in early attempts prepared via sol-gel methods. An interesting work by Rynkowski et al.[73] studied the redox properties of different mixtures of ceria-titania; precursors to Pt/CeO_2-TiO_2 catalysts in which Pt reactivity is enhanced by the presence of a reducible support. In their work mixed oxides with different stoichiometry were observed and furthermore ceria generally migrated towards the surface and in the case of the mixture with higher cerium content ceria was more easily re-oxidized. In

continuation of what was aforementioned above ceria has been studied in conjunction with other materials and substrates. Reddy et al.[74] performed a study on CeO_2-TiO_2 as well as other mixed oxides investigating their properties via various techniques. They observed a varied stoichiometry not found in other literature examples so that even after calcination at 1073 K no transformation of anatase to rutile was observed. This was explained by assuming the formation of Ti-O-Ce bonds that stabilized the anatase phase. Raman study of the thermally treated sample revealed peaks from CeO_2 and TiO_2 thus corroborating XRD data that showed that the samples were comprised of larger nanocrystals of CeO_2, TiO_2 and overlapping regions. UV-VIS diffuse reflectance spectroscopy revealed, in calcined samples, that effective band gap was lower in comparison to that of anatase and that incorporation of CeO_2 into TiO_2 induces a small red shift in the UV-Vis spectra with respect to pure anatase. This is because of the prevailing presence of $Ce^{3+} \leftarrow O^{2-}$ charge transfer. Of important notice was that an increase in volume was observed following the formation of oxygen vacancies and finally that oxygen storage capacity (OSC) studies demonstrated that the mixed oxide has better redox properties compared to pure CeO_2. This matter was further investigated by Dutta et al.[75] where increased OSC in the mixed oxide was due to weakly bound oxygen. A study by Fang et al.[76] centered on clarifying the interface and structure of CeO_2-TiO_2 mixed oxides prepared via sol-gel method revealed that ceria and titania were present in their respective cubic fluoride and anatase phases. Furthermore, in addition to showing higher surface area than pure oxides, Ce atoms initially nucleate as [CeO_8] cubic-like polyhedrons forming Ce-O-Ti bonds at the interface with anatase. These polyhedrons developed into cubic fluoride CeO_2 with increasing cerium content. Zhou et al.[77] confirmed this finding via XRD and thermodynamic measurements; $Ce_{0.8}Ti_{0.2}O_2$ and $Ce_{0.9}Ti_{0.1}O_2$ mixed oxides showed a fluorite single phase with an easier oxidation compared to the pure oxides. However, it was also observed that after calcination at 1323 K the mixed oxides separate into ceria and titania phases and enhanced reducibility is lost. An interesting study by Watanabe et al.[78] demonstrated that CeO_2-TiO_2 mixed oxides prepared via urea precipitation show a gradual structural transformation from anatase to fluorite with increasing Ce content. A gradual lattice enlargement and deformation was observed in respect to both CeO_2 and TiO_2 passing from one end to the other with either Ti or Ce content increase. In fact, at "mid-point" crystallites $Ti_{0.5}Ce_{0.5}O_2$ and $Ti_{0.7}Ce_{0.3}O_2$ were too small to be detected via XRD and thus a structure was difficult to attribute. These "mid-point" structures exhibited via H_2-TPR an increase of the onset temperature of H_2 consumption, and also a higher intensity, upon reaching $Ti_{0.5}Ce_{0.5}O_2$ with respect to the pure oxides, hence a higher reducibility in respect to the single pure oxides and thus a higher OSC. In addition, NH_3-TPD revealed acidity increase, and also a higher NH_3 oxidation capacity, with increasing Ti content in the mixed oxides. Finally, a novel study by Johnston-Peck et al.[79] revealed that on anatase nanoparticles ceria grows in a hierarchical structure with clusters, chains and nanoparticles and that Ti^{4+} can migrate into the ceria lattice at the oxide-oxide interface which favors the formation of Ce^{3+} which can be useful for catalytic processes. Ceria-titania nanoparticle find great use in many application from sunscreens[80] to desulfurization of light irradiated diesel fuel[81]. Less is known about the ceria-titania thin film systems although similarities with the nanoparticle structures exist. There are of course structural differences as first encountered by Rodriguez et al.[82] where the support, TiO_2(110), was observed to form TiO_x islands in the presence of 0.1 ML of CeO_x and in an oxidizing environment. The latter oxide was instead

observed to form dimers onto the substrate's surface. Furthermore, a recent study by Bruix et al.[83] shows that for the water-gas-shift reaction on a support such as CeO_x / TiO_2(110) oxygen is more easily transferred to Pt and thus the system is able to fully dissociate H_2O into H_2 and O_2. Due to the lack of a structural and electronic properties investigation of the ceria-titania thin film system, the scope of this work is to deposit from ultrathin to thicker films observing via LEED and UPS the onset of new phases electronic properties. We believe that this will contribute to increase the knowledge about the structure and composition of ceria/titania interface. The final goal is to be able to tailor catalysts with specific structures for specific purposes. In this light we have investigated the reactivity of this system with two well known probe molecules: methanol and ethanol. The choice of these two molecules stems from the fact that recently the dehydrogenation of alcohols has gained importance in fuel cell technology[84-86].

5.1.2 The CeO_2/TiO_2(110) model catalyst

The surface of CeO_2 that has atoms with the closest geometrical distribution to that of TiO_2(110) is the (111) surface. In Figure 5.2 the Cerium atoms that are closest to the rutile TiO_2(110) lattice cell, represented by the black rectangle, are highlighted in green. On the right we have reported the spatial dimensions of the two considered cells. On the left we have depicted the directions according to the CeO_2(111) surface.

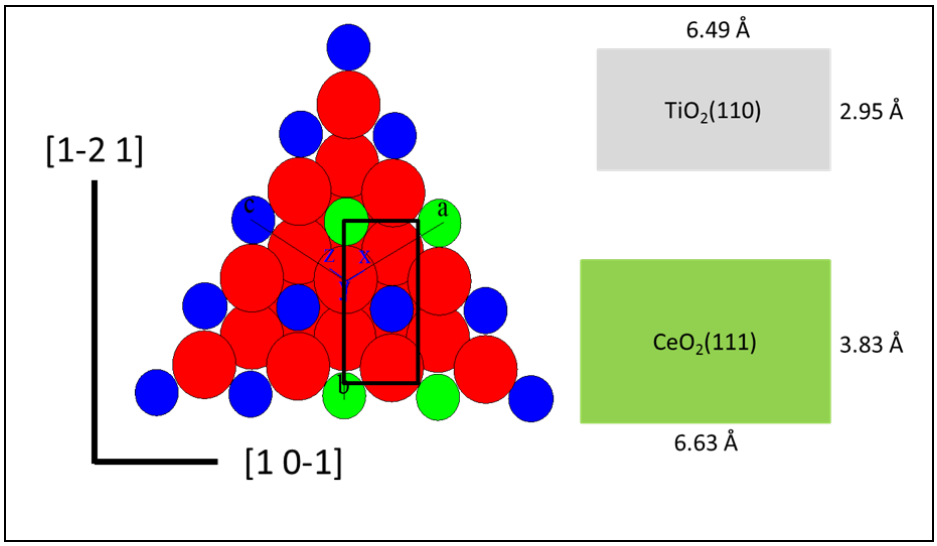

Figure 5.2: surface of CeO_2(111) and lattice dimensions for the cells of TiO_2(110) and CeO_2(111).

We can observe in figure 5.2 that there are differences between the two cells, due to the different lattice parameters of the two crystals, which suggest that the formation of an epitaxial film of CeO_2 should undergo a great strain. A possible epitaxial relation can be CeO_2(111)[1-2 1]//TiO_2(110)[1-1 0]. The mismatch between the two cells is:

along the [1 0-1] direction of CeO_2(111) $f = \frac{(3.83-2.95)}{3.83} = 22.98\ \%$

whereas along the [1-2 1] direction of CeO_2(111) $f = \frac{(6.63-6.49)}{6.63} = 2.11\ \%$

5.1.3 Cerium deposition and definition of monolayer

We have decided to deposit cerium by metal evaporation from a Mo crucible since the process is rather easy and garners clean deposits. During deposition the substrate was kept at 677 K and in an O_2 environment of $5.2 \cdot 10^{-6}$mbar, and, in order to obtain an ordered homogeneous surface the sample was further annealed in the same environment at 900 K. In this study the measure of the layers is expressed in monolayers (ML). Since we made the hypothesis that a growth of CeO_2(111) presents the least strain we considered 1ML of CeO_2 grown on TiO_2(110) as the "thickness" of the highlighted O-Ce-O trilayer (Figure 5.3), as roughly a third (3.12 Å) of the distance along the Ce-O-O-Ce bonds taken along the [111] direction (9.37 Å) as shown in the picture below

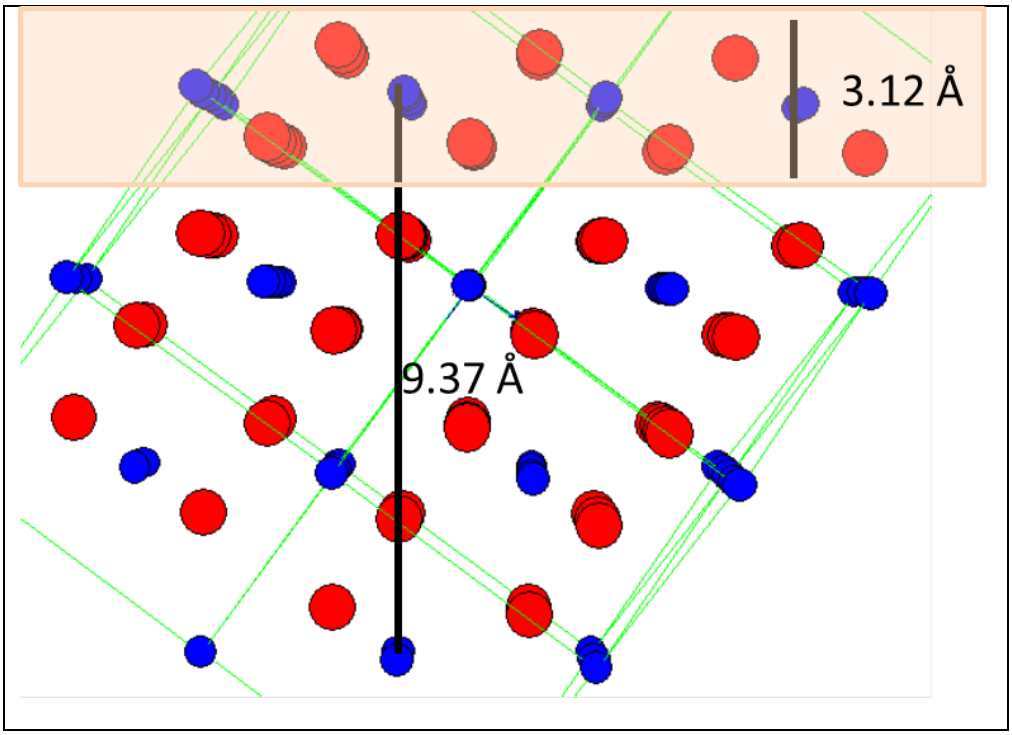

Figure 5.3: CeO_2(111) seen along the [01-1] direction, parallel to surface; highlighted is the considered layer.

5.1.4 Structure of the interface

The deposition of an ultra-thin, sub-monolayer, film of ceria onto rutile was first studied by Park et al. [87], in a research aimed to the preparation of a catalyst for the water-gas-shift reaction. In their study they observed that for small coverages of ceria on TiO_2(110), the CeO_x nanoparticles had an unusual coordination mode. STM and density-functional calculations revealed the presence of Ce_2O_3 dimers, which formed diagonal arrays that had specific orientations of 0, 24, and 42° with respect to the [1-1 0] direction of the titania substrate. At higher coverage of ceria on TiO_2(110), the surface exhibited two types of terraces. In one type, the morphology was not very different from that observed at low ceria coverage. However, in the second type, there was a compact array of ceria particles with structures that did not match the structures of CeO_2(111) or CeO_2(110) [88]. Instead, in our study we have observed three new different phases: p(2x2), c(12x2), and c(2x2); these were highly dependent on sample history and deposition time.

The p(2x2) phase:

This phase was obtained by 15 min reactive deposition in an oxygen pressure of $1.4x10^{-7}$ mbar under a Ce flux of 0.03 ML/min on a yellow TiO_2(110) crystal. In the figure 5.4(a) below we show the experimental LEED pattern (58 eV) together with the simulated reciprocal lattice patterns. By the patterns alone we have observed that the CeO_x pattern is double that of TiO_2(110).

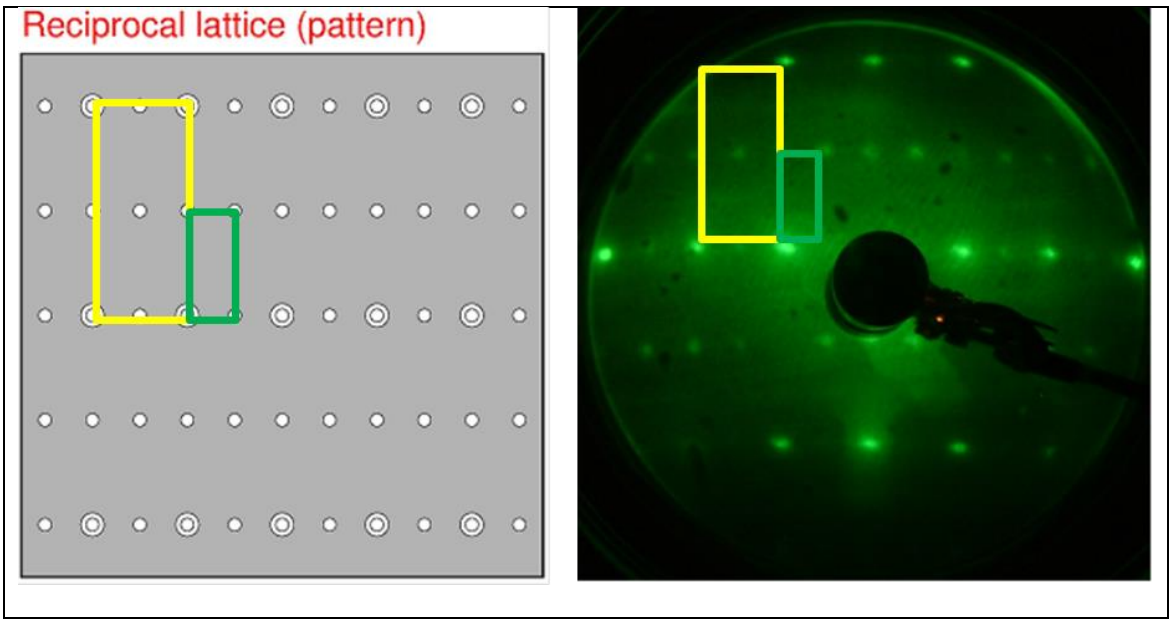

Figure 5.4(a): Reciprocal lattice pattern and LEED image of a p(2x2) pattern for a 0.45 ML of CeO_x on TiO_2(110) the LEED image was taken at 58 eV.

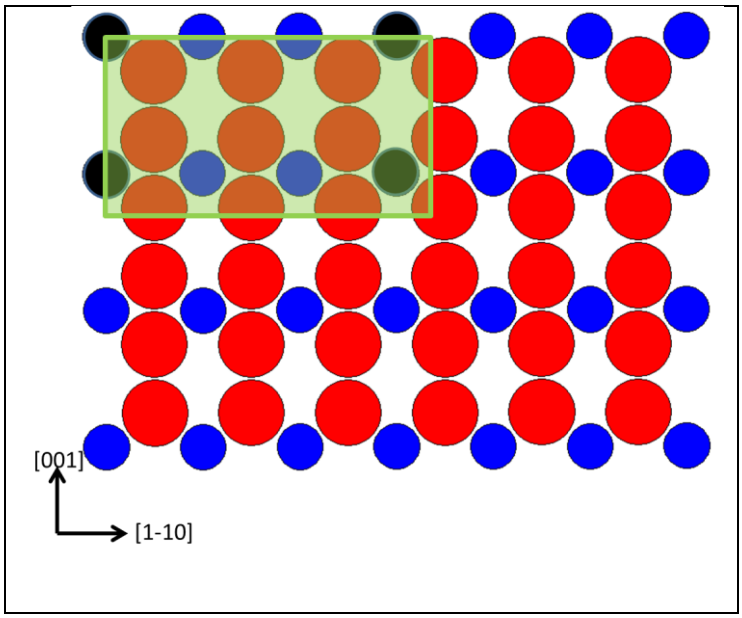

Figure 5.4(b): CeO_2(110) surface, in black principal directions parallel to surface. Cerium atoms are depicted in blue and O atoms in red. The green rectangle shows the CeO_x cell, the dimensions are proportional to the effective length.

By calculation the real CeO_x cell, depicted by a green rectangle in figure 5.4(b) has a length of 5.90 Å along the short side and 12.98 Å along the long one. In respect to the CeO_2(110) surface the black colored atoms are those that more closely resemble the rectangle with an effective length of 5.41 Å along the [001] direction and 11.48 Å along the [1-1 0] direction of CeO_2(110) this further demonstrates the great strain through which the structure is undergoing.

The c(12x2) phase:

This phase was obtained by 20 min reactive deposition in an oxygen pressure of $1.4x10^{-7}$ mbar under a Ce flux of 0.03 ML/min on a yellow TiO_2(110) crystal. This particular structure was found only once due to its high instability. According to the observed LEED image depicted in the figure below (Figure 5.6(a)) and its corresponding reciprocal lattice pattern the cerium oxide surface that best fitted was found to be CeO_2(111) giving the same mismatch coefficients as mentioned above. However, the distance at which the Ce atoms are placed from each other probably causes a high strain as depicted in figure 5.6(b).

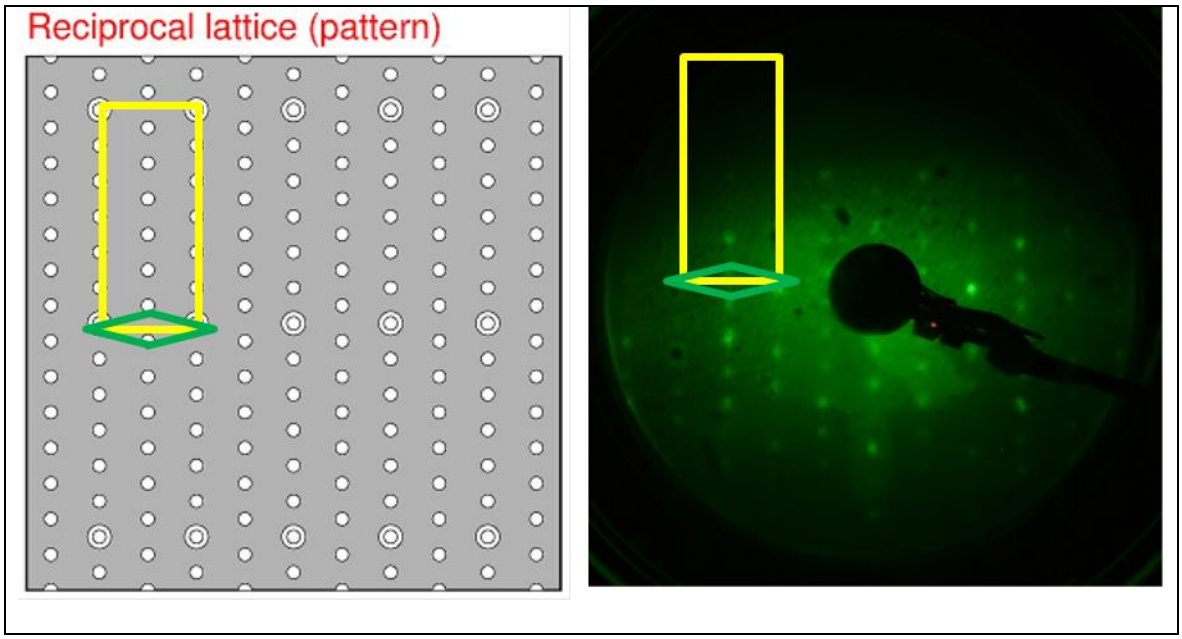

Figure 5.6(a): Reciprocal lattice pattern and LEED image of a c(12x2) pattern for a 0.6 ML of CeO_x on TiO_2(110) the LEED image was taken at 36.9 eV.

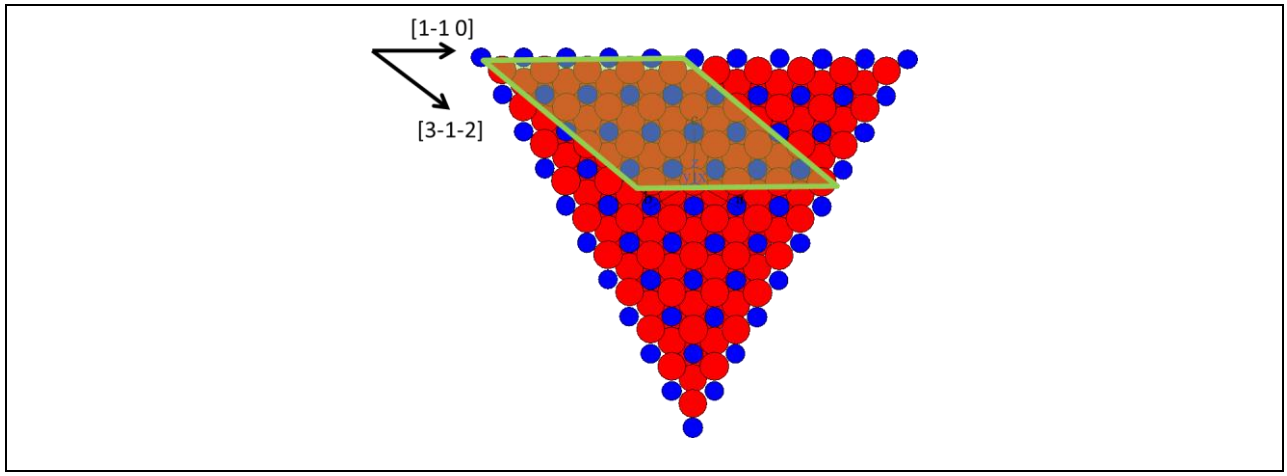

Figure 5.6(b): CeO_2(111) surface, in black, directions parallel to surface. Cerium atoms are depicted in blue and O atoms in red. The green rhombohedrum shows the c(12x2)CeO_x cell, the dimensions are proportional to the effective length.

The c(2x2) phase:

This phase that was the most stable was obtained by reactive deposition in an oxygen pressure of $1.4x10^{-7}$mbar under a Ce flux of 0.03 ML/min for 30 min. The the sample was heated under oxygen at 900K for 5 min. In the figure (Figure 5.7(a),(b)) below we can observe the obtained LEED image, in the simulated LEED image (left) the larger dots correspond to the substrate TiO_2(110) (1x1) pattern whereas

the smaller dots corresppond to the c(2x2) pattern of the cerium oxide film. Highlighted in both pictures are the unit cells.

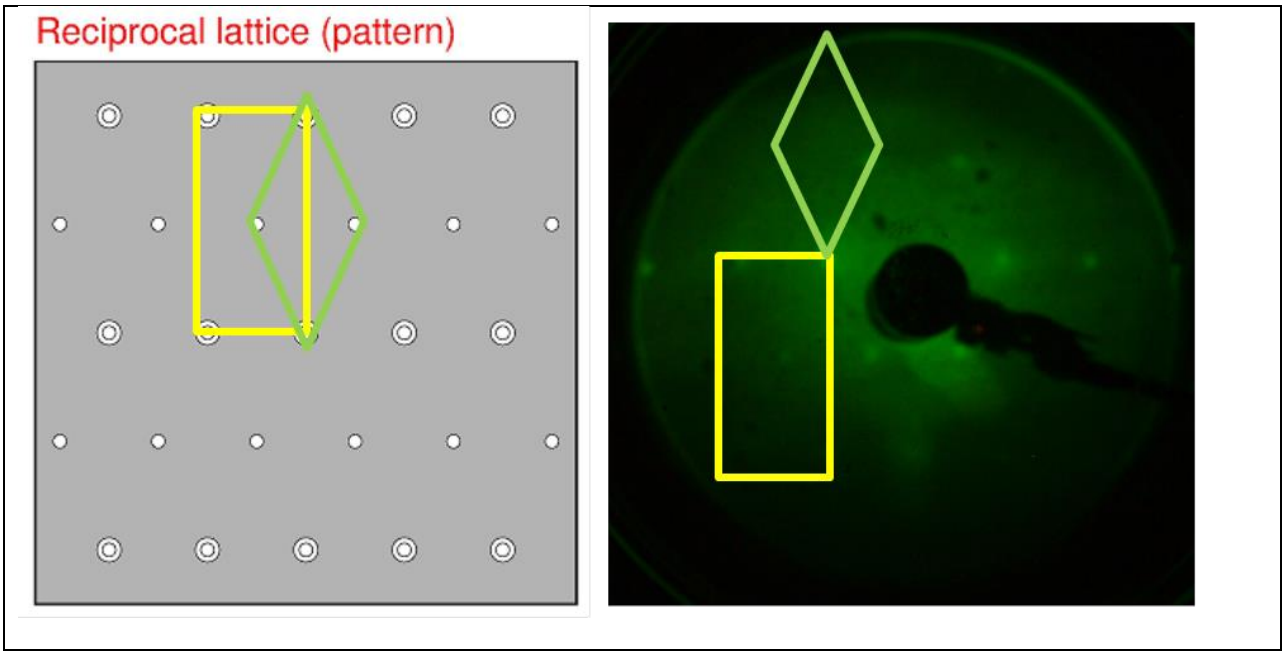

Figure 5.7(a): Reciprocal lattice patter and LEED image of a c(2x2) pattern for a 1ML of CeO_x on TiO_2(110) the LEED image was taken at 53 eV.

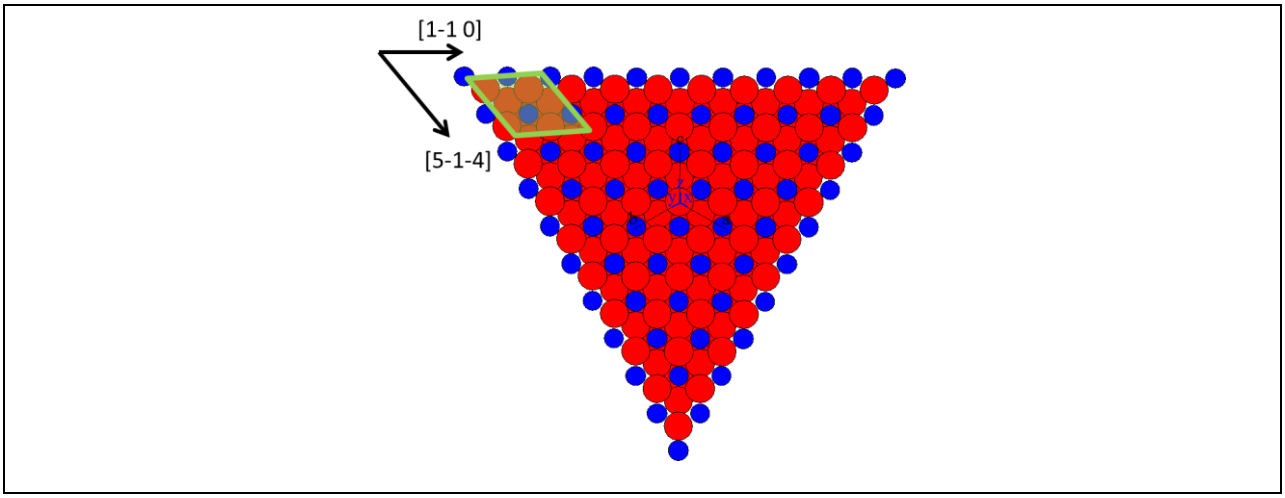

Figure 5.7(b): CeO_2(111) surface, in black, directions parallel to surface. Cerium atoms are depicted in blue and O atoms in red. The green rhombohedrum shows the c(2x2)CeO_x cell, the dimensions are proportional to the effective length.

By using CaRIne we made a hypothesis on how the film grew onto the surface. In the figure below (Figure 5.8) we have shown the surfaces of both substrate (110) and film of which we imagined to grow along the (111) direction. By this hypothesis we observed that the two Ce atoms along the [-1 2-1]

direction on the surface were separated by a distance of 6.63 Å; these almost matched the substrate's Ti atoms along the [1-10] direction of 6.49 Å. A study by Park et al. [88] demonstrated via STM that the first Ce atom depositing on the surface most likely interacted with surface O anions rather than Ti cations. Furthermore, the group showed these Ce atoms interacted with two bridging and one in-plane O atom of the TiO_2(110) surface. In short looking at the image below the cerium atom, according to the study, would place itself on the O atom (red) between the center and the shorter edges of the rectangle as the Ti atoms (gray) directly on top of an O atom are the five-fold coordinated Ti centers whereas the others share bridging oxygen atoms along the [001] direction.

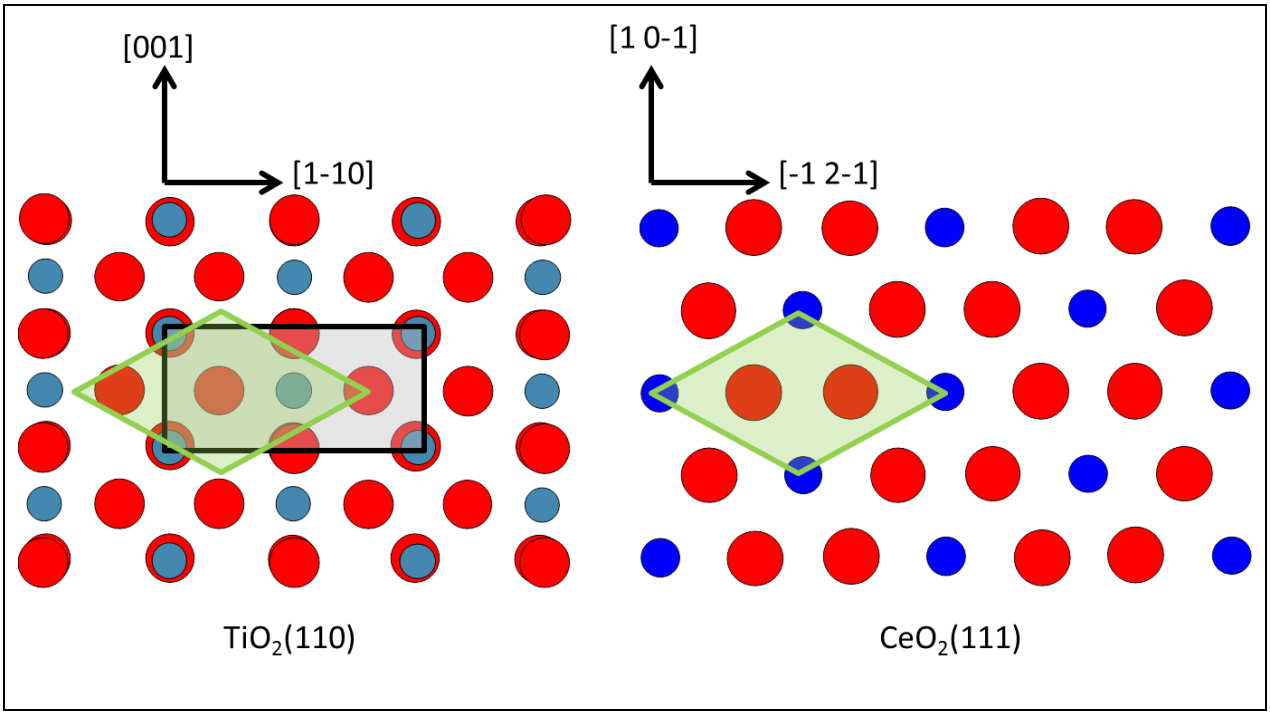

Figure 5.8: TiO_2(110) and hypothetical CeO_2(111) surfaces in black principal directions parallel to surface. Cerium atoms are depicted in blue, Ti atoms in gray and O atoms in red. Black rectangle shows the unit cell for the rutile surface whereas the green diamond that of ceria.

We have observed that further deposition of cerium made surface very rough and a LEED was no longer observable. This was very likely due to the great strain imposed from the substrate; the deposition of cerium didn't completely wet the surface, as such the continuous growth of 3D islands contributed to a polycrystalline film.

5.1.5 XPS characterization of the interface

In this paragraph I will briefly describe the very peculiar characteristics of Ce 3d XPS spectra. The first well-resolved Ce 3d XPS experimental spectra were published by Burroughs et al. [89] .These authors

studied the core electrons XPS spectra and the satellite structure of the Ce(IV) and Ce(III) oxides. A. Kotani et al.[90,91] showed that the Ce 3d satellite structures derive mainly from ligand to metal charge transfer transitions, i.e. coupled excitations of the O 2p to metal charge transfer type (O 2p → metal 4f transitions). These spectra are characterized by complex features that are related to final states occupation of the 4f level. This includes the ground-state configuration and the final-state interaction with the core hole because the structure of the core XPS is sensitive to the final-state interaction. The CeO_2 spectrum (Ce(IV)) is composed of two multiplets (v and u). These multiplets correspond to the spin-orbit split $3d_{5/2}$ and $3d_{3/2}$ core holes. The spin-orbit splitting is about 18.6 eV. Each spin-orbit component of the Ce 3d XPS spectrum is dominated by three features. The highest binding energy peaks, u''' and v''', respectively located, at about 916.9 and 898.3 eV, correspond to a Ce $3d^9 4f^0$ O $2p^6$ final state. The peak u''' associated to the Ce $3d_{3/2}$ is characteristic of the presence of Ce^{4+} ions in Ce compounds. The lowest binding energy states u, v, u'', v'', respectively located at 901.3, 882.7, 907.3, and 888.5 eV are assigned to Ce $3d^9 4f^2$ O $2p^4$ and Ce $3d^9 4f^1$ O $2p^5$ final states. In the cerium (IV) oxides, the satellites are apparently due to energy-gain (shake-down) rather than energy-loss (shake-up) processes. These are so-called 'shake-down' states.

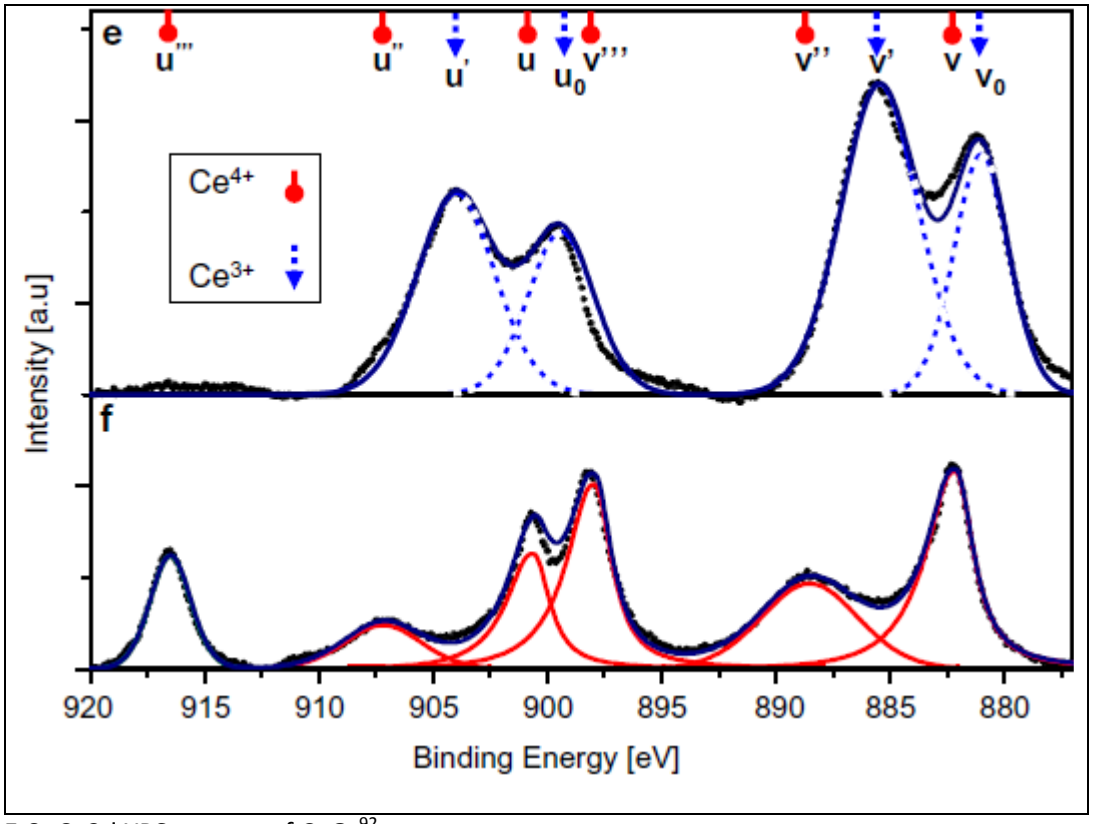

Figure 5.9: Ce3d XPS spectra of CeO_2[92].

In the case of reduced ceria, in this case Ce(III), the XPS spectrum of the Ce3d peak changes greatly and is composed of two multiplets (v and u) corresponding to the spin-orbit split $3d_{5/2}$ and $3d_{3/2}$ core holes. The spin-orbit splitting is about 18.2 eV. Each spin-orbit component of the Ce 3d XPS spectrum is

dominated by two features. Thus, four peaks corresponding to the pairs of spin-orbit doublets can be identified in the Ce 3d spectrum from Ce(III) oxides. The highest binding energy peaks, u' and v' respectively located at about 903.4 eV and 885.2 eV are the result of a Ce $3d^9 4f^1$ O $2p^6$ final state. The lowest binding energy states u^0 and v^0 respectively located at 899.1 eV and 880.9 eV are assigned [93,94] to Ce $3d^9 4f^2$ O $2p^5$. Thus the main feature that differentiates, in the XPS spectra of Ce3+ and Ce4+, their oxidation states is the presence, in the case of Ce^{4+}, of the peak at 916.9 eV. This "fingerprint" peak helped us in determining whether the cerium oxide was fully oxidized or not[95]. In the figures below we have depicted a few of our first trial depositions in which we have observed differences in the oxidation state of the cerium oxide film. In Figure 5.10 we have reported the XPS spectra of several depositions, corresponding to increasing amount of CeO2, carried onto a substrate held at RT or 600K with a flux of 0.27 Å/min in a background pressure of O2 = $5.0 \cdot 10^{-6}$mbar. It is easy to see that the 0.9 ML showed a remarkable similarity with the spectra of Ce(III) displayed in Figure 5.9. However, at thicker coverages the "fingerprint" peak at 916.9 eV became more and more visible thus signifying the further oxidation of the film although it still didn't quite resemble that of fully oxidized CeO_2.

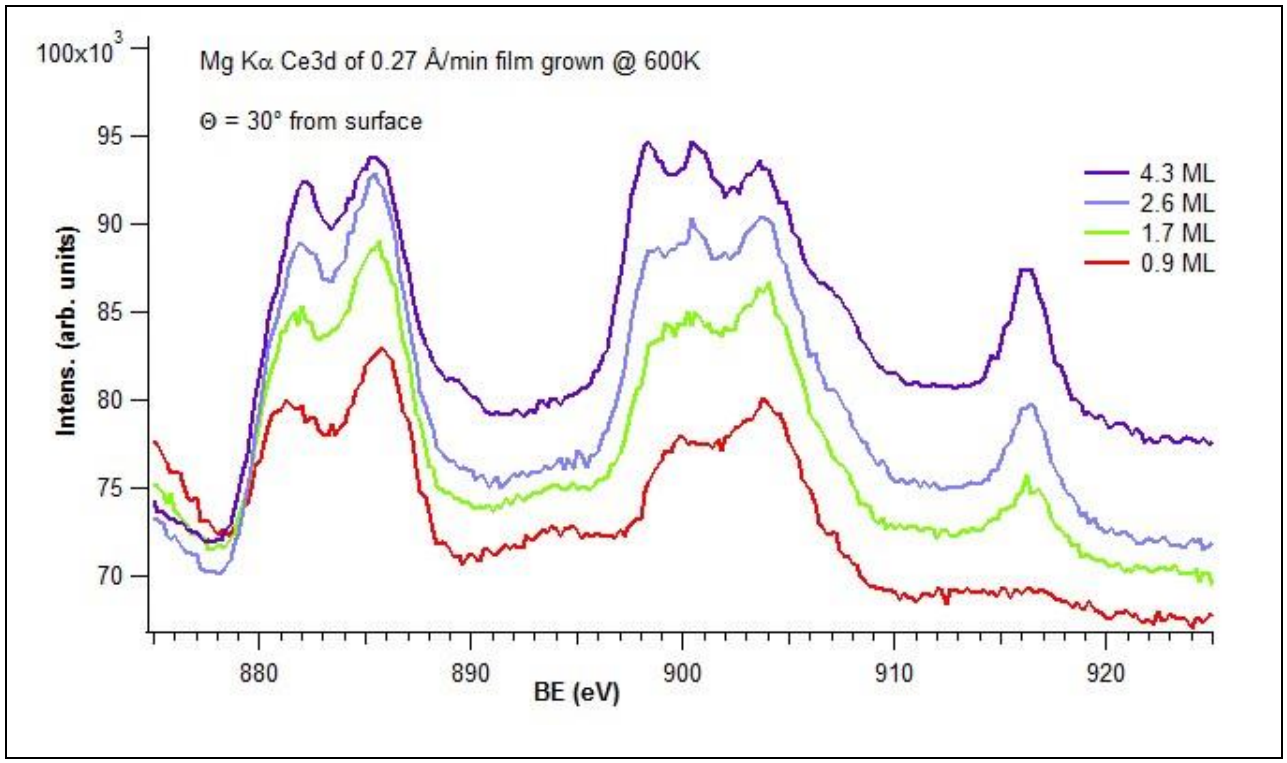

Figure 5.10: Ce3d XPS spectra taken after trial depositions on TiO_2(110) at 600K.

Other features characteristic of the fully oxidized ceria were present: for example the u multiplet component at 901 eV became gradually more distinguishable at 2.6 ML and the multiplets v^0 and u^0 respectively at 880.9 and 899 gradually shifted towards the binding energies of the fully oxidized ceria v and u respectively at 882.7 and 901.3 eV. Thus, at 4.3 ML we had the presence of both Ce(III) and Ce(IV). We repeated the experiment holding the rutile substrate a RT and observed that, for a similar thickness

the film was almost completely oxidized (Figure 5.11). In fact, by observing the spectrum of figure 5.11 the transformation from that typical of Ce(III) to that of Ce(IV) by the gradual disappearance of the former's components v' and u' respectively at 885 and 903 eV and of course the appearance of the "fingerprint" peak at 916.9 eV is evident.

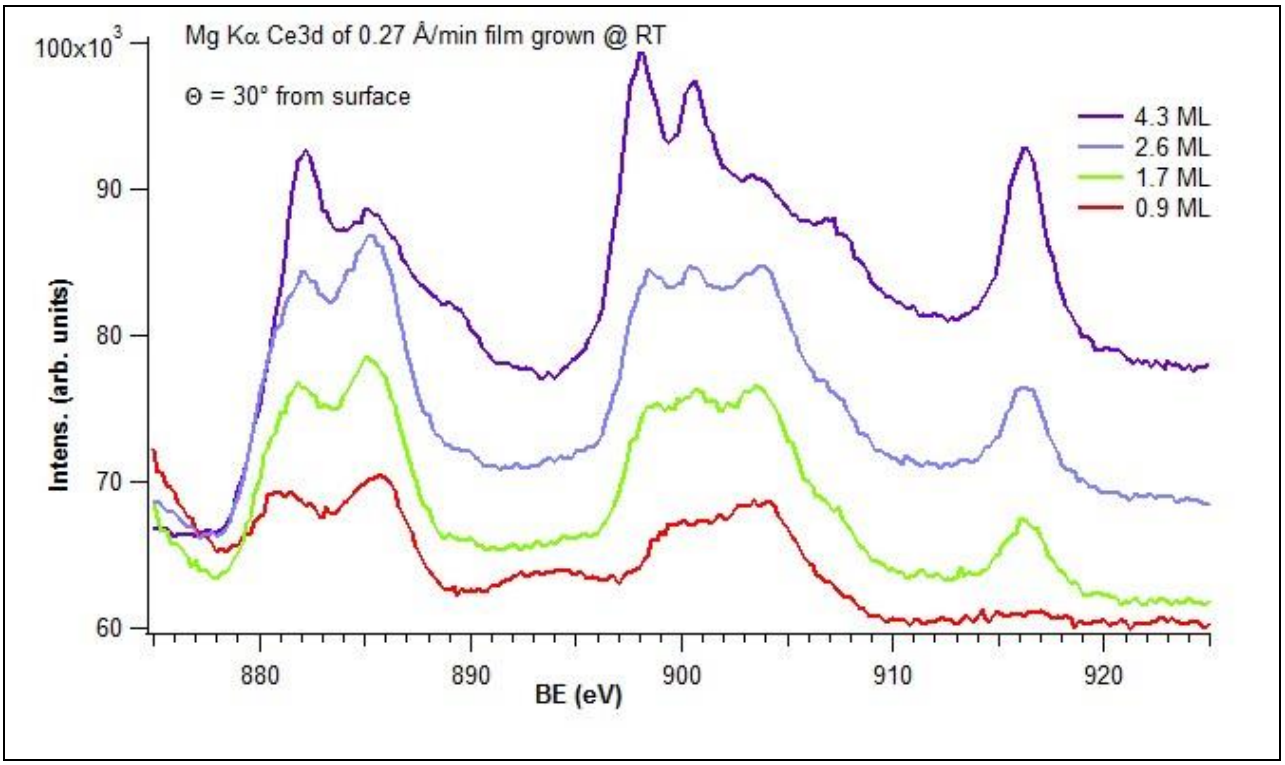

Figure 5.11: Ce3d XPS spectra taken after trial depositions on TiO_2(110) at RT.

Thanks to these trial depositions we concluded that for small coverages we always obtained at the interface a cerium(III) oxide film even under strongly oxidizing conditions.

The stabilization of the Ce(III) oxide was also noted by Graciani et al.[96] who demonstrated by DFT calculations that upon adsorption, a Ce atom ($6s^2 5d^1 4f^1$) formally releases three electrons from the 6s and 5d orbitals to the lower energy Ti 3d states in TiO_2 forming three Ti^{3+} atoms. No electrons are transferred from the Ce 4*f* levels because their energy is lower than the Ti3d states. The O2p states, which are at a lower energy than the Ce4*f* levels, are the only ones available. However, they are required to be empty to accept electrons and this is possible only if no Ti^{3+} sites are available. Oxygen preferentially bonds on these sites, thus once all Ti^{3+} are oxidized back to Ti^{4+} can Ce^{3+} be oxidized by O_2. However, at nanometer thicknesses, because of the decrease in energy of Ce 4*f* states operated by the mixing with the O 2*p* band of titania, supported Ce(III) is strongly stabilized with respect to either isolate particles or bulk crystal. As a matter of fact, fully in line with the study by Graciani et al. our trial depositions conducted in UHV confirmed the reduction of titania upon Ce deposition (Figure 5.12-13). The deposition of 1.5 ML of ceria was conducted with the substrate at RT, in order to better appreciate eventual changes and then in was heated in UHV first to 673 K and then to 873 K. The XPS spectra were

taken close to normal to better observe what happened at the interface. We noted that indeed cerium reduced titania upon deposition as evidenced by the shoulder typical of Ti^{3+} at 456.8 eV. However cerium did not show any component other than that of Ce(III). Furthermore, after annealing in UHV at 673 K the only noticeable change was the disappearance of the low binding energy shoulder of Ti2p probably due to the migration of interstitial oxygen to the interface. The annealing at 873 K showed a slight oxidation of cerium oxide film as confirmed by the appearance of the "fingerprint" peak at 916.9 eV.

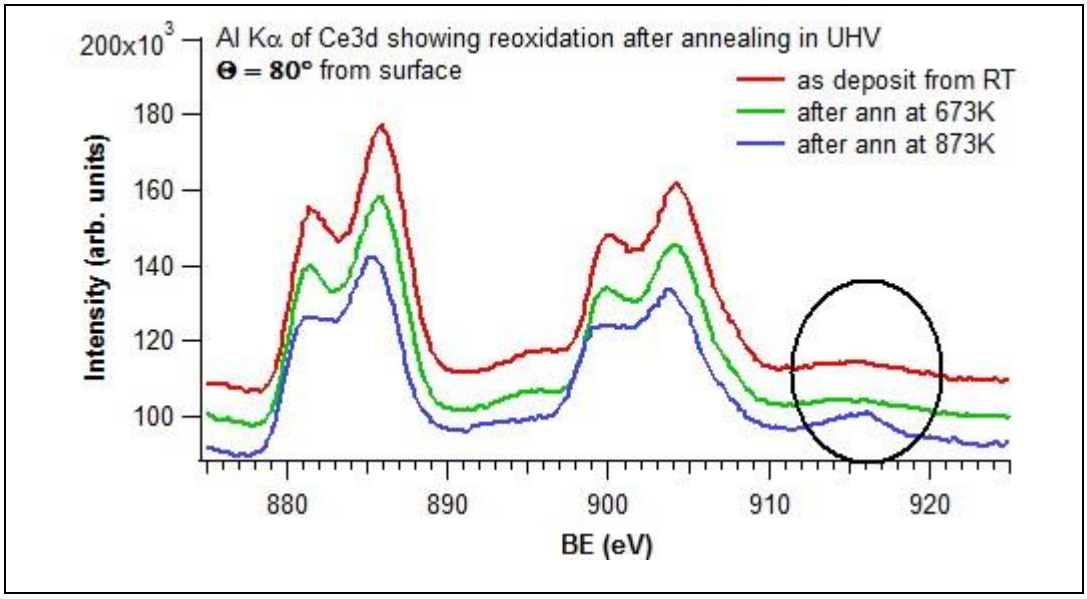

Figure 5.12: Ce3d spectra of 1.5 ML deposited cerium and then subjected to annealing in UHV. Highlighted the "fingerprint" peak at 916.9 eV signaling a degree of oxidation.

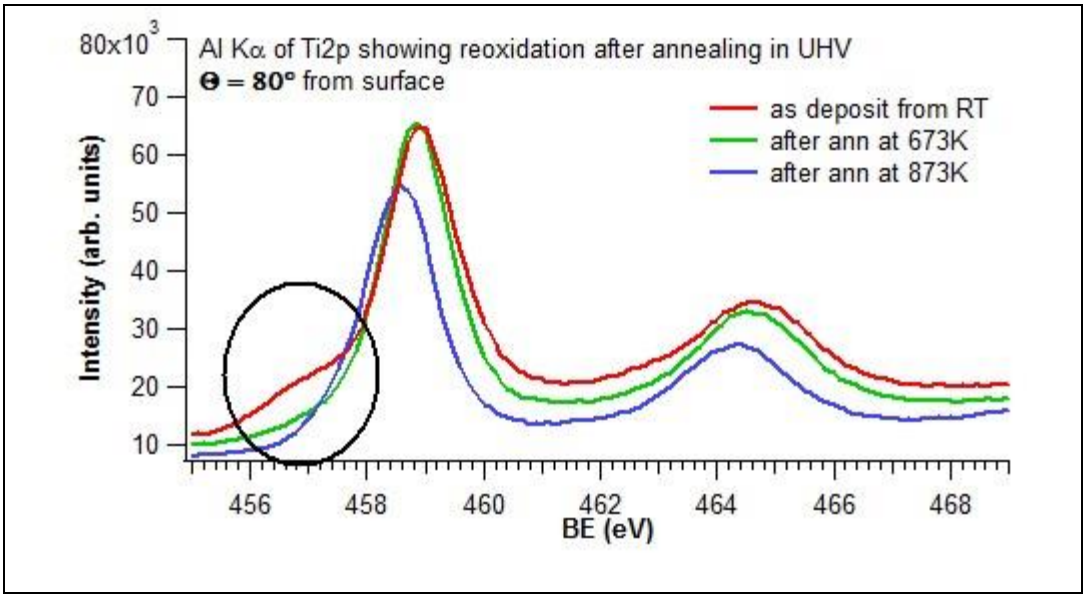

Figure 5.13: Ti2p spectra of TiO_2(110) substrate after 1.5 ML of cerium deposition and then subjected to annealing in UHV. Highlighted the shoulder peak at 456.8 eV signaling a degree of reduction.

A thermal treatment even at higher temperature (T=900K), either in oxygen or UHV, did not lead to the diffusion of ceria into the bulk, probably because of Ce(III) ions radius (1.02 Å). The species stabilized on the surface, are too large to be accommodated inside the rutile lattice (Ti(IV) radius: 0.68 Å) and, on the other hand, the formation of Ce(IV) is prevented by the above mentioned stabilization of the electrons in the Ce 4*f* levels. Therefore, our study suggests that for submonolayer coverage in a very wide range of oxygen chemical potential the most significant Ce species on the surface is Ce(III) and resulted to be quite prone either to reduction or oxidation and no dissolution into the bulk. This is confirmed by a recent experiment of Y. Zhou et al.[97] where they deposited Ti onto CeO_x(111) grown on Ru(0001) and observed that Ti atoms diffused within cerium oxide. At first it may seem odd, but M. Fronzi et al.[98] and R. Wang et al.[99] proved through DFT calculations, the former, and experiments on CeO_2 nanoparticles, the latter, that under reducing conditions, ceria shifts to Ce_2O_3 which is a more open structure where a Ti atom can easily fit in. The above reported results clearly indicate that annealing in O_2 at high temperature is the best way to obtain ordered epitaxial films. We have depicted below the XPS spectra of Ti2p, Ce3d and O1s, (Figure 5.14-16) for various film thicknesses. Depositions were conducted at $1.4x10^{-7}$mbar of O_2 under a Ce flux of 0.03 ML/min, afterwards the sample was heated under oxygen at 900K for 5 min. We remind that the spectra corresponding to 0.5 ML refer to the p(2x2) phase (0.45 ML) and c(12x2) phase (0.60 ML) while those corresponding to 1 ML coverage refer to the c(2x2) phase.

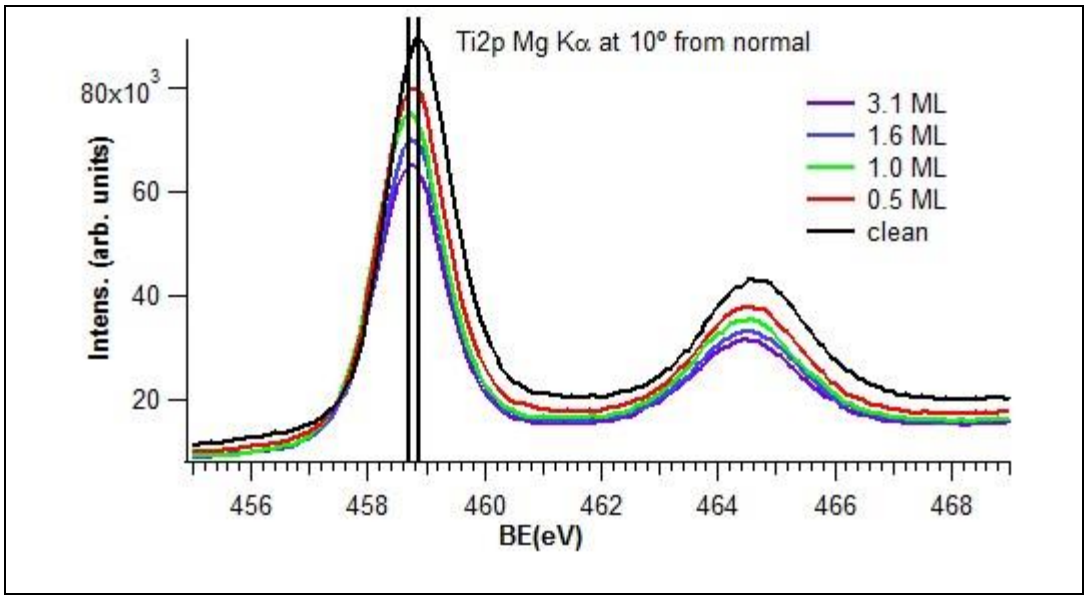

Figure 5.14: Ti2p spectra highlighted is the shifting in eV of the peak towards lower binding energies with increasing film thickness.

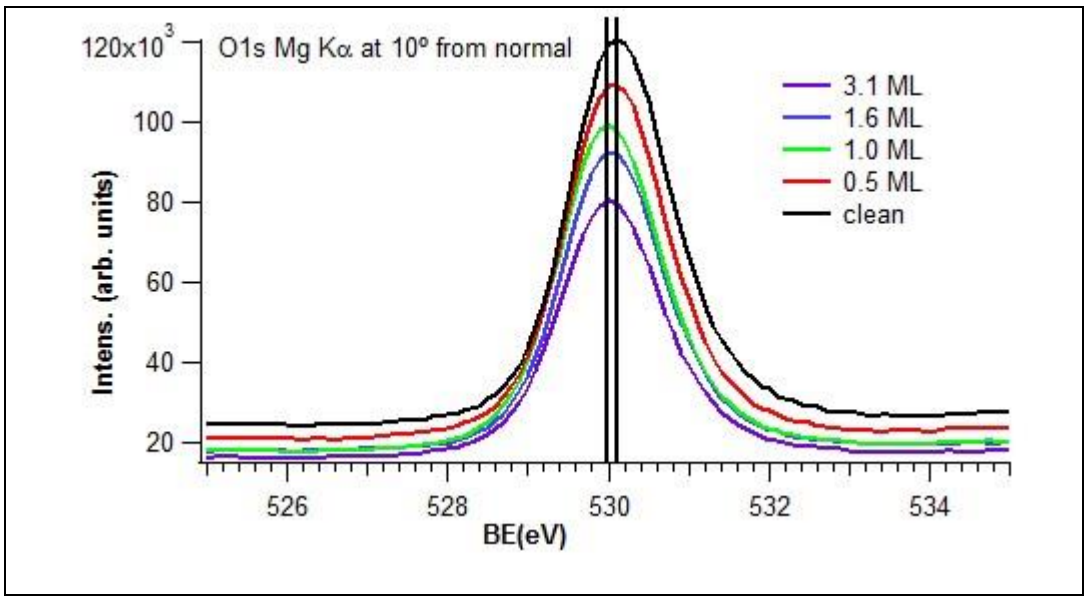

Figure 5.15: O1s spectra highlighted is the shifting in eV of the peak towards lower binding energies with increasing film thickness.

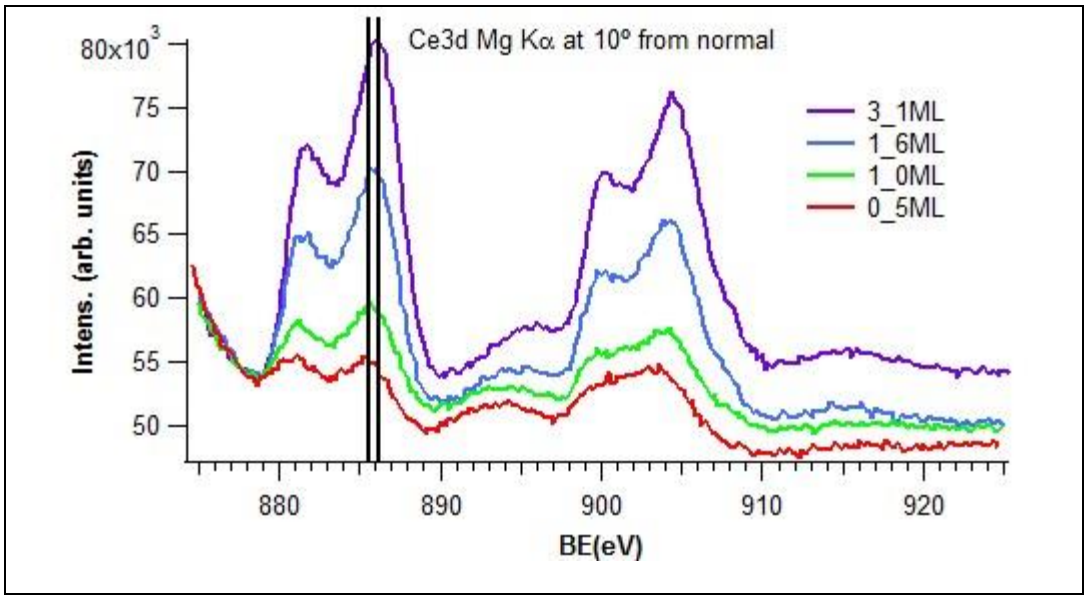

Figure 5.16: Ce3d spectra highlighted is the shifting in eV of the peak towards higher binding energies with increasing film thickness.

Both O 1*s* and Ti 2*p* core level peaks undergo a small shift towards lower BE (0.2-0.3 eV) corresponding to increasing amounts of ceria. This phenomenon can be explained by a downward band bending of titania determined by the surface redox reaction induced by the deposition cerium atoms, which increases the amount of Ti^{3+} and therefore of negative charges in the near surface region. This band bending has also the effect of decreasing the work function of the whole system, which is a critical parameter determining the growth mode and properties of supported nanoparticles.

5.1.6 UPS characterization of the interface

In regards to valence band spectra we report what observed by Pfau et al. [94] (Figure 5.17). In this picture it can be clarly seen that for an increasing reduction of a cerium dioxide sample a peak gradually grows in intensity at around 2 eV and that it progressively shifts to higher binding energies. This peak corresponds to Ce4f states that initially unoccupied in fully oxidized ceria become occupied when the oxide is reduced. The central peak from 4 to 8 eV is related to the O2p state. Finally the peak at 10.8 eV, observed only for sputtered samples is assigned to the O1s electronic state.

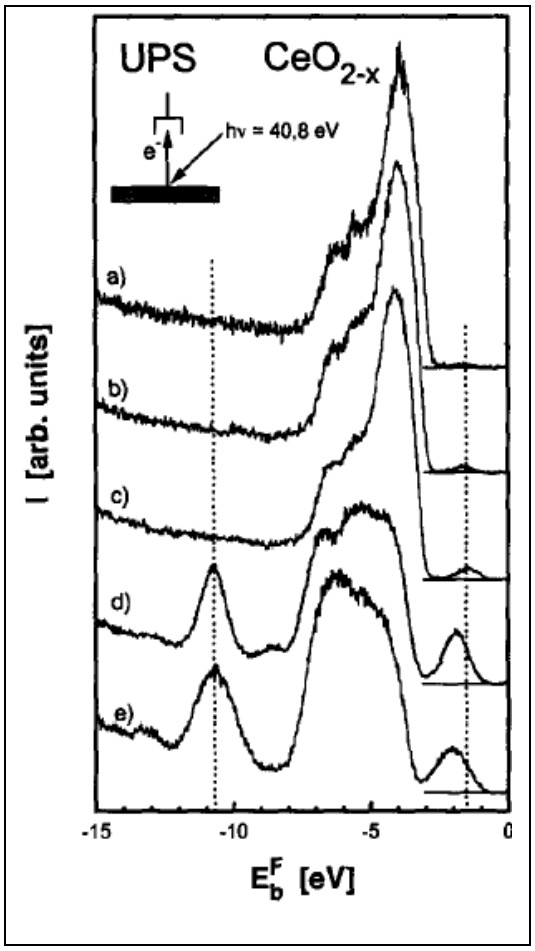

Figure 5.17: He II-excited UP spectra (photoemission intensity I versus binding energy E_b^F) of stoichiometric CeO_2, surfaces and nonstoichiometric CeO_{2-x} surfaces. For increasing reduction, from a (fully oxidized) to e, the valence band maximum and the Ce 4f states shift to higher binding energies which may be due to surface band bending[94].

In regard to the valence band spectra (Figure 5.18) of our films, a relevant shift of the whole band towards lower binding energy can be seen by increasing the film thickness. For increasing amount of ceria, a band connected to defects becomes progressively more intense and undergoes a remarkable energy shift, moving form 2 eV to just below the Fermi level. At low coverage, the energy position of this band is different from what expected for Ti *3d* states (normally lying below 1 eV), therefore it must be mostly related to Ce 4*f* levels, while for higher ceria dose it gets broader and probably overlaps with Ti 3d states. Something similar was observed by X. Shao et al.[100] where the Ce *4f* band broadens and down-shifts with increasing film thickness. It was proposed that in ultrathin films, all Ce ions sit in identical positions and have the same *f* state energies, while in thicker films Ce occupies interface, bulk-like, and surface regions. These different environments give rise to small shifts of the *f* band position.

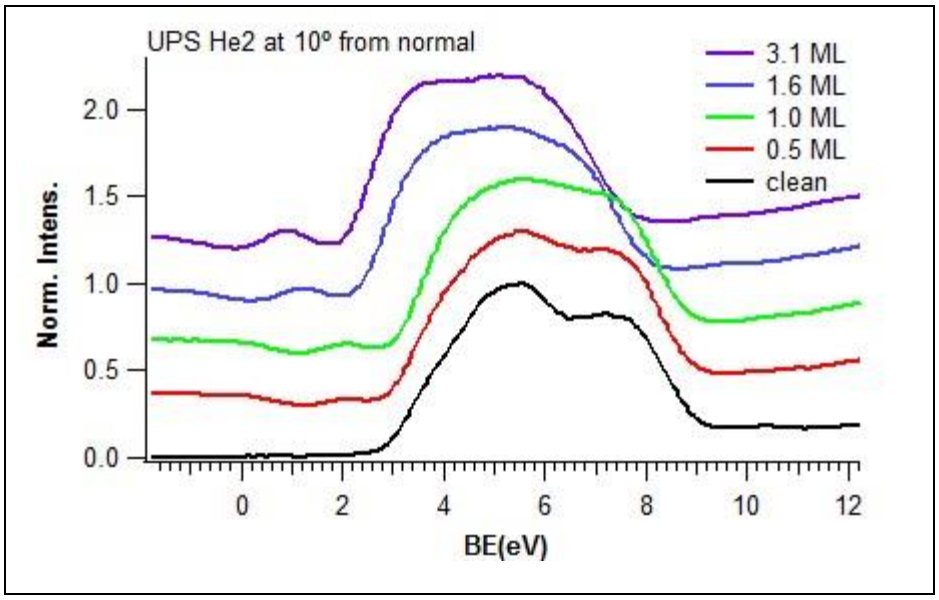

Figure 5.18: UPS He2 spectra of clean TiO_2(110) and after increasing coverage of cerium oxide film.

5.1.7 Conclusions:

In this first part of the study three novel phases were observed, via metal evaporation of cerium onto rutile, which have no counterpart in the bulk phase. Furthermore, such phases were dependent on substrate history and film thickness where the c(2x2) was found to be the most stable. Such long range order wasn't maintained for depositions over 45 min (1.35 ML) as the strain was probably too strong. The variety of phases obtained was surprising; a feature seldom found in literature and that garners, at least at the ultrathin level on TiO_2(110), a great potential for the uncovering of further structures and functionalities. In this last aspect we have conducted TPD experiments using methanol and ethanol as probe molecules and the results will be discussed in the following chapters.

5.2 STM, XPS AND TPD STUDIES OF CERIUM OXIDE NANOLAYERS ON TiO_2(110)

In this section I will attach a published paper about cerium oxide nanolayers, deposited on TiO_2(110) via metal evaporation in UHV. In this paper ultrathin films of cerium oxide of different thickness (0.05, 0.75 and 1.2 ML) are observed via STM. The methanol TPD studies presented in the article were obtained from a the c(2x2) CeO_x phase. Although not presented in their entirety the data obtained at 0.45 ML and 0.9 ML (where the c(2x2) phase was still distinguishable) show the complex interplay between overlayer and substrate.

Nanoscale

PAPER

Structure and special chemical reactivity of interface-stabilized cerium oxide nanolayers on TiO_2(110)†

Cite this: *Nanoscale*, 2014, 6, 800

Stefano Agnoli,*[a] Askia E. Reeder,[a] Sanjaya D. Senanayake,[b] Jan Hrbek[b] and José A. Rodriguez[b]

Novel interface-stabilized ceria nanophases have been grown on TiO_2(110) by physical vapor deposition. At low coverage, dumbbell nanostructures constituted by reconstructed titania and ceria clusters are formed, while long range ordered nanoxides can be obtained by increasing the ceria dose. Scanning tunneling microscopy and photoemission spectroscopy were used to characterize the electronic properties of the films, showing that the TiO_2 substrate can effectively stabilize ceria in reduced form over a wide range of experimental conditions. Epitaxial coupling is a very useful tool for tuning the chemical properties of mixed oxide systems. The special electronic properties of the films have a direct counterpart in the chemical activity, which has been investigated by temperature programmed desorption using methanol as a probe molecule. The experimental results indicate an exceptional activity of the ceria–titania interface in the selective dehydration of methanol to formaldehyde at an unprecedented low temperature (330 K).

Received 30th August 2013
Accepted 16th October 2013

DOI: 10.1039/c3nr04623k

www.rsc.org/nanoscale

1 Introduction

In the field of nanocatalysis, surface science studies are clearly delineating a consistent paradigm pointing to the use of interfaces as an effective tool for stabilizing highly active chemical species (especially the so-called coordinatively unsaturated sites),[1,2] or for creating totally new ones (*e.g.* by forcing uncommon geometry and coordination, or by interfacial hybridization of electronic states).[3–5] So far the most commonly used approach consists of supporting oxides on metals since it is possible to take advantage of the electronic interactions at the interface that can increase the adhesion of the oxide or modify its electronic properties. However, an alternative path, thus far less explored, is the formation of an authentic mixed oxide.[6] In this latter case, the benefit is a higher robustness and stability at different chemical and physical conditions.

Thanks to their ease of reducibility, ceria and titania are commonly used supports for metal catalysts.[7,8] The possibility of tailoring the functionality (chemical reactivity, easy oxygen supply, ability to stabilize nanoparticles, *etc.*) of these oxides by controlling their defects opens up the way for several diversified chemical applications.[9–11]

In the particular case of the ceria–titania system, it has been demonstrated theoretically that it is possible to stabilize Ce^{3+} ($4f^1$) species with respect to Ce^{4+} ($4f^0$) because of the energy decrease of the Ce 4f levels as a result of the mixing with the O 2p band of titania.[12] By exploiting these Ce^{3+} species as sites for water dissociation, an enhanced catalytic activity for the water–gas shift reaction has been achieved when metal nanoparticles were supported on a CeO_x–TiO_x(110) mixed oxide.[12,13] Powders of mixed titania–ceria oxides have proven to be extremely effective in a wide range of applications such as photocatalysis,[14] NO_x reduction,[15] low temperature CO oxidation[16] and the water–gas shift reaction.[13,17]

In the following sections we will report the structural evolution as a function of coverage of novel ceria nanolayers grown on rutile (110) in an oxygen atmosphere. Depending on the ceria coverage, different phases have been observed by scanning tunneling microscopy (STM): at low coverage monomers and dimers of ceria coexist with titania reconstructions. At higher coverage, a pseudo-hexagonal monolayer structure forms first, followed by a bilayer characterized by a rectangular unit cell.

In this study, we have also investigated the chemical properties of this mixed oxide system by studying its reactivity using methanol (MeOH), a simple C1 oxygenate. The activation of MeOH has significant importance to the conversion of liquid fuels for which TiO_2 and mixed oxides are important catalytic materials of choice when striving towards the MeOH economy.[18] In addition, MeOH is the simplest C1 alcohol and thus paves the way to understanding the chemistry of all alcohol functional

[a]*Department of Chemical Sciences, University of Padova, Via F. Marzolo 1, 35131 Padova, Italy. E-mail: stefano.agnoli@unipd.it*

[b]*Chemistry Department, Brookhaven National Laboratory, Upton, New York 11973, USA*

† Electronic supplementary information (ESI) available. See DOI: 10.1039/c3nr04623k

groups (R–OH). This probe molecule can reveal a lot about the oxide surface and has been studied extensively over stoichiometric and defected TiO_2 surfaces both experimentally and theoretically.[19–21] The photochemistry of MeOH and photooxidation of MeOH over TiO_2(110) has been investigated to find ways to break C–O and C–H bonds in a selective manner.[22–24] Steam reforming processes for the production of pure H_2 from MeOH has motivated others to study the reaction of H_2O and MeOH over TiO_2(110), including the photocatalytic decomposition of these reactants.[25–27]

Several works have involved the systematic study of a mixed oxide material that leads to the reactive conversion of MeOH.[28–36] In this respect, a very interesting system is vanadia nanostructures on ceria that has been thoroughly investigated using a surface science approach obtaining a very detailed understanding of the microscopic mechanism of MeOH decomposition.[28] Vanadia oligomers supported on ceria have been demonstrated to be extremely active catalysts for selective dehydrogenation of MeOH to formaldehyde even at a low temperature (370 K), because of the easy reducibility of the ceria support that can easily accommodate electrons in the 4f level that are transferred from vanadia during the oxidation of MeOH. This notable case exemplifies how the interplay of different oxide phases at the nanoscopic level can be exploited to achieve an enhanced reactivity, and the effectiveness of surface science methods at unraveling their special properties.

In general the MeOH molecule adsorbs molecularly and dissociatively (eqn (1) and eqn (2)) on the stoichiometric TiO_2(110) surface. Adsorption of MeOH in the presence of defects (sub-stoichiometric TiO_{2-x}) likely causes the molecule to dissociate to form methoxy and H that is likely to adsorb as OH on the surface. Desorption typically takes place either molecularly (eqn (3)) or recombinatively as methanol (eqn (4)).

$$CH_3OH\ (g) \rightarrow CH_3OH\ (a) \quad (1)$$

$$CH_3OH\ (g) + O\ (s) \rightarrow CH_3O\ (a) + OH\ (a) \quad (2)$$

$$CH_3OH\ (a) \rightarrow CH_3OH\ (g) \quad (3)$$

$$CH_3O\ (a) + OH\ (a) \rightarrow CH_3OH\ (g) + O\ (s) \quad (4)$$

The presence of O adatoms on the defected surface of TiO_2(110) (dissociative adsorption of O_2 to give O bound to defect sites), converts the methoxy to formaldehyde on the surface (eqn (5)). Desorption of formaldehyde surface species occurs in a low temperature (<300 K) and high temperature regime (>600 K) from the TiO_2(110) surface (eqn (6)).[19,37]

$$CH_3O\ (a) + O(s) \rightarrow CH_2O\ (a) + OH\ (a) \quad (5)$$

$$CH_2O\ (a) \rightarrow CH_2O\ (g) \quad (6)$$

Of equal importance to our mixed oxide system is the reactivity of MeOH over CeO_x; the pathways to methanol reaction were observed over CeO_2(111) surfaces in several studies.[38–40] Like TiO_2, CeO_2 is a reducible oxide with interchangeable oxidation states (Ce^{4+} and Ce^{3+}). This surface showed good propensity towards the formation of methoxy and the OH surface intermediate from the adsorption of methanol on stoichiometric (Ce^{4+}) and substoichiometric (Ce^{4+}–Ce^{3+}) surfaces. The desorption products on the stoichiometric surface are typically recombined MeOH (eqn (3)), aldehyde (eqn (5) and (6)) and H_2O (from the recombination of OH + H/OH (eqn (7) and (8))) at lower temperatures.[39,41]

$$OH\ (a) + H\ (a) \rightarrow H_2O\ (g) \quad (7)$$

$$OH\ (a) + OH\ (a) \rightarrow H_2O\ (g) + O\ (a) \quad (8)$$

In a clear demonstration of selectivity, the substoichiometric CeO_{2-x}, a surface rich in Ce^{3+}, showed the desorption of CO and H_2 (dehydrogenation) products *via* the decomposition of methoxy intermediate to aldehyde or carbonates (eqn (9)–(14)).[39]

$$CH_3O\ (a) \rightarrow CO\ (g) + 3/2H_2\ (g) \quad (9)$$

$$CH_3O\ (a) \rightarrow H_2CO\ (a) + H\ (a) \quad (10)$$

$$CH_3O\ (a) + 2O\ (s) \rightarrow CO_3\ (a) + 3H\ (a) \quad (11)$$

$$H_2CO\ (a) \rightarrow CO\ (g) + H_2\ (g) \quad (12)$$

$$CO_3\ (a) \rightarrow CO\ (g) + 2O\ (s) \quad (13)$$

$$H\ (a) + H\ (a) \rightarrow H_2\ (g) \quad (14)$$

In principle, the addition of both CeO_2 and TiO_2 together would, as a first approximation, be expected to yield a mixture of reactivity composed of both TiO_2(110) and CeO_2(111) surfaces. Alternatively, it is probable that this combination of materials is going to have a unique reaction mechanism, demonstrating a new selectivity with respect to its structure and relative chemical composition that holds no identifiable relation to either surface on its own.

2 Experimental

The STM studies were performed in an Omicron ultrahigh-vacuum (UHV) chamber with a base pressure of less than 1.0×10^{-10} torr. This chamber is equipped with a variable-temperature STM (VT-STM), an ion gun for surface cleaning, gas leak valves, and an e-beam metal evaporator. Experiments were carried out on a rutile TiO_2(110) crystal (Princeton Scientific Corp.). The surface was cleaned by cycles of Ne^+ ion sputtering at 1 keV for 20 min with an ion beam current of ~8 μA, followed by annealing to 950 K for 10 min. The high-resolution STM images of the surface exhibited bright Ti rows separated by 6.5 Å, as is typically observed for TiO_2(110)-(1 × 1).

In this work, the surface coverage of ceria is expressed in terms of monolayer equivalent (MLE) defined as equal to the atom density of Ce atoms on the CeO_2 (111) surface (6.6×10^{14} atoms per cm^2). The amount of Ce atoms evaporated was estimated from the cluster height, diameter, and number density observed in the STM images after metal cerium deposition. The

standard procedure to obtain ceria thin films consisted of the deposition of Ce with a flux of ~0.02–0.03 MLE per min in 2×10^{-7} torr of O_2 at 650 K and subsequently annealing the sample to 950 K for 10 min while keeping constant the oxygen pressure.

All the STM images were taken at room temperature using chemically etched tungsten tips (occasionally sputtered for cleaning) and using tunneling parameters in the range: 0.4–1.5 V and 0.05–0.2 nA.

Temperature Programmed Desorption (TPD) experiments were performed in a multitechnique chamber (base pressure 1.0×10^{-10} torr) equipped with a Hiden quadrupole mass spectrometer (QMS) ending with a small aperture, a Omicron DAR 400 conventional double-anode X-ray source, a VG CLAM 2 photoelectron analyzer, and an Omicron EMF-3 single e-beam water-cooled evaporator. The sample was fixed to the manipulator through Ta frame (diameter 0.3 mm) using conductive ceramic glue and a K-type thermocouple was clipped on the sample surface. A linear heating rate of 2 K $second^{-1}$ was used for obtaining all the TPD spectra.

3 Results and discussions

As previously reported,[13] when a small amount of ceria (<0.2 MLE) is deposited on TiO_2(110), tiny, round shaped clusters are formed on the surface. They are randomly distributed on the terraces without any tendency to decorate step edges, indicating therefore a limited surface mobility of these entities. It is possible to discriminate clearly between ceria-related features and oxygen-induced titania reconstructions[42] on the basis of their distinct apparent heights. At this stage, single monomers or dimers, typically oriented along particular substrate directions, are present (see Fig. 1).[43] Quite interestingly, for specific tunneling conditions, a dark halo can be observed around ceria clusters, while this feature is absent around titania related reconstruction (Fig. 1). This is a clear indication of the unique electronic structure of ceria clusters; these dark features on titania rows can be related to subsurface Ti^{3+} ions,[44] that are formed as a consequence of the deposition of Ce^0 atoms, which are promptly oxidized to Ce^{3+} by injecting electrons into the titania 3d band.[12] Very similar defects were also observed in the low coverage regime during the growth of other metal films[45] or reducible oxides on TiO_2(110).[46] In the case of the vanadia–ceria system, a very similar dark halo as been reported and interpreted in terms of a Ce^{3+} defect underneath the vanadium oxide cluster.[47] This direct interaction between oxide monomers and substrate defects has been rationalized by DFT calculations and related to an enhanced reactivity.[28]

Once the ceria coverage is increased (0.45 MLE of CeO_x, Fig. 1c and d) the surface morphology becomes much more complex: 5–10 nm long titania strands[42,48,49] are formed and ceria clusters decorate their edges, especially the ends, forming dumbbell-like structures (highlighted by black ellipses in Fig. 1d). An easy distinction between titania and ceria derived structures can be inferred from the very different bias dependence (compare Fig. 1c *vs.* d). Ceria clusters are usually arranged along the [001] direction of the substrate or 42° off with respect to it (as indicated by the black arrow in Fig. 1d), similar to what was observed for dimers at lower coverage.[13]

Interestingly, the extent of reconstructed titania is related to the ceria dosage. Fig. S1a† reports an STM image of the deposition of 0.55 MLE of ceria at 650 K followed by annealing at 750 K for 10 min, while in Fig. S1b,† it is shown a different area of the same sample shadowed to limit Ce deposition, but was otherwise exposed to the same oxygen amount at same temperature. It can be easy observed that, despite starting with smooth substrate before deposition, the region where ceria has been deposited has undergone a massive reconstruction. The surface morphology is very rough, likely because of the nucleation of (1×1) ad-islands, and the terraces display extended regions of $TiO_2(1 \times 2)$ strands, often cross-linked.[20,42] Under these temperature and oxygen rich conditions, reduced titanium ions can be extracted from the subsurface region and migrate on the surface to form Ti_2O_3 linear[49] or more complex interconnected structures like rosettes and (1×2) cross-linked patches.[20,42]

We suggest two possible explanations for this enhanced tendency of titania to reconstruct: first, as thoroughly described in ref. 12, the deposition of Ce atoms induces the reduction of Ti^{4+} ions to Ti^{3+} that subsequently can migrate to the surface and react with oxygen forming TiO_x nanostructures. Alternatively (and maybe synergistically), the presence of Ce metal or oxide clusters can facilitate the dissociation and sticking of O, and the consequent abundant supply of O can speed up the migration of the Ti interstitial from the substrate to the surface where they can form the resulting structures.

After the deposition of about 0.75 MLE of ceria, the STM images show three different kinds of regions as labeled in Fig. 2a. In addition to the previously described areas, where ceria clusters decorate titania strands (type I), there are few wide islands formed by closely packed clusters, apparently lacking even a short range order (type II). Typically, these structures are located at the lower side of step edges and they do not present any recognizable sign of titania reconstructions (neither strands, nor rosette-like features).[50] Starting from these disordered regions, we can observe the nucleation of long range ordered structures (type III) characterized by a striped appearance. These new types of nanostructures are not present just after the deposition at 650 K, but start to form after annealing at 950 K; a prolonged annealing does not lead to any significant ordering of the disordered type II region.

A high resolution STM picture of the structure III is presented in Fig. 2b: a centered rectangular unit cell can be easily identified, whose dimensions, 1.2 ± 0.1 nm $\times$ 26 ± 0.2 nm, are compatible with a $c(4 \times 4)$ superstructure, with respect to the TiO_2(110) surface. Indeed the $\times 4$ commensuration along the [1−10] direction can be easily verified by comparing STM pictures where the titania rows are visible. Since the unit cell of the TiO_2(110) surface is 2.96 Å $\times$ 6.5 Å (primitive rectangular) and the unit cells of ceria are 3.86 Å $\times$ 3.86 Å (CeO_2(111) hexagonal), 3.86 Å $\times$ 3.86 Å (CeO_2(100) square) and 3.86 Å $\times$ 5.46 Å (CeO_2(110) rectangular), a simple epitaxial match of bulk-like ceria would require the introduction of a relevant amount of strain. From the comparison of the images reported in Fig. 2, we can see that this phase is bias dependent, showing a rather

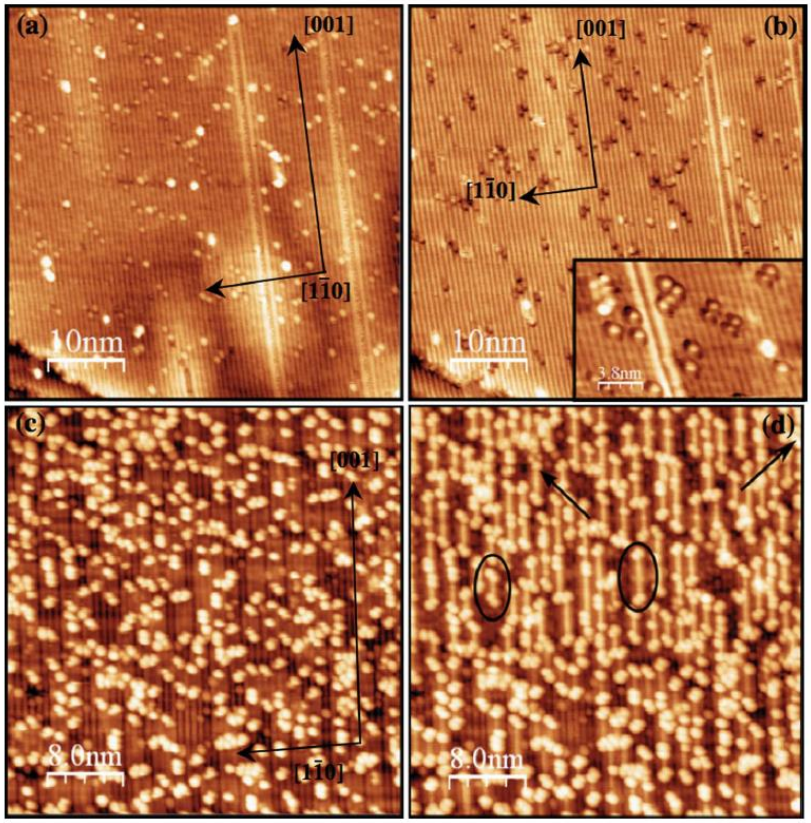

Fig. 1 (a) and (b) STM images of the same titania area after the deposition of 0.05 MLE Ceria with different tunneling parameters: (a): 1.1 V 0.07 nA, (b): 0.75 V, 0.07 nA. The inset in (b) displays a high-resolution image of the ceria clusters showing a peculiar shadowing on the surrounding titania. (c) and (d) STM pictures of the same region of 0.45 MLE CeO_x taken with different tunneling parameters (c): 1.3 V, (d) 1.5 V. Titania and ceria related features can be easily recognized thanks to the different bias dependence.[76]

distinct STM appearance (*e.g.* compare Fig. 2b *vs.* d). An apparent height of about 0.12–0.16 nm with respect to titania suggests that we are dealing with monolayer thick structures. Type III islands can nucleate either on titania terraces or more often on the lower side of step edges. When the coverage is increased to 0.9 MLE (Fig. 2c) there are no qualitative changes in the surface – all three distinct regions are observed – but there is a clear increase in the extension of the long range ordered islands and of the disordered ones (type III and II respectively), and a significant reduction of the areas covered by titania reconstructions decorated by clusters (type I). It is interesting to note that the ordered troughs on the islands can reach an extension of even 100 nm along the [001] direction, but the width along the [1−10] direction remains quite limited (~5–10 nm). High-resolution STM pictures (see Fig. 2d) show some troughs running along the [001] direction (see the dotted rectangle), which break the continuity of the islands, and are decorated by disordered clusters. An explanation for these peculiar features can be ascribed to the reduced mobility of some excess material (most likely titania), which cannot be accommodated during the growth of the new oxide and whose diffusion length is limited. Indeed, it can be generally observed that, on opposite sides of the troughs, the oxide islands have a different translational registry with respect to the substrate so these defective troughs can be considered antiphase domain boundaries.

When the coverage is increased to 1.2 MLE, a new kind of surface structure can be observed: once again, originating from type II disordered areas, new wide, long range ordered islands start to nucleate (type IV) as clearly shown in Fig. 3. As distinct from type III islands, these new structures are more corrugated (around 0.3 nm with respect to the titania substrate *i.e.* 0.15 nm higher than the average level of type II structure), so they are likely bilayer islands.

We never found type III and type IV nanostructures in the same region even when these two phases are stable at the same thermodynamic conditions, suggesting that kinetics factors are important for the growth of the particular ceria structures. The formation of type IV structures is favored when a higher ceria flux is used, while a slower deposition rate maximizes type III islands. The most striking feature of type IV structures is the frequent presence of extended line defects, which appear as

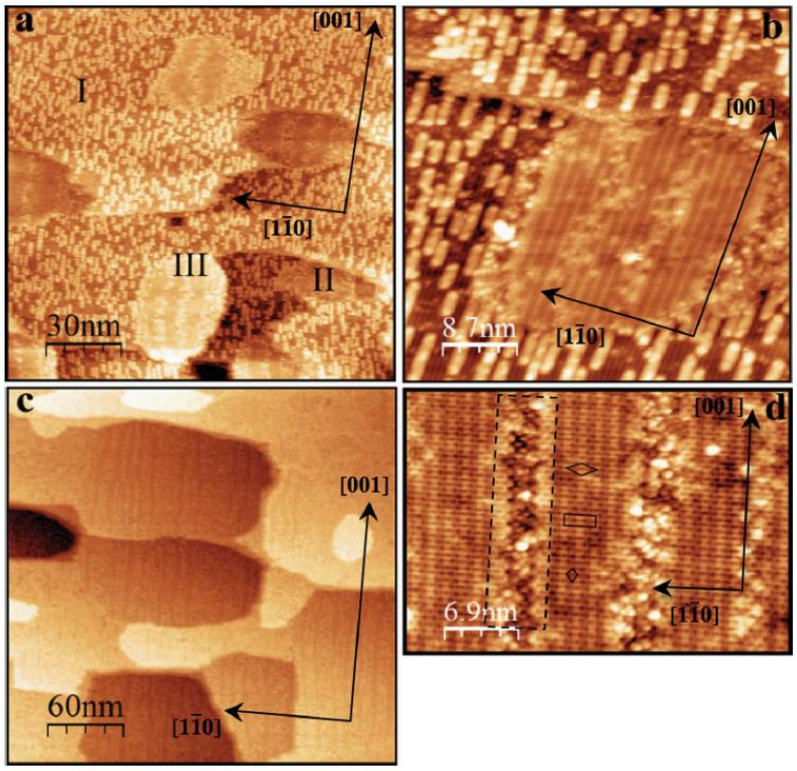

Fig. 2 STM images of (a) 0.75 MLE CeO_x; three distinct type of regions can be seen (1.1 V, 0.1 nA); (b) close up on a type III islands (1.1 V, 0.3 nA); (c) large scan area of the surface after the deposition of 0.9 MLE CeO_x (1.2 V, 0.1 nA); (d) zoom in on an island showing some troughs aligned along the [001] direction (0.46 V, 0.1 nA).

dark zig-zag lines in the STM images. They run at about 40–44° from the [001] direction crossing each other forming a 102° or 90° angle, and are parallel to one of the close packed directions of the bright dots observed within the islands (see Fig. 3b). The fact that even on small islands we can find many of these line defects suggests that these structures are strongly bound to the substrate and after the nucleation no easy rearrangement is possible. High-resolution STM images of this new phase show a rather complex motif with defects, whose appearance is strongly bias dependent as shown in the images reported in Fig. 3c. In more detail, for particular conditions of the tip and the tunneling parameters, the bright round features observed in most images can appear as small dimers arranged into a herringbone pattern (inset, Fig. 3c). On closer inspection however, a unique rectangular unit cell can be identified: from the comparison with the positions of the titania rows (see Fig. 3d) we conclude that the short side of the unit cell shows a ×2 (1.3 nm) periodicity along the [1−10] direction, while the longer one has a spacing very close to a ×6 (1.8 nm) periodicity. Also in this case the ceria nanolayer is epitaxially related to the substrate, however none of the low index surfaces of CeO_2 or Ce_2O_3 seems to have a close matching with this newly found structure. This could mean that either highly strained ceria surfaces are formed or an unknown mixed oxide comprising both cerium and titanium atoms is epitaxially stabilized by the interaction with the substrate, as observed in the case of ceria supported on anatase powders.[51,52] In addition, Ce^{3+} titanates[53] do not present any simple matching of low Miller's index surfaces with TiO_2(110). In Fig. 4 we report a phase diagram of the different ceria nanostructures observed on titania as a function of coverage and temperature, which summarizes the unprecedented structural versatility of reducible oxide-on-oxide systems. Interestingly, the interface between oxides is a treasure trove of unexpected nanostructures: simply by changing the ceria coverage while keeping constant the thermodynamic conditions is possible to move from dimers on flat TiO_2(110), to a Ti_2O_3–Ce_2O_3 mixed oxides composite rich in coordinatively unsaturated sites (the "dumbbell" structures), and then to flat long-range ordered high coverage phases, demonstrating how crucial and potentially useful can be the control at the atomic scale of the interface between two oxides. For comparison, the deposition of ceria on metal single crystals only leads to the formation of CeO_2(111) or Ce_2O_3(111) (indeed a CeO_2 monolayer with an ordered array of vacancies giving the overall Ce_2O_3 stoichiometry)[54–56] bulk-like phases according to different oxygen conditions. One notable exception is the case of Cu(111), where under particular conditions, a characteristic $CeO_{1.75}$ phase is stabilized by the metal substrate,[56] or

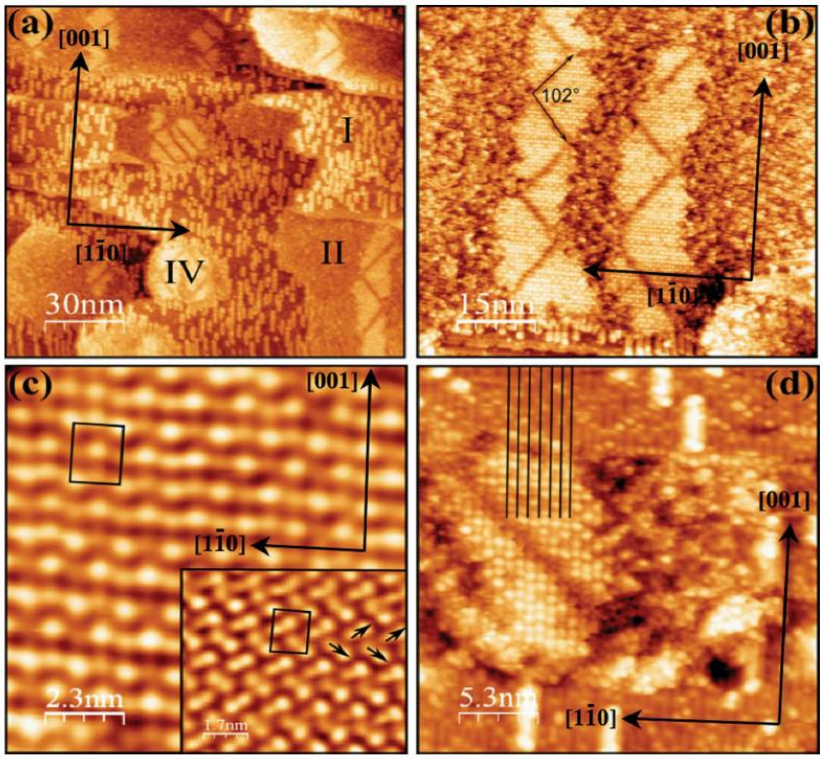

Fig. 3 1.2 MLE CeO_x on titania; (a) large scale image showing the three different regions; (b) close view of two cerium oxide islands showing the distinctive zig-zag pattern of the domain boundaries; (c) high resolution image (0.8 V, 0.12 nA) of an oxide island; inset shows the resolution of the same area obtained with a different tip condition and tunneling parameters (1.2 V, 0.7 nA); (c) STM image showing the epitaxial relationship between the oxide island and the titania substrate. The black lines are positioned on bridging oxygen rows of the TiO_2(110) surface.

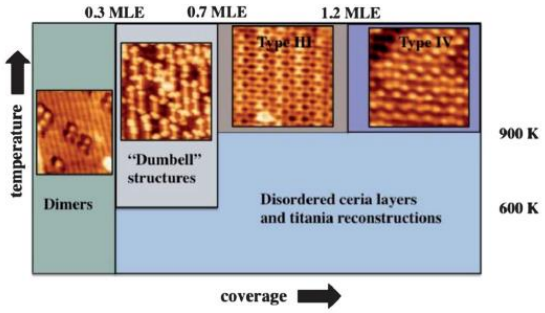

Fig. 4 Phase diagram summarizing the different ceria nanostructures that can be grown on TiO_2(110) as a function of temperature and coverage.

CeO_2(100) oriented islands can be grown by using as a template the *in situ* formed Cu_2O surface oxide.[57]

A detailed spectroscopic investigation of the ceria layer as function of coverage is reported in Fig. 5. The complex line shape of the Ce 3d (Fig. 5a) photoemission line is very sensitive to the oxidation state and in our case clearly indicates the presence of reduced ceria for every single preparation[58] despite the relatively high oxygen chemical potential used during deposition, as confirmed by the presence of the v° and v′ peaks, which correspond to $Ce3d^94f^1O2p^6$ and $Ce3d^94f^2O2p^5$ final states, respectively.[59]

The stabilization of the reduced form has been reported both theoretically[28] and experimentally,[60] at the oxide/oxide interface in the case of the vanadium oxide/ceria. In fact, under the same conditions, fully oxidized ceria layers are usually formed on metal substrates, (see ref. 61 and references therein). The stabilization of Ce^{3+} is impressive: post-annealing of the deposited film at 900 K in 10^{-5} torr oxygen does not lead to any significant change of the oxidation states of ceria. However, it can be observed that the satellite (u‴) at 915 eV, characteristic of Ce^{4+}, slightly increases as a function of coverage suggesting that only interfacial ceria in direct contact with titania surface is stabilized by the interface in low oxidation states, while thicker layers are not.[62] The ceria layer is also stable in UHV. A lack of any significant change of Ce 3d photoemission line indicates the absence of changes in the chemical state. In Fig. S2,† we plot the Ce 3d over Ti 2p ratio changes for annealing temperatures up to 980 K. A small 5% decrease of the ratio can be explained by a morphological rearrangement of the film rather than by ceria

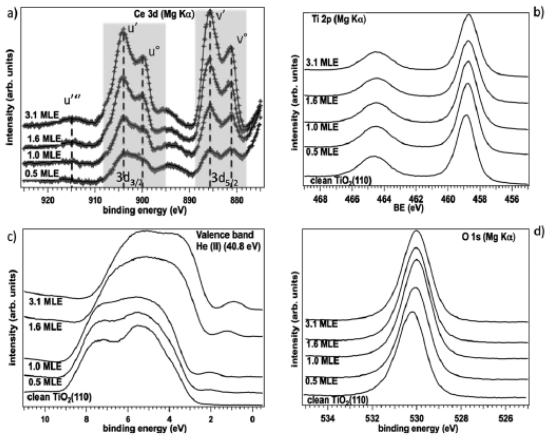

Fig. 5 Photoemission spectra as a function of ceria coverage. (a) Ce 3d spectra; (b) Ti 2p (c) valence band and (d) O 1s spectra (normal emission). The peaks in (a) have been labelled according to the standard nomenclature.[55]

diffusing into the bulk because Ce^{3+} ions (radius 1.02 Å), the species stabilized on the surface, are too large to substitute Ti^{4+} ions (radius: 0.68 Å) in rutile.

Both O 1s and Ti 2p core level peaks (Fig. 5b and c) undergo a small shift towards a lower binding energy (BE) (0.2–0.3 eV) with increasing coverage of ceria. This observation can be explained by a downward band bending of titania determined by the surface redox reaction induced by the deposition of cerium atoms. That leads to an increasing concentration of Ti^{3+} and therefore of negative charges in the near surface region. This band bending has also the effect of decreasing the work function of the whole system, which is a critical parameter determining the growth mode and properties of supported nanoparticles.[63] Similarly, in valence band spectra (Fig. 5d), the whole band shifts towards lower BE. With increasing coverage of ceria, a band connected to the defects grows in intensity and undergoes a visible energy shift, moving from 2 eV to 1 eV below the Fermi level. At low coverage, the energy position of this band is different from what is known for Ti 3d states normally lying below 1 eV.[64] We therefore suggest that the band is related mainly to Ce 4f levels. However at higher coverages (>1 MLE), it gets broader and probably overlaps with newly populated Ti 3d states, induced by the redox reaction of Ce atoms deposited on the surface.

The combination of these data clearly points to a modification of the electronic properties of the composite ceria–titania system with respect to bulk-like materials and consequently the reactivity of the CeO_x–TiO_2 system greatly differs from the simple sum of its components. As we will see in the next section, this has been verified by temperature programmed desorption experiments using methanol as a probe molecule.

3.1 Chemical properties of the CeO_x–TiO_2(110) systems: adsorption and decomposition of methanol

Upon characterizing the structure of the CeO_x–TiO_2(110) systems we have studied their reactivity towards methanol (MeOH). In Fig. 6, we show the thermal desorption spectra for a 5 L methanol dose at 230 K on the ceria layers constituted by ceria clusters on titania reconstructions (*i.e.* 0.45 MLE, see Fig. 1c and d), bottom panel, and a mixture of type II and type III nanostructures (*i.e.* 0.9 ML see Fig. 2), top panel.

Two different surface treatments for each ceria coverage were used: in one case prior to methanol exposure, 10 L of oxygen were dosed at 230 K in order to avoid the condensation of O multilayers, (solid line), while in the other no pre-treatment was used (dotted line).

The pre-dosing of oxygen has been used to investigate the role played by defects and atomic oxygen, which are the key species in determining the oxidation of methanol on oxide surfaces.[21] Even at low temperatures, molecular oxygen can dissociate on a bridging oxygen vacancy, and subsequently heal the defect with the formation of an oxygen atom adsorbed on the five fold-coordinated Ti atoms.[65] This latter species is known to be very active in the oxidation of methanol, promoting the scission of the carbon–hydrogen bond and leading to the formation of formaldehyde.[19] At low temperature, however, it is not possible to facilitate the extraction of Ti interstitials from the bulk and the formation of new surface structures.[42,66]

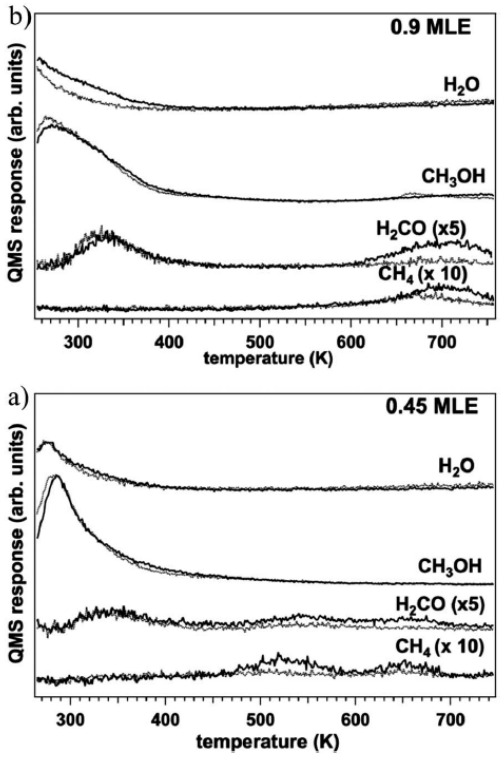

Fig. 6 Methanol desorption spectra corresponding to 0.45 MLE (a) and 0.9 MLE (b) ceria ultrathin films. Dotted lines: 5 L methanol exposure, solid lines 5 L methanol pre-dosed by 10 L oxygen at 230 K. Methanol and formaldehyde spectra have been corrected for the methanol cracking pattern.

The 0.45 MLE coverage of CeO_x (Fig. 6a), *i.e.* a film constituted by the dumbbell ceria and titania nano-composite (Fig. 2), showed three distinct temperature ranges of desorption of H_2O, CH_3OH, H_2CO and CH_4, specifically at <400 K, 450–600 K and 600–800 K. Initially, below 400 K, predominantly CH_3OH and H_2O desorb peaking at ~290 K. These two products are typical from both CeO_2 and TiO_2 sites that adsorb MeOH molecularly and dissociatively (eqn (1)–(4)). H_2O is often formed from the recombination of H and OH species that arise from the deprotonation of methanol (eqn (7) and (8)). Both MeOH and H_2O show a slowly decaying intensity up to 450 K, which fits well with the behavior observed in ceria[39] and titania[19] with a high degree of reduction.

The 330 K peak attributed to H_2CO is likely a product of conversion of the methoxy intermediate (eqn (5) and (6)). The formation of all products is insensitive to the presence of O from the pretreatment with O_2, and this shows that the sites likely healed from O and the O adatom itself are not involved in the conversion of methoxy to aldehyde in this temperature range. From 450–600 K and also 600–750 K, we see the desorption of CH_4 and H_2CO, considerably activated in the presence of O. The lower of the two temperatures is typical for formaldehyde desorption from both reduced TiO_2 and CeO_2. The origin of CH_4 is complex and requires the extraction of CH_3 (*i.e.* C–O bond breaking) from methoxy (eqn (15) and (16)). This is followed by the recombination of the CH_3 with H to desorb as CH_4. The formation of CH_4 has been previously observed on electron-beam reduced TiO_2 pre-dosed with oxygen at room temperature, and was explained by an oxygen-induced displacement of methoxy species from defects and by a competition between oxygen and methoxy for recombination with surface hydroxyls.[37] The CeO_2 surfaces were reported to form alkenes from alcohols that were greater than C2, but not from methanol, the presence of a C–C bond proving to be crucial.[40] No other products including CO, CO_2, H_2 or other CH_x products were observed.

$$CH_3O\ (a) + O\ (a) \rightarrow CH_3\ (a) + 2O\ (a) \quad (15)$$

$$CH_2O\ (a) + H\ (a) \rightarrow CH_3\ (a) + O\ (a) \quad (16)$$

$$CH_3\ (a) + H\ (a) \rightarrow CH_4\ (g) \quad (17)$$

Fig. 6b shows the desorption spectra from a surface with a higher coverage of CeO_x, 0.9 MLE. This surface is composed of mixture of type II and type III nanostructures (see Fig. 2) on TiO_2(110). This thermal desorption data has only two distinct regimes of desorption with a clear lack of the middle 450–600 K regime observed in Fig. 6a. The products observed are identical to the 0.45 MLE surface, including H_2O, CH_3OH, H_2CO and CH_4. In the low temperature regime, the desorption of H_2O appears to be enhanced when O is present from the O_2 pretreatment; H is likely to find more sites for adsorption and OH formation, and ultimately desorbs as H_2O in greater quantities than from the non O-treated surface. However, the other products appear insensitive to the O.

As in the previous case, at 330 K we can observe a clear desorption peak in the H_2CO desorption spectrum. This feature, indicative of an oxidative dehydrogenation path of methanol, is therefore clearly related to the presence of the ceria–titania nanocomposite, as confirmed by the fact that the formaldehyde yield (as determined by the ratio of the methanol and formaldehyde desorption peaks) increases with the amount of ceria deposited on the surface, is not affected by oxygen pre-dosing. This indicates that the reactivity of the ceria–titania nano-composite derives from some defects like uncoordinated sites, or special properties of the ceria–titania interfaces, and not an extrinsic phenomenon like in titania, where the low temperature (250 K) dehydrogenation of MeOH is active only on reduced surfaces pre-exposed at 150 K to molecular oxygen.[19]

In the high temperature range (600–750 K), we notice a significant difference in two products of H_2CO and CH_4 with respect to the lower coverage. The formation of H_2CO and CH_4 appears to be in greater quantity and is shifted to higher temperature. This high temperature reaction path is sensitively dependent on the presence of O, and is totally suppressed if the surface is not pre-exposed to O_2. Since the decomposition of MeOH to H_2CO and CH_4 is also active on reduced TiO_2(110),[37] we cannot exclude that the deposition of ceria induces a significant reduction of the substrate, which then becomes chemically active towards dehydrogenation (eqn (5)) and dehydration (eqn (15)–(17)) reactions. As in the case of the lower coverage, no other products such as CO, CO_2, H_2 or CH_x products were detected.

The TPD studies using methanol as a probe molecule indicate that the ceria–titania nanostructures possess a very special chemical activity for the selective, partial dehydrogenation of MeOH to H_2CO at an extremely mild temperature (330 K). This chemical reactivity identifies a substrate that mimics neither CeO_2(111) nor TiO_2(110) independently. A similar reactivity was observed in the case of vanadia oligomers on ceria (370 K),[28] and vanadia tetramers on TiO_2(110),[67] and was connected to the stabilization driven by the substrate of the reduced vanadia species produced as a consequence of MeOH oxidation. In particular, DFT calculations by Pirovano *et al.*[28] indicate that the dehydrogenation pathway is favored because instead of forming a $V^{4+}(d^1)$–$Ce^{4+}(4f^0)$ couple, the electron is transferred to the substrate forming a $V^{5+}(d^0)$–$Ce^{3+}(4f^1)$ compound. Based on previous DFT calculations and the stability of the ceria–titania system,[12] an analogous phenomenon involving the reduction of the substrate could be involved in the present case: electrons possibly populating the 6s and 5d band of ceria would be efficiently transferred to the Ti 3d band. However, we cannot exclude the possibility that the reaction path is controlled by the presence of active sites, likely as coordinatively unsaturated oxygen atoms responsible for the proton extraction from methoxy,[68] but in this case one would expect a stronger response to the reaction from oxygen pre-dosing.

Our results therefore together with other works investigating other "reducible oxides-on reducible oxides" help to substantiate a new paradigm in nanocatalysis, which identifies the common origin of the high chemical activity of these systems in the possibility of easily exchanging electrons in a reversible manner through defect states that act as a localized

electron reservoir. As demonstrated by the theoretical calculations,[12,13,28,67] in all these systems the reduced form of the oxidation catalysts undergoes a strong stabilization thanks to the electron transfer to the substrate, which in light of the Brønsted–Evans–Polyani principle (*i.e.* the activation energy is proportional to the enthalpy of reaction),[69] explains why these systems are so active at low temperatures. With this consideration any redox reaction can to be catalytically activated by reducible oxides on reducible oxides.

The reported highly selective dehydration path is quite interesting for developing new model systems and advanced catalysts for methanol chemistry.[70] Very recently on TiO_2(110), it has been demonstrated that starting from methanol it is possible to produce more complex molecules exploiting the photoinduced cross-coupling of formaldehyde with methoxy species.[24,71] The ceria–titania system is expected to have a great impact on this nascent research topic, since it can provide both reactants on the surface at relatively low temperatures, and furthermore has been demonstrated to possess improved photocatalytic performances with respect to the pure oxides.[14,72]

4 Conclusions

The growth of CeO_x overlayers was studied by STM and photoemission spectroscopy observing distinct oxide nanostructures as a function of ceria coverage. It has been demonstrated that the deposition of CeO_x strongly affects the titania morphology leading to the formation of extensive oxygen reconstructions and eventually of peculiar dumbbell nanostructures made by Ti_2O_3 strands decorated by Ce_2O_3. At higher ceria coverages, two long range ordered oxide phases, both characterized by ceria in exclusively reduced form (Ce^{3+}), have been identified. The chemical activity of these new nanostructures has been investigated using methanol as a probe molecule. The results indicate a specific reactivity favoring oxidative dehydrogenation at low temperature, which cannot be simply explained as the sum of the reactivity of ceria and titania.

In conclusion, the present work presented a comprehensive view on the several different ceria phases grown on TiO_2(110). Similarly to the case of oxide deposited on metals,[73] we have observed new nanostructures that have no counterpart in the bulk materials. This is the first time this rich epitaxial polymorphism is seen for oxide-on-oxide systems where so far only simple epitaxy (*e.g.* NiO/MgO cubic on cubic epitaxy[74]) or nanoclusters resembling gas phase structures (VO_x–SiO_2,[75] WO_3–TiO_2(110)[61] or VO_x–CeO_2(111)[28,47]) were observed. In contrast, the CeO_x–TiO_2(110) system demonstrates that at the ultrathin limit of oxide-on-oxide systems, there is an untapped range of oxides stoichiometries with great potential for new structures and new functionalities, as suggested by the strong stabilisation of Ce^{3+} species and the highly selective chemical activity observed towards methanol oxidative dehydrogenation in this study.

Acknowledgements

The research carried out at Brookhaven National Laboratory was supported by the US Department of Energy, Chemical Sciences Division (DE-AC02-98CH10886). The work performed at the University of Padova has been supported by the Italian MIUR through the FIRB Project RBAP115AYN 'Oxides at the nanoscale: multifunctionality and applications'.

Notes and references

1 Q. Fu, W.-X. Li, Y. Yao, H. Liu, H.-Y. Su, D. Ma, X.-K. Gu, L. Chen, Z. Wang, H. Zhang, *et al.*, *Science*, 2010, **328**, 1141.
2 X. Nie, H. Qian, Q. Ge, H. Xu and R. Jin, *ACS Nano*, 2012, **25**, 6014.
3 J. A. Rodriguez, S. Ma, P. Liu, J. Hrbek, J. Evans and M. Pérez, *Science*, 2007, **318**, 1757.
4 G. Zhou, L. Barrio, S. Agnoli, S. D. Senanayake, J. Evans, M. Estrella, A. Kubacka, J. C. Hanson, A. Martínez-Arias, M. Fernández-García, *et al.*, *Angew. Chem., Int. Ed.*, 2010, **49**, 9680.
5 M. Cargnello, J. J. Delgado Jaén, J. C. Hernández Garrido, K. Bakhmutsky, T. Montini, J. J. Calvino Gámez, R. J. Gorte and P. Fornasiero, *Science*, 2012, **337**, 713.
6 S. Colussi, A. Gayen, M. Farnesi Camellone, M. Boaro, J. Llorca, S. Fabris and A. Trovarelli, *Angew. Chem., Int. Ed.*, 2009, **48**, 8481.
7 A. Trovarelli, *Catalysis by Ceria and Related Materials*, Imperial College Press, London, 2002.
8 A. L. Linsebigler, G. Lu and J. T. Yates, *Chem. Rev.*, 1995, **95**, 735.
9 X. Han, L. Li and C. Wang, *Nanoscale*, 2013, **5**, 7193–7196.
10 A. S. Karakoti, J. E. S. King, A. Vincent and S. Seal, *Appl. Catal., A*, 2010, **388**, 262.
11 L. Adijanto, D. A. Bennett, C. Chen, A. S. Yu, M. Cargnello, P. Fornasiero, R. J. Gorte and J. M. Vohs, *Nano Lett.*, 2013, **13**, 2252.
12 J. Graciani, J. J. Plata, J. F. Sanz, P. Liu and J. A. Rodriguez, *J. Chem. Phys.*, 2010, **132**, 104703.
13 J. B. Park, J. Graciani, J. Evans, D. Stacchiola, S. Ma, P. Liu, A. Nambu, J. F. Sanz, J. Hrbek and J. A. Rodriguez, *Proc. Natl. Acad. Sci. U. S. A.*, 2009, **106**, 4975.
14 Y. Zhang, A. H. Yuwono, J. Wang and J. Li, *J. Phys. Chem. C*, 2009, **113**, 21406.
15 L. Zhang, D. Zhang, J. Zhang, S. Cai, C. Fang, L. Huang, H. Li, R. Gao and L. Shi, *Nanoscale*, 2013, **5**, 9821.
16 H. Zhu, Z. Qin, W. Shan, W. Shen and J. Wang, *Catal. Today*, 2007, **126**, 382.
17 I. Gonzalez, R. Navarro, M. Alvarezgalvan, F. Rosa and J. Fierro, *Catal. Commun.*, 2008, **9**, 1759.
18 G. A. Olah, *Angew. Chem., Int. Ed.*, 2005, **44**, 2636.
19 M. A. Henderson, S. Otero-Tapia and M. E. Castro, *Faraday Discuss.*, 1999, **114**, 313.
20 U. Diebold, *Surf. Sci. Rep.*, 2003, **48**, 53, and references therein.
21 C. L. Pang, R. Lindsay and G. Thornton, *Chem. Soc. Rev.*, 2008, **37**, 2328.
22 C. Zhou, Z. Ren, S. Tan, Z. Ma, X. Mao, D. Dai, H. Fan, X. Yang, J. LaRue, R. Cooper, *et al.*, *Chem. Sci.*, 2010, **1**, 575.

23 C. Zhou, Z. Ma, Z. Ren, X. Mao, D. Dai and X. Yang, *Chem. Sci.*, 2011, **2**, 1980.
24 K. R. Phillips, S. C. Jensen, M. Baron, S.-C. Li and C. M. Friend, *J. Am. Chem. Soc.*, 2013, **135**, 574.
25 U. Martinez, L. B. Vilhelmsen, H. H. Kristoffersen, J. Stausholm-Møller and B. Hammer, *Phys. Rev. B: Condens. Matter Mater. Phys.*, 2011, **84**, 205434.
26 Q. Guo, C. Xu, Z. Ren, W. Yang, Z. Ma, D. Dai, H. Fan, T. K. Minton and X. Yang, *J. Am. Chem. Soc.*, 2012, **134**, 13366.
27 A. Siokou and R. M. Nix, *J. Phys. Chem. B*, 1999, **103**, 6984.
28 M. V. Ganduglia-Pirovano, C. Popa, J. Sauer, H. Abbott, A. Uhl, M. Baron, D. Stacchiola, O. Bondarchuk, S. Shaikhutdinov and H.-J. Freund, *J. Am. Chem. Soc.*, 2010, **132**, 2345.
29 T. Feng and J. Vohs, *J. Catal.*, 2004, **221**, 619.
30 W. C. Vining, J. Strunk and A. T. Bell, *J. Catal.*, 2012, **285**, 160.
31 A. P. Vieira Soaresa, M. Farinha Portela and A. Kiennemann, *Catal. Rev. Sci. Eng.*, 2005, **47**, 125.
32 I. Baldychev, J. M. Vohs and R. J. Gorte, *Appl. Catal., A*, 2011, **391**, 86.
33 S. Wang, L. Zhao, W. Wang, Y. Zhao, G. Zhang, X. Ma and J. Gong, *Nanoscale*, 2013, **5**, 5582.
34 H. Y. Kim, H. M. Lee, R. G. S. Pala and H. Metiu, *J. Phys. Chem. C*, 2009, **2**, 16083.
35 K. Routray, W. Zhou, C. J. Kiely and I. E. Wachs, *ACS Catal.*, 2011, **1**, 54.
36 J. E. Molinari, L. Nakka, T. Kim and I. E. Wachs, *ACS Catal.*, 2011, **1**, 1536.
37 E. Farfan-Arribas and R. J. Madix, *Surf. Sci.*, 2003, **544**, 241.
38 V. Matolín, J. Libra, M. Škoda, N. Tsud, K. C. Prince and T. Skála, *Surf. Sci.*, 2009, **603**, 1087.
39 D. R. Mullins, M. D. Robbins and J. Zhou, *Surf. Sci.*, 2006, **600**, 1547.
40 D. R. Mullins, S. D. Senanayake and T.-L. Chen, *J. Phys. Chem. C*, 2010, **114**, 17112.
41 V. Matolín, I. Matolínová, F. Dvořák, V. Johánek, J. Mysliveček, K. C. Prince, T. Skála, O. Stetsovych, N. Tsud, M. Václavů, *et al.*, *Catal. Today*, 2012, **181**, 124.
42 M. Li, W. Hebenstreit, L. Gross, U. Diebold, M. A. Henderson, D. R. Jennison, P. A. Schultz and M. P. Sears, *Surf. Sci.*, 1999, **437**, 173.
43 J. B. Park, J. Graciani, J. Evans, D. Stacchiola, S. D. Senanayake, L. Barrio, P. Liu, J. Fdez Sanz, J. Hrbek and J. A. Rodriguez, *J. Am. Chem. Soc.*, 2010, **132**, 356.
44 Y. Sakai and S. Ehara, *Jpn. J. Appl. Phys.*, 2001, **40**, L773.
45 S. Agnoli, C. Castellarin Cudia, M. Sambi, S. Surnev, M. G. Ramsey, G. Granozzi and F. P. Netzer, *Surf. Sci.*, 2003, **546**, 117.
46 S. Agnoli, M. Sambi, G. Granozzi, C. Castellarin Cudia, S. Surnev and F. P. Netzer, *Surf. Sci.*, 2004, **562**, 150.
47 H. L. Abbott, A. Uhl, M. Baron, Y. Lei, R. J. Meyer, D. J. Stacchiola, O. Bondarchuk, S. Shaikhutdinov and H. J. Freund, *J. Catal.*, 2010, **272**, 82.
48 C. L. Pang, S. A. Haycock, H. Raza, P. W. Murray, G. Thornton, O. Guelseren, R. James and D. W. Bullett, *Phys. Rev. B: Condens. Matter Mater. Phys.*, 1998, **58**, 1586.
49 M. Blanco-Rey, J. Abad, C. Rogero, J. Mendez, M. Lopez, J. Martin-Gago and P. Andres, *Phys. Rev. Lett.*, 2006, **96**, 055502.
50 M. Li, W. Hebenstreit and U. Diebold, *Phys. Rev. B: Condens. Matter Mater. Phys.*, 2000, **61**, 4926.
51 C. Gionco, M. C. Paganini, S. Agnoli, A. E. Reeder and E. Giamello, *J. Mater. Chem. A*, 2013, **1**, 10918.
52 A. C. Johnston-Peck, S. D. Senanayake, J. J. Plata, S. Kundu, W. Xu, L. Barrio, J. Graciani, J. F. Sanz, R. M. Navarro, J. L. G. Fierro, E. A. Stach and J. A. Rodriguez, *J. Phys. Chem. C*, 2013, **117**, 14463.
53 A. Preuss and R. Gruehn, *J. Solid State Chem.*, 1994, **110**, 363.
54 D. C. Grinter, R. Ithnin, C. L. Pang and G. Thornton, *J. Phys. Chem. C*, 2010, **114**, 17036.
55 S. Eck, C. Castellarin-Cudia, S. Surnev, K. C. Prince, M. G. Ramsey and F. P. Netzer, *Surf. Sci.*, 2003, **536**, 166.
56 L. Szabová, O. Stetsovych, F. Dvořák, M. F. Camellone, S. Fabris, J. Mysliveček and V. Matolín, *J. Phys. Chem. C*, 2012, **116**, 6677.
57 F. Yang, Y. M. Choi, S. Agnoli, P. Liu, D. Stacchiola, J. Hrbek and J. A. Rodriguez, *J. Phys. Chem. C*, 2011, **115**, 23062.
58 W. Xiao, Q. Guo and E. G. Wang, *Chem. Phys. Lett.*, 2003, **368**, 527.
59 E. Bêche, P. Charvin, D. Perarnau, S. Abanades and G. Flamant, *Surf. Interface Anal.*, 2008, **40**, 264.
60 G. S. Wong and J. M. Vohs, *Surf. Sci.*, 2002, **498**, 266.
61 S. D. Senanayake, D. Stacchiola and J. A. Rodriguez, *Acc. Chem. Res.*, 2013, **46**, 1702.
62 V. Stetsovych, F. Pagliuca, F. Dvořák, T. Duchoň, M. Vorokhta, M. Aulická, J. Lachnitt, S. Schernich, I. Matolínová, K. Veltruská, T. Skála, D. Mazur, J. Mysliveček, J. Libuda and V. Matolín, *J. Phys. Chem. Lett.*, 2013, **4**, 866.
63 Q. Fu and T. Wagner, *Surf. Sci. Rep.*, 2007, **62**, 431.
64 Z. Zhang, S. Jeng and V. Henrich, *Phys. Rev. B: Condens. Matter Mater. Phys.*, 1991, **43**, 12004.
65 S. Wendt, R. Schaub, J. Matthiesen, E. K. Vestergaard, E. Wahlström, M. D. Rasmussen, P. Thostrup, L. M. Molina, E. Lægsgaard, I. Stensgaard, *et al.*, *Surf. Sci.*, 2005, **598**, 226.
66 W. Epling, C. Peden, M. Henderson and U. Diebold, *Surf. Sci.*, 1998, **413**, 333.
67 L. Artiglia, S. Agnoli, A. Vittadini, A. Verdini, A. Cossaro, L. Floreano and G. Granozzi, *J. Am. Chem. Soc.*, 2013, **135**, 17331.
68 J. Döbler, M. Pritzsche and J. Sauer, *J. Am. Chem. Soc.*, 2005, **127**, 10861.
69 J. T. Bligaard, J. K. Nørskov, S. Dahl, J. Matthiesen, C. H. Christensen and J. Sehested, *J. Catal.*, 2004, **224**, 206.
70 A. Wittstock, V. Zielasek, J. Biener, C. M. Friend and M. Bäumer, *Science*, 2010, **327**, 319.

71 Q. Yuan, Z. Wu, Y. Jin, L. Xu, F. Xiong, Y. Ma and W. Huang, *J. Am. Chem. Soc.*, 2013, **135**, 5212.
72 S. Kundu, J. Ciston, S. D. Senanyake, D. A. Arena, E. Fujita, D. Stacchiola, L. Barrio, R. M. Navarro, J. L. G. Fierro and J. A. Rodriguez, *J. Phys. Chem. C*, 2012, **116**, 2.
73 S. Surnev, A. Fortunelli and F. P. Netzer, *Chem. Rev.*, 2013, **113**, 4314–4372.
74 Q. Guo, C. Xu and D. W. Goodman, *Langmuir*, 1998, **14**, 1371–1374.
75 T. K. Todorova, J. Döbler, M. Sierka and J. Sauer, *J. Phys. Chem. C*, 2009, **113**(19), 8336–8342.
76 I. Horcas, R. Fernández, J. M. Gómez-Rodríguez, J. Colchero, J. Gómez-Herrero and M. Baro, *Rev. Sci. Instrum.*, 2007, **78**, 013705.

5.3 TPD STUDIES OF ETHANOL ON $CeO_x/TiO_2(110)$

The data reported in this paragraph will complete the TPD studies on the adsorption of methanol on $CeO_x/TiO_2(110)$ system described in the previous paragraph and published on Nanoscale.

The alcohol was dosed on cerium oxide overlayers of different thickness, exposed to O_2 in order to create a more oxidized surface. This was done with the aim of studying the effects of oxygen pre-dosing on the reactivity of ethanol towards the system. The choice of ethanol as a probe molecule stems from the importance of alcohol decomposition in fuel cell technology[101]. Recently, ethanol is being considered as a potential fuel of the future to be used either in substitution to conventional fossil fuels or as a source of H_2 for fuel cells[102] thereby dramatically reducing green-house gasses such as carbon dioxide. Ethanol is currently produced in two major routes: fermentation of sugars derived from biomass resources and hydration of ethylene where the first route contributes to almost the total global production. However, the aqueous ethanol produced via fermentation must be distilled to find use as gasoline additive. This is an energy-intensive process and contributes to over 50% to the total cost of ethanol production[103]. Recently Deluga et al.[104] have studied a way to avoid this distillation step by converting directly in a reactor via autothermal reforming where the water-gas-shift reaction was brought to completion by splitting H_2O in H_2 and O_2. Thus the entire process completes the carbon cycle adding little or no net carbon into the atmosphere. A major issue the group discovered was that the temperatures involved were still high, ca. 973 K, for the initial step and ca. 673 K for the WGS reaction, hence further research is needed to make this process possible at lower temperature and to enhance its portability. Furthermore, the use of ethanol as a H_2 source offers additional advantages such as safety and ease of handling, storage, transportation and an easier catalytic reformation compared to hydrocarbon fuels. The nature of the support also plays an important role in the catalytic performance. Acidic supports such as Al_2O_3 favor the dehydration of ethanol to produce ethylene where its presence hinders the overall H_2 production reaction by inducing carbon production and thus causing “coking” of the catalysts[102]. Although over basic supports carbon deposition can be minimized these supports also favor condensation of alcohols to higher oxygenates. Interestingly[103] supports such as CeO_2, ZrO_2, V_2O_5, TiO_2 and CeO_2-ZrO_2 mixed oxides have been found to be highly favorable for ethanol reforming and water-gas-shift reactions to produce high yields of H_2. Below[105] (Figure 5.19) is depicted a table of reaction pathways of steam reforming:

Reaction pathways of ethanol steam reforming

Reaction	Equation	Remarks
Sufficient steam supply	$C_2H_5OH + 3H_2O \rightarrow 2CO_2 + 6H_2$	Ideal pathway, the highest hydrogen production
Insufficient steam supply	$C_2H_5OH + H_2O \rightarrow 2CO + 4H_2$	Undesirable products, lower hydrogen production
	$C_2H_5OH + 2H_2 \rightarrow 2CH_4 + H_2O$	
Dehydrogenation	$C_2H_5OH \rightarrow C_2H_4O + H_2$	Reaction pathways for hydrogen production in practice
Acetaldehyde decomposition	$C_2H_4O \rightarrow CH_4 + CO$	
Acetaldehyde steam reforming	$C_2H_4O + H_2O \rightarrow 3H_2 + 2CO$	
Dehydration	$C_2H_5OH \rightarrow C_2H_4 + H_2O$	Undesired pathway, main source of coke formation
Coke formation	$C_2H_4 \rightarrow$ polymeric deposits (coke)	
Decomposition	$C_2H_5OH \rightarrow CO + CH_4 + H_2$	Coke formation, low hydrogen production
	$2C_2H_5OH \rightarrow C_3H_6O + CO + 3H_2$	
	$C_2H_5OH \rightarrow 0.5CO_2 + 1.5CH_4$	
Reaction of decomposition products		
Methanation	$CO + 3H_2 \rightarrow CH_4 + H_2O$	
	$CO_2 + 4H_2 \rightarrow CH_4 + 2H_2O$	
Methane decomposition	$CH_4 \rightarrow 2H_2 + C$	
Boudouard reaction	$2CO \rightarrow CO_2 + C$	
Water gas shift reaction (WGSR)	$CO + H_2O \rightarrow CO_2 + H_2$	Reduce coke formation, enhance hydrogen production

Figure 5.19: depicting desired and undesired reaction pathways for ethanol steam reforming.

An important aspect highlighted by the Vaidya et al.[106] for a CuO/CeO_2 catalyst is that ethylene formation can be prevented by working at such a low temperature that the production of methane becomes viable thus opening the path to the WGS reaction. Again, the probing of a CeO_2-TiO_2 system of different thicknesses of ceria towards ethanol adsorption/desorption would help us determine whether the support is viable for alcohol dehydrogenation/dehydration and at what cerium content.

5.3.1 Ethanol on TiO_2(110)

We will first present TPD data from the exposure of ethanol on clean stoichiometric and reduced TiO_2(110). The choice of investigating ethanol desorption from these two substrates stems from the fact that when cerium deposits onto rutile, three Ti^{4+} cations undergo reduction to Ti^{3+}. This reduction changes the chemical reactivity with respect to a stoichiometric surface and because we want to understand the properties of the CeO_x/TiO_2(110) system we need to collect data from both surfaces.

The substrate was cleaned via sputtering treatments of 2.0 keV with an Ar^+ flux of about $5 \cdot 10^{-7}$ mbar at an angle of 45˚ respect to surface normal for 20 minutes. This was followed by an annealing in UHV for 5 minutes at 923 K which helped to form a stoichiometric surface, via diffusion of bulk O^{2-}, and wide (110) terraces as well as, through the introduction of O vacancies, good sample conductivity. Various cleaning cycles were undertaken until the surface was free from contamination, chiefly Carbon and Potassium, and a well-defined LEED pattern was visible. Stoichiometric titania was still yellow colored[107] thus with a low number of bulk defects and stoichiometric surface after annealing. Reduced titania was instead formed after numerous cycles of annealing and sputtering until the achievement of a dark blue colored crystal. Both substrates were pre-treated with 10L of O_2 dosed at 230 K in order to heal any surface vacancies and to form O adatoms absorbed on Ti 5-fold coordinated (Ti_{5c}) sites[108-110]. As with methanol, the pre-dosing of oxygen helped to observe the role of defects and atomic oxygen in the oxidation of ethanol. Afterwards, 5L of ethanol were dosed onto the surface at 230 K and the TPD ramp was run at a

rate of 2 K/s. The masses 31 (ethanol), 29 (acetaldehyde), 28 (CO), 27 (ethylene), 18 (water) were monitored. Furthermore, to better observe the components the TPD traces were plotted considering their abundance and instrument relative sensitivity and then subtracting the main ethanol trace. For example, ethanol fragments into masses 31, 29 and 27, however neither acetaldehyde nor ethylene share mass 31. Thus by first normalizing the mass 31 trace to each of these components and then subtracting it from them one can observe a resulting trace connected to just a single chemical species.

A stoichiometric TiO_2(110) surface consists of two types of Ti atoms. Along the [001] direction rows of six-fold coordinated Ti^{4+} ions alternate with five-fold coordinated Ti^{4+} ions (Ti_{5c}) with a dangling bond perpendicular to the surface[107]. There are also two types of oxygen atoms as well: the ones within the surface plane that are three-fold coordinated, as in the bulk, and those perpendicular to the plane, also known as bridging oxygen (O_{br}). These are missing a bond to a Ti atom and thus are only two-fold coordinated. Due to their coordinative under-saturation these bridging oxygen atoms are thought to be removed relatively easily by thermal annealing. Thus, in the case of reduced TiO_2(110) bridging oxygen vacancies are formed where for every missing O-bridge two Ti^{3+} cations are fomed[111].

Below, (Figure 5.20) we report the TPD scans for the stoichiometric clean TiO_2(110) by first reporting the measurement without oxygen pre-dosage. Figure 5.20 (top) reproduces the literature results quite well: the main ethanol peak desorbs at 310 K and virtually no acetaldehyde was seen to desorb and only a minor quantity of ethylene was observed at 650 K. As pointed out by Gamble et al.[112] and Farfan-Arribas et al.[113] ethanol, like methanol, molecularly adsorbs TiO_2(110) and can dissociate forming surface ethoxys and hydroxyls. The ethoxys are either located on Ti_{5c} sites or on bridging oxygen vacancy (O_{br}) sites. The former favor a low temperature desorption, centered around 340 K according to these authors (however, much depends on sample preparation) whereas the latter a higher desorption temperature (centered around 600K for Farfan-Arribas et al.). Thus, the main peak at 310 K is due to molecular desorption of ethanol. The H_2O peak centered at 270 K derives from the water absorbed from the background as pointed out by Henderson et al.[114] and has no influence on the alcohol's reactivity towards the surface. However, a precise determination of minor desorption peaks of water and hydrogen was not possible due to the high back–ground pressure of water in our case. In the case of the pre-dosed substrate, ethanol showed two peaks, one at 310 K and a second one 640 K. The latter peak is due to the disproportionation of stranded ethoxys. This is due to the fact that O adatoms readily dissociate ethanol leaving OH groups located on Ti_{5c} sites that recombine as water at low temperature[114]. In fact, broad high temperature peaks, centered at 650 K were observed for acetaldehyde and ethylene.

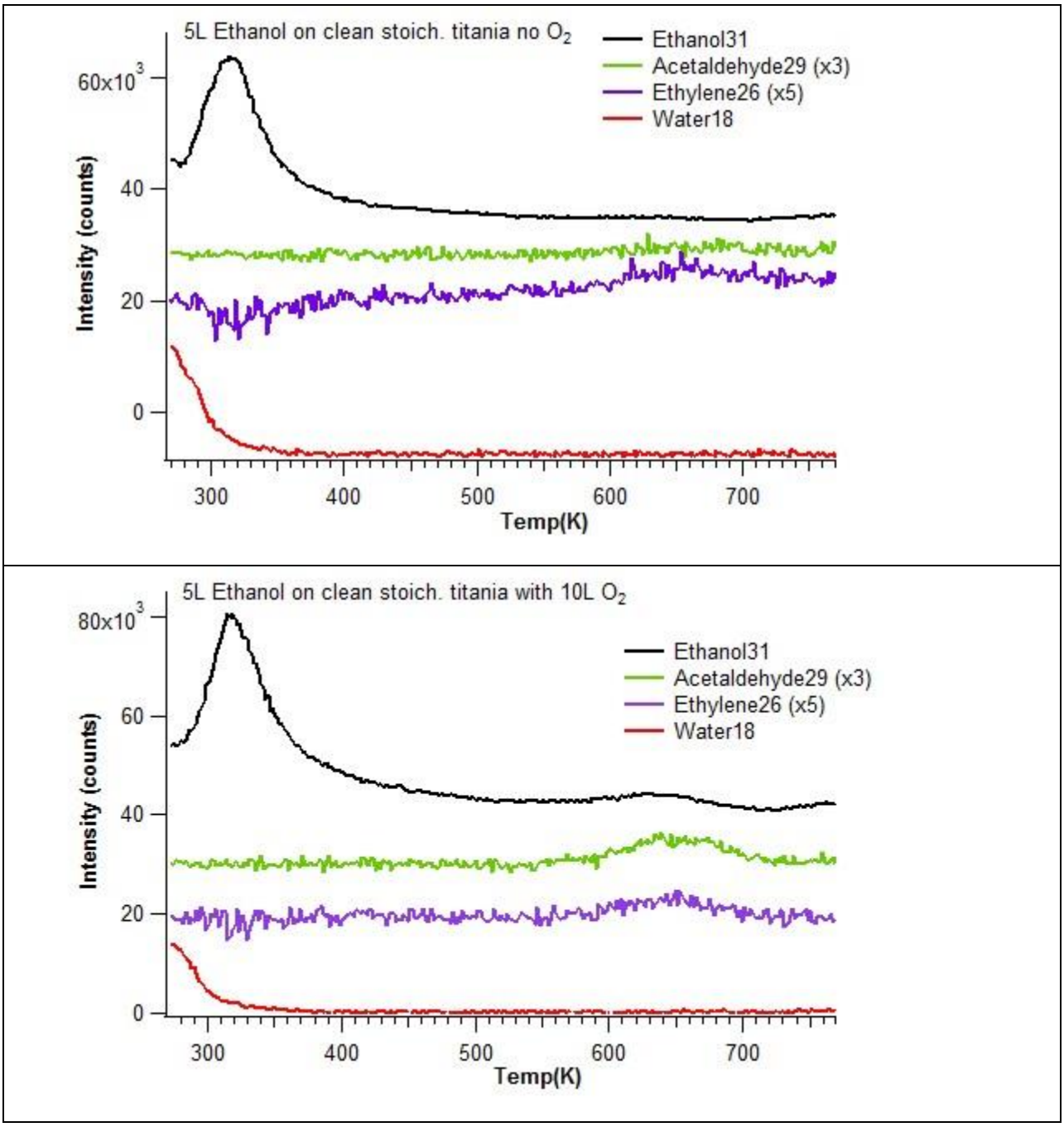

Figure 5.20: TPD scans of 5L of ethanol on stoichiometric TiO_2(110).

Below (Figure 5.21) we report the data of a 3L ethanol exposure on a reduced substrate. For the untreated surface, the main desorption peak of ethanol was observed at 320 K and no other peak was observed afterwards. No acetaldehyde was observed, although ethylene was seen to desorb from the surface at 580 K. This was expected. Gamble et al.[112] and Farfan-Arribas et al.[113] have obtained similar results, albeit a different onset temperature of ethylene desorption. The first author reports ethylene

desorption at 650 K, for the stoichiometric surface, and at 550 for the reduced surface. The second author reports ethylene desorption at 630 K for the stoichiometric titania and, with the gradual reduction of the surface, the peak shifts down to 517 K. Anyway, both authors assign this reaction channel to the presence of bridging oxygen vacancies as only ethanol dehydration to ethylene can refill them.

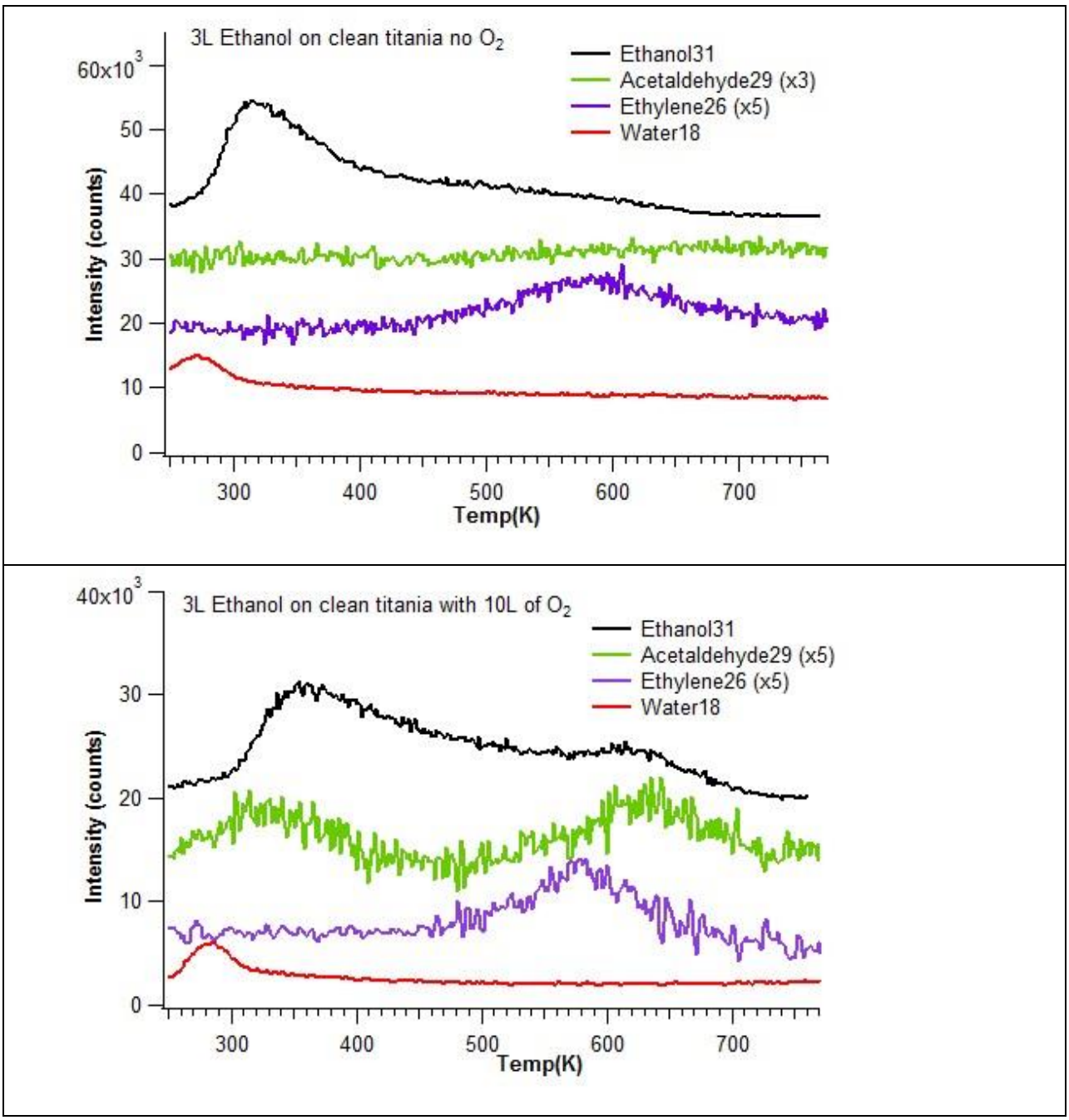

Figure 5.21: TPD scans of 5L of ethanol on reduced TiO_2(110). Upper graph refers to the as prepared surface, lower part to the oxygen pre-exposed surface.

In the case of a reduced substrate, pre-exposed to 10L of O_2 a markedly different behavior was observed. This requires some explaining.

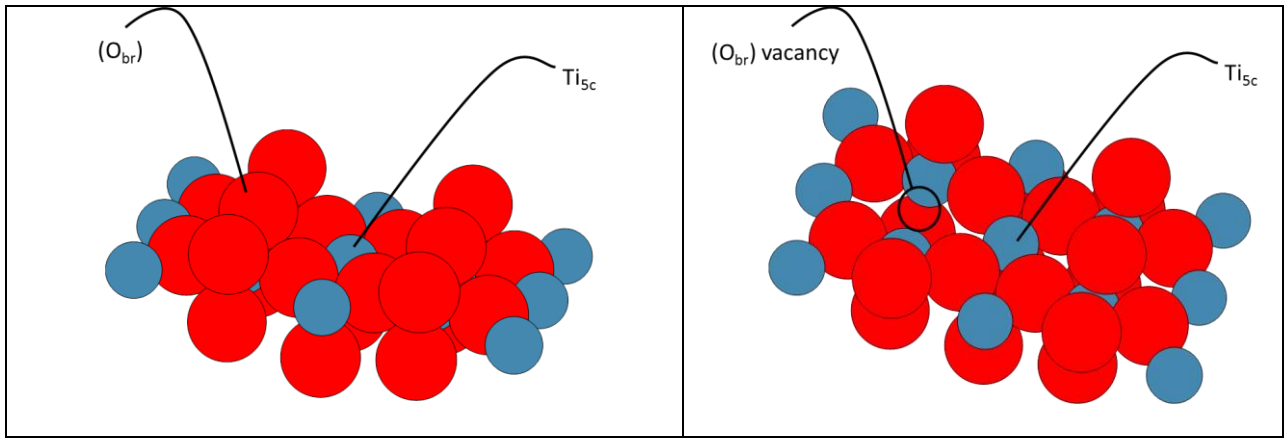

Figure 5.22: Showing O_{br} sites, Ti_{5c} sites and O_{br} vacancies.

Wendt et al.[115] verified that on reduced TiO_2(110) (Figure 5.22) oxygen dosed at 300 K did not heal all the bridging oxygen vacancies but, rather, partially formed oxygen adatoms on top of the Ti_{5c} sites. Thus when oxygen dissociates on the surface two paths occur: in the first one, oxygen splits and heals bridging oxygen (O_{br}) vacancy and occupies a Ti_{5c} site (O_{ot}). The second path, as pointed out by the authors, resides in the possibility of electron donation by Ti interstitials which results into oxygen splitting and occupation of two nearest neighbor Ti_{5c} sites (O_{ot}) instead of vacancies (Figure 5.23).

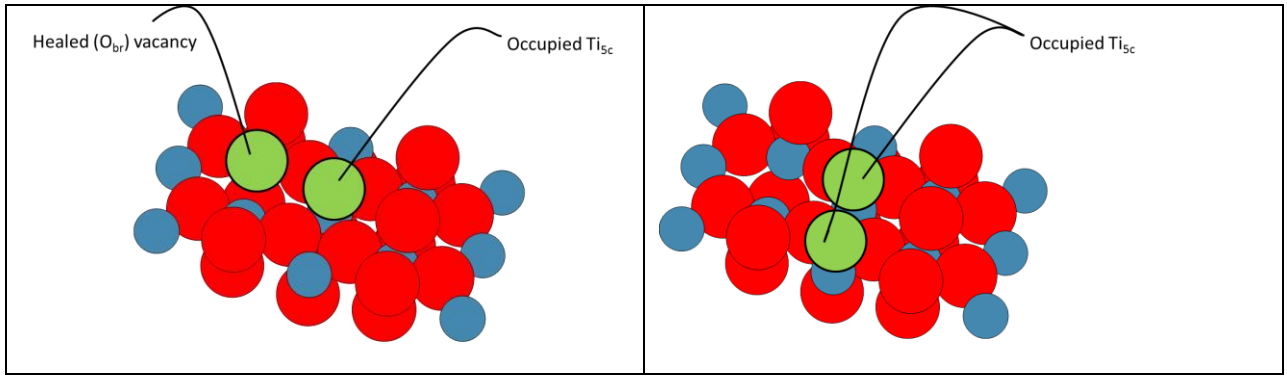

Figure 5.23: Dissociation at 300K of O_2 (light green) on TiO_2(110).

Thus, when ethanol approaches the surface various paths can occur: dissociation onto (O_{br}) vacancy sites, dissociation onto (O_{ot}) sites and molecular absorption/dissociation onto Ti_{5c} sites.

In the first case, an ethoxy is bound onto the (O_{br}) vacancy and a hydroxyl on a bridging oxygen. The bound hydrogen may: recombine with ethoxy to form ethanol, hop from row to row of bridging oxygen atoms, via mobile bound ethoxys on Ti_{5c} sites, and recombine into ethanol or combine into H_2O with terminal OH groups on Ti_{5c} sites. If left stranded, the ethoxy may desorb as ethylene thereby replenishing the (O_{br}) vacancy or disproportionate as acetaldehyde.

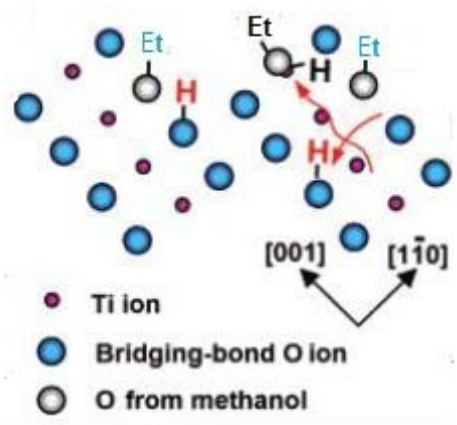

Figure 5.24: Dissociation of ethanol on TiO_2(110).

In the second case, ethanol readily dissociates into terminal OH, located on a Ti_{5c} site, and ethoxy. The proton from the alcohol will form a terminal OH group which can, at low temperature, desorb as water by combining with hydrogen bound on a bridging oxygen. The bound ethoxy which will presumably be bound on a (O_{br}) vacancy will either disproportionate to acetaldehyde or desorb as ethylene by filling the (O_{br}) vacancy.

$2\ CH_3\text{-}CH_2O \rightarrow CH_3\text{-}CH_2OH + CH_3\text{-}CHO$

$CH_3\text{-}CH_2O \rightarrow CH_2{=}CH_2 + O_{br}\text{-}H$

Finally, in the last case hydrogen, bound on a (O_{br}), will either recombine with its starting ethoxy or hop from row to row of (O_{br}) to combine with an ethoxy and form ethanol or combine with a terminal OH to form water. Ethoxy can recombine with its hydrogen (bound on a bridging oxygen) and form ethanol or move along the Ti_{5c} rows and recombine with a different hydrogen.

After these considerations we can interpret the shifting of the ethanol low temperature desorption peak to 360 K as due to its recombination on the surface after having dissociated on a (O_{ot}) site[108]. The high temperature peak at 640 K derives from the recombination of ethoxy from an (O_{br}) vacancy. In the case of formaldehyde TPD trace we observed a peak at 320 K, which is at a lower temperature than the main desorption peak from ethanol and a peak at 640 K. The high temperature peak derives from the disproportionation of an ethoxy bound on an (O_{br}) vacancy. The low temperature acetaldehyde is an aspect not found in literature therefore we will give a hypothesis. The fact that the main desorption of ethanol is at 360 K means that all of the alcohol has dissociated onto the surface. Furthermore, literature states that acetaldehyde obtained via the disproportionation of ethoxy desorbs at about 650 K. this excludes the intervention of any ethoxy bound to an (O_{br}) vacancy. Therefore we propose that low temperature acetaldehyde desorbs via disproportionation of two ethoxys bound on Ti_{5c} sites. Ethylene was observed to desorb at 580 K which in the light of what said is due to desorption of ethoxy, bound on (O_{br}) vacancies, as ethylene.

5.3.2 Ethanol on $CeO_x/TiO_2(110)$

In this section we report the TPD data for the desorption of 5L of ethanol from $CeO_x/TiO_2(110)$ films of increasing thickness. To observe the influence of pre-adsorbed oxygen towards ethanol each sample was analyzed with and without oxygen pre-dosage.

Unfortunately CeO_2 has less literature data than titania so that a detailed explanation of sites involved in the reactivity is not possible. Moreover, an STM study of the surface before and after the desorption experiments have been performed would be of great help. Many authors have investigated the reactivity towards methanol, or higher alcohols, of thin CeO_2 films with diverse results depending on the type of substrate used. In their study Siokou et al.[116] studied the desorption of methanol on sub-monolayer (< 1ML), intermediate (~3 ML) and high (> 10 ML) CeO_x thicknesses at 300 – 340 K deposited on Cu(111). TPD scans were run on annealed films and pre-oxidized (not annealed but exposed to 30 L of O_2 at 300 K) films. The authors found that in the case of 10 ML films, either as-grown or pre-exposed to oxygen, all products, namely methanol, formaldehyde, CO, CO_2, H_2 and H_2O desorbed at about 580 K. For intermediate thicknesses (~3 ML) the as grown films showed only trace amounts of water and methanol while formaldehyde and H_2 desorbed at 560 K while CO desorption peak was found at 580 K. Differences appeared for pre-oxidized films where all products were observed desorbing at around 560 K, however also low temperature peaks were observed for all products: methanol (370 K), formaldehyde (390 K), CO (390 K), CO_2 (480 K), H_2 (370 K), and H_2O (450 K). In the case of sub-monolayer coverages stark differences appeared. For the annealed films no high temperature product appeared excluding H_2 and CO (both at 545 K) that were also low in intensity. Instead, for the pre-oxidized films those authors observed H_2 (370 K), CO_2 (500 K) and formaldehyde (370 K). The low temperature peaks are due to the fact that at low thicknesses, ceria aggregates into islands that expose side microfacets. These have labile oxygen atoms and thus are more reactive towards methoxys, especially when pre-oxidized. Siokou and Nix[116] have observed that, methoxys bound on these sites, have their oxygen coordinated to two cerium ions while their methyl group will be more inclined towards the copper substrate as evidenced via IR measurements. Another group, Ferrizz et al.[117], studied the effects a different structure has on methanol reactivity. These authors compared three sample types: CeO_2 single crystal, 10 ML CeO_2 film grown on yttrium stabilized zirconia (YSZ), and 10 ML CeO_2 film on α-$Al_2O_3(0001)$. They verified that zirconia greatly enhances the reducibility of ceria. Thus ceria films on YSZ present more oxygen vacancies and are less thermally stable than either single crystal or CeO_2/α-$Al_2O_3(0001)$. Furthermore, it was found that methanol desorbs from a nearly stoichiometric sample as methanol, formaldehyde and water at 680 K in the case of the single crystal, whereas these species desorbed at 600 K and 630 K on CeO_2/YSZ and CeO_2/α-$Al_2O_3(0001)$ respectively. On highly reduced ceria methanol was observed to go through complete dehydrogenation to CO and H_2 that occurred at 670 K. The last group we cite are Mullins et al.[118] that have conducted a study on the desorption of methyl, ethyl and propyl alcohols on a 5 nm $CeO_x(111)$ thin film grown on Ru(0001). In the case of ethanol, the desorbing products, from a reduced surface (Ce(III)), such as ethylene, acetaldehyde and H_2 were observed to desorb at 580 K, whereas ethanol desorbed as a broad peak from 200-300 K and no high temperature peaks were observed.

Below (Figure 5.25) we report the TPD scan of 5L of ethanol adsorbed onto 0.45 ML of CeO_x on TiO_2(110). On the untreated surface ethanol shows two desorption peaks one at 300 K and the other at 670 K. Acetaldehyde also shows two peaks one at 280 K and the other at 670 K. No ethylene was observed and the peak at 270 K for H_2O derives from the water absorbed from the background. The effect of cerium oxide is immediately apparent because a clean reduced titania substrate would show some ethylene desorption. The reaction is instead pushed towards ethanol dehydration as expected for CeO_2. The main differences from the pure oxides are the high temperature ethanol peak and the low temperature acetaldehyde peak. Thus, the low temperature ethanol peak can be explained as molecular desorption/ recombination from Ti_{5c} sites and CeO_x vacancy sites. The high temperature peak, which is common to both oxides, probably derives from disproportionation of ethoxys bound on Ti_{5c} sites and (O_{br}) vacancies, from Ti_{5c} sites and CeO_x vacancies, or from two CeO_x vacancies. In the case of acetaldehyde the low temperature peak is characteristic of pre-oxidized reduced rutile and is independent from oxygen treatment and thus may be explained as oxydehydration of ethoxy on CeO_x. The high temperature peak instead, derives from what was said for ethanol.

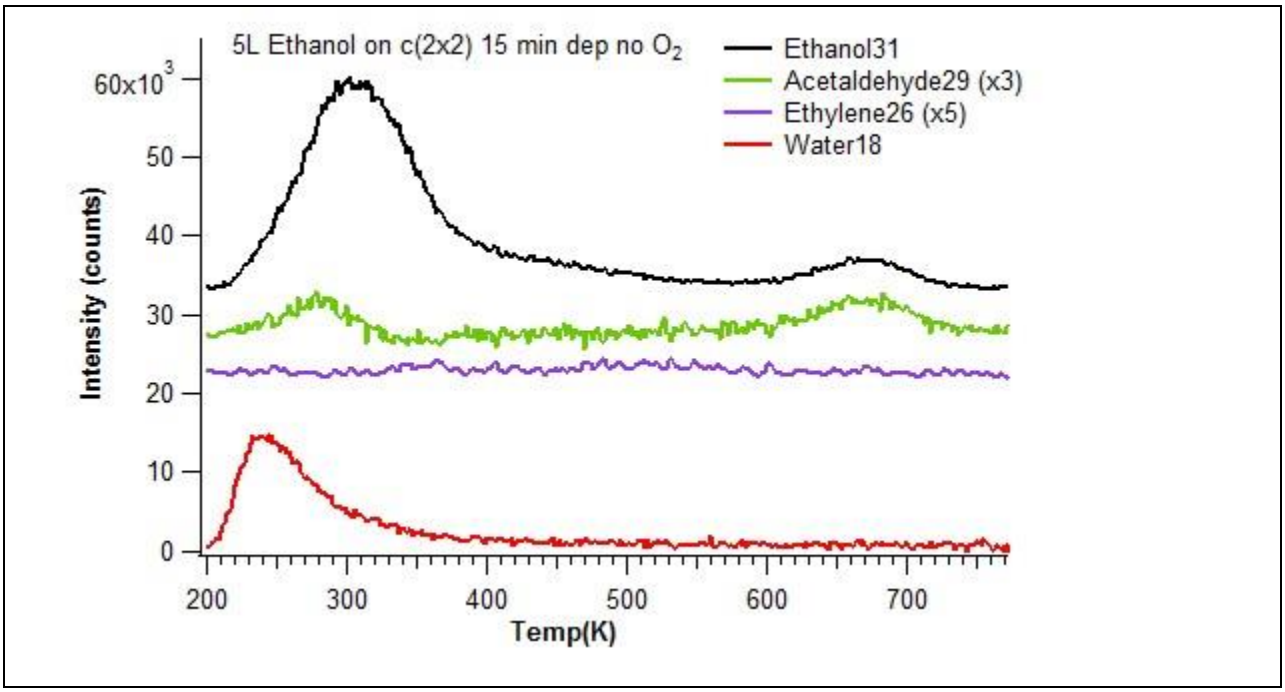

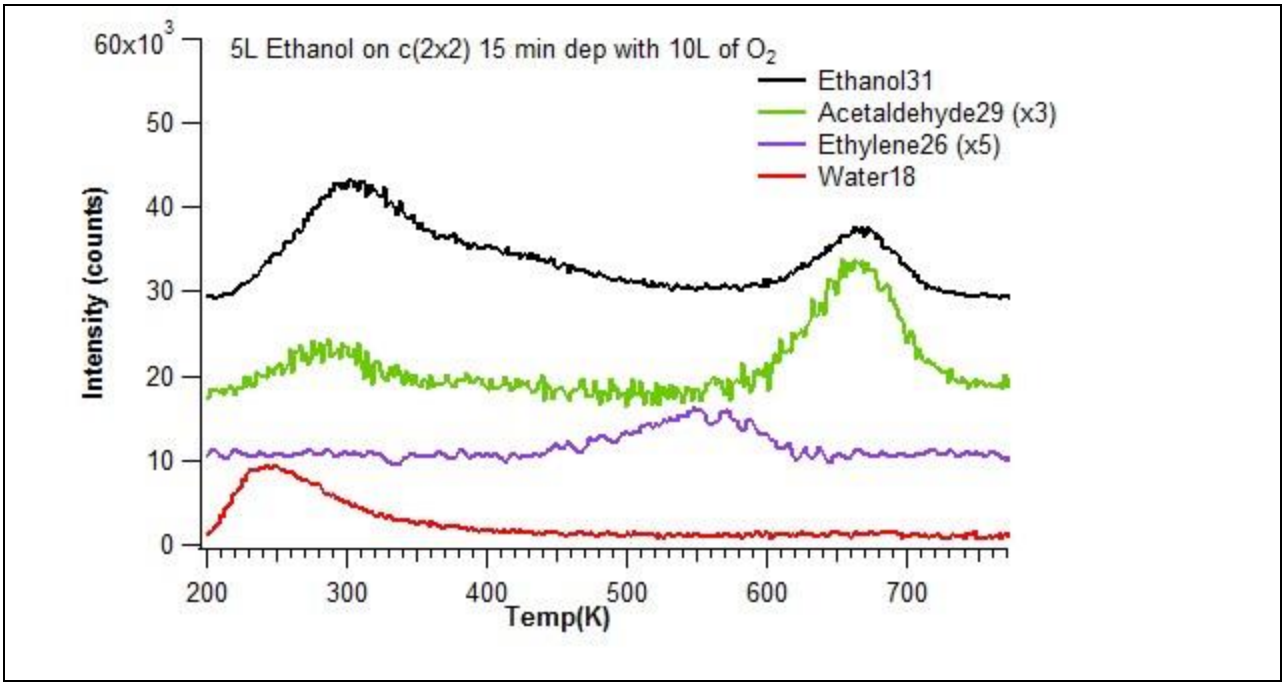

Figure 5.25: TPD scans of 5L of ethanol on a 15 min (0.45 ML) film of c(2x2) CeO_x on TiO_2(110). Upper graph refers to the as grown surface, lower part to the oxygen pre-exposed surface.

In the case of a pre-oxidized sample three new features appear. A shoulder for ethanol desorption centered at 420 K, an ethylene peak at 550 K and a more intense acetaldehyde desorption peak. These can be explained by the fact that on CeO_x/TiO_2(110) sample oxygen preferentially binds on Ti^{3+} atoms[96]. The dosing of cerium creates three Ti^{3+} atoms two of which are Ti_{5c} sites so that oxygen will dissociate and bind on these two sites on which ethanol will readily dissociate forming terminal OH that desorbs as water. Furthermore, the dosing of oxygen on CeO_x/TiO_2(110) also forms TiO_x islands as seen by STM[82, 87]. Thus, the ethanol shoulder can be explained as ethanol recombination while ethylene as desorption of stranded ethoxys on TiO_x. The higher intensity of high temperature acetaldehyde derives from the higher quantity of ethoxys present on the surface.

In the case of 0.9 ML of CeO_x on TiO_2(110)(Figure 5.26) we observed a similar behavior to the one just described except for a lower intensity of the low temperature acetaldehyde peak which can be explained with a lesser availability of Ti_{5c} sites.

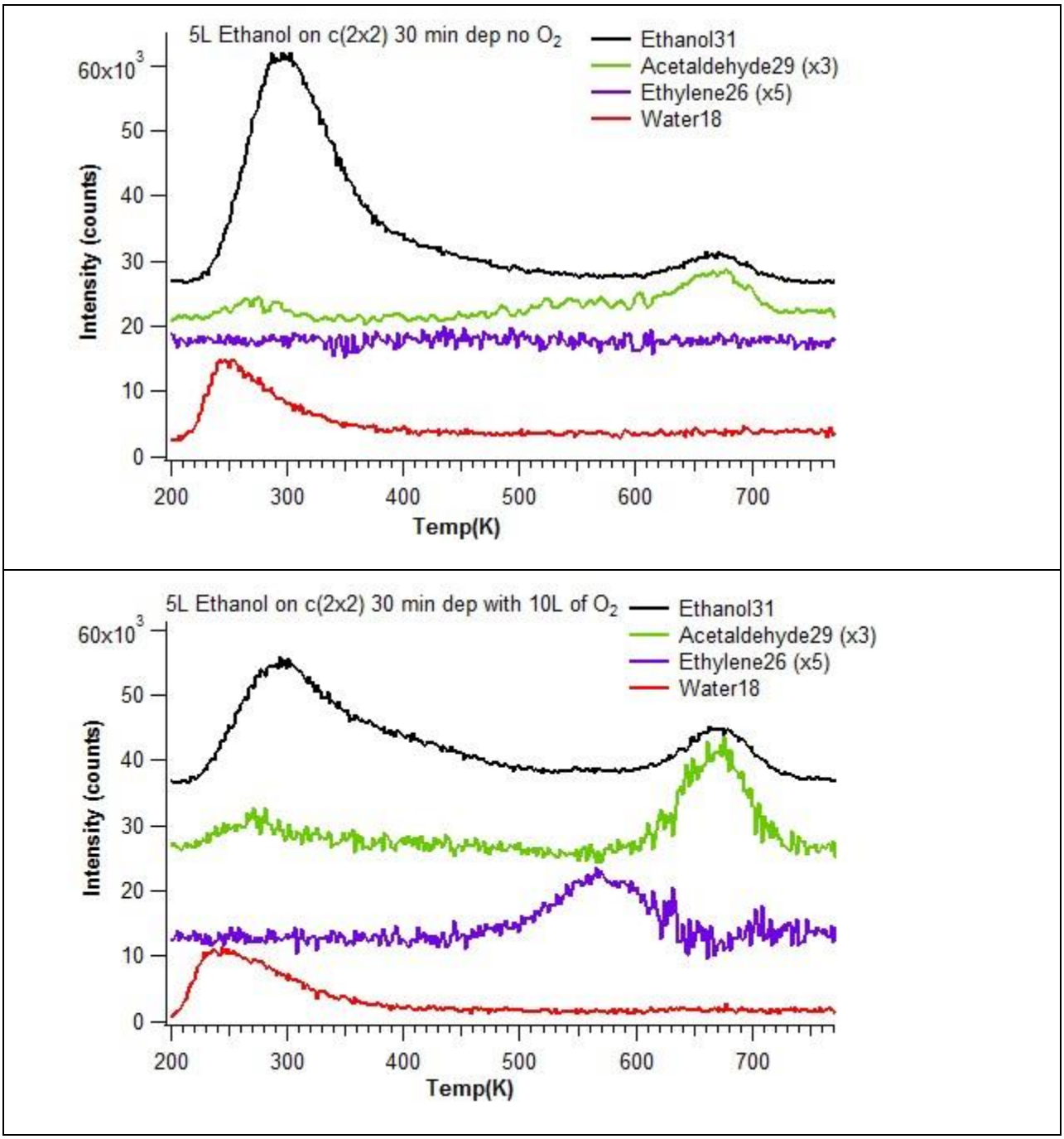

Figure 5.26: TPD scans of 5L of ethanol on a 30 min (0.9 ML) film of c(2x2) CeO_x on TiO_2(110). Upper graph refers to the as grown surface, lower part to the oxygen pre-exposed surface.

In the case of a 1.35 ML film of CeO_x (Figure 5.27) we can use the same considerations as above due to the fact that cerium oxide does not completely wets the surface of titania. Thus, we can still find uncovered rutile surface which still contributes to the low temperature desorption peak of acetaldehyde and desorption of ethylene in the pre-oxidized sample.

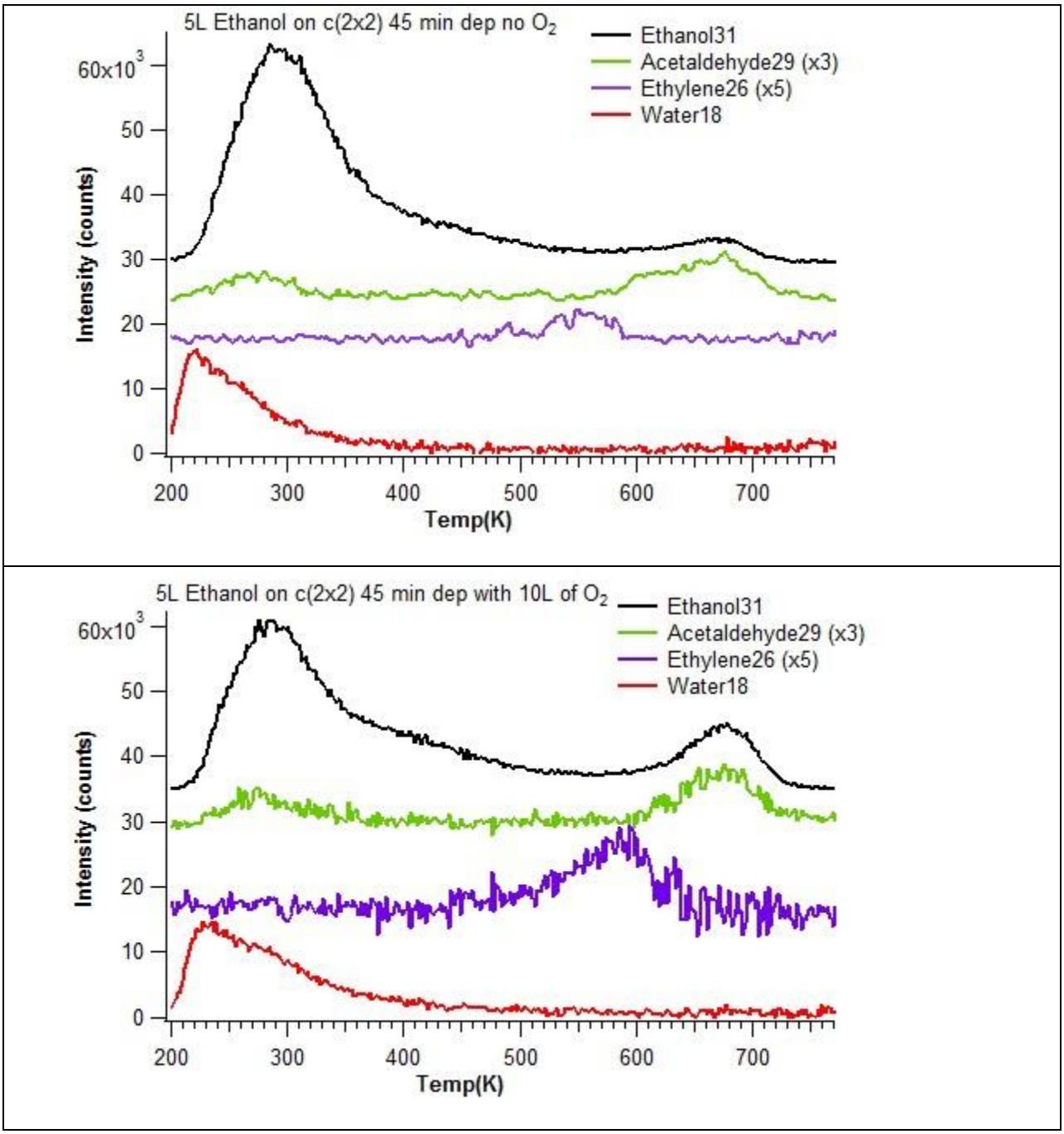

Figure 5.27: TPD scans of 5L of ethanol on a 45 min (1.35 ML) film of c(2x2) CeO_x on TiO_2(110). Upper graph refers to the as grown surface, lower part to the oxygen pre-exposed surface.

We have observed a remarkable change in products for a 2.25 ML thick film (Figure 5.28). In fact, no long range order was observable (no LEED pattern) so that the growth of a polycrystalline film was assumed. Furthermore, XPS spectra showed that cerium was still present as Ce^{3+} and thus highly reduced. For the untreated sample ethanol mainly desorbed at 300 K with only a small shoulder at 680 K

due to disproportionation. Similar features were encountered by Ferrizz et al.[117] for a CeO_2(100) surface probably favored by the presence of the yttrium stabilized zirconia support which greatly enhanced its reducibility. Acetaldehyde peaks were less intense; the low temperature peak is due to dehydrogenation whereas the high temperature peak is due to disproportionation of an ethoxy group. The broadness of the peak probably stems from the film's high disorder.

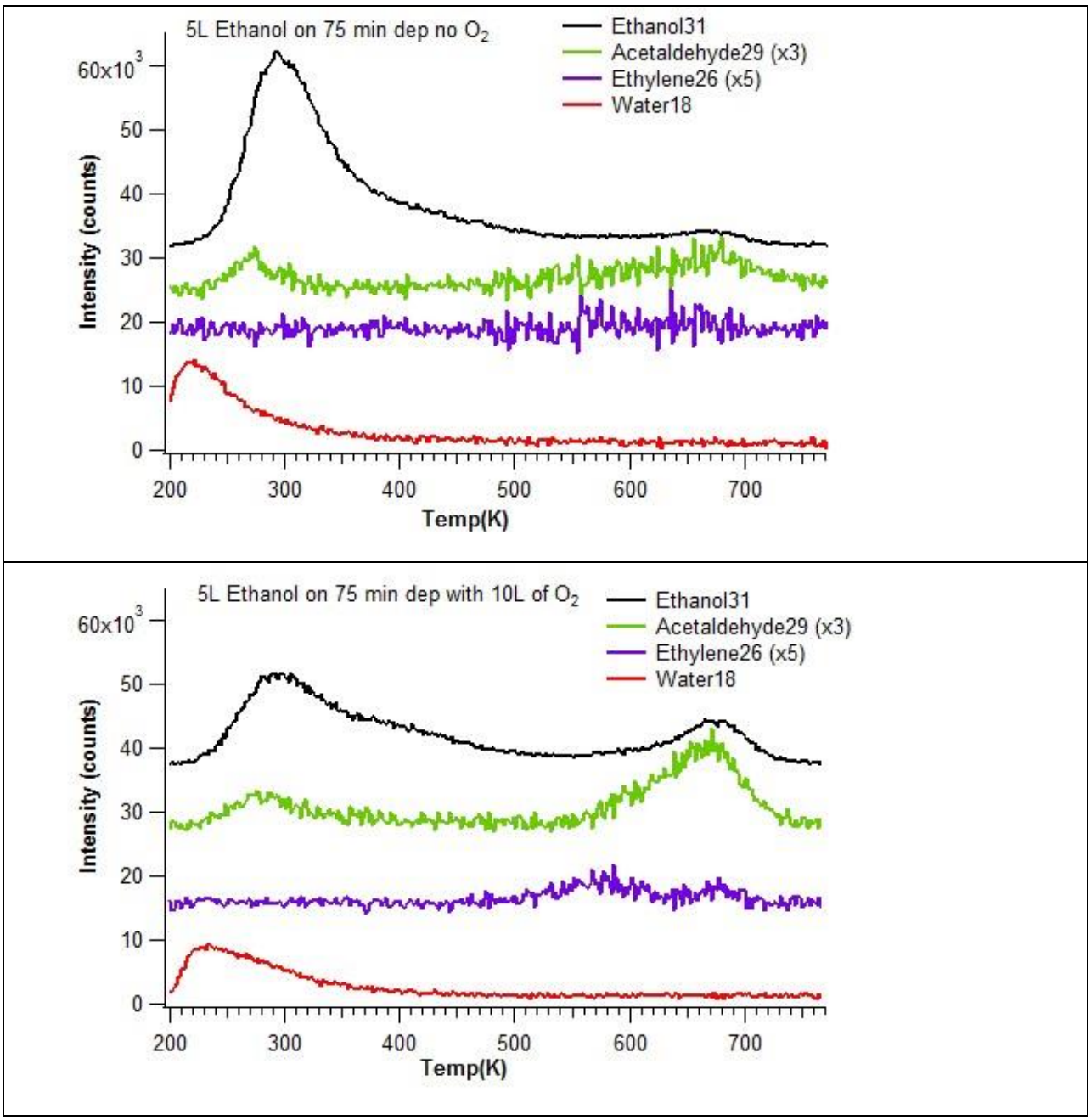

Figure 5.28: TPD scans of 5L of ethanol on a 75 min (2.25 ML) film of c(2x2) CeO_x on TiO_2(110). Upper graph refers to the as grown surface, lower part to the oxygen pre-exposed surface.

When oxygen was pre-dosed we observed an increased intensity for both high temperature peaks of ethanol and acetaldehyde. This is probably due to the fact that adsorbed oxygen adatoms dissociate ethanol into ethoxys that either undergo oxydehydrogenation to form acetaldehyde at 270 K or recombine to form ethanol at 300 K. Stranded ethoxys then undergo a disproportionation reaction to form acetaldehyde and ethanol at 650 K[117].

Similar results were obtained in the case of a 3.6 ML film of CeOx.

5.3.3 Conclusions:

We have studied by TPD the desorption of ethanol from $CeO_x/TiO_2(110)$ surfaces of different thickness. The results indicate a specific reactivity that favor the oxidative dehydrogenation of alcohol at low temperature, which cannot be simply explained as the sum of the reactivity of ceria and titania but is an important property of this $CeO_x/TiO_2(110)$ system. We have observed that coverages lower than 1.35 ML exhibited ethylene desorption under oxidative conditions as the oxide-oxide system loses selectivity; This behavior is unwanted since it can cause carbon poisoning of the surface. Ferrizz et al.[117] did not observe low temperature evolution of formaldehyde from CeO_2/YSZ although for a fully oxidized surface methanol showed a complete dehydrogenation as CO and H_2. The low temperature desorption peak of acetaldehyde, found by us, seems promising and thus further study would be needed.

References:

51. U. Martinez, L. B. Vilhelmsen, H. H. Kristoffersen, J. Stausholm-Møller and B. Hammer, *Phys Rev B*, 2011, **84**, 205434.
52. A. Trovarelli, C. de Leitenburg, M. Boaro and G. Dolcetti, *Catal Today*, 1999, **50**, 353-367.
53. A. Trovarelli, *Catalysis Reviews-Science and Engineering*, 1996, **38**, 439-520.
54. J. Kašpar, P. Fornasiero and M. Graziani, *Catal Today*, 1999, **50**, 285-298.
55. S. Imamura and M. Ando, *Ind Eng Chem Res*, 1989, **28**, 1452-1456.
56. Q. Fu, A. Weber and M. Flytzani-Stephanopoulos, *Catal Lett*, 2001, **77**, 87-95.
57. Q. Fu, H. Saltsburg and M. Flytzani-Stephanopoulos, *Science*, 2003, **301**, 935-938.
58. P. Jasinski, T. Suzuki and H. U. Anderson, *Sensors and Actuators B: Chemical*, 2003, **95**, 73-77.
59. M. Stoukides, *Catalysis Reviews*, 2000, **42**, 1-70.
60. S. Park, J. M. Vohs and R. J. Gorte, *Nature*, 2000, **404**, 265-267.
61. S. Armini, J. De Messemaeker, C. M. Whelan, M. Moinpour and K. Maex, *J Electrochem Soc*, 2008, **155**, H653-H660.
62. A. Asati, S. Santra, C. Kaittanis, S. Nath and J. M. Perez, *Angewandte Chemie International Edition*, 2009, **48**, 2308-2312.
63. M. Mogensen, N. M. Sammes and G. A. Tompsett, *Solid State Ionics*, 2000, **129**, 63-94.
64. W. Xiao, Q. Guo and E. G. Wang, *Chem Phys Lett*, 2003, **368**, 527-531.
65. J. A. Kilner, *Chem Lett*, 2008, **37**, 1012-1015.
66. C. T. Campbell and C. H. F. Peden, *Science*, 2005, **309**, 713-714.
67. C. Sun, H. Li and L. Chen, *Energ Environ Sci*, 2012, **5**, 8475-8505.
68. S. Tsunekawa, R. Sahara, Y. Kawazoe and K. Ishikawa, *Appl Surf Sci*, 1999, **152**, 53-56.

69. S. Deshpande, S. Patil, S. V. Kuchibhatla and S. Seal, *Appl Phys Lett*, 2005, **87**, -.
70. T. Yu, J. Joo, Y. I. Park and T. Hyeon, *Angewandte Chemie International Edition*, 2005, **44**, 7411-7414.
71. D. Wang, Y. Kang, V. Doan-Nguyen, J. Chen, R. Küngas, N. L. Wieder, K. Bakhmutsky, R. J. Gorte and C. B. Murray, *Angewandte Chemie*, 2011, **123**, 4470-4473.
72. S. T. Bromley, I. d. P. R. Moreira, K. M. Neyman and F. Illas, *Chem Soc Rev*, 2009, **38**, 2657-2670.
73. J. Rynkowski, J. Farbotko, R. Touroude and L. Hilaire, *Applied Catalysis A: General*, 2000, **203**, 335-348.
74. B. Reddy and A. Khan, *Catal Surv Asia*, 2005, **9**, 155-171.
75. G. Dutta, U. V. Waghmare, T. Baidya, M. S. Hegde, K. R. Priolkar and P. R. Sarode, *Chem Mater*, 2006, **18**, 3249-3256.
76. J. Fang, H. Bao, B. He, F. Wang, D. Si, Z. Jiang, Z. Pan, S. Wei and W. Huang, *The Journal of Physical Chemistry C*, 2007, **111**, 19078-19085.
77. G. Zhou, J. Hanson and R. J. Gorte, *Applied Catalysis A: General*, 2008, **335**, 153-158.
78. S. Watanabe, X. Ma and C. Song, *The Journal of Physical Chemistry C*, 2009, **113**, 14249-14257.
79. A. C. Johnston-Peck, S. D. Senanayake, J. J. Plata, S. Kundu, W. Xu, L. Barrio, J. Graciani, J. F. Sanz, R. M. Navarro, J. L. G. Fierro, E. A. Stach and J. A. Rodriguez, *The Journal of Physical Chemistry C*, 2013, **117**, 14463-14471.
80. T. Masui, K. Fukuhara, N. Imanaka, T. Sakata, H. Mori and G.-y. Adachi, *Chem Lett*, 2002, **31**, 474-475.
81. J. Xiao, X. Wang, Y. Chen, M. Fujii and C. Song, *Ind Eng Chem Res*, 2013, **52**, 15746-15755.
82. J. A. Rodriguez and D. Stacchiola, *Phys Chem Chem Phys*, 2010, **12**, 9557-9565.
83. A. Bruix, J. A. Rodriguez, P. J. Ramirez, S. D. Senanayake, J. Evans, J. B. Park, D. Stacchiola, P. Liu, J. Hrbek and F. Illas, *J Am Chem Soc*, 2012, **134**, 8968-8974.
84. L. V. Mattos and F. B. Noronha, *J Catal*, 2005, **233**, 453-463.
85. C. Xu, R. Zeng, P. K. Shen and Z. Wei, *Electrochim Acta*, 2005, **51**, 1031-1035.
86. G. Jacobs, R. A. Keogh and B. H. Davis, *J Catal*, 2007, **245**, 326-337.
87. J. B. Park, J. Graciani, J. Evans, D. Stacchiola, S. Ma, P. Liu, A. Nambu, J. Fernandez Sanz, J. Hrbek and J. A. Rodriguez, *Proceedings of the National Academy of Sciences of the United States of America*, 2009, **106**, 4975-4980.
88. J. B. Park, J. Graciani, J. Evans, D. Stacchiola, S. D. Senanayake, L. Barrio, P. Liu, J. F. Sanz, J. Hrbek and J. A. Rodriguez, *J Am Chem Soc*, 2010, **132**, 356-363.
89. P. Burroughs, A. Hamnett, A. F. Orchard and G. Thornton, *Journal of the Chemical Society, Dalton Transactions*, 1976, 1686-1698.
90. A. Kotani, H. Mizuta, T. Jo and J. C. Parlebas, *Solid State Commun*, 1985, **53**, 805-810.
91. T. Jo and A. Kotani, *Solid State Commun*, 1985, **54**, 451-456.
92. R. Wrobel, Y. Suchorski, S. Becker and H. Weiss, *Surf Sci*, 2008, **602**, 436-442.
93. E. Beche, P. Charvin, D. Perarnau, S. Abanades and G. Flamant, *Surf Interface Anal*, 2008, **40**, 264-267.
94. A. Pfau and K. D. Schierbaum, *Surf Sci*, 1994, **321**, 71-80.
95. Y. A. Teterin, A. Y. Teterin, A. M. Lebedev and I. O. Utkin, *Journal of Electron Spectroscopy and Related Phenomena*, 1998, **88**, 275-279.
96. J. Graciani, J. J. Plata, J. Fdez Sanz, P. Liu and J. A. Rodriguez, *J Chem Phys*, 2010, **132**.
97. Y. Zhou and J. Zhou, *Surf Sci*, 2012, **606**, 749-753.
98. M. Fronzi, A. Soon, B. Delley, E. Traversa and C. Stampfl, *J Chem Phys*, 2009, **131**.
99. R. Wang, P. A. Crozier and R. Sharma, *J Phys Chem C*, 2009, **113**, 5700-5704.

100. X. Shao, J.-F. Jerratsch, N. Nilius and H.-J. Freund, *Phys Chem Chem Phys*, 2011, **13**, 12646-12651.
101. M. Nielsen, E. Alberico, W. Baumann, H.-J. Drexler, H. Junge, S. Gladiali and M. Beller, *Nature*, 2013, **495**, 85-89.
102. A. Haryanto, S. Fernando, N. Murali and S. Adhikari, *Energ Fuel*, 2005, **19**, 2098-2106.
103. V. Subramani and C. Song, in *Catalysis: Volume 20*, The Royal Society of Chemistry, Editon edn., 2007, vol. 20, pp. 65-106.
104. G. A. Deluga, J. R. Salge, L. D. Schmidt and X. E. Verykios, *Science*, 2004, **303**, 993-997.
105. M. Ni, D. Y. C. Leung and M. K. H. Leung, *Int J Hydrogen Energ*, 2007, **32**, 3238-3247.
106. P. D. Vaidya and A. E. Rodrigues, *Chem Eng J*, 2006, **117**, 39-49.
107. U. Diebold, *Surface Science Reports*, 2003, **48**, 53-229.
108. C. L. Pang, R. Lindsay and G. Thornton, *Chem Soc Rev*, 2008, **37**, 2328-2353.
109. W. S. Epling, C. H. F. Peden, M. A. Henderson and U. Diebold, *Surf Sci*, 1998, **412–413**, 333-343.
110. W. S. Epling, C. H. F. Peden, M. A. Henderson and U. Diebold, *Surf Sci*, 1998, **412-13**, 333-343.
111. G. Lu, A. Linsebigler and J. T. Yates, *The Journal of Physical Chemistry*, 1994, **98**, 11733-11738.
112. L. Gamble, L. S. Jung and C. T. Campbell, *Surf Sci*, 1996, **348**, 1-16.
113. E. Farfan-Arribas and R. J. Madix, *The Journal of Physical Chemistry B*, 2002, **106**, 10680-10692.
114. M. A. Henderson, S. Otero-Tapia and M. E. Castro, *Faraday Discuss*, 1999, **114**, 313-329.
115. S. Wendt, P. T. Sprunger, E. Lira, G. K. H. Madsen, Z. Li, J. Ø. Hansen, J. Matthiesen, A. Blekinge-Rasmussen, E. Lægsgaard, B. Hammer and F. Besenbacher, *Science*, 2008, **320**, 1755-1759.
116. A. Siokou and R. M. Nix, *J Phys Chem B*, 1999, **103**, 6984-6997.
117. R. M. Ferrizz, G. S. Wong, T. Egami and J. M. Vohs, *Langmuir*, 2001, **17**, 2464-2470.
118. D. R. Mullins, S. D. Senanayake and T. L. Chen, *The Journal of Physical Chemistry C*, 2010, **114**, 17112-17119.

5.4 CERIA -TITANIA MIXED OXIDES in POWDER FORM

In this section I will attach a published paper on the structural characterization and reactivity of CeO_2-TiO_2 mixed oxide powders synthesized using the sol-gel technique by a group from the University of Turin. The XPS measurements that I did during my thesis helped in determining the chemical composition of different powders with increasing cerium content. These studies also showed what is the maximum amount of titanium content so that cerium is present in its Ce^{3+} state. This information, coupled with the previous methanol and ethanol TPD data, increased the knowledge on how to tailor the system in order to isolate or enhance specific reaction mechanisms, namely, dehydration and dehydrogenation of alcohols.

Journal of Materials Chemistry A

RSC Publishing

PAPER

Structural and spectroscopic characterization of CeO_2–TiO_2 mixed oxides

Cite this: J. Mater. Chem. A, 2013, 1, 10918

Chiara Gionco,[a] Maria Cristina Paganini,[a] Stefano Agnoli,[b] Askia Enrico Reeder[b] and Elio Giamello*[a]

Mixed CeO_2–TiO_2 systems have been synthesized using the sol–gel technique in a symmetric range of nominal compositions (10, 50 and 90 mol% CeO_2). The solid materials were characterised using a variety of diffractometric and spectroscopic techniques. The intimate contact between the two components during the synthesis leads to heterogeneous systems which are based on the presence, besides the two individual oxide phases, of a mixed phase of a cerium titanate ($Ce_2Ti_2O_7$, pyrochlore structure) which contains Ce^{3+} ions that impart particular optical properties to the solid (a pronounced red shift with respect to the band gap transition of the two oxides). Ce^{3+} ions are present at the surface of the systems together with tetravalent Ce and Ti ions. The mixed solids can be reduced by annealing under vacuum and, upon reoxidation under mild conditions with O_2, form superoxide species adsorbed on Ce^{4+} which have, as already reported for low loading CeO_2–TiO_2 systems, peculiar spectroscopic properties with respect to superoxide adsorbed on bare cerium dioxide.

Received 22nd May 2013
Accepted 4th July 2013

DOI: 10.1039/c3ta12018j

www.rsc.org/MaterialsA

Introduction

Metal oxides are strategic systems for modern material science not only because of their well-known structural properties, but particularly for their applications in many sophisticated devices as functional materials. Research in the field of metal oxides is therefore continuously searching for new systems with stimulating and unprecedented properties. This can be done in several ways, including the systematic study of complex mixtures of simple oxides. Two or more metal oxides can interact in several ways, for instance, resulting in the formation of new compounds, the formation of solid solutions (in a given compositional range) or the simple formation of solid–solid interfaces, constituting a heterojunction between two non-miscible phases.

A system involving cerium dioxide and titanium dioxide has been the object of many investigations in the past, as the two individual oxides have many interesting properties and consequent applications, so the exploration of mixed systems is expected to produce promising results.[1–4]

Cerium dioxide is well known because of its redox properties, allowing easy transitions between the oxidized and reduced states, depending on the external conditions. Its oxygen storage capacity makes ceria suitable for several applications such as those in automotive three-way catalysts[5–7] and, in oxidation catalysis.[8–13] Cerium dioxide is also used in sensors,[14,15] in fuel cell technology as a solid state electrolyte,[16,17] and even in cosmetics.[18] Oxygen storage (and release) in ceria seems to be favoured by its fluorite structure. The oxygen ions in such crystals lie in parallel planes, allowing efficient oxygen diffusion in a network of oxygen vacancies favouring the oxidative action of the solid. The oxygen storage capacity (OCS) is greatly enhanced when Zr is introduced into the cubic ceria structure, and in particular upon the formation of phases with the pyrochlore structure, such as $Ce_2Zr_2O_7$.[19–21] The strong optical absorption of cerium dioxide at around 400 nm (with a weak tail in the visible range capable of imparting a pale yellow colour to the material) has also stimulated studies devoted to the use of this material as a possible photocatalyst.[22]

Titanium dioxide has been widely studied in the last few decades because of its photochemical and photophysical properties.[23–25] This oxide is a component of photovoltaic devices (dye-sensitized solar cells, DSSCs [26]) and is an active photocatalyst commonly used in several reactions of environmental interest.[27]

TiO_2 exists in three crystallographic forms: rutile, anatase and brookite, all of which are characterized by octahedrally-coordinated Ti^{4+} ions. Although rutile is the most stable phase, anatase shows higher activity for photochemical and photocatalytic applications.

In the present paper we report an investigation on CeO_2–TiO_2 (ceria–titania) mixed oxide systems prepared using the sol–gel technique, with high loadings of CeO_2 (from 10 to 90 mol%), at variance with analogous systems consisting of low amounts of ceria dispersed on the TiO_2 surface, which have previously been investigated.[28–32] The sol–gel technique, due to the intimate mixture of the various components in the starting liquid phase,

[a]Università degli Studi di Torino, Dipartimento di Chimica and NIS, Via P. Giuria 7, Torino, Italy. E-mail: elio.giamello@unito.it; Fax: +39 011670 7855; Tel: +39 011670 7574

[b]Università degli Studi di Padova, Dipartimento di Scienze Chimiche, Via F. Marzolo 1, Padova, Italy

is, among the possible synthetic routes, one of the more suited techniques to favour a deep interaction between the two phases.

Despite the previous research concerning this system, some of which was devoted to improve the thermal stability of CeO_2,[30,31,33–36] several questions about its structural and electronic features have not yet found a clear answer. For instance, the insertion of one type of cation (Ce^{4+}or Ti^{4+}) into the lattice of the other oxide (TiO_2 or CeO_2) has been questioned in the literature. The two oxides are largely immiscible due to the different crystal structures and the different cationic sizes (Ce^{4+} 0.92–0.97 Å; Ce^{3+} 1.14 Å, Ti^{4+} 0.61–0.68 Å). However, some authors[1,2,37–39] assert that while the insertion of cerium in the TiO_2 lattice is unlikely because of the different size, the insertion of weak concentrations of Ti^{4+} in CeO_2 should be possible. On the contrary, other authors[3,29] claim that cerium ions can actually enter the titania lattice,[4,40] indicating a notable value (5 mol%) for the maximum concentration. In general, however, most authors agree about the coexistence of the two oxide phases and the formation of small domains of mixed phases at the interface.

The materials synthesized for the present investigation were characterized by a variety of techniques including X-ray Diffraction (XRD), N_2 adsorption to evaluate the BET surface area, diffuse reflectance UV-Vis spectroscopy, μ-Raman spectroscopy, transmission electron microscopy (TEM with EDS), X-ray photoemission spectroscopy (XPS) and electron paramagnetic resonance (EPR). The aim of this investigation was to gain a deep insight into the properties of this mixed oxide. We focused our attention mainly on the features of the oxide–oxide interface, on the optical properties of the system and, due to the high CeO_2 content, on its reactivity towards oxygen. As it will be shown, the features of the mixed systems, prepared in this way, are original and not amenable to those of a simple mixture of the two oxides.

Materials and methods

Preparation of the samples

All of the reactants employed in this work were purchased from Aldrich and used without any further purification. In particular, the cerium nitrate was free from other rare earth element impurities.

Mixed Ti–Ce oxides were prepared *via* sol–gel synthesis following the procedure described by Fang *et al.*[2] For each sample, a solution A was prepared stirring 10 g of $Ti(OC_4H_9)_4$, 3 mL of CH_3COOH and 40 mL of C_2H_5OH. The pH of this solution was adjusted to 2.3–2.7 using HNO_3. Solution B was prepared with a stoichiometric amount of $Ce(NO_3)_3 \cdot 6H_2O$, 3 mL of distilled water and 20 mL of C_2H_5OH. Solution B was added dropwise to solution A while stirring, until a stable sol was formed. The sol was aged in air until a gel formed, and then was dried at 343 K for 72 hours. Finally the powder was calcined at 723 K in air for 2 hours.

The concentrations of the three mixed oxides prepared by the described procedure were 10, 50 and 90 mol% CeO_2; these materials will be hereafter labeled as CT10, CT50 and CT90, respectively.

Some of the properties of these mixed oxides were compared with those of pure TiO_2 (anatase polymorph) prepared using the same method (starting from $Ti(OC_3H_7)_4$, C_3H_7OH and distilled water) and with those of a CeO_2 sample prepared via sol-gel starting from $Ce(OC_3H_7)_4$.

Characterization of the samples

Powder X-ray diffraction (XRD) patterns were recorded with a PANalytical PW3040/60 X'Pert PRO MPD diffractometer using a copper Kα radiation source (0.154056 nm). The intensities were obtained in the 2θ range between 20° and 70°. X'Pert High-Score software was used for data handling. MAUD 2.26 (ref. 41) software was used for the Rietveld refinement. To determine the instrumental broadening, the pattern obtained by a well-crystallized silicon standard (crystallite size 1 μm) was used.

The surface area measurements were carried out on a Micromeritics ASAP 2020/2010 apparatus using the Brunauer–Emmett–Teller (BET) model for N_2 adsorption measurements. Prior to the adsorption run, all of the samples were outgassed at 573 K for 3 h.

Micro-Raman (μ-Raman) spectra were recorded on a Jobin Yvon LabRam HR800 spectrometer, equipped with a He–Ne laser (632.8 nm) and connected to an Olympus BX41 microscope.

TEM analysis of the powder samples deposited on a copper grid was performed using a Jeol JEM 3010 (300 kV) microscope equipped with an EDS detector by Oxford Instruments.

The UV-Vis absorption spectra were recorded using a Varian Cary 5 spectrometer, coupled with an integration sphere for diffuse reflectance studies, using a Carywin-UV/scan software. A sample of PTFE with 100% reflectance was used as the reference.

Electron Paramagnetic Resonance (EPR) spectra, recorded at room temperature and at liquid nitrogen temperature, were run on a X-band CW-EPR Bruker EMX spectrometer equipped with a cylindrical cavity operating at a 100 kHz field modulation and computer simulation of the spectra were obtained using the SIM32 programme developed by Prof. Sojka (Jagellonian University, Cracow, Poland[42]).

The XPS measurements were carried out in an ultrahigh vacuum system equipped with a VG MkII Escalab electron analyzer, working at a base pressure of 10^{-10} mbar. Photoemission spectra were taken at room temperature in normal emission using a non-monochromatized Al/Mg twin anode X-ray source. Powder samples were suspended in bidistilled water and drop casted on high purity copper foils. After drying in air, the obtained films were introduced into the ultrahigh vacuum chamber and outgassed overnight. The charging observed during measurements was corrected using adventitious carbon as the internal reference.

Results and discussion

X-ray diffraction patterns and transmission electron microscopy

XRD patterns of the samples investigated in this work are shown in Fig. 1. The diffraction peaks of the mixed materials are broad in comparison with those of bare ceria, reaching a maximum for CT50.

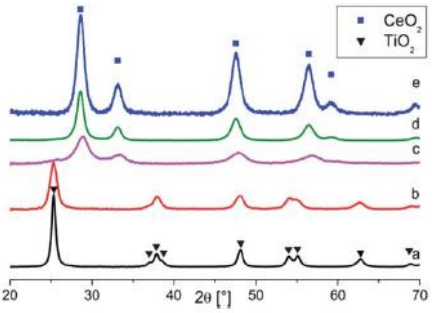

Fig. 1 XRD of CeO_2–TiO_2 mixed oxides: (a) TiO_2 (sol–gel); (b) 10 mol% CeO_2, CT10; (c) 50 mol% CeO_2, CT50; (d) 90 mol% CeO_2, CT90; (e) CeO_2.

Because of the high Ce atomic mass, the peaks of cerium dioxide dominate the diffractograms of the CT90 and CT50 samples (in these cases the main TiO_2 peak, at $2\theta = 26°$, is barely visible). However the sample containing 10 mol% of ceria (CT10) essentially shows peaks corresponding to the TiO_2 anatase phase, indicating a strong dispersion of cerium dioxide in this sample.

Table 1 lists the relative abundance of the two phases, the lattice parameters and the average crystal size calculated using a Rietveld refinement. The specific surface areas measured by the BET method are also listed.

The lattice parameters of the ceria and anatase phases in the mixed materials are not significantly modified with respect to those of the bare oxides. This suggests, also considering the large difference in ionic radius of the two cations involved, that the presence of solid solutions in the mixed samples is rather unlikely. From the XRD data analysis, it can be seen that the average crystallite size decreases on moving from the bare oxides to the mixed samples, with the smallest crystallites being observed in the case of the 50 mol% sample. All of the prepared powders consist of nanocrystals. The highest BET surface area ($130\ m^2\ g^{-1}$) is obtained for CT10. In general, all of the mixed oxides show a higher surface area with respect to the surface area of bare ceria.

Fig. 2 reports the atomic maps of the mixed samples obtained by EDS. The maps show a good spatial dispersion of the two metals. The difference in brightness only depends on the time employed for the measurement. In conclusion, on the basis of the structural results reported here, we can state that the two oxides mix together quite efficiently.

μ-Raman spectroscopy

The μ-Raman technique was used to further investigate the phase distribution in the mixed samples. Both ceria and titania have a good response in Raman spectroscopy, and their typical peaks are observed in distinct spectral regions with limited reciprocal interference. Furthermore, μ-Raman analysis has

Table 1 Cell parameters, weight percentage and crystallite size obtained from the Rietveld refinement of the XRD patterns of the bare and mixed Ce–Ti oxides. R_{wp} is the weighted residual error, *a* and *c* are the lattice parameters, mol% is the molar percentage of the cerium dioxide phase, and *d* is the average crystallite size. S_{BET} is the surface area derived from the nitrogen adsorption measurements

	R_{wp} (%)	Cerium dioxide			TiO_2-Anatase			S_{BET} ($m^2\ g^{-1}$)
		mol%	*a* (Å)	*d* (nm)	*a* (Å)	*c* (Å)	*d* (nm)	
TiO_2	7.84	0			3.785 ± 0.002	9.500 ± 0.009	22 ± 1	85 ± 4
CT10	7.52	10 ± 2	5.41	~2	3.792 ± 0.003	9.503 ± 0.003	14 ± 1	130 ± 7
CT50	9.00	54 ± 8	5.404 ± 0.002	6 ± 1				75 ± 4
CT90	6.94	92 ± 3	5.409 ± 0.008	13 ± 1				83 ± 4
CeO_2	2.73	100.0	5.412 ± 0.002	12 ± 1				50 ± 3

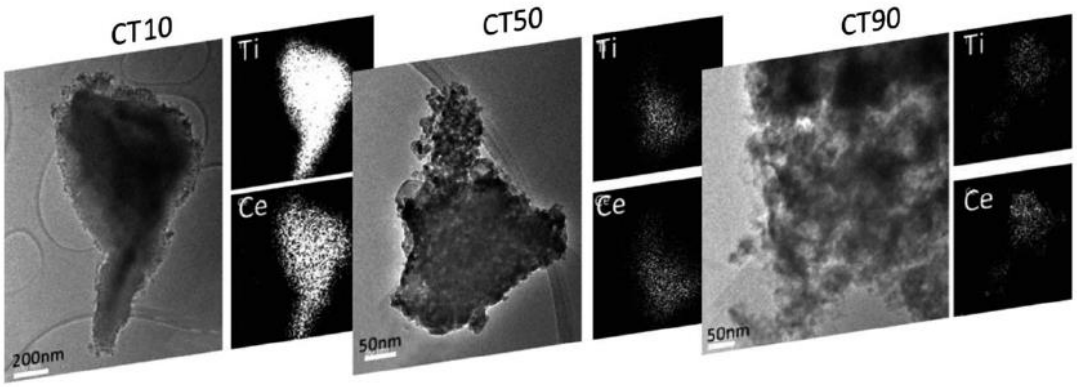

Fig. 2 TEM images of the crystal aggregates and related EDS atomic maps of Ti (upper picture) and Ce (lower picture) for CT10, CT50 and CT90.

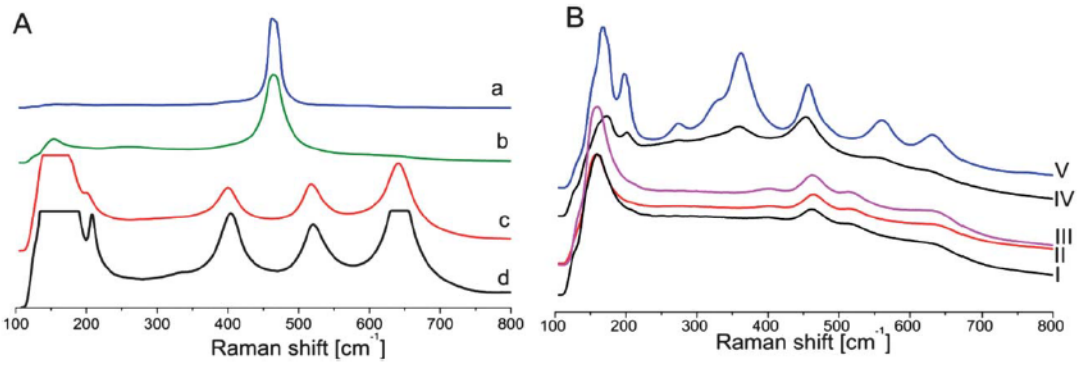

Fig. 3 (A) μ-Raman spectra of: CeO_2 (a), CT90 (b), CT10 (c), TiO_2 (d). (B) Spectra obtained for CT50 in different points of the sample.

good spatial resolution. Therefore, to check the homogeneity of the materials, five acquisitions in different regions were performed for each sample.

The spectra obtained are shown in Fig. 3. Fig. 3a reports a typical spectrum for the more homogeneous samples here considered (CT10, CT90), while in Fig. 3b, the spectroscopic responses at five different points of CT50 are reported to check the spatial distribution of the various phases in this quite heterogeneous material. The Raman spectrum of cerium dioxide shows a main peak at 466 cm^{-1} (Fig. 3a). For a fluorite structure like that of CeO_2, six degenerate Raman active (F_{2g}) modes are expected.[2,36,43–46] The TiO_2 spectrum (Fig. 3d) shows bands at 150, 199, 396, 511, 633 cm^{-1}, in agreement with what has been reported in the literature for the anatase phase.[2,36,43,44]

The results in Fig. 3A for CT10 and CT90 are in agreement with those obtained from the XRD analysis (Fig. 1, Table 1) as the former sample mainly consists of anatase, while the second sample is essentially based on the ceria phase, with only a relatively minor peak related to anatase being visible at 150 cm^{-1}.

The CT50 sample is quite inhomogeneous, as shown by the spectra displayed in Fig. 3B. Three of the spectra (I to III) in fact show the typical bands of ceria and anatase, which are thus both present into the material, while the last two traces (IV and V) show the onset of a new set of lines at 168, 197, 275, 326, 362, 456, 560 and 631 cm^{-1} which can be assigned to the cerium titanate $Ce_2Ti_2O_7$ phase.[44] The presence of this phase, not detected by XRD for reasons discussed later, indicates that a strong interaction has occurred between ceria and titania in the mixed material.

Diffuse reflectance UV-Vis spectroscopy

UV-Vis diffuse reflectance spectra obtained from the mixed oxides are shown in Fig. 4, where they are compared with the spectra of bare TiO_2 (Fig. 4a), bare CeO_2 (Fig. 4c) and with that of an equimolar mechanical mixture of the two oxides obtained by the gentle and prolonged mixing of the two powders (Fig. 4b).

All three mixed oxides show a net red shift in the main optical transition with respect to the pure oxides and their mechanical mixture, indicating that the sol–gel method

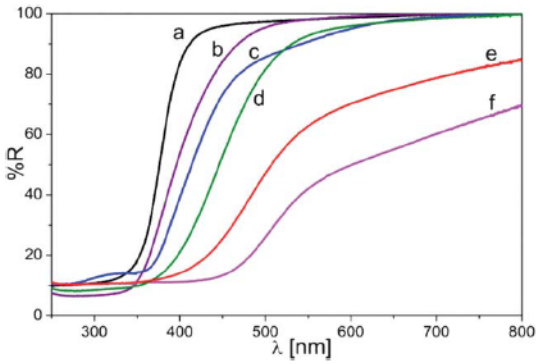

Fig. 4 Absorption spectra of (a) TiO_2, (b) a 1 : 1 mechanical mixture of TiO_2 and CeO_2, (c) CeO_2 (d) CT90, (e) CT10 and (f) CT50.

adopted for preparation favours an intimate interaction of the two components and that this interaction imparts peculiar optical properties to the mixed solids.

The present results differs from those reported by Coronado *et al.*[28] concerning CeO_2–TiO_2 materials prepared with a low Ce loading and by the wet impregnation of a TiO_2 matrix, for which the red shift observed with respect to the optical transition of titania is very small. This observation outlines the role of the preparation method in determining the physical properties of mixed oxides. The behaviour of the samples described here may be for more than one reason. The main reason seems to be the formation of cerium titanates, the presence of which was directly detected ($Ce_2Ti_2O_7$) by Raman spectroscopy, at least in the case of CT50. Pure $Ce_2Ti_2O_7$ (pyrochlore structure) contains Ce^{3+} and Ti^{4+} ions of eight-fold and six-fold coordination respectively. This compound is a brown solid, whose colour is due to the presence of Ce^{3+} ions with one electron in the strongly localized 4f orbitals.[47] In the case of CeO_2, the 4f states lie around the middle of the band gap and are empty in the case of fully oxidized ceria, while they are occupied ($4f^1$) when Ce^{3+} is formed in the reduced materials. The 4f electron of Ce^{3+} generates a pair of spin-orbit split states ($^2F_{5/2}$ $^2F_{7/2}$).[48] In the

more complex case of cerium titanates, the situation is similar to that of reduced CeO_2 with 8-coordinated Ce^{3+} ions. The same type of spin-orbit split state can thus be assumed to be present, which can absorb visible light *via* a charge transfer transition from 4f to the empty orbitals of Ti^{4+}.[44]

The strong coloration assumed by the mixed samples, (which reaches a maximum in the case of CT50, Fig. 4), is assigned to the presence of $Ce_2Ti_2O_7$, even though the presence of minor amounts of either Ce^{3+}-containing cerium titanates (Ce_2TiO_5), or of reduced Ce^{3+} ions in the CeO_2 matrix or at the oxide–oxide interface, cannot be excluded. Cerium titanates are likely to occur at the interfaces between ceria and titania crystals where their formation, upon the solid-state reaction during calcination, is more probable. Another form of oxide–oxide interaction is in principle possible when, at the heterojunction between two particles, charge transfer occurs, as in the case reported by Diwald and coworkers for the ZrO_2–TiO_2 system.[49]

XPS spectroscopy

Photoemission spectra of the Ce 3d and Ti 2p core levels of the different samples are displayed in Fig. 5. The Ce 3d photoemission peak undergoes changes as a function of Ce concentration.

At a low Ce content (CT10), the spectrum presents the typical line shape of Ce^{3+} compounds:[50] two main components can be detected at 881.2 eV and 885.5 eV, usually referred to as v^0 and v' in the literature, which are replicated by spin-orbit splitting (18.2 eV) at 899.4 eV and 903.7 eV, respectively.[36] The first peak is related to the emission from the Ce 3d states with a Ce $3d^94f^2$ O $2p^5$ final state, while in the second case the hole produced by the photoemission experiments is screened by a $3d^94f^1$ O $2p^6$ state. A very weak feature is also visible at 916.9 eV, (u'''), which is usually used as a qualitative fingerprint of the presence of Ce^{4+} ions and is connected to the poorly-screened Ce $3d^94f^0$ O $2p^6$ final state. Therefore the distinct structure of the Ce 3d photoemission line indicates the presence of a dominant phase, where Ce is present as Ce^{3+}, and a minority, fully oxidized CeO_2 phase.

The existence of ceria in the reduced state is well in line with previous photoemission data reported by several authors, either on materials obtained by sol–gel synthesis[2] or by wet impregnation.[51] In particular it has been demonstrated that at the interface between ceria and titania, Ce^{3+} ions are strongly stabilized thanks to the energy decrease of the Ce 4f levels as a result of the mixing with the O 2p band of titania.[52] However, the role of the size of the nanoparticles (the smaller the particle, the higher the defect concentration) influencing the abundance of reduced cerium ions cannot be excluded.

By increasing the amount of ceria (CT50 and CT90), the Ce 3d spectrum becomes very similar to the spectrum of stoichiometric ceria. In the Ce $3d_{5/2}$ peak, the most intense features are the peaks at 882.7 eV (v) and 888.5 eV (v''), which stem from different types of the final state screening of Ce^{4+} ions, Ce $3d^94f^2$ O $2p^4$ and Ce $3d^94f^1$ O $2p^5$, respectively. These two features are wider and less sharp than in the CeO_2 reference, indicating the residual presence of the v' component connected to Ce^{3+} species. However, as opposed to the CT10 sample, the u''' satellite is quite intense. We can therefore conclude that despite a prominent presence of oxidized ceria, in the CT50 and CT90 samples there are still Ce^{3+} ions present. Unfortunately, it is not possible to determine if these reduced species are present as interfacial defects or as a $Ce_2Ti_2O_7$ mixed oxide since there is no significant

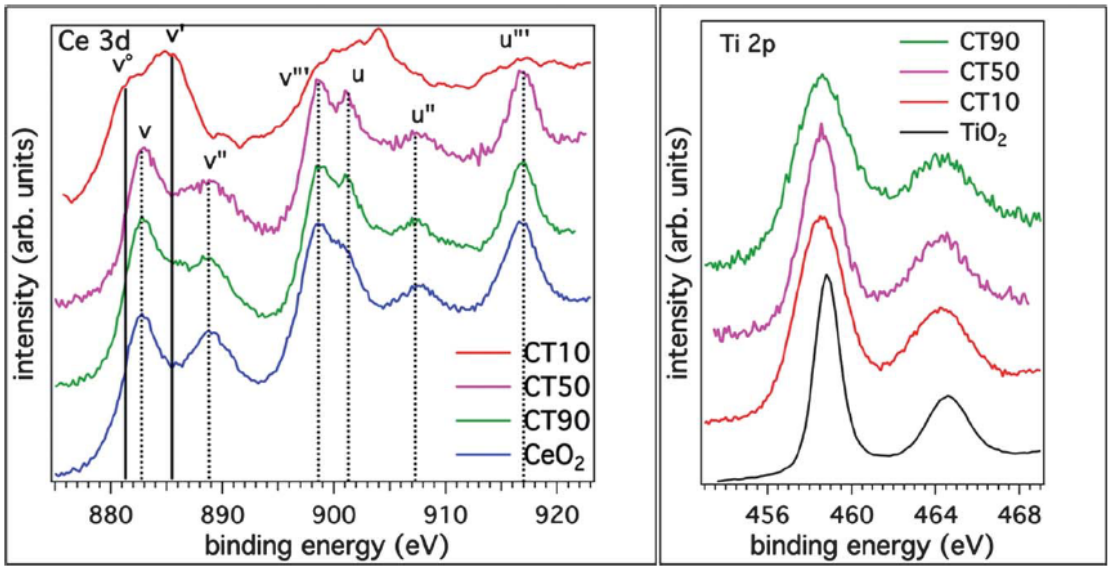

Fig. 5 Left: Ce 3d photoemission spectra. The different features due to the different final state configuration and oxidation state of ceria, are labelled according to the literature. The v and u components refer to different spin orbit degeneracies, *i.e.* $3d_{5/2}$ and $3d_{3/2}$ levels, respectively. The full lines indicate Ce^{3+}-related peaks, while the dotted lines highlight the photoemission from Ce^{4+} ions. Right: evolution of the Ti 2p photoemission spectra as a function of ceria content.

Table 2 Elemental analysis (molar percentage) of the different samples as determined by photoemission spectroscopy (XPS)

	% O	% Ce	% Ti	% CeO_2[a]
CT10	73.2	6.1	20.7	23
CT50	70.3	18.4	11.3	62
CT90	73.0	25.0	2.0	93

[a] This column reports the Ce molar concentration (in the region explored by XPS), expressed as CeO_2. This value is directly comparable with the nominal bulk concentration of each sample indicated by the label (10%, 50%, 90%).

chemical shift between cerium titanate or Ce_2O_3 (ref. 53) and the co-presence of the predominant CeO_2 phase prevents reliable separation of the chemically shifted components.

It is interesting to note that, despite the presence of Ce^{3+} species in the CT10, CT50 and CT90 samples, their optical absorption is quite different, suggesting that not only the compositional aspects but also the structural aspects (*i.e.* formation of an actual cerium titanate) should be taken into account to draw a thorough picture of this advanced material.

The spectrum of the Ti 2p core level indicates that titanium is always fully oxidized, as confirmed by the constant position of the peak maximum at 458.8 eV, which is typical of octahedrally coordinated Ti^{4+} ions.[54] However, it can be noted that the full width at half maximum of the Ti $2p_{3/2}$ peak for the composite is much higher than that of the reference TiO_2 powder. This can be interpreted as being due to the formation of a very intimate composite between the two oxides which determines a variability in the structural environment of the Ti^{4+} ions, or by the formation of ceria–titania hetero-interfaces characterized by different band bending and consequently small shifts of the core level positions.

By means of photoemission we also determined the composition of the different samples, as reported in Table 2. The intensity of the photoemission spectra has been normalized using the differential cross sections and asymmetry parameters provided by Yeh and Lindau[55] and the inelastic mean free path calculated using the TPP2 algorithm.[56]

As can be seen from Table 2, the data qualitatively reproduce the trend expected on the basis of the molar ratio used for the preparation, and we do not observe the previously reported enhancing of titanium species in the surface region.[2] In contrast, in the subsurface region monitored by photoemission spectroscopy, the concentration of Ce is higher (in particular for the CT10 and CT50 samples) than the stoichiometric value, indicating the propensity of the Ce component to disperse through the TiO_2 crystals. Moreover, oxygen is consistently in excess with respect to the theoretical value (66.6%), probably due to the presence of adsorbed water and hydroxyls.

Surface reactivity with oxygen and EPR spectroscopy

It is well known that bare CeO_2 easily loses and reincorporates oxygen under reductive and oxidative conditions respectively. This redox cycle occurs in the conditions of catalytic processes. However, simple annealing under a vacuum at moderate temperature is sufficient to cause oxygen loss, vacancy formation and excess electron release. When the annealed solid is in contact with oxygen under mild conditions (RT or lower temperature), electron transfer occurs with the formation of reduced oxygen species, including adsorbed O_2^- superoxide ions which are visible in EPR. The chemistry of superoxide adsorbed on ceria has been thoroughly described in a paper by J. C. Conesa and coworkers[57] who specifically adopt this reactivity as a tool to investigate the level of defects of the surface of the oxide. We have investigated the reactivity of our ceria–titania mixed materials after a mild reduction by annealing for 2 h at 573 K under a vacuum. In these conditions the system behaves similarly to pure cerium oxide, forming surface O_2^- superoxide ions upon the adsorption of O_2 onto the annealed samples. Fig. 6 compares the EPR spectra of adsorbed O_2^- obtained for CT10 and CT50 with that recorded for pure ceria (also prepared *via* the sol–gel method).

The spectrum related to ceria (Fig. 6a) shows the typical features already reported for this species[57] with the low field component of the g tensor at $g_{zz} = 2.039$ (the z direction corresponds to the oxygen internuclear axis) and with an anomalous value of the high field component which, instead of having the free spin value ($g_e = 2.0023$) as expected by the ionic model of adsorbed superoxide,[58] is at $g_{xx} = 2.010$ and is very close to g_{yy}, so producing an unresolved perpendicular line. The anomalous value of g_{xx} shown by superoxide ions on cerium

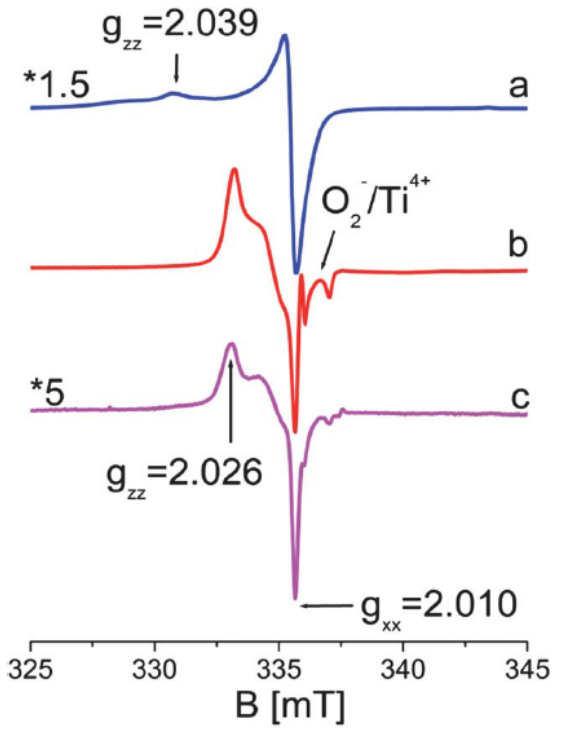

Fig. 6 EPR spectra recorded at 77 K of superoxide species adsorbed on (a) CeO_2, (b) CT10 and (c) CT50.

Table 3 EPR parameters (g values) of superoxide species

Centre	g_{zz}	g_{yy}	g_{xx}	Assignment
1	2.039	2.010–2	2.010–2	O_2^- on Ce^{4+} ions (bare oxide)
2	2.027	2.018	2.010	O_2^- on Ce^{4+} ions (mixed oxides)
3	2.027	2.010	2.004	O_2^- on Ti^{4+} ions

dioxide has already been discussed[57,59] in terms of a model involving some degree of covalence in the interaction of adsorbed oxygen with the 4f cerium orbitals and causing deviations from the purely ionic model (Table 3).

The spectra of O_2^- on mixed CT samples have a different line shape (Fig. 6b and c) to that recorded for bare cerium oxide (Fig. 6a). The spectra in the case of mixed materials, in fact, are more symmetric and cover a reduced magnetic field range. The lowest g component of the signal is the same as observed for CeO_2 ($g = 2.010$), thus suggesting that the adsorption site is a cerium ion in the case of the mixed materials. The low field g component is instead at $g_{zz} = 2.026$, much lower than that reported for ceria (2.039). The proximity of the three components causes the unusual line shape of the spectra in Fig. 6(b and c), as already reported in ref. 59.

Furthermore, particularly in the case of CT10, a few weak lines due to superoxide on Ti^{4+} ions are also present, likely due to the spillover of some superoxide from the Ce surface sites to Ti, because no reduced Ti^{3+} was observed on the sample prior to oxygen adsorption to suggest the direct electron transfer from Ti to oxygen. This detail confirms the presence of Ti sites at the surface of the mixed solids. The described spectra are similar to those reported by Coronado *et al.*[28] which were obtained on a CeO_2–TiO_2 sample with a low cerium loading (0.5%), prepared by the wet impregnation of titania. Similar spectra were also observed by the same authors on Cl-containing unsupported CeO_2 samples.[60]

The spectra of superoxide species adsorbed on mixed CeO_2–TiO_2 oxides in the present work are only partially affected by pumping at room temperature: under these conditions a fraction of superoxide disappears and another fraction remains adsorbed at the surface, producing the spectra in Fig. 6. This residual fraction disappears only if evacuation is performed at $T \geq 373$ K. This is the main difference between the present case and the spectra reported by the Madrid group on analogous systems.[28,45,60]

The pronounced differences between the two types of superoxide spectra (bare CeO_2 and mixed materials) prompted us to further investigate the superoxide adducts. The same experiment related to Fig. 6b was recorded using ^{17}O-enriched oxygen in order to observe the hyperfine structure of the ^{17}O nucleus (nuclear spin $I = 5/2$). Such a hyperfine structure (not reported for sake of brevity) indicates the presence of two magnetically equivalent oxygen atoms in the superoxide moiety[58,61] exactly as was observed in the case of pure CeO_2.[59] This points to the presence of a symmetric side-on moiety and excludes the presence of an end-on superoxide adduct capable of rotation around the Ce–O bond (and consequent g value averaging), for instance in the case of surface Co–O_2 species.[62]

Summarizing, the superoxide species formed by O_2 adsorption on pre-reduced mixed materials (Fig. 6b and c) have different g_{zz} values and therefore different spectral profiles from those formed on the bare oxide (Fig. 6a and ref. 57).

However, both types of species are adsorbed onto Ce^{4+} ions and are symmetrically adsorbed (side-on) on the top of the ion. The formation mechanism, despite the non-detectability of the EPR spectrum of Ce^{3+} was already proposed by Conesa and coworkers:

$$Ce^{3+} + O_{2\ (gas)} \rightarrow Ce^{4+}/O_2^- \quad (1)$$

The reason for the different lineshapes of the two types of superoxide species in Fig. 6 therefore needs to be searched for in the different environments of cerium in the bare and mixed oxides. This point is the object of further investigation in our group.

Conclusions

Three types of CeO_2–TiO_2 mixed oxides in a symmetrical range of compositions and with the molar fraction of each oxide not lower than 0.10 (CT10, CT50 and CT90) were prepared in this work. These particular compositions are distinguishable from the solids investigated in other systems by other authors, containing a small concentration of ceria dispersed in the TiO_2 matrix. The sol–gel method adopted for the preparation results in complex systems whose main features are described in the following.

1. The degree of mixing of the two phases is quite high (TEM-EDS), and the less abundant oxide component (cerium oxide in CT10 and titanium oxide in CT90) tends to disperse in the second phase, thus becoming undetectable by XRD (Fig. 1).

2. The two oxide components chemically interact to some extent, producing a mixed phase of cerium titanate ($Ce_2Ti_2O_7$, pyrochlore structure). In this compound the cerium is present as Ce^{3+}. The formation of the titanate is greatest in the case of CT50. The formation of the titanate is not revealed by X-ray diffraction but is observed by Raman spectroscopy and by optical absorption. The mixed materials in fact exhibit a band gap red shift with respect to the pure oxides (Fig. 4), which causes a pronounced absorption in the visible range. This is due to the presence of Ce^{3+} in the stoichiometry of the titanate (pyrochlore structure) which absorbs in the visible region, due to the presence of partially populated 4f levels ($4f^1$).

3. The surface of the system is complex and not homogeneous. XPS reveals the presence, in the surface and subsurface layers, of both Ce^{4+} and Ce^{3+} and of Ti^{4+} ions.

4. The mixed solids, when contacted with oxygen after annealing under vacuum, form superoxide species which are symmetrically adsorbed onto the Ce^{4+} ions (side on). However, the EPR signal of this species is markedly different from that of the corresponding species on CeO_2. The reason of such a difference (which is not due to the structure of the adduct) will be found in the particular type of Ce^{4+} adsorbing centers available at the surface of the mixed materials, which likely allows a different chemical interaction with oxygen. This topic,

which could be relevant to the catalytic properties of the mixed oxides, is currently under investigation in our laboratory.

Finally, the strong absorption in the visible region of the mixed solids (Fig. 4) prompted us to test the photochemical properties of the systems. The presence of photogenerated electrons and holes at the surface of the solid under irradiation with visible light was therefore investigated, using a methodology already illustrated in our previous work.[63] No trace of photogenerated charge carriers was observed. This indicates it is very likely that the heterogeneity of the system favours rapid electron–hole recombination. The potential applications of the oxide systems studied here are therefore more in the field of heterogeneous catalysis (where systems based on cerium have a prominent role) than in of photocatalysis.

Acknowledgements

This work has been supported by the Italian Ministry of University and Research, MIUR, through the "Programs of National Relevance" (PRIN-2009), the "National Funding for Basic Research" (FIRB) with a project entitled "Oxides at the Nanoscale: Functionalities and Applications" (FIRB RBAP11AYN), and a Local Project from University of Torino, ID: ORTO11RRT5, titled "Advances in Nanostructured Materials and Interfaces for Key Technologies".

Notes and references

1 Z. L. Liu, B. Guo, L. Hong and H. X. Jiang, *J. Phys. Chem. Solids*, 2005, **66**, 161–167.
2 J. Fang, X. Bi, D. Si, Z. Jiang and W. Huang, *Appl. Surf. Sci.*, 2007, **253**, 8952–8961.
3 P. Periyat, K. V. Baiju, P. Mukundan, P. K. Pillai and K. G. K. Warrier, *J. Sol-Gel Sci. Technol.*, 2007, **43**, 299–304.
4 F. Galindo, R. Gomez and M. Aguilar, *J. Mol. Catal. A: Chem.*, 2008, **281**, 119–125.
5 A. Trovarelli and P. Fornasiero, *Catalysis by Ceria and Related Materials*, Imperial College Press, London, 2nd edn, 2013.
6 J. Kaspar, P. Fornasiero and N. Hickey, *Catal. Today*, 2003, **77**, 419–449.
7 F. Esch, S. Fabris, L. Zhou, T. Montini, C. Africh, P. Fornasiero, G. Comelli and R. Rosei, *Science*, 2005, **309**, 752–755.
8 A. Trovarelli, C. de Leitenburg, M. Boaro and G. Dolcetti, *Catal. Today*, 1999, **50**, 353–367.
9 M. Cargnello, J. J. D. Jaen, J. C. H. Garrido, K. Bakhmutsky, T. Montini, J. J. C. Gamez, R. J. Gorte and P. Fornasiero, *Science*, 2012, **337**, 713–717.
10 S. K. Meher, M. Cargnello, H. Troiani, T. Montini, G. R. Rao and P. Fornasiero, *Appl. Catal., B*, 2013, **130**, 121–131.
11 A. L. Camara, M. Monte, A. Martinez-Arias and J. C. Conesa, *Catal. Sci. Technol.*, 2012, **2**, 2436–2439.
12 D. Gamarra, A. L. Camara, M. Monte, S. B. Rasmussen, L. E. Chinchilla, A. B. Hungria, G. Munuera, N. Gyorffy, Z. Schay, V. C. Corberan, J. C. Conesa and A. Martinez-Arias, *Appl. Catal., B*, 2013, **130**, 224–238.
13 A. Martinez-Arias, A. B. Hungria, A. Iglesias-Juez, M. Fernandez-Garcia, J. A. Anderson, J. C. Conesa, G. Munuera and J. Soria, *Catal. Today*, 2012, **180**, 81–87.
14 P. Jasinski, T. Suzuki and H. U. Anderson, *Sens. Actuators, B*, 2003, **95**, 73–77.
15 N. Izu, W. Shin, N. Murayarna and S. Kanzaki, *Sens. Actuators, B*, 2002, **87**, 95–98.
16 S. D. Park, J. M. Vohs and R. J. Gorte, *Nature*, 2000, **404**, 265–267.
17 A. B. Stambouli and E. Traversa, *Renewable Sustainable Energy Rev.*, 2002, **6**, 433–455.
18 S. Yabe and T. Sato, *J. Solid State Chem.*, 2003, **171**, 7–11.
19 T. Montini, M. A. Banares, N. Hickey, R. Di Monte, P. Fornasiero, J. Kaspar and M. Graziani, *Phys. Chem. Chem. Phys.*, 2004, **6**, 1–3.
20 T. Montini, N. Hickey, P. Fornasiero, M. Graziani, M. A. Banares, M. V. Martinez-Huerta, I. Alessandri and L. E. Depero, *Chem. Mater.*, 2005, **17**, 1157–1166.
21 P. R. Shah, T. Kim, G. Zhou, P. Fornasiero and R. J. Gorte, *Chem. Mater.*, 2006, **18**, 5363–5369.
22 G. R. Bamwenda and H. Arakawa, *J. Mol. Catal. A: Chem.*, 2000, **161**, 105–113.
23 A. L. Linsebigler, G. Q. Lu and J. T. Yates, *Chem. Rev.*, 1995, **95**, 735–758.
24 A. Gallo, T. Montini, M. Marelli, A. Minguzzi, V. Gombac, R. Psaro, P. Fornasiero and V. Dal Santo, *ChemSusChem*, 2012, **5**, 1800–1811.
25 J. C. Conesa, *J. Phys. Chem. C*, 2010, **114**, 22718–22726.
26 A. Hagfeldt and M. Gratzel, *Chem. Rev.*, 1995, **95**, 49–68.
27 N. Serpone and E. Pelizzetti, *Photocatalysis: Fundamentals and Applications*, Wiley & Sons, Chicister, 1989.
28 J. M. Coronado, A. J. Maira, A. Martinez-Arias, J. C. Conesa and J. Soria, *J. Photochem. Photobiol., A*, 2002, **150**, 213–221.
29 Q. Z. Yan, X. T. Su, Z. Y. Huang and C. C. Ge, *J. Eur. Ceram. Soc.*, 2006, **26**, 915–921.
30 J. Lin and J. C. Yu, *J. Photochem. Photobiol., A*, 1998, **116**, 63–67.
31 A. W. Xu, Y. Gao and H. Q. Liu, *J. Catal.*, 2002, **207**, 151–157.
32 S. W. Chen, J. M. Lee, K. T. Lu, C. W. Pao, J. F. Lee, T. S. Chan and J. M. Chen, *Appl. Phys. Lett.*, 2010, **97**, 012104.
33 J. Rynkowski, J. Farbotko, R. Touroude and L. Hilaire, *Appl. Catal., A*, 2000, **203**, 335–348.
34 S. Pavasupree, Y. Suzuki, S. Pivsa-Art and S. Yoshikawa, *J. Solid State Chem.*, 2005, **178**, 128–134.
35 T. Lopez, F. Rojas, R. Alexander-Katz, F. Galindo, A. Balankin and A. Buljan, *J. Solid State Chem.*, 2004, **177**, 1873–1885.
36 B. S. Liu, X. J. Zhao, N. Z. Zhang, Q. N. Zhao, X. He and J. Y. Feng, *Surf. Sci.*, 2005, **595**, 203–211.
37 H. Yang, K. Zhang, R. Shi and A. Tang, *J. Am. Ceram. Soc.*, 2007, **90**, 1370–1374.
38 Y.-H. Xu, H.-R. Chen, Z.-X. Zeng and B. Lei, *Appl. Surf. Sci.*, 2006, **252**, 8565–8570.
39 B. Murugan and A. V. Ramaswamy, *J. Phys. Chem. C*, 2008, **112**, 20429–20442.
40 S. Watanabe, X. Ma and C. Song, *J. Phys. Chem. C*, 2009, **113**, 14249–14257.

41 L. Lutterotti, *Nucl. Instrum. Methods Phys. Res., Sect. B*, 2010, **268**, 334–340.

42 A. Adamski, T. Spalek and Z. Sojka, *Res. Chem. Intermed.*, 2003, **29**, 793–804.

43 B. M. Reddy and A. Khan, *Catal. Surv. Asia*, 2005, **9**, 155–171.

44 M. Martos, B. Julian-Lopez, J. Vicente Folgado, E. Cordoncillo and P. Escribano, *Eur. J. Inorg. Chem.*, 2008, 3163–3171.

45 A. Martinez-Arias, M. Fernandez-Garcia, L. N. Salamanca, R. X. Valenzuela, J. C. Conesa and J. Soria, *J. Phys. Chem. B*, 2000, **104**, 4038–4046.

46 M. L. Dos Santos, R. C. Lima, C. S. Riccardi, R. L. Tranquilin, P. R. Bueno, J. A. Varela and E. Longo, *Mater. Lett.*, 2008, **62**, 4509–4511.

47 S. Otsuka-Yao-Matsuo, T. Omata and M. Yoshimura, *J. Alloys Compd.*, 2004, **376**, 262–267.

48 A. Pfau and K. D. Schierbaum, *Surf. Sci.*, 1994, **321**, 71–80.

49 N. Siedl, M. J. Elser, J. Bernardi and O. Diwald, *J. Phys. Chem. C*, 2009, **113**, 15792–15795.

50 P. Burroughs, A. Hamnett, A. F. Orchard and G. Thornton, *J. Chem. Soc., Dalton Trans.*, 1976, 1686–1698.

51 S. Kundu, J. Ciston, S. D. Senanayake, D. A. Arena, E. Fujita, D. Stacchiola, L. Barrio, R. M. Navarro, J. L. G. Fierro and J. A. Rodriguez, *J. Phys. Chem. C*, 2012, **116**, 14062–14070.

52 J. Graciani, J. J. Plata, J. F. Sanz, P. Liu and J. A. Rodriguez, *J. Chem. Phys.*, 2010, **132**, 104703.

53 E. Beche, P. Charvin, D. Perarnau, S. Abanades and G. Flamant, *Surf. Interface Anal.*, 2008, **40**, 264–267.

54 V. V. Atuchin, V. G. Kesler, N. V. Pervukhina and Z. Zhang, *J. Electron Spectrosc. Relat. Phenom.*, 2006, **152**, 18–24.

55 J. J. Yeh and I. Lindau, *At. Data Nucl. Data Tables*, 1985, **32**, 1–155.

56 S. Tanuma, C. J. Powell and D. R. Penn, *Surf. Interface Anal.*, 1993, **20**, 77–89.

57 J. Soria, A. Martinez-Arias and J. C. Conesa, *J. Chem. Soc., Faraday Trans.*, 1995, **91**, 1669–1678.

58 M. Che and A. J. Tench, *Adv. Catal.*, 1983, **32**, 1–148.

59 M. Che, J. F. J. Kibblewhite, A. J. Tench, M. Dufaux and C. Naccache, *J. Chem. Soc., Faraday Trans. 1*, 1973, **69**, 857–863.

60 J. Soria, J. C. Conesa and A. Martinez-Arias, *Colloids Surf., A*, 1999, **158**, 67–74.

61 M. Chiesa, E. Giamello, M. C. Paganini, Z. Sojka and D. M. Murphy, *J. Chem. Phys.*, 2002, **116**, 4266–4274.

62 E. Giamello, Z. Sojka, M. Che and A. Zecchina, *J. Phys. Chem.*, 1986, **90**, 6084–6091.

63 G. Barolo, S. Livraghi, M. Chiesa, M. C. Paganini and E. Giamello, *J. Phys. Chem. C*, 2012, **116**, 20887–20894.

CHAPTER 6

6.1 CONCLUSIONS AND PERSPECTIVES

ZTB was a quite convenient precursor for the formation of zirconia films. The obtained Zirconia films for coverages higher than 3-4 ML were free from carbonaceous species. The optimization of the deposition procedure allowed us to obtain a satisfactorily, reproducible, linear film growth, even by varying the pressure. We have observed a great difference in respect to the sol-gel preparation techniques, highly used in the industry, for a deposition of a thin film in UHV. In the former methods a mixed oxide with highly acidic properties is reasonably obtainable whereas in the case of zirconia deposition via ZTB on silicon, copper and rutile no mixed oxides were clearly observed. However and definitely more important the interface study for these three substrates was the richest in information of interfacial properties. Ranging from the formation of micro-dimensional grains on silicon, to hexagonal LEED patterns on copper and finally to Zr_2O_3 nanochains on TiO_2(110). Computational studies demonstrated how methanol and water dissociate at bridging oxygen vacancies and at reduced step edges thus a plausibile hypothesis would be that initial ZTB molecules would adsorb onto these sites. Further studying of this work's system via STM would clarify structure of Zr_2O_3 nanochains and especially verify the hypothesis. Furthermore, a study of the zirconia-titania system obtained via metal evaporation would be interesting as carbon contamination would be avoided and thus probably a long range order would be observed on TiO_2(110) or even the obtaining of a superficial alloy.

The growth of CeO_x overlayers was studied by STM and photoemission, observing distinct oxidic nanostructures as a function of ceria coverage. It has been demonstrated that the deposition of CeO_x strongly affects titania morphology leading to the formation of extensive oxygen reconstructions and eventually of peculiar dumbbell nanostructures made by Ti_2O_3 strands decorated by Ce_2O_3. At higher coverage, three long range ordered oxide phases, both characterized by ceria in reduced form, have been identified. The variety of phases obtained was surprising; a feature seldom found in literature and that garners, at least at the ultrathin level on TiO_2(110), a great potential for the uncovering of further structures and functionalities. The observed band bending and shifting of the valence spectra clearly points to a modification of the electronic properties of the composite ceria–titania system with respect to bulk-like materials and consequently the reactivity of the CeO_x–TiO_2 system greatly differs from the simple sum of its components. The chemical activity of these new nanostructures has been investigated using methanol and ethanol as probe molecules. The TPD studies indicate that the ceria–titania nanostructures possess a very special chemical activity for the selective, partial dehydrogenation of alcohols to aldehydes at an extremely mild temperature (330 K). The comparison with the data obtained without oxygen pre-exposure, indicated the pivotal role played by oxygen in the high temperature reaction paths. As a matter of fact, the absence of oxygen suppresses almost totally the formation of

methane and ethylene respectively from methanol and ethanol. We can also notice that oxygen pre dosing affects the water spectrum: the desorption peak in presence of oxygen is much larger and extends to higher temperature. In case of both investigated films, pre-dosing of oxygen does not kill the reactivity of the system by healing defects or oxidizing reduced species, but on the other hand it greatly affects selectivity. This chemical reactivity identifies a substrate that mimics neither CeO_2(111) nor TiO_2(110) independently. The CeO_x/TiO_2(110) system is expected to have a great impact on the field of photo-induced cross-coupling of formaldehyde with methoxy species to produce more complex molecules, since it can provide both reactants on the surface at relatively low temperatures. Finally, ceria-titania mixed oxide powders were characterized via XPS and we have observed that for increasing amount of cerium the element gradually became present at its highest oxidation state Ce(IV). By XPS we have also determined the formation of a very intimate composite between the two oxides by observing the increasing full width at half maximum of the Ti2p peak for increasing amounts of cerium. Furthermore, compositional calculation showed that cerium had the tendency to disperse within the titania particles. These data helped to uncover a possibly good recipe for the formation of cerium titanate a composite with good oxygen storage capacity.

Acknowledgements

These four years of research have been interesting and I have learned many things as well as a completely new point of view. More importantly, each person I have met along this road has contributed to my betterment. Truly this work would not have been finished without the help of these people.

Thus first and foremost I want to thank my supervisor Prof. Gaetano Granozzi for the support, infinite patience and source of inspiration in classes and proposed seminars.

Next I want to thank Prof. Gian Andrea Rizzi whose long standing friendship has supported me in distressful times.

I want to warmly thank Dr. Stefano Agnoli for the work we have done together and for the continuing support.

I especially want to thank my wife whose love and support have always made my step lighter. Furthermore, she honored me with the birth of our splendid daughter Maria Ester whose big brown eyes have always warmed my heart and made me shed a little tear.

Next I want to thank my parents (Joe Henry and Maria Teresa), god-parents (Giuliano and Tina), all my in-laws (Giuseppe, Pierina, Gessica, Lides, Lara and Michele, Agostino and Glenda, Margherita), my brother Mattia, my niece Shaneesja Chandra, my nephews Giuseppe and Gregorio, my relatives (Carlo, Paola, Anna, Michela, Aunt Maggie, Aunt Mary, Barbara, Akilah, Tina, Anthony and all the rest of the Reeder and Tonegato families). Their love, friendship and support have always brought a smile on my face no matter how cloudy the day.

I want to thank friends Amardharmachandrananansing Khanye and wife Shirley with whom I have enjoyed long years of friendship and trust. Stefano Parrella whose jokes have always made me laugh and lighted my heart. Michele Fazzini and his family, Fabio Bidinost and his family, Matteo Treossi and many, many more..

Finally I wish to thank my colleagues: Luca Artiglia, Dmytro Chirkov, Jian Zheng and Ling-ling, Giuseppe Giallongo, Marco Favaro and Mattia Cattelan.

Thank you, thank you all!